HYDRODYNAMIC SIMULATION OF BIOLOGICAL PROPULSION SYSTEMS AND APPLICATION ON THE DESIGN OF OPTIMAL MARINE PROPULSORS

A Thesis Submitted by

VASILEIOS Th. TSARSITALIDIS

Naval Architect & Marine Engineer MEng
NTUA

Computational Mechanics MSc
NTUA

to

SCHOOL OF NAVAL ARCHITECTURE AND MARINE ENGINEERING

Of

NATIONAL TECHNICAL UNIVERSITY OF ATHENS

In Partial Fulfilment of the Requirements for the Degree of Doctor of Engineering, Specializing in marine hydrodynamics and propulsion / Division of Marine Hydrodynamics

Athens, January 2015

European Union
European Social Fund

OPERATIONAL PROGRAMME
EDUCATION AND LIFELONG LEARNING
investing in knowledge society
MINISTRY OF EDUCATION & RELIGIOUS AFFAIRS
MANAGING AUTHORITY

NSRF 2007-2013
programme for development
EUROPEAN SOCIAL FUND

Co-financed by Greece and the European Union

National Technical University of Athens

School of Naval Architecture and Marine Engineering

Division of Ship and Marine Hydrodynamics

Hydrodynamic Simulation of Biological Propulsion Systems and Application on the Design of Optimal Marine Propulsors

PhD Thesis

VASILEIOS Th. TSARSITALIDIS

Supervisor: G. Politis

Three member consultant committee: G. Politis

G. Tzabiras

G. Triantafyllou

Examination Committee

.

……..	……..	……..
G. Politis	G. Tzabiras	G. Triantafyllou
Professor	Professor	Professor
School of Naval Architecture and Marine Engineering	School of Naval Architecture and Marine Engineering	School of Naval Architecture and Marine Engineering
NTUA	NTUA	NTUA
……..	……..	……..
A. Papanikolaou	K. Belibassakis	S. Voutsinas
Professor	Associate Professor	Associate Professor
School of Naval Architecture and Marine Engineering	School of Naval Architecture and Marine Engineering	School of Mechanical Engineering
NTUA	NTUA	NTUA

……..

V. Riziotis

Lecturer

School of Mechanical Engineering

NTUA

-

This research has been co-financed by the European Union (European Social Fund – ESF) and Greek national funds through the Operational Program "Education and Lifelong Learning" of the National Strategic Reference Framework (NSRF) - Research Funding Program: Heracleitus II. Investing in knowledge society through the European Social Fund.

" To the dolphin alone, nature has given that which the best philosophers seek: Friendship for no advantage. Though it has no need of help from any man, it is a genial friend to all and has helped mankind."

- Plutarch

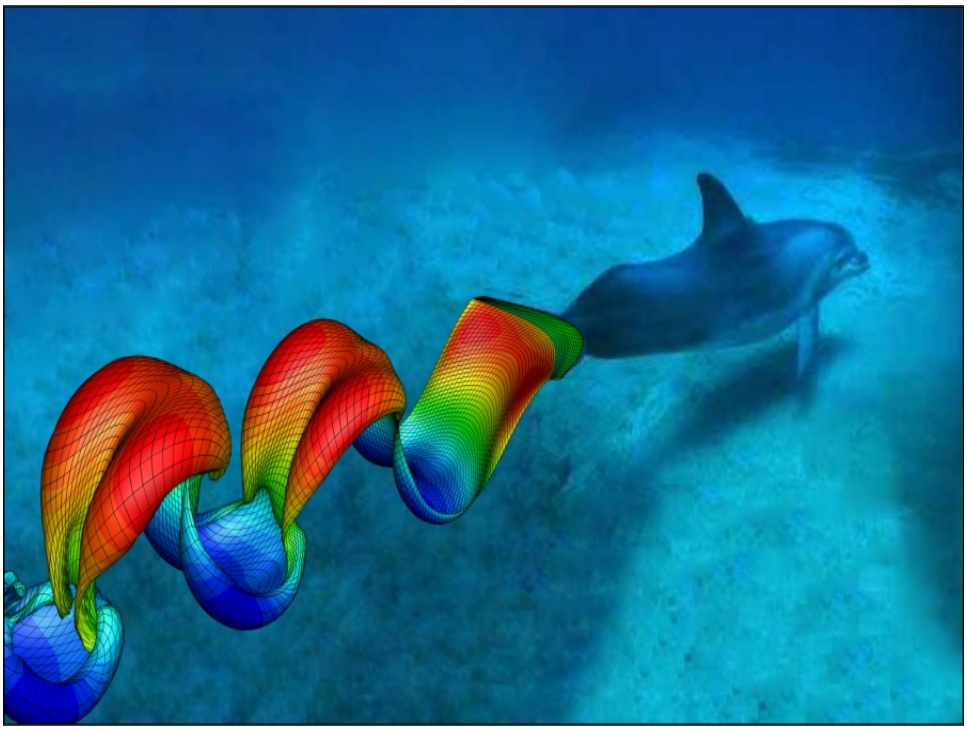

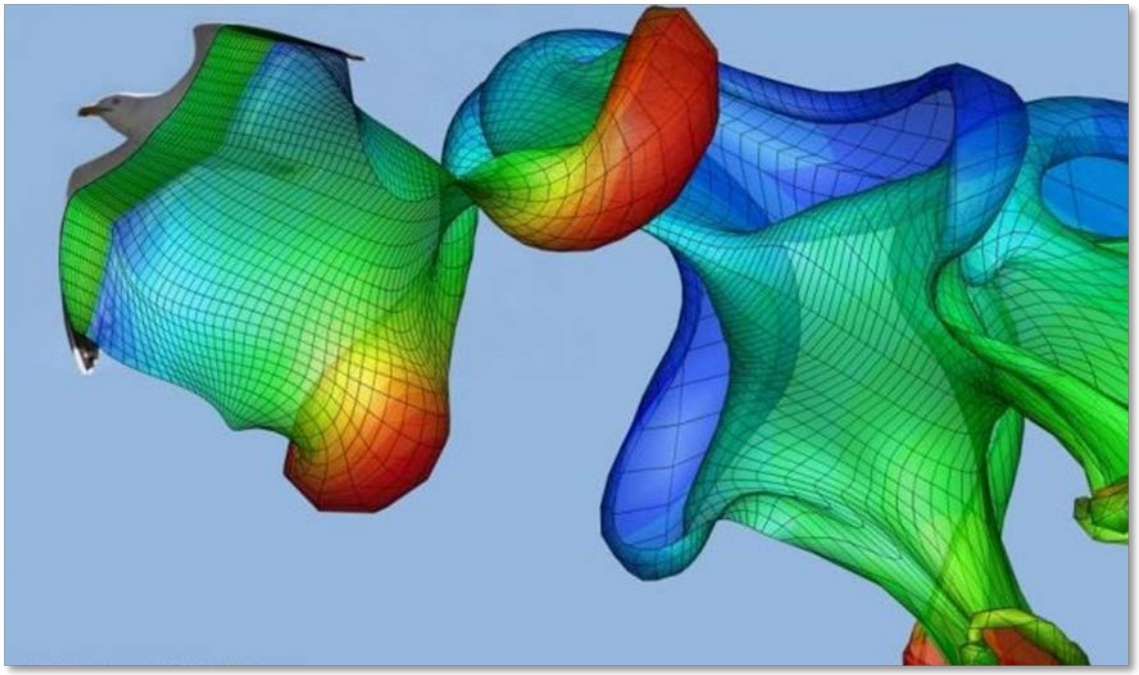

ABSTRACT IN GREEK: ΥΔΡΟΔΥΝΑΜΙΚΗ ΠΡΟΣΟΜΟΙΩΣΗ ΒΙΟΛΟΓΙΚΩΝ ΣΥΣΤΗΜΑΤΩΝ ΠΡΟΩΣΗΣ ΚΑΙ ΕΦΑΡΜΟΓΗ ΣΤΗ ΣΧΕΔΙΑΣΗ ΒΕΛΤΙΣΤΩΝ ΣΥΣΤΗΜΑΤΩΝ ΠΡΟΩΣΗΣ ΠΛΟΙΟΥ

(αγγλικός τίτλος: "Hydrodynamic Simulation of Biological Propulsion Systems and Application on the Design of Optimal Marine Propulsors")

Καθ' όλη την καταγεγραμμένη ιστορία του, ο άνθρωπος στρεφόταν στην φύση για έμπνευση όταν έψαχνε για αποδοτικά μέσα. Από την αρχαία μυθολογία μέχρι την επιστημονική φαντασία, παρουσιάζονται ιπτάμενες μηχανές που μοιάζουν με πουλιά (ορνιθόπτερα) και υποβρύχια που μοιάζουν με ψάρια. Πολλοί εφευρέτες προσπάθησαν να αντιγράψουν την φύση, αλλά οι περισσότεροι αποθαρρύνθηκαν από την πολυπλοκότητα της κατασκευής και της μηχανικής των ρευστών

Μετά από εκατομμύρια χρόνια εξέλιξης, τα ψάρια ανέπτυξαν ικανότητες μακράν ανώτερες από τα μεγαλύτερα επιτεύγματα της σύγχρονης ναυπηγικής. Ενστικτωδώς, χρησιμοποιούν τα σώματά τους, ώστε να πετυχαίνουν υψηλή απόδοση, επιτάχυνση και ελικτική ικανότητα.

Τα δελφίνια, για παράδειγμα, κολυμπούν με χάρη και προφανή ευκολία δίπλα σε πλοία που ταξιδεύουν με 20 κόμβους. Θαλάσσιοι βιολόγοι αναφέρουν ότι κιτρινόπτεροι τόνοι τραβούν την πετονιά με ταχύτητες που ξεπερνούν τους 40 κόμβους, ενώ οι σολομοί πηδούν κόντρα στο ρεύμα του ποταμού με απότομες επιταχύνσεις που συχνά ξεπερνούν τα 20G.

Ενώ η σύγχρονη αεροναυπηγική, εξελίσσεται ραγδαία τα τελευταία 100 χρόνια, οι ιπτάμενες μηχανές της φύσης, με 150 εκατομμύρια χρόνια εξέλιξης, παραμένουν μακράν ανώτερες. Μία απλή σύγκριση, όπως τίθεται από Triantafyllou & Triantafyllou (1995) εκπλήσσει τους πάντες. Οι άνθρωποι κινούνται με μέγιστη ταχύτητα 3-4 μήκη σώματος το δευτερόλεπτο, ένα άλογο αγώνων, περίπου 7 και το ταχύτερο τετράποδο (cheetah),πετυχαίνει 18 μήκη σώματος το δευτερόλεπτο. Ένα υπερηχητικό αεροσκάφος σαν το SR 71 Blackbird που ταξιδεύει με Mach 3 καλύπτει περίπου 32 μήκη το δευτερόλεπτο. Από την άλλη, ένα κοινό περιστέρι κινείται με 75 μήκη σώματος το δευτερόλεπτο, το ψαρόνι πετάει στα 120, ενώ είδη χελιδονιού ξεπερνούν τα 140. Η ταχύτητα περιστροφής (roll rate) ενός αεροβατικού αεροσκάφους σαν το (A4 skyhawk) λέγεται ότι είναι 270 μοίρες το δευτερόλεπτο, σπουργίτια και χελιδόνια ξεπερνούν τις 5000 μοίρες το δευτερόλεπτο, ενώ ξεπερνούν τα 14G επιταχύνσεων εκατοντάδες φορές την ημέρα, ενώ τα καλύτερα μαχητικά αεροσκάφη μόλις που αντέχουν 10-11G.

Ως μηχανικοί (και άνθρωποι εν γένει), έχουμε έμφυτη την αναζήτηση της βελτίωσης, η οποία εκφράζεται στην περίπτωση της πρόωσης, στην ανάγκη για αύξηση της απόδοσης. Το γεγονός αυτό, μαζί με την σύγχρονη τάση του για μέσα φιλικά προς το περιβάλλον, κάνει ακόμα πιο επιτακτική την ανάγκη να διερευνηθούν εναλλακτικά μέσα πρόωσης.

Όπως πολύ σωστά ετέθη από τον Rozhdestvensky (2003), είναι εμφανές ότι το ενδιαφέρον για βιομιμητικά συστήματα δικαιολογείται, καθώς τέτοια συστήματα:

- Μπορούν να θεωρηθούν 'καθαρά' από οικολογικής άποψης

- Λειτουργούν σε σχετικά χαμηλές συχνότητες
- Λειτουργούν με αρκετά υψηλή απόδοση
- Είναι πολυχρηστικά, με την έννοια της ικανότητας να λειτουργούν σε διάφορες καταστάσεις κίνησης και φόρτισης
- Συνδυάζουν τη λειτουργία του προωστήρα, της επιφάνειας ελέγχου και του μέσου σταθεροποίησης
- Μπορούν να παρέχουν στατική ώση, αλλά και μεγάλη ελικτική ικανότητα
- Κατέχουν καλύτερα χαρακτηριστικά σπηλαίωσης από συμβατικές έλικες
- Έχουν μικρή (σχετικά) αντίσταση στην ανενεργή κατάσταση
- Επιτρέπουν (ενίοτε απαιτούν) την χρήση σύγχρονων τεχνολογιών, όπως προχωρημένα συστήματα ελέγχου, πιεζοηλεκτρικά σύνθετα υλικά, τεχνητούς μύες κ.α.

Σε αυτό το κλίμα και έχοντας όλα τα παραπάνω υπ' όψιν, η παρούσα εργασία προσανατολίζεται στην χρήση της μεθόδου των συνοριακών στοιχείων (κώδικας UBEM) για την προσομοίωση βιολογικών συστημάτων πρόωσης, με στόχο την κατανόηση φαινομένων και την εξαγωγή συμπερασμάτων που θα οδηγήσουν στην σχεδίαση βέλτιστων προωστήρων πλοίου. Η χρήση της συγκεκριμένης μεθόδου ενδείκνυται, καθώς μπορεί με μεγάλη (σχετικά) ταχύτητα να προσομοιώσει μη μόνιμα φαινόμενα, καθώς και να παράξει αρκετή, συγκεντρωμένη πληροφορία για τα φαινόμενα που εκτυλίσσονται.

Πιο συγκεκριμένα, αφού γίνει μία γενική παρουσίαση του τυπικού προβλήματος ενός βιομιμητικού προωστήρα, παρουσιάζεται το μαθηματικό μοντέλο των συνοριακών στοιχείων, η αριθμητική εφαρμογή αυτού και η τελική υλοποίησή του σε ένα πρόγραμμα.

Ύστερα, παρουσιάζονται κατά σειρά, οι διερευνήσεις που πραγματοποιήθηκαν ως προς την πλειοψηφία των ελεύθερων παραμέτρων του προβλήματος, αλλά και των διαφορετικών περιπτώσεων, δείχνοντας τα αποτελέσματα που παρουσιάστηκαν στις (παρακάτω αναφερόμενες) δημοσιευμένες εργασίες, αλλά και πρόσθετα αποτελέσματα, από τα οποία προκύπτει μία εκτεταμένη συστηματική σειρά προωστήρων, που μπορεί να χρησιμοποιηθεί κατά συμβατό τρόπο με τις γνωστές ως τώρα μεθόδους σχεδίασης. Η ανεπτυγμένη μεθοδολογία, μαζί με εφαρμογές αυτής παρουσιάζονται και συγκρίνονται με συμβατικούς προωστήρες, όπου και αποδεικνύεται η υπεροχή των υπό μελέτη συστημάτων.

Τέλος, παρουσιάζονται οι τελευταίες εξελίξεις που αφορούν την εφαρμογή υδροελαστικότητας κατά την έννοια του ελαστικά εδρασμένου πτερυγίου (ένας βαθμός ελευθερίας - pitch) και κάποια πρώτα αποτελέσματα της συστηματικής διερεύνησης αυτού, καθώς και η χρήση ενεργού ελέγχου. Η δυνατότητα χρήσης αυτών σε περιβάλλον τυχαίων κινήσεων, δείχνει την δυνατότητα χρήσης των βιομιμητικών προωστήρων ως συστήματα εξοικονόμησης ενέργειας, ενώ στην κατακλείδα παρουσιάζονται προτεινόμενες εφαρμογές σε μετατροπή υπαρχόντων πλοίων, σε νέους σχεδιασμούς, αλλά και εφαρμογή σε πλοίο μηδενικών ρύπων.

Οι δημοσιεύσεις που προέκυψαν στα πλαίσια του προγράμματος είναι:

Politis, G.K. & Tsarsitalidis, V.T (2009). 'Simulating Biomimetic (Flapping Foil) Flows for Comprehension, Reverse Engineering and Design'. First International Symposium on Marine Propulsors, smp'09, Trondheim, Norway.

Politis, G.K. & Tsarsitalidis, V.T (2010). 'Understanding Birds's flight, using a 3-D BEM method and a time stepping algorithm'. 4th IC-SCCE 2010, Athens, Greece.

Politis, G.K. & Tsarsitalidis, V.T (2011). 'Exploring the Potential of an Oscillating Duct as a Marine Propulsor'. Second International Symposium on Marine Propulsors, smp'11, Hamburg, Germany.

Politis, G. & V. Tsarsitalidis (2012). "Flexible Oscillating Duct: An approach to a novel propulsor." Applied Ocean Research (Journal) 36: 36-50.

Politis, G.K., Tsarsitalidis, V.T., (2013). "Biomimetic Propulsion using twin oscillating wings". Third International Symposium on Marine Propulsors, SMP'13. Tasmania, Australia

Politis, G.K., Ioannou, T., Tsarsitalidis, V.T., (2013). "Flexible Elliptic Oscillating Duct. Taking the FOD one step further". Third International Symposium on Marine Propulsors, SMP'13. Tasmania, Australia

Politis, G.K., Tsarsitalidis, V.T., (2014). "Flapping Wing Propulsor Design: An approach based on systematic 3D-BEM simulations". Ocean Engineering (Journal) Vol 84, pp. 98-123

Part I INTRODUCTION

Throughout his whole history, man has sought in nature for inspiration, in his quest for effective ways of *transportation*. From ancient mythology to science fiction, there are ornithopters and fish-like submarines. Up to very recently, many inventors have tried to imitate nature, but most have been discouraged by the complexity of construction and fluid dynamics and lack of powerful design tools. Nature on the other hand, had more time and patience.

Over millions of years, marine animals have evolved into avid swimmers, with capabilities far superior in many ways to any achievement of nautical science and technology. Their superbly streamlined bodies are used by instinct, to exploit fluid-mechanical principles in ways naval architects today can only imagine, achieving outstanding propulsive efficiencies, acceleration and maneuverability.

Dolphins, for instance, move through water gracefully and easily, following and playing around ships cruising at 20 knots or more. It has also been reported that yellowfin tuna caught on a fishing line can pull the line at speeds exceeding 40 knots. The aggressive pike overcomes its prey with short bursts of acceleration that can exceed 20G.

While aeronautical technology has advanced rapidly over the past hundred years, nature's flying machines, which have evolved over 150 million years, are still impressive. A simple comparison, as very finely put by Triantafyllou and Triantafyllou (1995) can astonish anyone. “Humans move at top speeds of 3-4 body lengths per second, a race horse runs approximately 7 body lengths per second, and the fastest terrestrial animal, a cheetah, accomplishes 18 body lengths per second. A supersonic aircraft such as the SR 71 Blackbird travelling near Mach 3 (~2000 mph) covers about 32 body lengths per second. Yet a common pigeon frequently attains speeds of 50 mph; this converts to 75 body lengths per second. A European Starling (Sturnus vulgaris) is capable of flying at 120 and various species of Swifts over 140 body lengths per second The roll rate of highly aerobatic aircraft (e.g., A-4 Skyhawk) is said to be approximately 720 degrees per second, while a Barn Swallow (Hirundo rustics) has a roll rate in excess of 5000 degrees per second. The maximum positive G-forces permitted in most general aviation aircraft is 4-5Gs and select military aircraft withstand 8-10Gs. However, many birds have been calculated to routinely experience (i.e., hundreds of times each day) positive G-forces in excess of 10Gs and up to 14Gs.”

As it was very well expressed by Rozhdestvensky (2003), It is evident that the interest in biomimetic devices is justified because such systems:

“

- can be viewed as “ecologically” pure,
- are relatively low-frequency systems,
- possess sufficiently high efficiency,
- are multi-functional in the sense of being capable of operating in different regimes of motion,
- can combine the function of propulsor, control device, and stabilizer,
- can provide static thrust,
- can provide high maneuverability,
- possess more acceptable cavitation characteristics than conventional propellers,
- have relatively low aerodynamic drag in the “switched-off” position,
- allow the use of modern controls, MEMS, piezoelectric, reciprocating chemical muscles (RCM), and other technologies.

”

The above quotations alone, provide enough motivation for any researcher to pursue the subject further and convince that, when fully exploited, such systems will surpass the existing technologies.

I.1 Thesis - scope

Biomimetics is a vast and fast advancing region of science and engineering. As it is obvious to most engineers, three million years of natural evolution have produced much more remarkable results than a century of manmade engineering. Consequently, it is becoming clear that reverse engineering of nature can help us produce more efficient machines, materials and can show the way to advanced technologies.

Following this trend, in order to make more efficient marine propulsion systems, it is necessary to observe and imitate the most advanced sea creatures (specifically big fishes like tuna or sharks and sea mammals)

From the mechanics point of view, there have been many patents over the last decade and many kinds of mechanism that can imitate the movement of the fish. Lately driven by the new regulations for reduced emissions, higher efficiency, and increased safety, several projects have been pushed to initial commercial application (o-foil, streamline) and attempts to renew research that started during the 70's petroleum crisis, but were abandoned afterwards, as the technology was considered not mature enough.

All the above bring up the necessity of acquiring more knowledge on the hydrodynamics behind these remarkable "swimming machines" in order to optimize and control such systems, with the final purpose of placement of "flapping foil propulsion" to ships.

Thesis of this work is that production of a propulsor that employs biomimetic characteristics is feasible and more efficient, compared to conventional systems, at a level that it can also be cost effective. To support such a thesis, capability of simulating reliably most of biomimetic propulsion systems is necessary, along with a method that will enable the designer to select the proper system and settings for optimal operation.

For this purpose, the CFD program UBEM, which is using a boundary element time stepping method with free wake, capable of simulating any given body and motion (Politis 2011), was employed, and data generation (geometry generation and animation) programs were created in order to be able to simulate any given wing/body (or more than one) under any harmonic flapping motion given by the user, as well as any other prescribed motion. With the knowledge gathered form the prescribed motions simulations, insight of the governing phenomena was attained and a design method for such systems was introduced. After the systematic investigation of prescribed motions, the ability to simulate the behavior of a wing on spring loaded mountings was also added to the programs used. All the aforementioned programs were combined in a way, by which simulations can be executed in packages of systematically varying parameters. Post processing programs were also made in order to process the results, nondimentionalize and produce charts that can be used for investigation of effects and application of the developed design method on virtual paradigms of ships propelled by such systems.

I.2 State of the Art - Historical reference

The idea of studying nature and mimicking it is far from new. According to Alexander, in 'The history of fish mechanics', Aristotle considers in some of his works the anatomy and locomotion of swimming creatures. Leonardo Da' Vinci had also made many designs of bird like flying machines, which would be successful had he today's technology. After this, however, it took a long time before fish mechanics really made progress.

From about 1700–1800 research on fish propulsion did not make any significant progress. Its revival started after the further development of apparatuses for pressure measurement and to the invention of photography and film which allowed the recording of the movements of the fish. Some first investigators are A. Moreau regarding measurements at the bladder and E.J. Marey for the recording of fish movements.

Between 1910 and 1950 research was done, both by zoologists, and engineers, producing interesting results. For instance, wooden models of fish were towed through water having their resistance measured. Also, this resistance was investigated by letting weighted dead fish sink, head first, in a tank and by using optical arrangements for measuring their velocity. In this period Breder in 'The locomotion of fishes' published a review of fish swimming in which he gave names to a number of swimming forms of which the following three are mentioned:

"

- the anguiliform which is named after the swimming of the eel;
- the carangiform, where the front part of the body has little flexibility and the flexural movements are confined to the rear half or the rear one-third of the body length;
- the balistiform, where the propulsion is caused by the synchronized movements of dorsal and anal fins, while the body and the caudal fin are held rigid, by which the latter is of no direct use for the propulsion of the fish.

"

For other forms of swimming reference can be made to Blake in his book 'Fish locomotion'.

In the years around 1935 J. Gray studied the waves travelling posteriorly along the body of some fish such as the eel or the whiting. For this he used a machine for artificially imposing a wave motion to a flexible model or a dead fish.

One of the early mathematically oriented investigators of the swimming of aquatic animals was G.I. Taylor, who published the article 'Analysis of the swimming of long and narrow animals' in which he developed a "resistive theory". A bending wave travels with constant speed along the body of the animal. The forces per unit of length of each element of the swimming body are assumed to be the same as the resistance experienced per unit of length by a long cylinder with the same surface structure as that of the body and moving through the fluid with the same but now steady velocity and having the same inclination to the direction of the relative flow. This theory is suitable for the swimming of snakes, leeches and certain marine worms. Later theories are often of a different type, for instance the "reactive theory". Contrary to the aforementioned resistive theory, this type of theory considers the flow of the fluid outside the thin boundary layer on the fish's body. By this the inertial effects of the fluid are dominant and inviscid fluid models can be used.

A thorough review of theoretical background can be found in Sparenberg (2002) Extensive reviews of computational and experimental work in biomimetics can be found in the papers of Shyy, Aono et al. (2010) regarding aerodynamics and aeroelasticity; of Triantafyllou et al (2004). regarding experimental developments and of Rozhdestvensky & Ryzov (2003) regarding all types of applications, even full scale, with additional care given to the work done by eastern scientists (i.e. Russians and Japanese). Interesting information is also included in the books of Bose (2008) and Taylor et al. (2010). A thorough review of progress on numerical simulations of fish swimming and bird flight from the biologist's point of view mostly, is given by Deng (2013)

Nevertheless, a short review of the most important and relative to this thesis works is given for reasons of completeness.

I.2.1 Modern History of biomimetic propulsion

The history of modern research on flapping foil propulsion starts in 1936 with Gray's paradox. The famous paradox was formulated by J. Gray in his article 'Studies in animal locomotion VI. The propulsion powers of the dolphin'. Gray estimated among others the power needed for a dolphin of length 1·82 m to swim at a speed of 10·1 m/s. This was done by calculating the dolphin's resistance by means of a drag coefficient based on a turbulent boundary layer. He found that the required power was in the order of seven times the estimated muscular power available for propulsion. This yields the paradox which is considered by a large number of investigators. The paradox is, however, rather difficult to tackle due to the lack of a common opinion among investigators on the influence of the swimming motion on the resistance of the body. Some opinions are that the resistance of the swimming body can be increased by a factor of three with respect to the resistance of the body when it glides motionless through the water; (see for instance M.J. Lighthill's 'Large-amplitude elongated-body theory of fish locomotion')

The term 'flapping' is commonly used to describe the wing motion of birds and insects and is comprised of a rolling oscillation of the wing about the shoulder joint while the pitch angle of the wing changes via a wing rotation about its spanwise axis. Pectoral fins of fish are also moved in essentially similar ways. However, these fins can be passively or actively deformed, significantly increasing the complexity of the fin kinematics. In several studies, this 'pitching and rolling' motion has been simplified to a 'pitching and heaving' motion wherein the rolling motion of the wing is replaced by a heaving motion. In addition to serving as a model for flapping wing/fin kinematics, pitch-and-heave is also representative of the essential kinematics of caudal-fin motion in carangiform propulsion (Lighthill 1977).

Past studies have successfully employed pitching-and-heaving foils to model the flapping of wings and gained useful insight into the fluid dynamics of flapping flight as well as carangiform propulsion.

Before the state of the art in the area is presented any further, it is necessary to introduce the generalized problem of biomimetic flows, meaning the kinematics and the parameters that describe the problem, in order to make it easy for the reader to understand the description of each work, as well as the way they are distinguished.

I.2.1.1 Introduction to the Generalised problem of biomimetic propulsion

In a wing of given chord length and span ,moving at steady speed , and at an angle of attack, the parameters of relevance are (a) wing outline (rectangular, delta-shaped, etc.); (b) the section geometry (c) the aspect ratio (AR), defined to be equal to the ratio s^2 / S_f , where s is the span and S_f is the projected wing surface (for the case of rectangular wings, it degenerates to the ratio of an average span s over an average chord c) ; (d) the angle of attack ; and (e) the Reynolds number ,$\mathrm{Re} = Uc/\nu$ $\mathrm{Re} = Uc/\nu$ where U the translational velocity and ν is the kinematic viscosity of the fluid. The forces are classified as lift, the component perpendicular to the velocity U, and drag, the component parallel to U.

In unsteadily moving wings, the motion of the wing has to be formulated. For the simplest case of a wing of chord c, moving forward at average velocity U, and oscillating harmonically with a linear (heave) motion h(t) , transversely to the velocity , and an angular (pitch) motion θ(t) the equations of motion are:

$$h(t) = h_0 \sin(2\pi ft) \quad \text{(I.1)}$$

$$\theta(t) = \theta_m + \theta_0 \sin(2\pi ft + \psi) \quad \text{(I.2)}$$

where ψ is the phase angle between heave and pitch, h_0 the heave amplitude, θ_0 the pitch amplitude, θ_m the average pitch angle, and f the frequency of oscillation. This is the simplest case of biomimetic propulsion, which is a simplification of the motion of a whale tail. Figure I.2.1-1 depicts such motion, where the forward velocity U is done on the direction of X axis, heave oscillation is done on the Y axis and pitch oscillation is done around Z axis. Figure I.2.1-2 depicts a projection of the previous figure on the XY plane, where the advancing velocity U and the instantaneous heaving velocity $\dot{h}(t)$ produce the instantaneous apparent velocity. The difference of the angle of apparent velocity and pitch angle, gives the instantaneous angle of attack $a(t)$

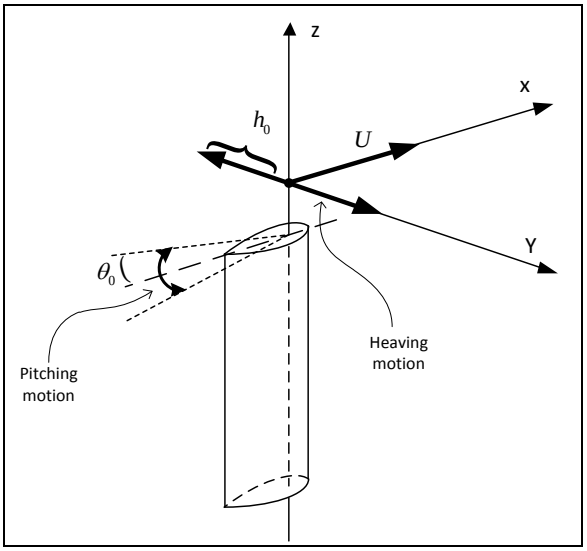

Figure I.2.1-1 Pitching and Heaving motion (simplification of whale tail motion)

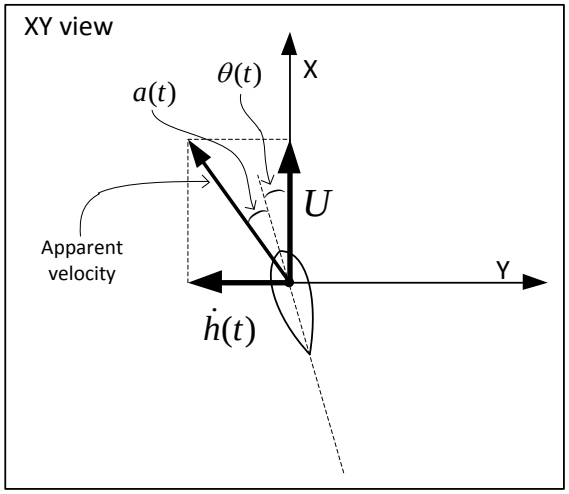

Figure I.2.1-2 XY view of a wing in pitching and heaving motion. Elemental and apparent velocities are presented, along with pitch angle $\theta(t)$ and instantaneous angle of attack $a(t)$

.

In the case of bird like flapping wing, the heave motion is substituted by a rolling motion and (1.1) is substituted by:

$$\varphi(t) = \varphi_0 \sin(2\pi ft) \qquad \text{(I.3)}$$

Where $\varphi(t)$ the angular position and φ_0 the maximum rolling angle. Figure I.2.1-3 depicts such motion, where the advancing velocity is done on the X axis and the roll rotation is done

around X axis. Pitching rotation is done around the bodybuilt axis, which executes the rolling and advancing motion. It should be noted, that for each wing section, the amplitude of motion, depends on the distance of the section to the center of rotation. Thus, for the case of bird – like motion, an equivalent amplitude can be defined for the section at 70% of span, as follows:

$$h_{0.7} = 0.7s \cdot \sin(\varphi_0) \tag{I.4}$$

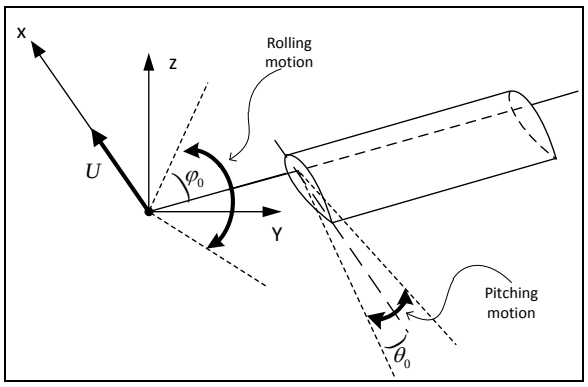

Figure I.2.1-3 Pitching and Rolling motion (simplification of bird wing motion)

Then the following nondimensional parameters can be defined for both cases (by applying the corresponding definition of amplitude), in addition to those for a steadily moving foil:

1) Heave to chord ratio $h^* = h_0 / c$

2) Maximum pitch angle θ_0

2) Maximum unsteady angle of attack $a_{\max}$

3) Reduced frequency $k = fc / U$

4) Strouhal number, defined as $St = Af / \mathrm{U}$, where A is the is the width of the wake of the foil*

5) Mean pitch angle, which is equal to θ_m .

6) The phase angle between the two motions ψ

* The Strouhal number is often approximated by taking $A = 2h_0$,

i.e.,

$$St = \frac{Af}{U} = 2h_0 f / U \tag{I.5}$$

The maximum angle of attack is defined as the maximum value

of the angle $a(t)$, which is given by:

$$a(t) = \theta(\mathrm{t}) - ATAN\left(\frac{dh(t)}{dt}/U\right) \tag{I.6}$$

It should be noted, that for the case of bird – like motion, the equivalent heave, gives a representative value and not the actual for the whole span. The maximum angle of attack was used mostly as a mean to make sure that there is no leading edge separation.

Some authors prefer the use of the reduced frequency to the Strouhal number, but this later has been shown to be more suitable for the propulsion studies [see discussions, e.g., in Triantafyllou et al. (1991) or Ramamurti and Sandberg (2001)].

The resulting force (thrust) and the required power are nondimensionalized as follows

$$C_T = \frac{T}{0.5\rho U^2 S}, C_P = \frac{P}{0.5\rho U^3 S} \tag{I.7}$$

Where T, P denote the period-mean open water thrust and power of the flapping wing, ρ denotes fluid density, U denotes the translational velocity of the wing and S denotes the wing surface area or the swept area ($S = sA = 2sh_0$) depending on the choices each author makes.

Lastly, the efficiency is defined as

$$\eta = \frac{T \cdot U}{P} = \frac{C_T}{C_P} \tag{I.8}$$

I.2.1.2 Distinction of previous works in categories

Then, it is important to distinguish the works done into the big categories of theoretical, experimental and numerical, but also to subcategorize according to the background, application and purpose of each work.

I.2.1.2.1 Theoretical works

Many qualitative investigations of flapping flight were conducted by the end of the 19th century, but the first explanation of the physics of flapping wings was only given independently by Knoller and Betz in (1909)and (1912), respectively. Both noted that the wing oscillations induce longitudinal thrust force and vertical lift force components of the aerodynamic force.

In (1922) Katzmayr conducted the first experimental investigations which verified the Knoller–Betz effect. The tests involved a wing which was placed into an oscillating flow.

In the same year Prandtl formulated the problem of unsteady motion of a wing in incompressible flow and noted that vortices are shed from sharp trailing edges. In 1924 Birnbaum developed a linearized solution of Prandtl's formulation and presented quantitative results for the thrust force generated by a flapping airfoil. He drew attention to the fact that a flapping airfoil can be regarded as a “two-dimensional propeller”.

In (1935) von Karman and Burgers proposed an explanation for the occurrence of drag or thrust based on the observed positions and orientation of vortices in the wake of the oscillating airfoil.

In the same year Keldysh and Lavrentiev (1935) obtained (in the linear formulation) expressions for the thrust generated by a harmonically oscillating flat plate. The solution was obtained with the method of conformal mappings.

In (1936) Garrick determined the thrust force on a harmonically oscillating flat plate in incompressible flow using Theodorsen's thin airfoil theory. In the same year Sedov using the theory of complex variables, presented a solution for a flat plate which performs heaving and pitching oscillations in incompressible flow.

Also, in (1936) Pavlenko proposed to use wings elastically attached to ship hulls as auxiliary propulsors and anti-rolling devices. He was able to show theoretically (with the use of quasi-steady theory) that such wings can function as propulsors because of the wave motion to which they are exposed.

In 1942 Schmidt (republished in (1965)) demonstrated a “wave propeller” which consists of a flapping/stationary tandem wing configuration. He confirmed that the Knoller–Betz effect takes place both on the stationary hind-wing, and on the flapping forewing. He demonstrated that the stationary foil placed in the wake of the oscillating foil increases the efficiency of the tandem system to almost 100%. Due to the mechanical complexity of generating pure heaving

motions, he replaced the heaving motion by a wing motion along a circular path with fixed angle of attack.

In the 1940s Golubev (1944, 1946) developed a flapping-wing theory, different from Prandtl's model, based on the "discrete" Karman form of the wake arrangement. Using the momentum theorem, he obtained an integral equation whose solution allowed him to obtain the aerodynamic characteristics, including the thrust of the flapping wing.

In 1948 Polonsky and in (1953) Bratt performed flow visualization experiments which confirmed the observations of von Karman and Burgers. They also showed the existence of different types of vortex structures behind the oscillating airfoil, including asymmetric ("skewed") vortex structures.

In the last years little additional work has been done with the works of Lighthill (1969), Wu (1971) , Newman J.N & Wu T.Y.(1973), James E.C. (1975) , Coene R (1975), Chopra M.G. (1976), Levi Enzo (1983), Sparenberg (2002) and Godoy-Diana R., Marais C., Aider J.-L., Wesfreid J.E. (2009) standing out. Especially Sparenberg (2002) made a thorough review of the mathematical theory behind biomimetic flows, refreshing and continuing Lighthill's work.

I.2.1.2.2 Non engineers and General Case problems

A great wealth of information can be found by biologists and experimentalists who work for them in the journal of experimental biology alone, more than 110 papers have been published on the subject of biomimetic propulsion, mostly on motion classification and performance evaluation of specific cases. Most representative are the works of, Fish F.E. (1984), Norberg U.M. (1986), Drucker E.G., Pennycuick C.J.(1996), Jensen J.S. (1996,1997), Ellington C.P. (1996) Brackenbury J.(2002), Combes S.A, Daniel T.L. (2002), Sane S.P., Dickinson M.H. (2001, 2002, 2003, 2007), Borrell B.J., Goldbogen J.A., Dudley R. (2007), Tobalske et al (2001, 2003, 2007, 2007, 2009, 2009), Ramamurti R., Sandberg W.C. (2002, 2007), Borazjani I., Sotiropoulos F. (2008, 2009).

More specifically, a number of studies have examined the fluid dynamics and force production of finite aspect-ratio flapping foils/wings. Liu et al. (2009) have conducted numerical simulations of a hawk moth wing model of aspect ratio 6.34 and experimental studies the fluid dynamics of this same wing have been carried out Usherwood & Ellington (2002) Dickinson and co-workers (Dickinson, Lehmann et al. 1999, Sane and Dickinson 2001) have performed systematic experimental studies with a dynamically scaled fruit fly flapping wing with aspect ratio of about 3.8 and Ramamurti & Sandberg (2002) and Sun & Tang(2001) have used this same wing in their numerical simulations. Techet et al. (2005) have examined the thrust performance of a three-dimensional flapping foil with an aspect ratio of 4.5. Detailed experiments of pectoral fin hydrodynamics in controlled experiments with swimming fish have also been carried out (Walker and Westneat 1997, Drucker and Lauder 2002)). The comprehensive particle image velocimetry (PIV) measurements carried out for a swimming bluegill sunfish (Lauder and Drucker 2004) are of particular interest. In these experiments, the fish swims almost steadily in an incoming stream using only its pectoral fins. That the fish is swimming at very nearly a constant speed is confirmed by the fact that the body of the fish maintains its position to within a few millimeters over many fin strokes (Lauder and Tytell

2005). Thus, in this situation, the thrust produced by the fin is almost exactly balanced by the drag on the body of the fish. In this mode, fin hydrodynamics is primarily determined by the fin flapping frequency, fin amplitude and the flow speed which can be expressed in terms of a fin Strouhal number, normalized amplitude and fin Reynolds number. In general, for fish with different sizes and swimming speeds, these three non-dimensional parameters can vary over a wide range. Because of this, most studies that attempt to gain general insights into the performance of fins, flapping foils or flapping wings find it convenient to examine the problem in terms of these non-dimensional parameters (Freymuth 1988) (Triantafyllou, Triantafyllou et al. 1991) (Anderson, Streitlien et al. 1998); (Walker and Westneat 2002); (Wang 2000); (Daniel and Combes 2002); (von Ellenrieder, Parker et al. 2003); (Lewin and Haj-Hariri 2003); (Prempraneerach, Hover et al. 2003), (Hover, Haugsdal et al. 2004),; Blondeaux et al. 2005a (Blondeaux, Fornarelli et al. 2005), Techet et al. 2005). A similar approach has been adopted in the current study.

In the particular case of labriform propulsion, since the very near wake of the pectoral fin is not affected by the wake of the fish body, the fin near-wake can be examined in order to assess the thrust production of the fin. The study of Drucker & Lauder (2002) showed that the pectoral fins of the sunfish produce a train of vortex rings which are associated with momentum addition in the fin wake and consequently to a production of force on the fin. Through modification in the fin gait, the fish can alter the axis and direction of travel of these vortex rings and through this, control the direction and magnitude of the forces and moments on the fin. Ramamurti et al. (2001) simulated the flow associated with the pectoral fin of a bird-wrasse which was the subject of the study by Walker & Westneat (1997) and examined in detail the flow structure and force production of this fin. Von Ellenrieder et al. (2003) examined the flow associated with a rectangular flapping foil of aspect ratio 3.0 at a Reynolds number of 163. The Strouhal number in this study varies from 0.2 to 0.35 and pitch angle amplitude from 0 to 20 degrees. The dye visualization study of von Ellenrieder et al. (2003) was conducted over a range of flapping amplitudes and frequencies and the effect of these parameters on the vortex topology was elucidated. They found that the wake of these flapping foils was dominated by sets of loops and rings and they describe the evolution of these vortex structures. This configuration was studied numerically by Blondeaux and co-workers (Guglielmini, Blondeaux et al. 2004, Blondeaux, Fornarelli et al. 2005, Blondeaux, Fornarelli et al. 2005, Blondeaux, Guglielmini et al. 2005) have examined the wake evolution at Strouhal numbers of 0.175 and 0.35 and the simulations show that a vortex ring is shed every half-cycle from the flapping foil. Also, Blondeaux et al. (2005) indicate that as the Strouhal number is increased, there is an increased interaction between adjacent rings. The vortex structures in the numerical study were found to be different from those observed in the experiments of von Ellenrieder et al. (2003). In particular, Blondeaux et al. (2005) point out that in contrast to the experiments, the simulations do not show the presence of distinct vortex loops in the wake associated with the trailing-edge vortex. It should be noted that neither the experiments nor any of these simulations have examined the force generation by this flapping foil, therefore it is not clear if the foils are indeed generating thrust, which is a prerequisite for a properly formed vortex wake.

I.2.1.2.3 Fish– Type Propulsion

The main distinction of the category is that the motion is the simplest of all, made by the combination of pitching and heaving. A review of the theoretical work of the area can be found in Sfakiotakis M., Lane D.M., Davies J.B.C. (1999) and in Triantafyllou M.S., Hover F.S., Techet A.H., Yue D.K.P. (2005)

Numerical investigations.

Katz & Weihs (1978) analyzed the unsteady large amplitude linearized motion of a chordwise flexible slender (AR<1) wing in inviscid incompressible fluid. The local deflections of the chord are calculated from the hydrodynamic forces acting on it, which are dependent on the foil shape. The problem was solved in a non-inertial system attached to the foil. In the statement of the unsteady Bernoulli's equation second order disturbances were neglected. Another assumption in the analysis of the deflections was that the foil is linearly elastic, so that no "memory" effects have to be taken into account. The foil span is not allowed to bend under the action of the forces. The slenderness assumptions lead to the neglecting of the term in the Laplace's equation so as to return the flow in the so-called cross-flow plane. The authors (Katz & Weihs), in this publication concluded that the thrust and efficiency increase when the heaving amplitude h/c grows. Another conclusion was that if the path curvature is increased (e.g. if the frequency grows while h/c remains constant) the efficiency will decrease. The thrust coefficient is highest when the phase difference is close to 90^{o}. The same authors, in a later publication discussed the wake roll-up and the Kutta condition for airfoils oscillating at high frequency. They showed that the Kutta condition can be applied for force and moment prediction in unsteady small amplitude non-separated flows even when the reduced frequency is well above 1. Wake roll-up calculations, based on the Kutta condition showed good agreement with available flow visualization data. It was concluded therefore that when trailing edge displacement is small (A/c<0.1) the range of linearized theory calculations using the Kutta condition can be extended far beyond reduced frequencies of 1 (one). They also showed that in high frequency motions the contribution of the potential time derivative $\partial\Phi/\partial t$ to the lift becomes more important, i.e. force due to the acceleration of the surrounding fluid is considerably increased relative to the far wake influence. In (1978), they analyzed the problem of a thin foil with flexible chord of constant length C which varies its shape passively owing to the hydrodynamic forces acting on it. The propulsor was taken to move in water at high Reynolds number so that the analysis could be based on incompressible potential theory. The trajectory S was such that the flow disturbance caused by the foil stayed small and no point of the foil traverses the wake. The displacement of the foil was small ($h(x,t)<<1$) so that the downwash velocity $w(x,t)/V(t) << 1$ where V(t) is the velocity of the point where the body attached frame of reference was attached. They assumed in the analysis that the foil was clamped at its leading edge and that its elastic behavior can be estimated by the cantilever model. The wake model consisted of discrete vortices and after each time step its distortion as a result of the velocity field induced by the foil and its wake was estimated. In cases where the foil did not come close to its wake the influence was usually found to be negligible. They concluded that for a rigid propulsor the thrust grows as H/C increases. The wake deformation may be neglected in modestly oscillating motions (reduced frequencies smaller than 0.3). It

was also obvious that a phase difference of π/2 between the heaving and pitching motions gave both high thrust and high efficiency.

Zervos (1984) presented the model of a two dimensional propulsor having infinitely thin and flexible walls. At each instant the exact form of the walls and the vortex wake were taken into account. Large oscillating amplitudes were applied in order to achieve practical thrust levels. The results showed that the pressures were distributed in such a manner that at each instant, a propulsive force is created. In order to have propulsion it was shown that V_o/C must be less than 1 where C is the velocity of wave propagation and Vo is the advance velocity of the foil. The influence of l/λ on the efficiency (η) and propulsive coefficient (CT) is very important. In the aforementioned ratio l is the length of the propulsor and λ the wavelength of propagation so that l/λ is the number of waves constituting the body. Its augmentation ameliorates the efficiency under the condition that does not get bigger than 2.0 but diminishes, at the same time the corresponding values of CT. Increase of A/H produces a slight decrease of the efficiency, but it is accompanied with an important increase of the CT. In the above ratio A is the total amplitude of the motion and H is the distance covered in one period T_o .

Poling & Telionis (1986) offered some experimental evidence on the physical characteristics of unsteady flow in the neighborhood of a sharp trailing edge. They provided measurements of two periodic problems. The first was the classical pitching airfoil and the second was the flow over a fixed airfoil immersed in a periodic wake that represents essentially a periodic change on the angle of attack. The experimental data obtained indicated that for periodic flows with reduced frequencies larger than k=2 and not very small amplitudes, the classical Kutta condition is never satisfied. As classical Kutta condition it is meant that the trailing stagnation streamline is tangent to the bisector of the wedge at the trailing edge. In the viscous region there was ample evidence of finite normal pressure gradients and therefore nonzero trailing edge loadings. It is also stated that for unsteady flow the loading near the trailing edge varies very sharply with the distance from the trailing edge. Even a few percent of the chord length may have a significant effect on global characteristics like instantaneous or averaged lift and drag.

Tuncer, Wang & James Wu (1990) developed an integro-differential formulation of the Navier-Stokes equations. The formulation of the viscous flow analysis confined computations only to the viscous flow zone and lead to an efficient zonal solution procedure. In the simplified vortical flow analysis, computational demands were greatly reduced by the partial analytic evaluations. Vorticity transport equation was solved only in the viscous flow zone. In addition, attached boundary layer and detached recirculating flow regions in the viscous flow zone were treated individually. On the other hand the integral equations for velocity permitted the velocity vector in the viscous flow zone to be evaluated explicitly. The results of the study showed that during the upstroke the computed lift coefficient increases linearly until the leading-edge vortex forms. The formation of the leading edge vortex then causes a steep increase in the lift. At maximum angle of attack the lift coefficient reached a local maximum as a result of the burst of the bubble at the trailing edge and the shedding of clockwise vorticity. Due to the suction generated by the trailing edge vortex, it subsequently rises to a second local maximum. During the downstroke, following the shedding of the trailing-edge vortex the lift initially decreases rapidly. As the flow reattaches at the trailing edge and as the secondary vortex structures develop, the lift curve flattens. The minimum lift is observed just before the flow attaches fully on the upper surface. The development of the leading edge suction then drives the lift towards the steady state values. However, the low

pressure aft of the midchord on the upper surface delays the recovery process. For different reduced frequencies the events mentioned above occur at different angles of attack during the oscillatory motion, and as a result, the aerodynamic loading differs significantly. It was observed that as the reduced frequency increases, the flow reversal originates at a smaller angle of attack. The conclusion was that the dynamics of the leading edge vortex has a dominant effect on the dynamic stall behavior. As the reduced frequency of the oscillatory motion increases, the formation of the leading edge vortex delays until higher angles of attack are reached.

Wang, Wu and Qian (1991) generalized the above two dimensional zonal procedure to treat three-dimensional general viscous flow problems. The three non-zero vorticity components in a three dimensional problem satisfy the vorticity divergence-free condition through a numerical filter mechanism. Flow around fast pitched flat plate wings were computed by the generalized zonal procedure. This is summarized as follows: In an external flow problem when the Reynolds number is not small, a large potential region, where the vorticity and hence all viscous effects are absent, coexists with flow zones where viscous effects are important. As it turns out an isolated potential region is removable from the computation process. This fact results from the absence of vorticity in the potential region. The potential region once isolated needs not be involved in further computations. The information about the flow in a removed potential flow region is not lost but is stored in the boundary velocity values that have already been counted for this region. With prescribed velocity boundary condition the zonal approach follows the development of the vorticity field. The solution advances from an initial time level at which the velocity and vorticity fields are known to a subsequent new time level by using a computational loop. Numerical errors may accumulate and grow so that, over a period of time the divergence of the vorticity field becomes significantly different from zero, violating the physics of incompressible fluid. Numerical studies showed that the divergence or the numerical error of the vorticity field is greater if finer grids are used near the wing edges, especially near the wing tip. A filtering mechanism based on the concept of vortex loop in space was devised to control the growth of the divergence of the vorticity field. At any instant of time, if a vorticity field can be approximated by vortex filaments in space where these filaments are the local summations of strengths of existing vortex loops in space, the vorticity field is regarded divergence-free in the numerical sense. The conclusion of this study was that the generalized zonal approach was successfully used to study unsteady flows around stationary and rapidly pitched flat plate wings. The roles of the leading edge recirculating flow and tip vortices are identified to the contributions of the normal force experienced by the pitching wing.

Neil Bose (1992) presented a two dimensional time domain constant potential panel method used for the analysis of chordwise flexible oscillating hydrofoils as oscillating propulsors. The oscillating motions as well as the chordwise deflections were of large amplitude. The foil surface was discretized into panels following a cosine spacing over the chord and assuming a constant value of the doublet potential and source strength over each panel. All memory effects were included in the foil wake which contains the shed vorticity from the foil but at a given time step this is fixed. The calculation proceeded in a series of time steps and the wake was made up of segments or panels. The wake panels were left in the fluid flow where they were formed. No attempt was made to allow the wake to move with the local induced flow. The first wake panel was assumed to leave the trailing edge along the bisector of the trailing edge angle. A linear variation of potential was applied on the wake panel immediately behind

the trailing edge because this makes the calculation relatively insensitive to the time step size. A method based on a linearized pressure coefficient was used for the Kutta condition formulation. A dummy doublet potential value ΦN+1 was introduced at the upper surface at the trailing edge. The linearized pressure coefficient was included as an N+1 th equation for the potential values. A first order differentiation was used for the term $\partial\Phi/\partial t$ in the linearization of pressure coefficient. The analysis lead to the conclusion that the propulsive efficiency increased as thrust coefficient reduced. Efficiency varied strongly with changes in heave amplitude ratio and pitch amplitude. It was also shown that flexibility increases propulsive efficiency but reduces thrust. In addition for a given thrust a flexible foil has a higher propulsive efficiency than a rigid foil.

K. Streitlien, M.S. Triantafyllou & G.S. Triantafyllou (1995) presented closed form expressions for the force and moment on a Joukowski profile in arbitrary motion, surrounded by point vortices that are free to convect with the local flow. The foil shape was represented as the conformal mapping of a circle making use of the theory of complex functions. The wake of the profile was discretized into point vortices and the circle theorem insured that the body boundary condition is satisfied everywhere on the foil. It was shown that the force and moment acting on the Joukowski profile consist of added mass terms as if the flow were free of vortices plus the summed effect of all vortices in the flow. One of the example calculations presented concerned the large amplitude symmetric foil oscillation. The illustration showed that periodic time dependence was established in very short time, indicating that the added mass forces are dominant in this case. Another interesting example illustrated was the case of a vortex released at a point upstream of a stationary cambered foil, convecting with the free stream. The force record obtained showed that the maximum lift on the foil occurs as the vortex passes over the trailing edge.

Sarpkaya (1975) presented a potential flow model of 2D vortex shedding behind an inclined plate. The calculated normal force coefficients were about 20% larger than those obtained experimentally.

Basu & Hancock (1978) presented a numerical method developed for the calculation of the pressure distribution, and loads on a 2D airfoil undergoing an arbitrary unsteady motion in an inviscid incompressible flow. Results of the algorithm were presented for a sudden change in incidence, a high frequency oscillation and entry into a sharp-edged gust.

M. Vezza & R.A McD. Galbraith (1985), presented a model for the calculation of the incompressible, inviscid flow around an arbitrary airfoil undergoing unsteady motion. The same authors extended their model to include fixed upper surface separation. The analysis was based on the assumption that the flow is irrotational over the entire region except at the body and its wake elements. The separation point was a necessary input into the algorithm. The pressure distribution predicted was compared with experimental results in the case of step change in incidence from 0 to 20.05 deg and agreement was evident.

V. Riziotis & S. Voutsinas (1996), reported a 2D vortex type stall model. The separated flow over an airfoil was considered in constant large incidence and in pitching motion. The wake was represented by a set of freely moving vortex particles. A result from various attempts to attack the dynamic stall was that the influence of the details of the shape of the hysteresis loop on the force coefficients was not significant. Another conclusion was that the separation point delay loop is a dominant feature for the valid estimation of the forces acting on a pitching airfoil.

Most of these past studies have assumed that the aspect ratio of the foils is large and have therefore restricted their attention to two-dimensional flapping foil configurations.

With the evolution of Computers direct simulations of the fully 3D fish propulsion problems start to emerge either using 3D BEM formulations or Navier Stokes solvers. Liu and Bose (1997) presented a 3D BEM method in the lines of the commercial code VSAERO but properly adapted to treat unsteadiness of the flow. They have applied the code to study the effect of wing flexibility in the efficiency of a whale's fin. Their model uses a frozen wake assumption and a linear Kutta condition at trailing edge. Liu and Bose (1999) enrich their 3D panel code with a 2D boundary layer inner solution and apply their method to estimate the effect of shape of wing plan-form to the propulsive performance. Politis and Belibasakis (1998), employ a 3D panel code based on a Hess and Smith formulation of the unsteady problem to simulate a flapping foil motion. He et al (2007) presented a 3D panel code to treat tandem oscillating foils. Zhu et al (2002) has employed a 3D panel code together with experimental data to establish the 3D features of the flow around fish-like bodies. Willis D.J., Peraire J., White J.K. (2007) made a combined pFFT-multipole code, employing an unsteady panel method with vortex particle wakes. There have also been some 2d attempts by La Mantia M., Dabnichki P. (2008, 2009).

Viscous methods have also been used. Even though they are considerably slower, most of cases were made specifically for performance tests. Most representative examples are those of Blondeaux P., Fornarelli F., Guglielmini L., Triantafyllou M.S., Verzicco R. (2005), Borazjani I., Sotiropoulos F. (2009) where numerical investigation of the hydrodynamics of anguilliform swimming in the transitional and inertial flow regimes were conducted. Exception to them was Dong H., Mittal R., Najjar F.M. (2006) where wake topology and hydrodynamic performance of low-aspect-ratio flapping foils was systematically investigated.

Experimental works

Extensive experimental work, on either single or double foil configurations, has been made by Professor Triantafyllou and its co-workers (Hover, Techet)(1991, 1995, 1999, 2001, 2004, 2004, 2008), who investigated the effect of aspect ratio, Strouhal number and angle of attack, while some useful visualizations were made.

The effect of wing outline, which has also to be taken into account was experimentally explored by Luska Luznik and Neil Bose (1998). Pengfei Liu and Neil Bose (1999) also studied the hydrodynamic efficiency of a foil with aft-swept wing tips. The effect of elasticity was investigated by Paidousis M.P. (1976), McLetchie K.-M.W. (2003), Yamaguchi N. (2001).

Among experimental works, construction of robots AUVs (autonomous underwater vehicles) and UUVs (unmanned Underwater Vehicles) and their control have a long literature. Most representative are the works of Mason Richard, Burdick Joel W. (2000), Morgansen K.A., Duindam V., Mason R.J., Burdick J.W., Murray R.M. (2001), Muramatsu K., Watanabe M., Kobayashi N. (2001), Anderson J.M., Chhabra N.K. Trianatfyllou (Robo tuna) (2002), Singh S.N., Simha A., Mittal R. (2004), Kim E., Youm Y. (2004), Mojarrad Mehran (1997, 2000), Narasimhan M., Dong H., Mittal R., Singh S.N. (2006), Menozzi A., Leinhos H. (2007),

Nakabayashi M., Kobayashi R., Kobayashi S., Morikawa H. (2008, 2009), Nakadoi H., Sobey D., Yamakita M., Mukai T. (2008) and Low K.H (2006, 2007, 2009). , Su Y., Wang Z., Li Y., Qin Z., Chen W. (2009).

Use of exotic materials such as bending actuators were used by Menozzi A., Bandyopadhyay P., Warren S. (2005), Menozzi A., Leinhos H. (2007), McGovern S.T., Spinks G.M., Xi B., Alici G., Truong V., Wallace G.G. (2008). Also Ming A., Huang Y., Fukushima Y., Shimojo M. (2008) used Piezoelectric composites in order to actuate their foils.

Full scale applications

Apparently, one of the first tests of full-scale vehicles with flapping-wing propulsors was conducted by Grebeshov in the 1970s when he tested a full-size cutter on hydrofoils. This cutter used the hydrofoils not only as lifting but also as propulsive elements. The hydrofoils' prescribed translational–rotational oscillations made it possible to accelerate the cutter to the foil-borne regime and to maintain it there.

Japanese researchers (Bull Soc Naval Architects) (1989) tested a wing, installed at the bow of a 15.7 m long trawler of 19.9 ton displacement. By varying the stiffness of the connections of the wing to the frame, it was possible to maximize the wing thrust in a certain range of wavelengths encountered by the ship. These tests confirmed that this system could reduce the wave drag and be used in practice as a "passive" propulsor. The Norwegian Fishing Industry Institute of Technology carried out full-scale tests of a "passive" propulsor, comprising two wings with elastic links, installed at the bow of a 180 ton research fishing ship FisketsGang (1987). The tests showed that the efficiency of such a propulsor reached 95% and that it could be used as a "passive" wing propulsor together with a conventional screw propeller. At a speed of 15 knots in waves up to 3 m 22% of the thrust was provided by the wing propulsors. Using only the "passive" wing propulsor the ship was able to reach speeds up to 8 knots.

The Swedish companies Ellingsen and Associates AS and Kirkines Engineering AS developed an oscillating-wing propulsor and its control system for a small 10 m long fishing boat FisketsGang (1987).

N. Isshiki, H. Marikawa, H. Kato et al (1980)used a suspended engine to oscillate a wing or a wing system. This engine–propulsor complex was tested on a full-size 3.5 m long dinghy. They found that for some regimes of oscillations this propulsor was as efficient as a screw propeller (for the same expended power). The wing elements of the propulsor were either two vertically mounted wings, operating in opposite phase, or a horizontal wing, operating near a stationary plate, located above the wing. These full-scale experiments showed that the flapping wing can be more preferable than a screw propeller because, for the same efficiency, the wing propulsor creates less noise and vibration.

The full-scale tests of a 174 ton Russian research fishing vessel equipped with a wing device for extracting sea wave energy by Nikolaev MN, Savitskiy AI, Senkin YUF (1995), showed that such a device could increase the engine power up to 45–87% and reduce the ship motions by a

factor of 2–2.5. Figure I.2.1-4 and Figure I.2.1-5 show the full scale attempts made by Soviets and Norwegians, as described by Nikolaev et al (1995) and Jakobsen (1983) accordingly.

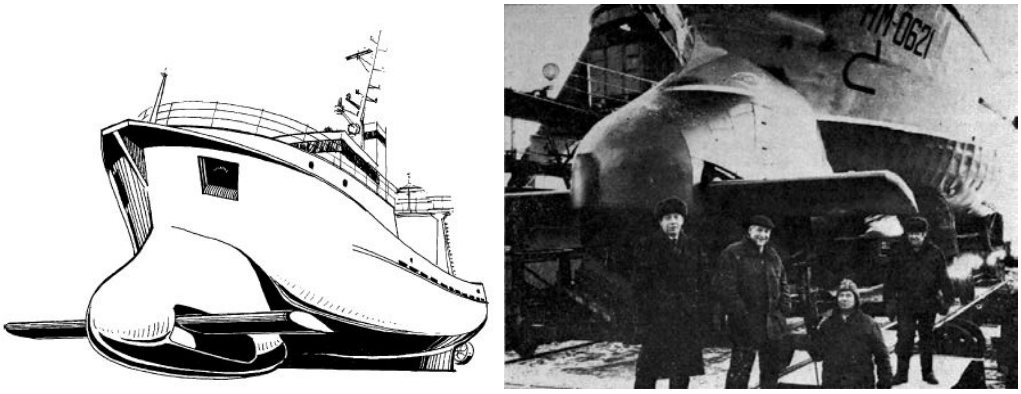

Figure I.2.1-4 Russian ship with bow-wings, Nikolaev et al (1995)

Figure I.2.1-5 Norwegian ship achieves fuel savings 15-20% by wave-energy extraction, Jakobsen (1983)

I.2.1.2.4 Insect and Bird Applications.

Several numerical investigations such as those of AP Willmott , FR. Menter(1993), CP Ellington and A.L.R Thomas (1996), SM Walker, ALR Thomas and GK. Taylor (2009), TJ Muller (2001), KD von Ellenrieder, K Parker and J. Soria, (2008), have been conducted, and mainly experiments were made towards construction of MAVs (micro air vehicles), as shown by W Shyy, Y Lian, J Tang, D Viieru and H. Liu (2008), W Shyy, P Ifju and D. Viieru (2005) R.

Żbikowski, S.A. Ansari and K. Knowles (2006), DJ Pines and F. Bohorquez (2006) M Platzer, K Jones, J Young and J. Lai, (2008) Y Lian, W Shyy, D Viieru and B. Zhang (2003), BK Stanford, P Ifju, R Albertani and W. Shyy (2008), W. Shyy, Y. Lian, J. Tang, H. Liu, P. Trizila and B. Stanford et al., (2008). Numerical investigations were also made by biologists S.A. Combes and T.L. Daniel (2003),

Additionally, Sane S.P., Dickinson M.H.(2001,2002), Sun et al (2002, 2003), Wang Z.J., Birch J.M., Dickinson M.H. (2004), Watts P., Mitchell E.J., Swartz S.M.(2001), used viscous commercial codes and conducted experiments for specific cases, which provided good insight, but no systematic investigation of effects. On the other hand, engineers who used viscous and potential codes were AP Willmott, CP Ellington and A.L.R Thomas (1997) R. Żbikowski, S.A. Ansari and K. Knowles (2006), who used them in simulating simplified motions, in their attempts to uncover wake patterns and through them the main mechanisms of birds flight. Aeroelastic effects were also investigated. Experimentalists have also made serious progress but it is usually restricted to simpler types of motion where a man-made mechanism can be constructed. Detailed review of them is made in Shyy, Aono et al. (2010)

I.2.2 Latest Developments (timeframe of present work)

During the period 2002-2008, the code UBEM, initially developed to treat propeller problems (Politis 2004), was expanded to include any 3-D unsteady incompressible non-viscous flow around an arbitrary system of interacting non-lifting/lifting rigid/flexible bodies, Politis (2009, 2011). In (Politis and Tsarsitalidis 2009), there was a first attempt to systematically investigate the effect of flapping wing propulsor geometry, on its open water performance using UBEM. By further developing specialized data generation codes, further simulations of flapping wings were presented, Politis & Tsarsitalidis (2014), of bird flight, (Politis and Tsarsitalidis 2010) and of a Flexible Oscillating Duct propulsor, Politis & Tsarsitalidis (2012), Politis et al. (2013), twin wing propulsors Politis & Tsarsitalidis (2013)

At the same time several other teams have been working on the same problem. From the Naval Architect point of view, biomimetic propulsion as a main propulsor or as an energy saving system has been numerically investigated by (Floc'h, Phoemsapthawee et al. 2012), (Eloy 2012, La Mantia and Dabnichki 2012, Lauder, Flammang et al. 2012, Politis and Politis 2012, Belibassakis and Politis 2013, Filippas and Belibassakis 2013, Filippas and Belibassakis 2014). The performance of a "wavepropulsor" has also been experimentally investigated by Steen and Bochmann (2013,2014) with very promising results, even for fixed (yet elastic) foils.

Part II TOOLS USED FOR THE SIMULATIONS

It is clear from the introduction, that in order to simulate and systematically investigate biomimetic marine propulsors, it is necessary to use tools that can provide accurate results for highly unsteady cases , where the vertical motion (i.e. normal to the translational velocity) are of the order of the chord length, at the lowest computational cost possible. Viscous CFD methods (i.e. URANS or LES) can be extremely demanding, even for the simplest three dimensional case, making a potential based, Boundary Element Method, the best practical choice (within limitations that will be explained later). The solver code UBEM, originally developed by Professor G. Politis for propeller simulations (Politis 2004, Politis 2005), was adapted in order to simulate flapping foils (Politis 2009) and further developed to handle any unsteady problem (Politis 2011, Politis 2011). For the purposes of this thesis, around the UBEM core, additional software was created. Data generation programs have been developed, for the production of input files, as well as post processing programs for the collection and presentation of systematic simulations results. Efforts have been also made, to accelerate the solver and to create interfaces between the programs that facilitate the conduction of systematic simulations in packages both by creation of input files and the collection of the results in an organized fashion.

In this section, the tools of choice are being presented with emphasis on the ones created for the purposes of this thesis and are not presented in detail in previous literature. The main aspects of the theory behind the programs are to be analyzed, as well as implementation aspects and the architecture of the programs used. Verification tests are then presented and the limits of the method in hand are to be discussed. Finally, a compact way of presenting grid independence tests is presented and explained, so they can be employed for the purposes of each case later on.

It should be clarified, that in this part, the general formation of the tools used is explained and cases that may be more complex, are defined through paradigms. Specific tools made for each case, are to be explained when necessary in their corresponding section.

II.1.1 Boundary Element Methods

Flow simulations using BEM is a well-developed and successful mathematical/numerical theory with very good predictions for cases where lift is the main mechanism of force production. The first 3-D BEM for analyzing the flow around arbitrary non-lifting bodies can be attributed to Hess & Smith (1969). The first 3-D BEM for analyzing the steady flow around a marine propeller can be attributed to Hess & Valarezo (1985), where the classical Hess & Smith lifting formulation has been utilized for the representation of a steadily translating and rotating propeller using a prescribed wake shape to model trailing vortex sheets. In the following years, various alternative formulations of the panel method have been presented for the solution of flow problems. A brief presentation of the historical aspects of propeller related BEM formulations can be found in Politis (2004). This paper also presents the formulation and solution of the problem of an unsteadily moving propeller with the potential as the basic boundary unknown, Morino & Kuo (1974). The main innovation in this work (Politis (2004)) was the incorporation into the solution procedure of the dynamics of the free vortex sheets. This eliminates the need for simplifying assumptions regarding free vortex sheet geometry, like the frozen wake or generalized wake models, since its position is calculated by the code. During the period 2002-2008, this code, initially developed to treat propeller problems, was expanded to include any 3-D unsteady incompressible non-viscous flow around an arbitrary system of interacting non-lifting/lifting rigid/flexible bodies, Politis (2009, 2011). In Politis & Tsarsitalidis (2009), there was a first attempt to systematically investigate the effect of flapping wing propulsor geometry, on its open water performance using UBEM. By further developing specialized data generation codes, the authors presented further simulations of flapping wings, Politis & Tsarsitalidis (2013), of bird flight, Politis & Tsarsitalidis (2010) and of a Flexible Oscillating Duct propulsor, Politis & Tsarsitalidis (2012), Politis et al. (2013).

II.1.1.1 Formulation

The formulation of the boundary element method used in the solver code UBEM is thoroughly discussed in the aforementioned papers of Prof. G. Politis (2004, 2009, 2011) (as well as the notes handed for the BEM course taught) and the mathematical part is well discussed in the existing literature. For reasons of completeness, the key points of the method are presented in this part, as well as matters that make the implementation in hand different to others.

II.1.1.1.1 Geometric considerations.

In this formulation, the geometry of complex systems of bodies is built using surface patches. Each patch consists of a number of bilinear quadrilateral elements. Two types of patches are allowed: (i) lifting patches and (ii) non-lifting patches. By combining patches lifting and/or non-lifting bodies are built. For the former case the user has to determine the line of flow separation in the surface of each lifting patch.

Let M denote the number of (surface) patches of our system. Introduce an index set $M \equiv (1,2,...M)$ for (all) patches. Let $SB^n(t), n \in M$ denotes the defining surface of the n^{th} patch at time t. Lifting patches are distinguished from non-lifting by supplying to the former a flow separation line, denoted by $L^n(t)$ where $n \in M'$ and $M' \subset M$ denotes an index subset of

M characterizing the lifting patches: $L^n(t) \in SB^n(t), n \in M'$. Each separation line $L^n(t)$ is the generator of a free shear layer. Two distinct parts of each free shear layer can be considered: (1) the strip directly adjacent to the (bound to the surface $SB^n(t)$) line $L^n(t)$ and (2) the remaining part of the free shear layer. This strip is called, the 'Kutta strip' and is denoted by $SK^n(t), n \in M'$. The remaining part of each free shear layer surface is denoted by $SF^n(t), n \in M'$. Thus each free shear layer surface at time t is expressible as $SK^n(t) \cup SF^n(t), n \in M'$.

Total system surface (M patches – Notice that in general the number of patches is greater than the number of bodies constituting our system) at time t is denoted by $SB(t)$:

$$SB(t) = \underset{n \in M}{\cup} SB^n(t) \tag{II.1}$$

Total system kutta strip surface at time t is denoted by:

$$SK(t) = \underset{n \in M'}{\cup} SK^n(t) \tag{II.2}$$

Total system free shear layer surface at time t, excluding Kutta strips, is denoted by:

$$SF(t) = \underset{n \in M'}{\cup} SF^n(t) \tag{II.3}$$

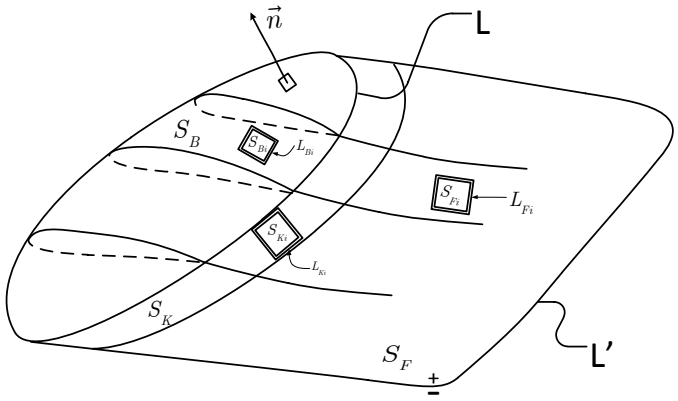

Figure II.1.1-1 Figurative representation of the discussed notation

II.1.1.1.2 Velocity and potential representation theorems.

An inertial (built on earth surface) frame of reference is used for the definition of velocities (body or fluid). A corresponding coordinate system (assumed Cartesian-orthogonal) is denoted by OXYZ.

As a result of the (known) unsteady motion of our system of bodies, in the region outer to $SB(t) \cup SK(t) \cup SF(t)$, a velocity (perturbation) potential ϕ exists which, at each time step, is expressible through its traces $\phi, \nabla\phi$ on the boundary points $Q \in SB(t) \cup SK(t) \cup SF(t)$.

Introduce:

$$F(P) = -\frac{1}{4\pi}\int_{SB(t)} \frac{\vec{n}\cdot\nabla\phi}{r} dS + \frac{1}{4\pi}\int_{SB(t)} \phi\frac{\vec{n}\cdot\vec{r}}{r^3} dS + \frac{1}{4\pi}\int_{SK(t)} \mu\frac{\vec{n}\cdot\vec{r}}{r^3} dS + \frac{1}{4\pi}\int_{SF(t)} \mu\frac{\vec{n}\cdot\vec{r}}{r^3} dS \quad \text{(II.4)}$$

$$\vec{H}(P) = \frac{1}{4\pi}\int_{SB(t)} (\vec{n}\cdot\nabla\phi)\frac{\vec{r}}{r^3} dS + \frac{1}{4\pi}\int_{SB(t)} (\vec{n}\times\nabla\phi)\times\frac{\vec{r}}{r^3} dS + \frac{1}{4\pi}\int_{SK(t)} \vec{\gamma}\times\frac{\vec{r}}{r^3} dS + \frac{1}{4\pi}\int_{SF(t)} \vec{\gamma}\times\frac{\vec{r}}{r^3} dS - \frac{1}{4\pi}\int_{L'(t)} \mu\frac{d\vec{l}\times\vec{r}}{r^3} \quad \text{(II.5)}$$

where: P is the evaluation point (or control point) for either F or $\vec{H}$, $\vec{n}$ is a unit normal vector at the boundary integration point $Q \in SB(t) \cup SK(t) \cup SF(t)$ showing inside the flow region, $\vec{r} = \vec{QP}$, $r = \left|\vec{QP}\right|$, μ is the dipole intensity with support on $SK(t) \cup SF(t)$ and $\vec{\gamma}$ the corresponding (to μ) vorticity intensity given by:

$$\mu = \phi^+ - \phi^- \quad \text{(II.6)}$$

$$\vec{\gamma} = \vec{n}\times\nabla\mu \quad \text{(II.7)}$$

Finally $L'(t)$ (integration region of the last line integral in the right hand side of equation (II.5)) is defined by: $L'(t) = \partial(SK(t) \cup SF(t)) - L(t)$ where $L(t) = \underset{n\in M'}{\cup} L^n(t)$ i.e. it is the free part of the line bounding the free shear layers.

With the aid of relations(II.4), (II.5) representation theorems for $\phi, \nabla\phi$ become:

$$\left.\begin{aligned} \phi(P) &= F(P) \\ \nabla\phi(P) &= \vec{H}(P) \end{aligned}\right\} P \notin (SB(t) \cup SK(t) \cup SF(t)) \quad \text{(II.8)}$$

$$\left.\begin{aligned} \phi(P) &= \frac{1}{2}\phi(P) + F(P) \\ \nabla\phi(P) &= \frac{1}{2}(\vec{n}\cdot\nabla\phi)\cdot\vec{n} + \frac{1}{2}(\vec{n}\times\nabla\phi)\times\vec{n} + \vec{H}(P) \end{aligned}\right\} \Leftrightarrow \left\{\begin{aligned} \frac{1}{2}\phi(P) &= F(P) \\ \frac{1}{2}\nabla\phi(P) &= \vec{H}(P) \end{aligned}\right\} P \in SB(t) \quad \text{(II.9)}$$

$$\left.\begin{aligned} \phi^{+,-}(P) &= \pm\frac{1}{2}\mu(P) + F(P) \\ \nabla\phi^{+,-}(P) &= \pm\frac{1}{2}\vec{\gamma}(P)\times\vec{n}(P) + \vec{H}(P) \end{aligned}\right\} P \in SF^{+,-}(t) \quad \text{(II.10)}$$

and similarly for $SK^{+,-}$. In relation (II.10) the superscripts $(^{+,-})$ denote the two sides of the free shear (or vorticity) layer surfaces, while the unit normal $\vec{n}$ is directed from (-) to (+). Notice that some of the surface integrals for F or $\vec{H}$ in relations (II.9) or (II.10) contain strong

surface singularities of the Cauchy type. Thus their meaning is realizable only in the principal value sense, Mikhlin (1965).

II.1.1.1.3 The integral equation.

Let $\vec{v}_A$ denotes the (known) velocity of the boundary point $A \in SB(t)$ and $\vec{n}$ a unit vector normal to body surface at A with direction pointing into the flow region. Then, the no-entrance condition at A has the form:

$$\nabla\phi \cdot \vec{n} = \vec{v}_A \cdot \vec{n} \tag{II.11}$$

Substituting (II.11) to the first of equations (II.9) and using (II.4):

$$\frac{1}{2}\phi(P) - \frac{1}{4\pi}\int_{SB(t)} \phi \frac{\vec{n}\cdot\vec{r}}{r^3} dS - \frac{1}{4\pi}\int_{SK(t)} \mu \frac{\vec{n}\cdot\vec{r}}{r^3} dS = -\frac{1}{4\pi}\int_{SB(t)} \frac{\vec{n}\cdot\vec{v}_A}{r} dS + \frac{1}{4\pi}\int_{SF(t)} \mu \frac{\vec{n}\cdot\vec{r}}{r^3} dS, P \in SB(t) \tag{II.12}$$

This is a second kind Fredholm type Cauchy singular boundary integral equation for the determination of ϕ and μ on points of $SB(t)$ and $SK(t)$ respectively. In the right hand side of (II.12) the first term is a known integral (as far as the motion of the system of bodies is known) and the second term is known from the solution of the problem at previous time steps. The unknowns in the left hand side of (II.12) are the potential ϕ on $SB(t)$ and the dipole intensity μ on $SK(t)$. For their determination the additional required condition is the Kutta condition at the separation lines (trailing edges in case of wing flow w/o separation).

II.1.1.1.4 Kutta condition.

Let the point $A \in SB(t)$. Let $\left.\frac{d}{dt}\right|_A$ denote the time derivative for an observer built on the point A of the moving body and let $\vec{v}_A$ denote the known velocity of A. Then unsteady Bernoulli equation takes the form:

$$\frac{p - p_\infty}{\rho} = -\left.\frac{d\phi}{dt}\right|_A - \frac{1}{2}\left(\nabla\phi - \vec{v}_A\right)^2 + \frac{1}{2}\vec{v}_A^2 \tag{II.13}$$

According to a pressure type Kutta condition, as the trailing edge point is approached from either pressure side (superscript +) or suction side (superscript -), the pressure should be continuous, i.e.:

$$p^+ = p^- \tag{II.14}$$

Using (II.13), this becomes a quadratic (nonlinear) relation between $\phi^+, \nabla\phi^+, \phi^-, \nabla\phi^-$.

Assuming steady linearized flow, Bernoulli equation degenerates to the famous Morino condition:

$$\mu_{\text{approaching L(t) from shear layer}} = (\phi^+ - \phi^-)_{\text{approaching L(t) from body points}} \quad \text{(II.15)}$$

which is a linear equation in ϕ, μ. It should be noted that the Morino condition, contrary to the pressure type Kutta condition, allows for a pressure jump at the trailing edge.

II.1.1.1.5 *Shear layer dynamics.*

Kinematic and dynamic conditions on a free vortex sheet expressed in terms of the dipole intensity of the sheet results in the following equation, Politis (2004):

$$\frac{D\mu}{Dt} = 0 \quad \text{(II.16)}$$

where D/Dt denotes a material derivative for μ based on the mean perturbation velocity of the shear layer. Mean perturbation velocity $>\vec{v}<$ on points of the shear layer can be found using(II.10):

$$>\vec{v}<= \frac{\nabla\phi^+ + \nabla\phi^-}{2} = \vec{H}(P) \quad \text{(II.17)}$$

Thus relation (II.16) becomes:

$$\frac{D\mu}{Dt} = \frac{\partial\mu}{\partial t} + \left(>\vec{v}<\cdot\nabla\right)\mu = \frac{\partial\mu}{\partial t} + \left(\vec{H}(P)\cdot\nabla\right)\mu = 0 \quad \text{(II.18)}$$

Equation (II.18) informs us that the dipole surface $SF(t)$ with intensity $\mu(\xi,\eta)$ is travelling with velocity $>\vec{v}<$, where ξ,η denotes a set of curvilinear surface coordinates for the points on $SF(t)$. Thus, if a μ surface exists at time t, its new position can be found, at time $t+dt$, by deforming it by $>\vec{v}<\cdot dt$. Notice that formula (II.17), for the calculation of $>\vec{v}<$, contains infinities at shear layer boundaries (i.e. as P approaches $L'(t)$) which, although they are connected with the vortex rollup, they have to be treated with caution in numerical calculations. Furthermore, notice the Kelvin-Helmholtz instability, inherently present in such type of problems, Saffman (1992), Wu (2006). For the previous reasons calculation of $>\vec{v}<$ requires special attention.

II.1.1.1.6 *Calculation of forces, moments, power and efficiency.*

Pressure forces on element centroids can be calculated using(II.13). Forces and moments are then calculated using

$$\vec{F} = \int_{\partial L}\left(p\cdot\vec{n} + \vec{D}\right)\cdot dS, \vec{M} = \int_{\partial L}\vec{r}_1\times\left(p\cdot\vec{n} + \vec{D}\right)\cdot dS \quad \text{(II.19)}$$

Where $\vec{D}$ denotes a viscous drag correction force given by

$$\vec{D} = \frac{1}{2} C_D \rho |\vec{v}_{tot}| \vec{v}_{tot} \quad \text{(II.20)}$$

And $\vec{v}_{tot}$ is total velocity relative to an observer in the moving system and C_D is the sin friction coefficient, given by Blevins (1992):

$$C_D = \frac{0.0986}{(\log_{10} \frac{Ux}{\nu} - 1.22)^2} \quad \text{(II.21)}$$

Where $\frac{Ux}{\nu}$ is the local Reynolds number at each position.

II.1.1.2 Numerical Implementation.

II.1.1.2.1 Discretization and solution.

Subdivide $SB(t)$ into N_B elements. Subdivide $SK(t)$ into N_K elements. Subdivide $SF(t)$ into N_F elements. Four node quadrilateral elements have been used for the subdivision of bodies and shear layer boundaries. Assume piecewise constant ϕ and $\vec{n} \cdot \nabla \phi$ for all elements on $SB(t)$. Assume piecewise constant μ for all elements on $SK(t) \cup SF(t)$. Denote these constant values by $\phi_i, \sigma_i (= (n \cdot \nabla \phi)_i), \mu_i$ where the range of index (i) is adapted accordingly.

With the aid of the previous assumptions/notation integral equation (II.12) becomes:

$$\frac{1}{2}\phi_i - \sum_{j=1,N_B} B_{i,j}\phi_j - \sum_{j=1,N_K} B_{i,j}\mu_j = \sum_{j=1,N_B} A_{i,j}\sigma_j + \sum_{j=1,N_F} B_{i,j}\mu_j \quad \text{(II.22)}$$

where:

$$A_{i,j} = -\frac{1}{4\pi}\int_{E_j} \frac{dS}{|QP_i|}, B_{i,j} = \frac{1}{4\pi}\int_{E_j} \frac{\vec{n}(Q)\cdot\overrightarrow{QP_i}dS}{|QP_i|^3} \quad \text{(II.23)}$$

and E_j denotes the surface of the j^{th} element from either $SB(t), SK(t), SF(t)$ and P_i denotes the i^{th} control point (centroid of E_i) on $SB(t)$.

Relation (II.22) applied at the N_B centroids of the body elements, gives N_B linear equations for the determination of element potentials. The N_K additional equations required for the calculation of μ_j are taken from the satisfaction of the Kutta condition on $L(t)$. There are three alternatives for the satisfaction of a Kutta condition, and thus completion of the system of equations:

(i) The first alternative uses a linear Morino condition in the form of (II.15) which in discretized form becomes:

$$\mu_i = \phi_{i^+} - \phi_{i^-} \qquad \text{(II.24)}$$

where i^+ and i^- denote element numbers on body, neighboring to trailing edge from different sides (i.e. pressure side and suction side to use terminology from wings) and i denotes element number on kutta strip, neighboring to the same point of the trailing edge.

(ii) The second alternative uses a pressure type Kutta in the form of $p^+ = p^-$. This is a nonlinear equation between the unknowns ϕ_j, μ_j. There are two ways to implement numerically the nonlinear pressure type Kutta. The first is to express velocities in (II.13) as functions of the unknowns ϕ_j, μ_j using the representation theorems. The second is to evaluate velocities from surface potentials by using finite differences in a body surface curvilinear system. The second method has been decided to be used, since the computational cost for calculating velocity induction factors needed in the first formulation, is high. Notice that in a preliminary development stage both alternatives have been programmed and similar results have been found, although the first is much more computationally intensive than the second.

(iii) The third alternative uses a mixed type Kutta i.e. partly Morino and partly Pressure type. More specifically from calculations of flows around flexible bodies (fish tails and bird wings) it was found that at higher loadings, a pressure type Kutta at blade tips is too strong and occasionally leads to a destruction of the shear layer geometry at those regions. Thus, the decision was taken to introduce, as a third alternative, the "mixed Kutta" i.e. a Morino condition at the tips of the separation line and a pressure type Kutta at all other points.

If alternatives (ii) or (iii) have been selected, the resulting system of equations is nonlinear and it is solved by using a Newton iteration method, with starting value taken from a Morino type Kutta (first alternative). Usually three iterations are enough to converge. After the system of equations has been solved, the code calculates and prints forces, moments, power and efficiency. It also prepares a number of graphic output files ready to be used by the commercial program TECPLOT to visualize the complex unsteady phenomena in video form. Finally notice that in most cases conditions (ii) and (iii) give similar results regarding the integrated loads. But there are cases where condition (ii) leads to divergence while condition (iii) converges.

Solution of the problem is implemented by a time stepping algorithm as follows:

At each time step, the SOLVER-CODE:

1. Reads the next position of the system of bodies which is calculated by a GPP/MPP (Geometric Preprocessor Program, Motion Preprocessor Program –explained in a next section).
2. Generates corresponding Kutta strips, for the case of lifting bodies, introducing thus the extra unknowns required for the Kutta condition satisfaction.
3. Solves the system consisting of the "no-entrance" and "Kutta" conditions. In case of pressure type Kuttaa Newton iteration is used at this step.
4. Deforms the free shear layers to their new positions by applying a special filtering technique to calculate induced velocity

5. Output results (pressures, forces, velocities, position of free shear layers) for this time step.
6. Proceeds to the next time step and repeats the calculation from step (1).

The algorithm is graphically presented in Figure II.1.1-2

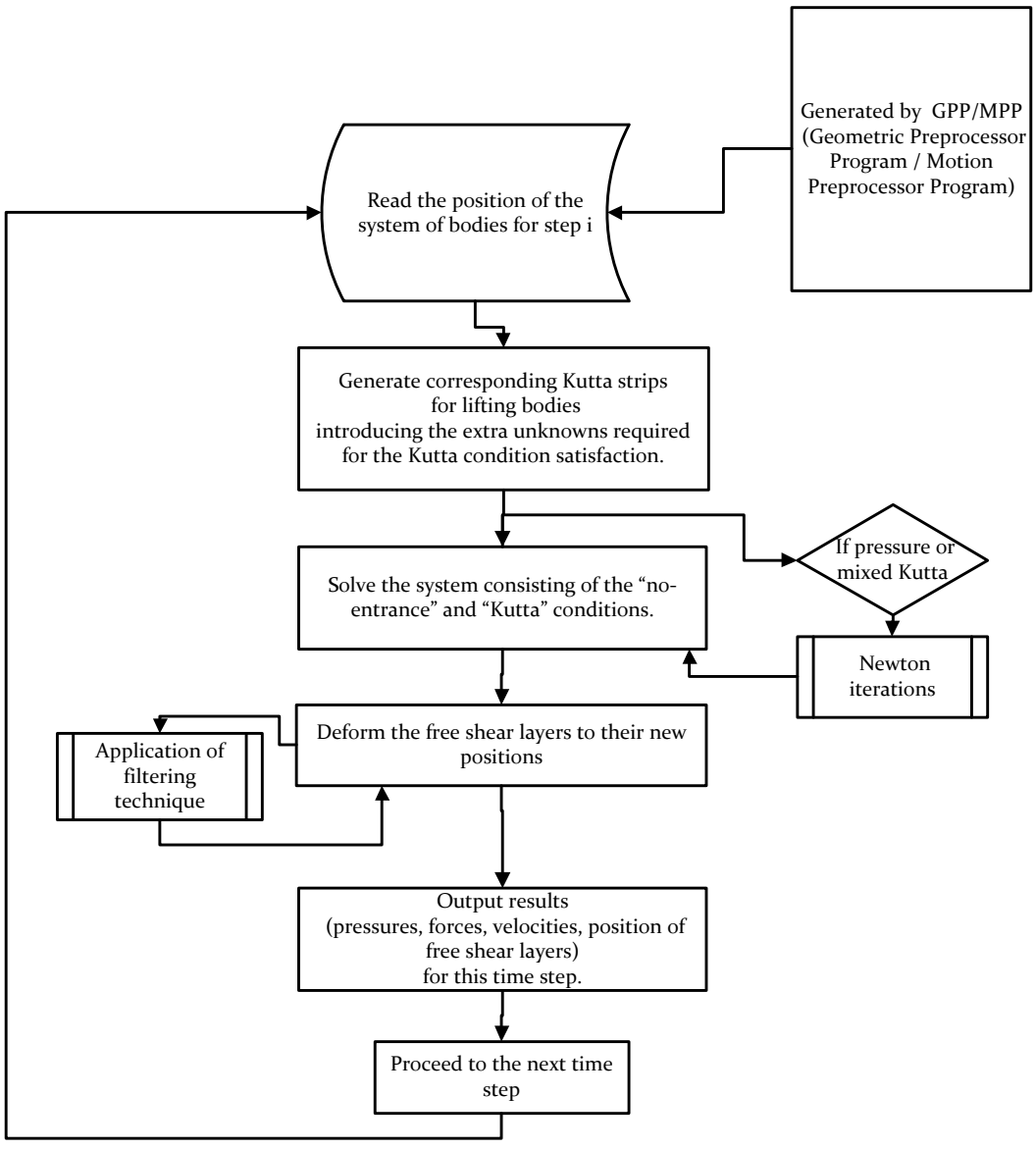

Figure II.1.1-2 Schematic presentation (flowchart) of the algorithm of UBEM

II.1.1.2.2 Strong interactions and the filtering technique.

In case of a lifting (or non-lifting) body moving in the wake of another lifting body, the shear layer of the front body may pass very close or even intersect the trailing body surface or the free shear layer of a trailing body or both. This is a problem of "strong interaction" between lifting bodies.

From the phenomenological point of view the physical mechanisms of strong interactions are mainly viscous and as such are excluded from the modeling capabilities of a BEM formulation. Furthermore flow fields in the vicinity of shear layers show peculiar/non-physical performance due to the following reasons: (a) the boundary of a shear layer (e.g. $L(t)$ in the aforementioned formalism) induces infinite velocities in its neighborhood, Saffman (1992), (b) approaching a point of a shear layer from either sides results in different values of self-induced velocities and induced potentials. Thus formulas for induced velocities/potentials used in BEM cannot be applied to strong interaction cases, where viscosity rules, without modification.

An approach to simulate the viscous reality in the context of potential flow methods can be found in either the 'Lamb-Oseen' or the "Burgers vortex" where the azimuthal velocity of a vortex filament is given by the equation $v = \frac{\Gamma}{r}(1-e^{-a\cdot r^2})$. Both vortices are special exact solutions of the Navier-Stokes equations, Wu et al (2006). The function $(1-e^{-a\cdot r^2})$ mollifies the singularity at $r=0$ substituting it by a viscous vortex core with finite diameter, controlled by the parameter a. Functions like $(1-e^{-a\cdot r^2})$ act as filters (mollifiers) removing the generic singularities of a BEM. A further discussion on the subject can be found in Sarpkaya (1989) and Cottet and Koumoutsakos (2000). In the formulation used, the following mollifiers have been applied to the kernel functions with singularities appearing in BEM integrals:

$$f(r,a,p) = 1-e^{-ar^p} \qquad \text{(II.25)}$$

where r is the distance, p a parameter which depends on the order of the singularity of the kernel function and a a parameter controlling the range of action. By selecting a p with a value equal or greater than the order of the singularity of the kernel function and a proper value for the range parameter a, full control on the smoothness of interactions in the vicinity of interacting surfaces is obtained. In the formulation used, parameter p can take non-integer values as well.

The previous ideas are shown schematically in Figure II.1.1-3. More specifically, the singular kernel $1/r$ as well as the result of applying to it two different mollifiers: $f(r,a=4,p=1.3)$, $f(r,a=8,p=1.3)$ are plotted. It is observed that the mollified kernel tends smoothly (governed by an analytic function of position) to zero as $r \to 0$. Notice finally the effect of a in the action range of the mollifiers: for $a=4$ the range is $r<1.114464$ while for $a=8$ the range is $r<0.65389$, etc. For those results to be obtained, it was assumed that a 'radius' R of a mollifier can be defined (for all practical purposes), as that r, where $f=0.99$. The relation

between R, a, p can directly been obtained by rearranging the terms in (II.25) and taking the logarithms, i.e.: $R = (-\ln(1-f)/a)^{1/p}$.

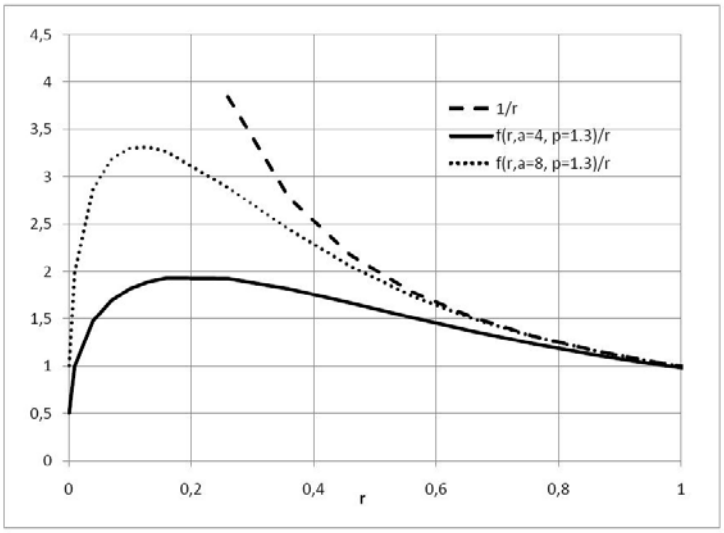

Figure II.1.1-3 comparison of mollifier effects

II.1.2 Architecture of code for prescribed motion simulations

According to UBEM architecture (Politis 2011) a body (lifting or non-lifting) can be built by a number of patches. Thus for each case to be modelled, a specialized GPP (Geometry Preprocessing Program) and MPP (Motion Preprocessing Program) has to be developed. In the sequel of this section shall be presented the developed code to treat the geometry and motions of a single wing. Notice that this code with minor of major alterations can be adapted to solve other problems e.g. the twin oscillating wings or other wing configurations. The developed code is written in an object oriented, fully structured manner, that allows for modularity, upgradeability and scalability. Each process and subprocess has a clearly defined interface with other processes, so it can be upgraded, changed and/or run in parallel.

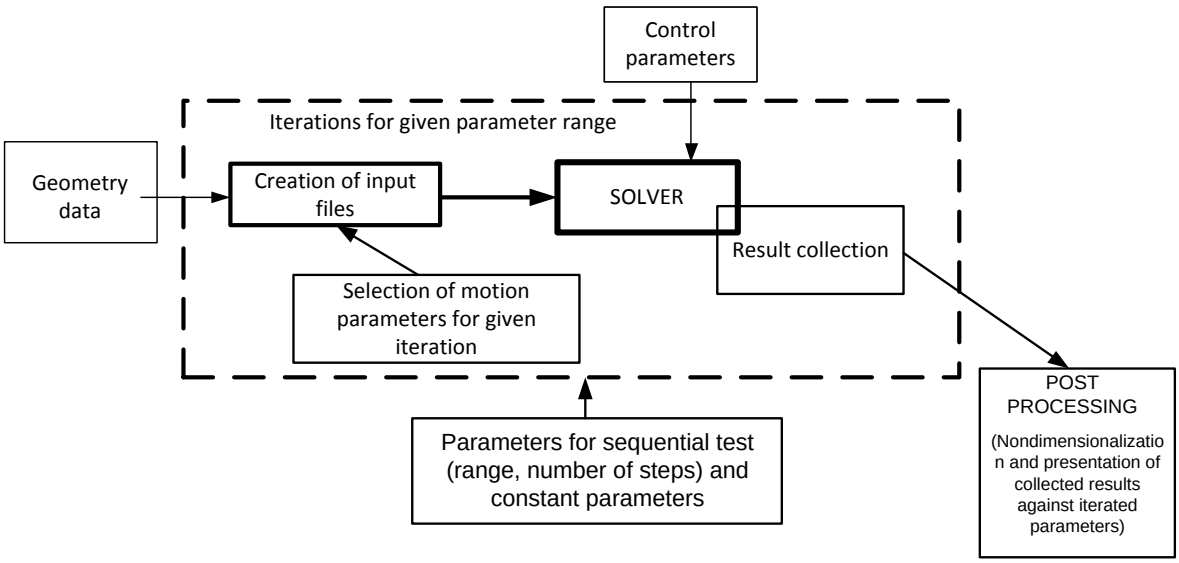

Figure II.1.2-1 Schematic of program used architecture.

As shown in Figure, for the systematic exploration of parameters of movement to performance characteristics, a sequence of simulations is executed. The initial geometry parameters have to be given, along with a set of fixed parameters and the parameters that will be systematically changed in the sequence. For each step, an intermediate sub program gives the specific parameters to the geometry pre-processing program, which in turn makes the time history (animation) of movement to be input for the solver. The solver in turn, exports result files signified by the parameters of each simulation. Lastly, an insert data collection subprogram gathers user defined data from all iterations and exports them into a single file (for each set of variables) in order to make it easy to extract summary plots for the whole set of systematic runs performed.

II.1.2.1 Input file generation

As discussed previously, a file containing the description of geometry (in animated panel mesh form), is necessary for the solver. Since the architecture is modular, input file generators are built according to purpose. Figure II.1.2-2, depicts the structure of the in house program that

has been created for wing simulations. The whole structure employs a module that contains all the common linear algebra and geometry functions.

The whole process can be defined in two parts. The creation of the geometry (initial mesh) and its animation (position at each timestep). For the case of deforming bodies, the geometry is created anew at each step.

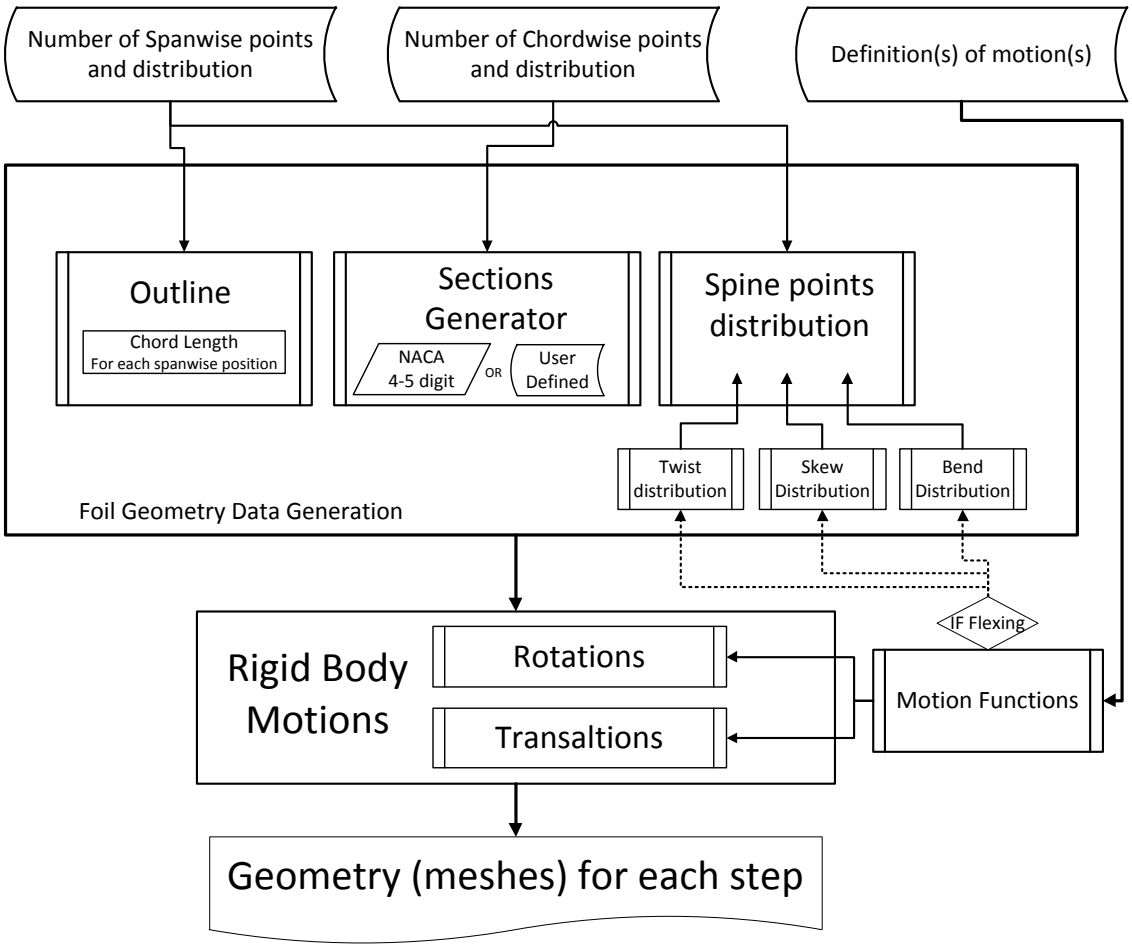

Figure II.1.2-2 Schematic of geometry generation program architecture

II.1.2.1.1 Initial geometry creation

Each body, when described as initial geometry, is equipped with a set of curves that help in the construction of it, a spine and two rails, which are (the rails) the leading and trailing edge curves. For each wing, the geometry is described by the user, by giving the number (quantity) of spanwise and chordwise elements and distribution (iso spacing, cosine, etc.), the number (code) of a NACA section (or the description of another section) and the description of spine curve (as distributions of skew and bend), outline (as distribution of chord lengths) and twist distribution. With the aforementioned knowns, the geometry is constructed as follows: According to number of spanwise points and distribution, the necessary points of spine and

outline are found via b-spline interpolation. Then, each chord is rotated according to the twist distribution. With the spine and rail points given for a section, a single set of points is generated for the given section and point distribution and positioned finally at the corresponding location, dictated by the spine and rail points. The algorithm is depicted in Figure II.1.2-4. A schematic of given, interpolated and generated points, is shown in Figure II.1.2-3.

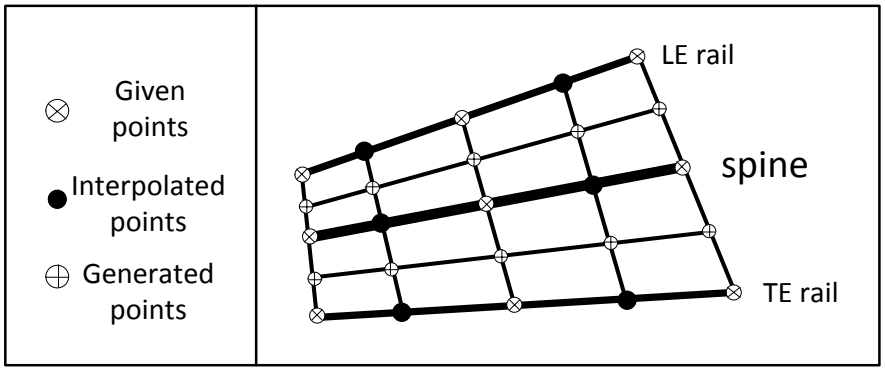

Figure II.1.2-3 Initial geometry points

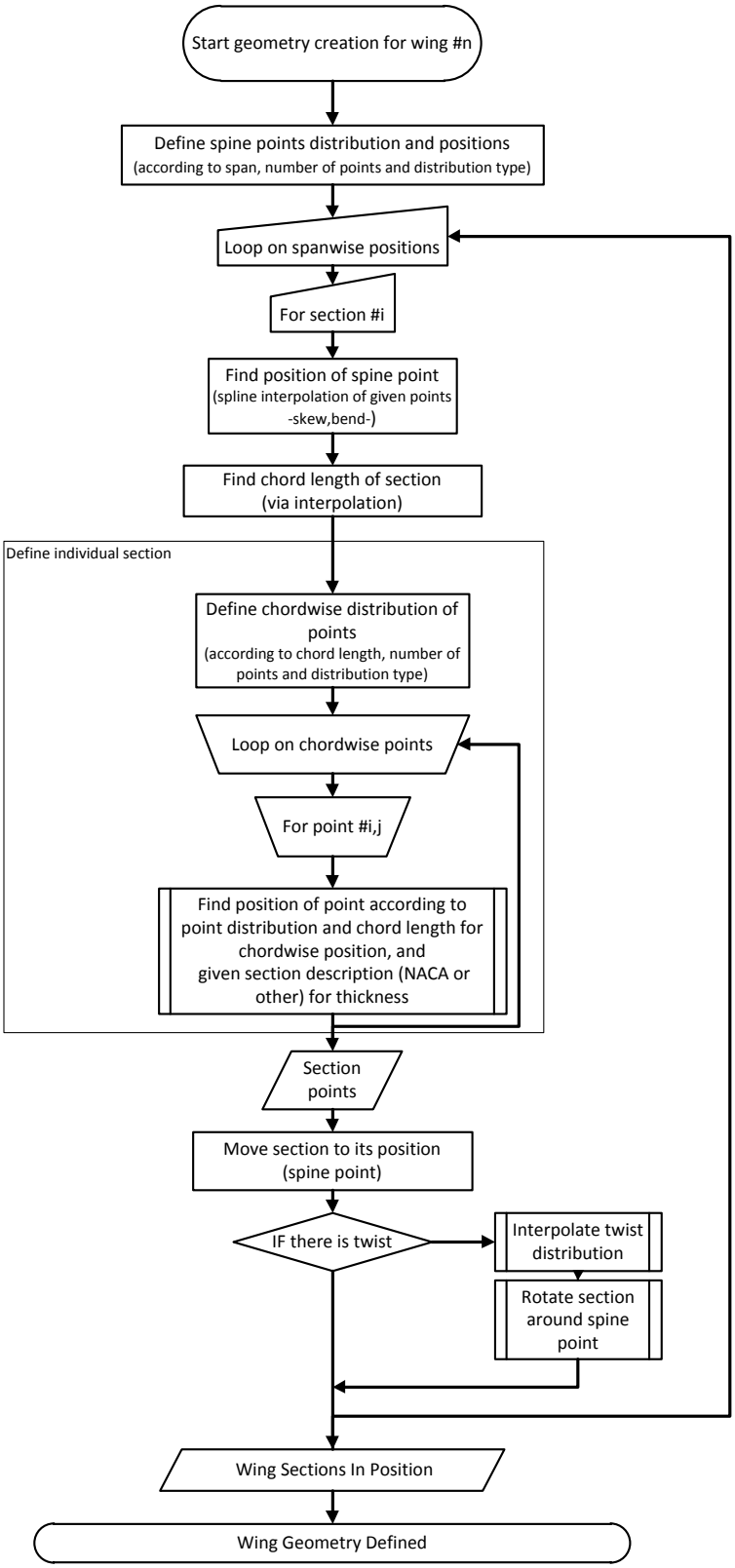

Figure II.1.2-4 Wing geometry creation algorithm

II.1.2.1.2 Animating a given geometry.

The Motion pre-processing subprogram, is actually superimposing user defined rigid (rotations and translations of the whole body) and flexing motions. If flexing motions are employed, they are performed before the rigid motions, but the rigid motions are explained first in order to set the equations of motion, as they are also used internally for the flexing motions.

- ***Rigid body motions:***

In the most general case an instantaneous motion is a result of an instantaneous rotation around a given axis and an instantaneous translation along another given axis. For the minimization of errors, instead of incremental motion (i.e. moving the geometry from the position of the previous step to that of the next), a direct approach is taken, where one rotation and one translation is applied to the initial geometry at each step in order to arrive at the desirable position. The movements of each point are done by means of vector translation and rotation relative to given point and axis or the absolute center of reference using the aforementioned linear algebra/geometry functions. Then, the definition of motions is a matter of defining the rotation angle and vector, and the translation vector in time.

For instance, for the simple motion of pitching and heaving, the following are the descriptive functions:

$\theta(t) = \theta_y \sin(2\pi ft)$ for the pitch rotation around y axis

and

$\vec{h}(t) = \overrightarrow{h_z} \sin(2\pi ft + \phi) + \overrightarrow{v_x} t$ for the heave along the z axis and the advancing speed along x axis.

Or for the case of a propeller rotating and translating it would be:

$\theta(t) = \omega_x t$ and $\vec{h}(t) = \overrightarrow{v_x} t$ around and along the x axis

- ***Flexing Motions of Wings***

For the flexing deformation of wings, the spline interpolations used for the generation of the initial geometry are fed with new points, at each step, found by the corresponding equations of motion. The schematic of Figure II.1.2-5 illustrates the original and deformed geometry.

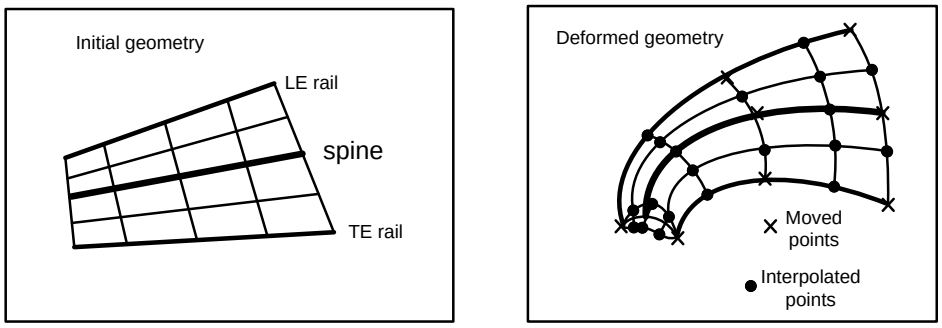

Figure II.1.2-5 Initial and Bent wing after interpolations.

More specifically, the part of the program that creates the initial geometry, is called at each step and after the spine points are moved to their new position (according to given motion parameters, as for rigid motions), the new geometry is fitted following the existing algorithm. After that, any additional (global) motions (i.e. traveling at a given velocity) are applied as normal.

It has to be noted, that in really strong deformations, it is not certain that the resulting surfaces will be smooth. Especially in the case of joints, extra care has to be taken so that the sections will not be overlapping.

In addition to these, some more care has to be taken on the sequence of the motions and deformations, so that the desired result will be achieved.

After this description, it is understood, that by such program, it is possible to simulate any movement, as long as care is given to the correct application of the sequence of motions.

II.1.3 Testing the code

For the purpose of comparing simulation with experiment, data were extracted from the papers 'Performance of flapping foil propulsion' (2005) by L. Schouveiler, F. S. Hover, M. S. Triantafyllou and 'Forces on oscillating foils for propulsion and maneuvering'(2003) by D.A. Read, F.S. Hover, M.S. Triantafyllou. More specifically, time domain results for cases 1 and 2 are from the first paper and case 3 is from the second. Table II.1.3-1 shows the motion characteristics that define each case. Systematic results of time averaged forces were taken from both papers, giving extra gravity to the first, as it is newer than the other. Another reason for choosing to compare with the specific experimental papers is that directly measured forces are given both in time domain and time averaged values, as well as measurements for non-symmetrical (biased) motion. In all cases NACA 0012 foils of 0.1m chord length were used, with AR=6 travelling at such a speed that Re=4000 while h/c=1. It should be noted that the foil was equipped with end plates, in an attempt to reduce 3D effects in the experiment, fact that is expected to induce discrepancies.

Table II.1.3-1 Definitions of the cases used for time domain comparisons

Case	Str	θ_o	bias	source
1	0.3	23.3^o	0.0^o	Schouveiler et al (2005)
2	0.3	23.3^o	15.0^o	Schouveiler et al (2005)
3	0.4	18.3^o	10.0^o	Hover et al (2003)

II.1.3.1 Time domain results: Grid independence, stability, consistency and accuracy.

For all cases, five different discretizations were made in order to perform the grid independence checks as shown in Table II.1.3-2. The number of steps per period is chosen in a way that the wake elements emanating from the trailing edge have an acceptable aspect ratio and are comparable to the elements of the trailing edge.

Table II.1.3-2 Discretizations used for grid independence tests

name	Number of elements	Steps per period
Grid1	30X20	50
Grid2	60X30	60
Grid3	80X40	65
Grid4	120X50	70
Grid5	160X60	75

II.1.3.1.1 Results and comparison for Case 1

Starting with the simplest of cases in hand, there is the symmetrical medium loaded condition where St=0.3 and θ_o=23.3° (a_{max}=20°). In the following figures, cFx and cFy are the force coefficients of the respective forces, calculated in the same manner Thrust coefficient is defined already in I.2.1.1, equation (I.7) and following the notation of the paper ($S = s \cdot c$).

As show in Figure II.1.3-1 and Figure II.1.3-2, only grid1 does not agree with the other grids, for cFx showing that there is grid independence for grids denser than grid2. Nevertheless, grid1 also follows the trend very well. The difference only in the thrust calculation and not in lateral force, can be attributed to the possibility that grid1 is not dense enough to satisfactorily simulate leading edge suction. Figure II.1.3-3 and Figure II.1.3-4 also show the agreement with the experimental results. It should be noted, that the experimental results, have been put through no processing further than magnification, in order to be visible and then the scales of the produced results were matched to it. The data have not been digitized and/or filtered, as such action would add uncertainties to the comparison. It is very interesting to observe, that even though the BEM model assumes attached flow and the 20degrees are well beyond the static stall limit, the agreement between experiment and simulation is good. This means that either the flow does not separate, or that the leading edge vortex that might be created reattaches to the flow with minor effects on the resulting forces.

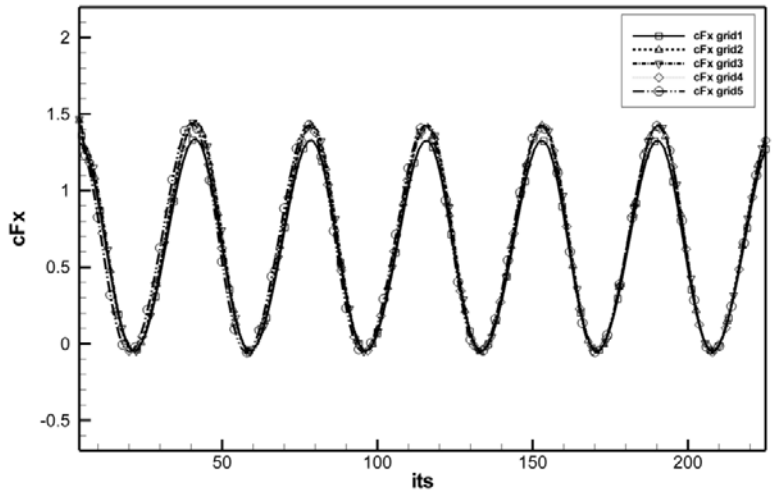

Figure II.1.3-1 Effect of grid on CFx for case 1

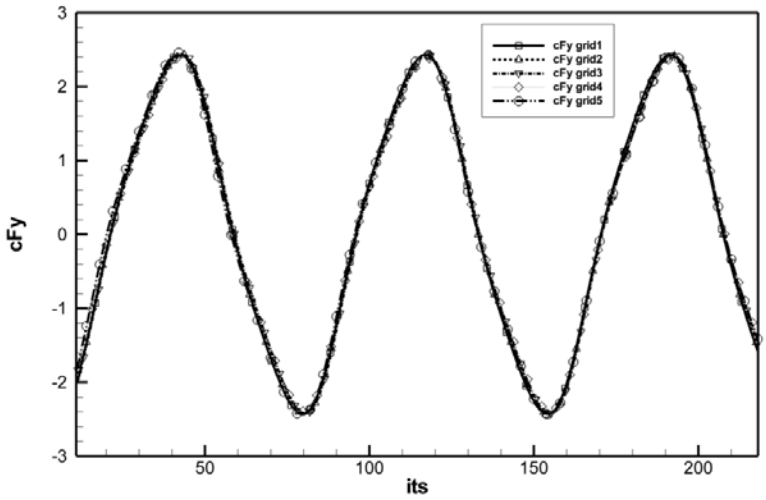

Figure II.1.3-2 Effect of grid on CFy for case 1

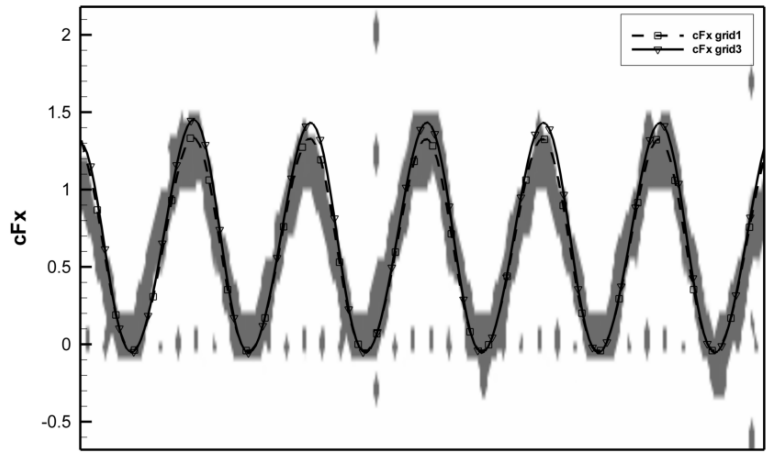

Figure II.1.3-3 Comparison of CFx with experimental data (as scanned) for case1

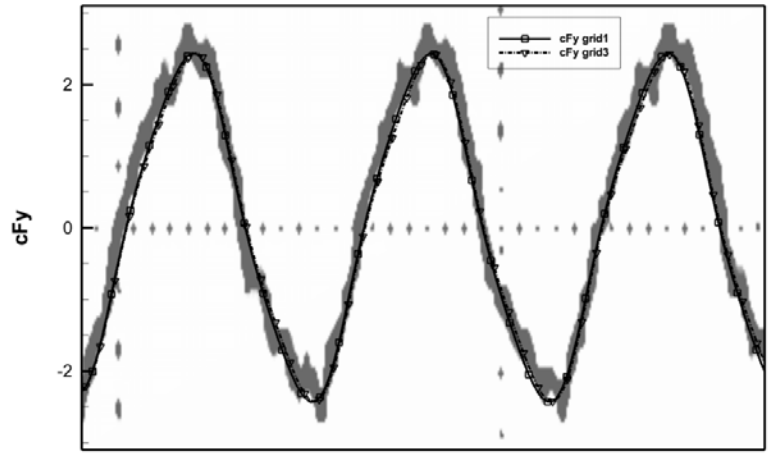

Figure II.1.3-4 Comparison of CFy with experimental data (as scanned) for case1

II.1.3.1.2 Results and comparison for Case 2

From the same publication with the previous case, case 2 has the same parameters of movement (St=0.3, θ_o=23.3°). with sole difference, the fact that the movement is not symmetrical, but biased. The mean angle of attack is 15°. This makes it a case of higher loading, while instantaneous angles of attack reach 35 degrees, beyond the theoretical limits of dynamic stall. Consequently, flow separation is expected, meaning that it is expected to have differences between simulation and experiment.

Figure II.1.3-5 and Figure II.1.3-6 show the grid independence and comparison with the experimental data. As expected, there is difference from the experimental, but not that significant. It is known that in the experiment, end plates were used for the purpose of minimizing 3d effects. This was attempted to be simulated with the usage of higher aspect ratio, Figure II.1.3-7 and Figure II.1.3-8 show the resulting comparison. As it can be seen, the increase of aspect ratio brings the measured forces a little closer, but there are still discrepancies. Since at the extreme conditions of this experiment where separation possibly rules the results, it was decided to try applying additionally a Morino kutta condition at the trailing edge, which allows for finite pressure jumps at this region. Figure II.1.3-9 and Figure II.1.3-10 show that comparison, along with experimental data. As it can be seen, the results seem to be improved, still having difference from the experiment. More specifically, Y forces seem to be the problem, there the peaks are under estimated by the pressure kutta condition and over estimated by Morino, but both within the uncertainty of the results.

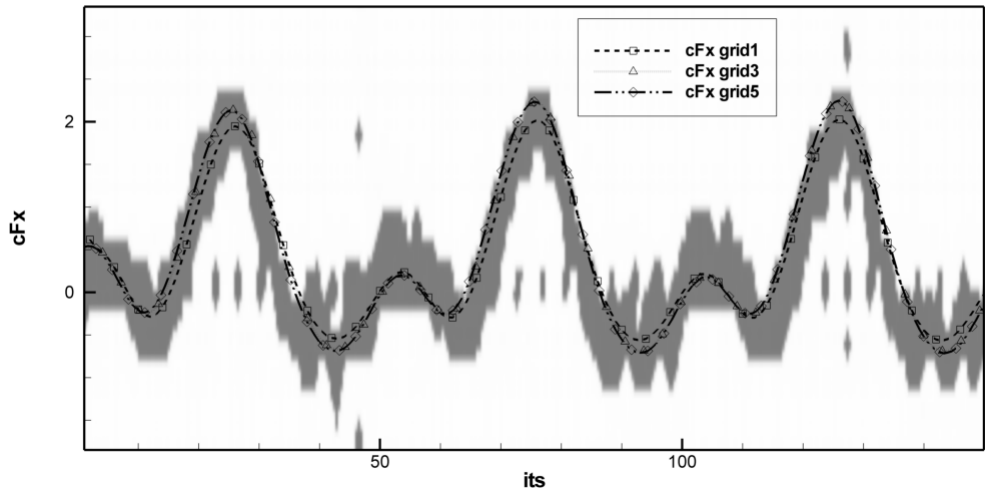

Figure II.1.3-5 Convergence and comparison of CFx with experimental, for case 2

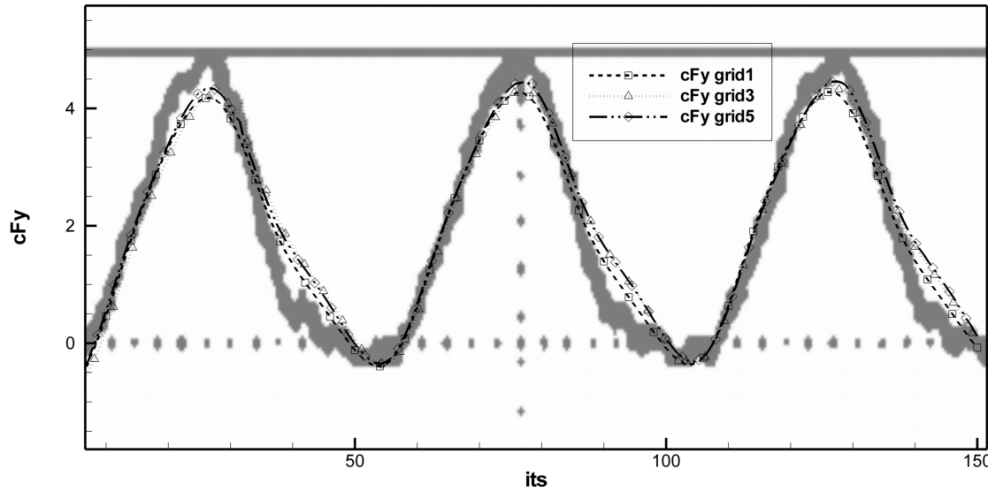

Figure II.1.3-6 Convergence and comparison of CFy with experimental, for case 2

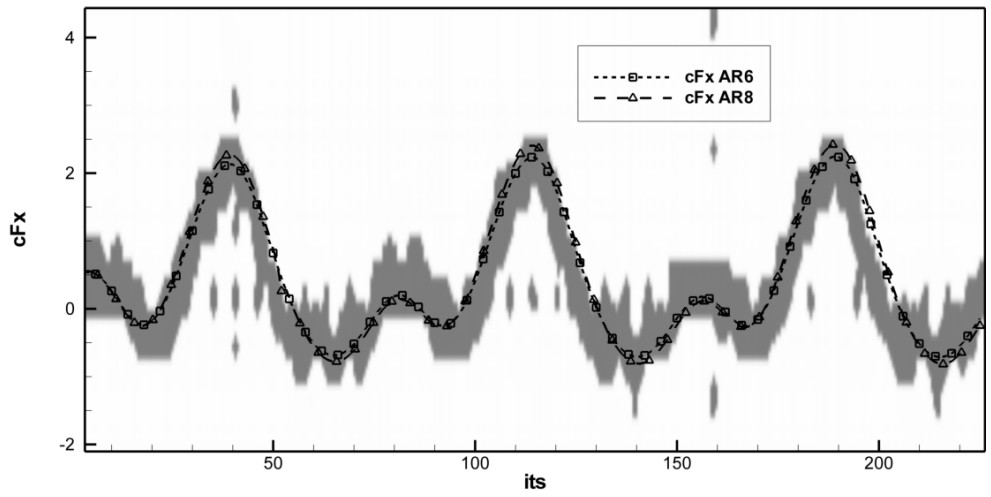

Figure II.1.3-7 Effect of Aspect Ratio for CFx Compared to Experimental for Case 2

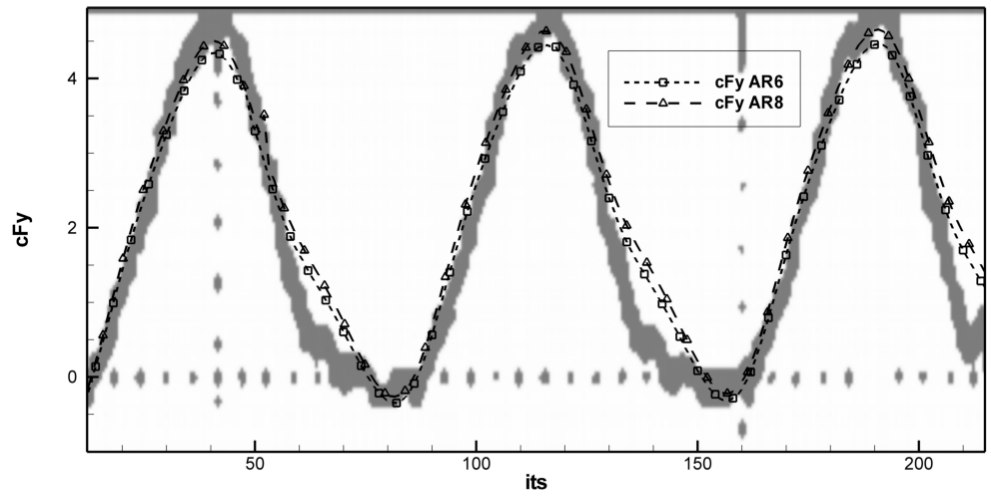

Figure II.1.3-8 Effect of Aspect Ratio for CFy Compared to Experimental for Case 2

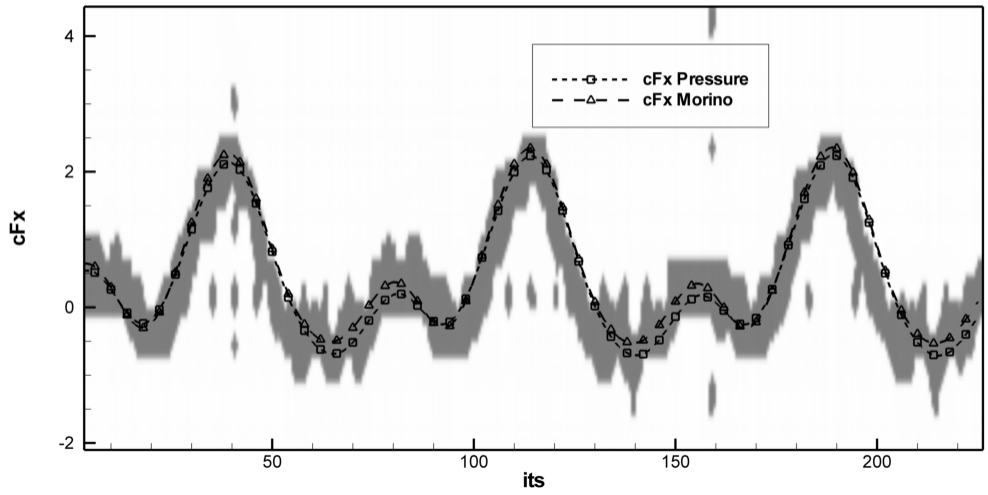

Figure II.1.3-9 Effect of Kutta condition on CFx compared to Experiment for case 2 (AR=6)

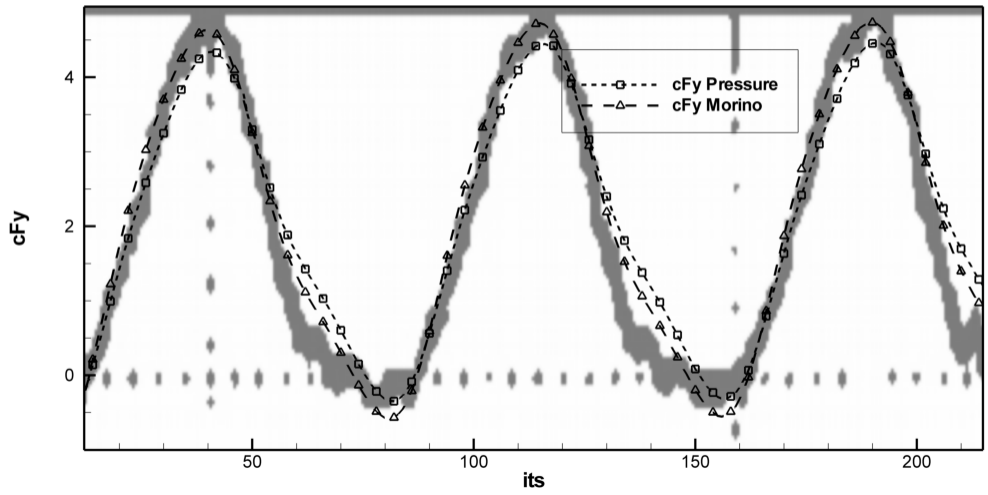

Figure II.1.3-10 Effect of Kutta condition on CFx compared to Experiment for case 2 (AR=6)

II.1.3.1.3 Results and comparison for Case 3

This case was taken from Read, Hover, Triantafyllou (2003) and is similar to the previous (having the same Reynolds number, chord length, AR, heave to chord ratio) with the difference of having St=0.4, θ_o=18.3°. (so the case has higher loading than the previous), while the bias angle is 10 degrees. The maximum instantaneous angle of attack is 35 degrees as in the previous case. Since the effect of end plates is unknown, simulations with larger AR were decided to be conducted. Figure II.1.3-11 and Figure II.1.3-12 show that comparison for the grid 3, where grid independence is achieved. With varying AR, it appears, that the 3D effects are diminished after AR=8, as the difference after AR=10 is minimal. The effect of AR is investigated further in the systematic series, presented in III.1.1. After observation of the results, it is found that the peak values of experimental data are enclosed between AR=8 and AR=6, but are underestimated in the second half of the period. It could be speculated, that such discrepancy might be a matter of boundary condition, possible viscous effects or stronger interaction with the wake. Consequently different Kutta conditions were simulated to investigate. Figure II.1.3-13 and Figure II.1.3-14 show that comparison for AR=6. In this case, the Morino condition seems to approximate better the peak values and the area around them, but not the lower ones.

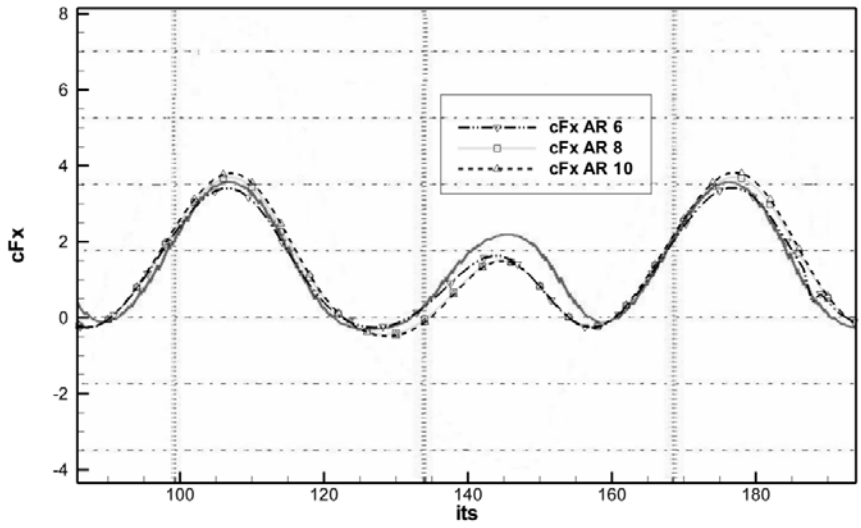

Figure II.1.3-11 Effect of aspect Ratio on CFx compared to Experiment for case 3

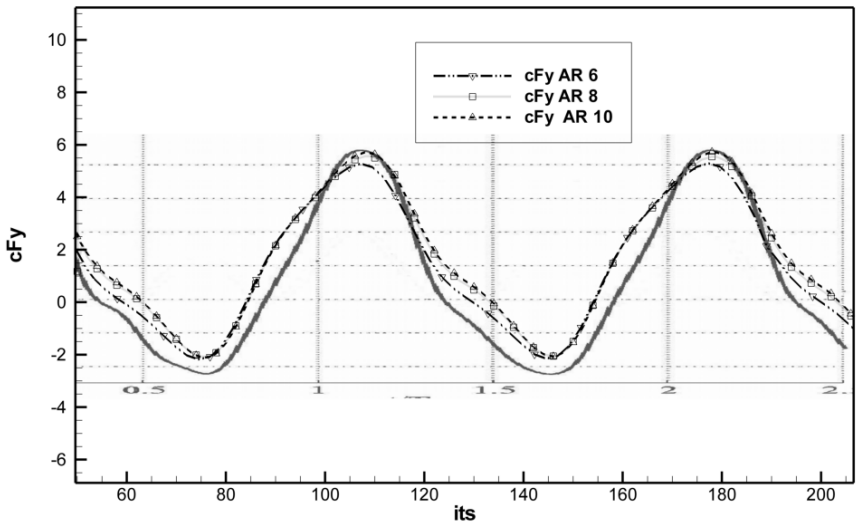

Figure II.1.3-12 Effect of aspect Ratio on CFy compared to Experiment for case 3

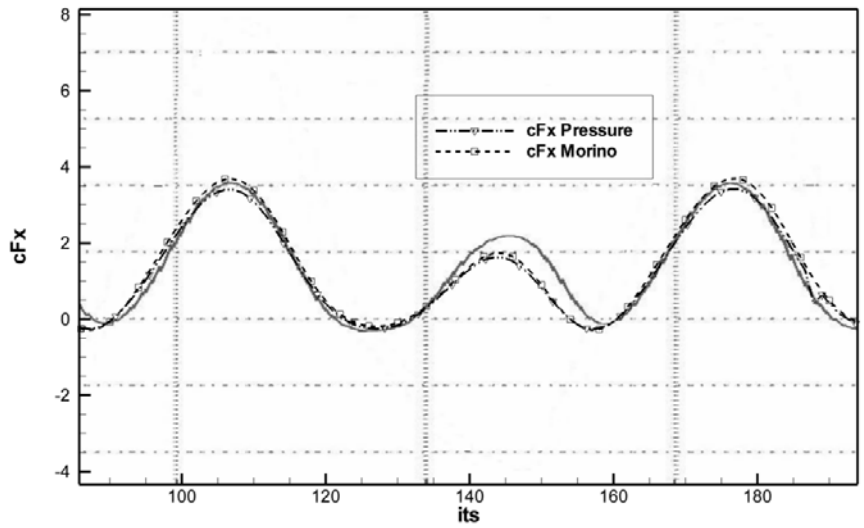

Figure II.1.3-13 Effect of Kutta condition on CFx compared to Experiment for case 3

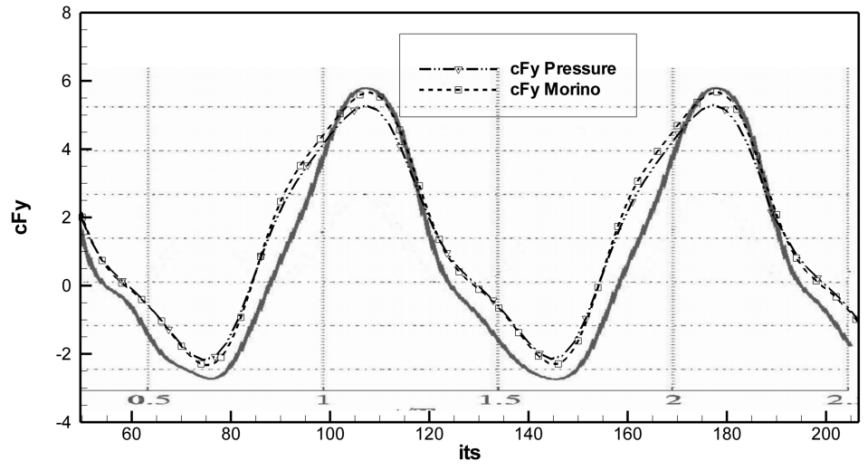

Figure II.1.3-14 Effect of Kutta condition on CFx compared to Experiment for case 3

II.1.3.2 Time averaged Results

II.1.3.2.1 Grid independence of the UBEM predictions.

In order to analyze the effect of the grid density to the calculated open water flapping wing performance, the systematic BEM calculations for a range of θ_0, Str (will be described further in III.1.1) have been repeated with three different grid densities, according to Table II.1.3-3:

Table II.1.3-3. Grid densities.

name	No of chordwise elements(face + back)	No of spanwise elements		
		$s/c=2$	$s/c=4$	$s/c=6$
Grid1	**20**	**30**	**50**	**80**
Grid2	**35**	**45**	**80**	**120**
Grid3	**50**	**70**	**130**	**200**

The timestep has been defined for each single simulation by calculating the maximum translation of the trailing edge (per step) and keeping it in comparable size to that of the used elements. For the time averaging of calculated forces, moments and power, the mean corresponding value is calculated, over one period, which has to start after all transient phenomena have passed. For that reason, each case has to be investigated for transient phenomena and the proper simulation period has to be selected. As it will be shown later in III.1.1.2, for single wings, the second period is adequate. For the comparison among grids, the following procedure has being used: For each configuration and for each grid of table 1, systematic simulations for a range of θ_0, Str can be produced. Considering the results (θ_0, Str, C_T), a graphical representation is made in the form of a 3D plot with θ_0, Str along the XY axis and C_T along Z axis. Thus a C_T surface can be created. By inserting any two such surfaces in a plotting software, it is easy to obtain the mean and maximum deviation between them. Those data for the case of a single (pitching and heaving) wing of a range of s/c and h/c as described in III.1.1 are shown on Table II**.1.3-4**, with the following convention: Above diagonal are overall mean of the %differences of mean thrust values and below diagonal are the maximum of the %differences of mean thrust values.

It can be seen that Grid2 (as well as Grid3) can be considered as a reliable discretization for systematic simulations. Nevertheless, Grid1 in spite of lacking accuracy, it is good enough to show trends and could be used for getting quick exploratory results.

Table II.1.3-4. Mean (above the diagonal) and maximum (below the diagonal) %deviations in mean thrust calculation.

	Grid1	Grid2	Grid3
Grid1	0	4.50%	5.02%
Grid2	8.09%	0	0.52%
Grid3	10.45%	2.21%	0

II.1.3.2.2 Experimental verification of the UBEM predictions for time averaged results.

To verify the predictive ability of UBEM, experimental data was taken from the works of Prof. Triantafyllou and his team. More specifically figures 8 and 9 in Read et al. (2003), contain experimental measurements of mean thrust loading coefficient (based on wing plan form surface $S = sc$) and efficiency, for a rectangular wing with $s/c = 6$, for a range of Strouhal numbers and maximum angles of attack corresponding to the thrust producing regime. The wing has a rectangular outline with $c = 0.1m, s = 0.6m$ and it is equipped with endplates, to enforce 2D flow in most part of the wing surface. The pitch axis is located at $b/c = 1/3$ from leading edge, the heave to chord ratio has been selected as $h_0/c = 1.0$ and the phase angle has been selected as $\psi = 90^0$. Furthermore figures 5a,b in Schouveiler et al. (2005), contain analogous experimental results for the same wing but with different heave to chord ratio $h_0/c = 0.75$. Notice that the experimental data provided in the above papers are plotted in a different format than that used in the present work. More specifically instead of a $C_T(Str) - \theta_0$ plot used in the present work (the reason and function for which is discussed in the III.2.2.1 and III.2.2.2 respectively), a $a_{\max}(C_T) - Str$ plot is used in the source, where $a_{\max}$ is the maximum angle of attack. Also instead of a $C_P(Str) - \theta_0$ plot used in the present work, a $a_{\max}(\eta) - Str$ plot is given, where η denotes the efficiency, equation (**III.**5). The previous experimental measurements have been digitized and transformed to the form $C_T, C_P - \theta_0$, consistent with the definitions used in the present work. Comparisons of the experimental data with calculations using UBEM are shown in Figure II.1.3-15 thru Figure II.1.3-18. A general remark is that experimental measurements and UBEM predictions follow similar trends and there is a good coincidence in the areas of high efficiency ($\theta_0 = 30^0 \div 50^0, Str \le 0.45$). Discrepancies are also evident and can be attributed to UBEM, the existence of endplates in

experiments (which are not present in the numerical simulation) and the experimental uncertainty. Since the selection of h_0 / c has major effect on the range of thrust producing pitch angles, through modulation of the angle of attack of wing sections, the results of Figure II.1.3-15 and Figure II.1.3-16 shall be discussed. Similar conclusions can be drawn from Figure II.1.3-17 and Figure II.1.3-18 but with displaced range of the pitch angle. More specifically, the existence of endplates in the experimental setup increases the wing tip loading over the whole range of parameters. This effect is more pronounced for higher wing loadings i.e. for greater values of the Strouhal number ($Str > 0.45$) and lower to medium values of the pitch angle ($35^0 < \theta_0 < 50^0$). This explains the difference in slope of the $C_T, C_P - \theta_0$ curves (at constant Strouhal) between UBEM and experiments, for this range of parameters. This effect on the slope of the $C_T, C_P - \theta_0$ curves will be observed with the variation of s/c and will be discussed later. As parameters change, towards the region of maximum efficiency, UBEM and experiments are in good agreement. For smaller $\theta_0 < 25^0 - 30^0$ (higher maximum angles of attack), UBEM overestimates the thrust, as effects of leading edge separation are neglected. Finally an additional source of differences between experiments and UBEM is the uncertainty in the experimental thrust and efficiency, which is estimated to be 4% and 7% (maximum) respectively, Schouveiler et al. (2005).

In overall, the method can produce reliable results for the practical design area where efficiency is maximized and acceptable trends for the off design points.

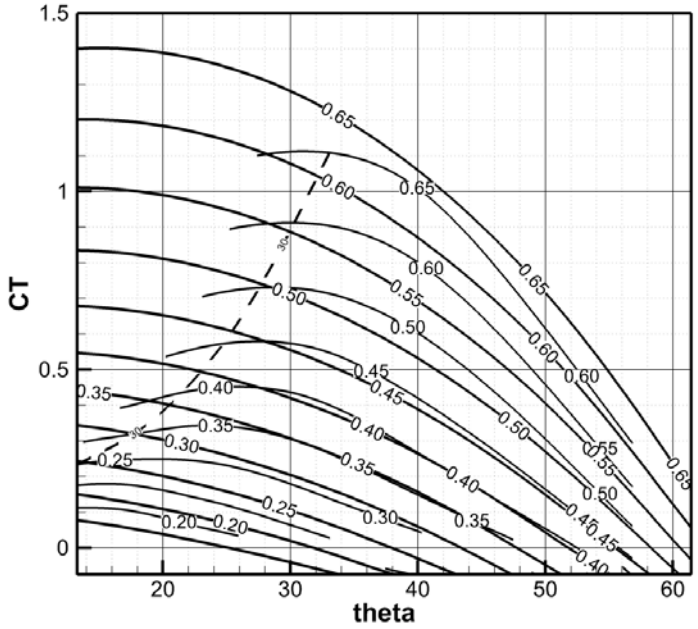

Figure II.1.3-15 $C_T - \theta_0$ **for** $s/c = 6, h_0/c = 1.0, b/c = 1/3$**. Thicker lines are for UBEM results and thinner, are for experimental, Read et al. (2003). Dashed line is for 30 degrees maximum angle of attack.**

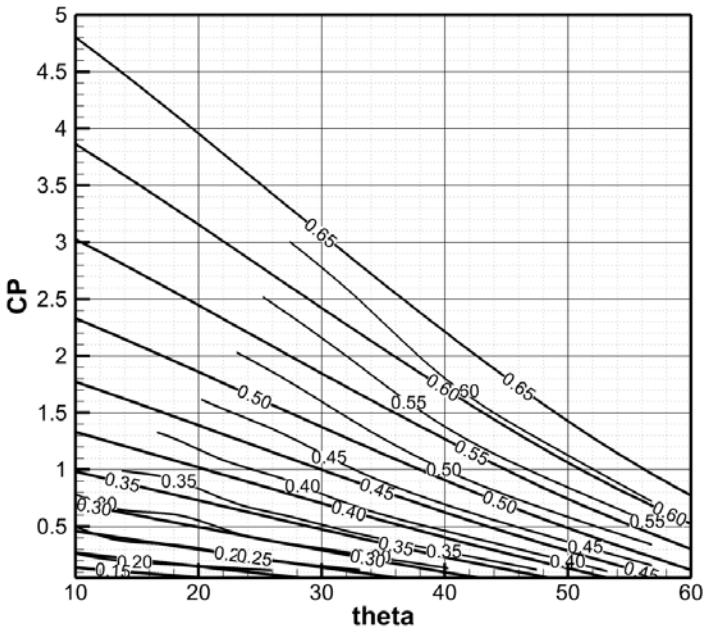

Figure II.1.3-16 $C_P - \theta_0$ **for** $s/c = 6, h_0/c = 1.0, b/c = 1/3$**. Thicker lines are for calculated results and thinner, are for experimental, Read et al. (2003).**

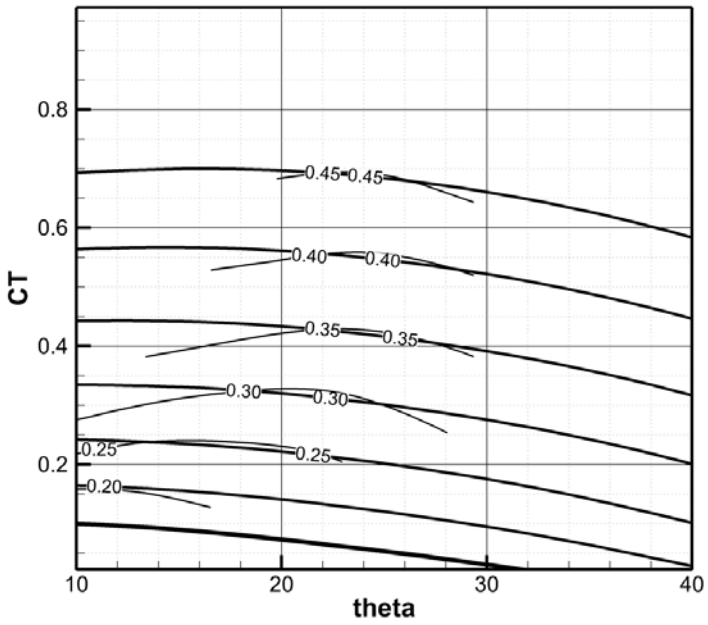

Figure II.1.3-17 $C_T - \theta_0$ **for** $s/c = 6, h_0/c = 0.75, b/c = 1/3$ **. Thicker lines are for calculated results and thinner, are for experimental, Schouveiler et al. (2005).**

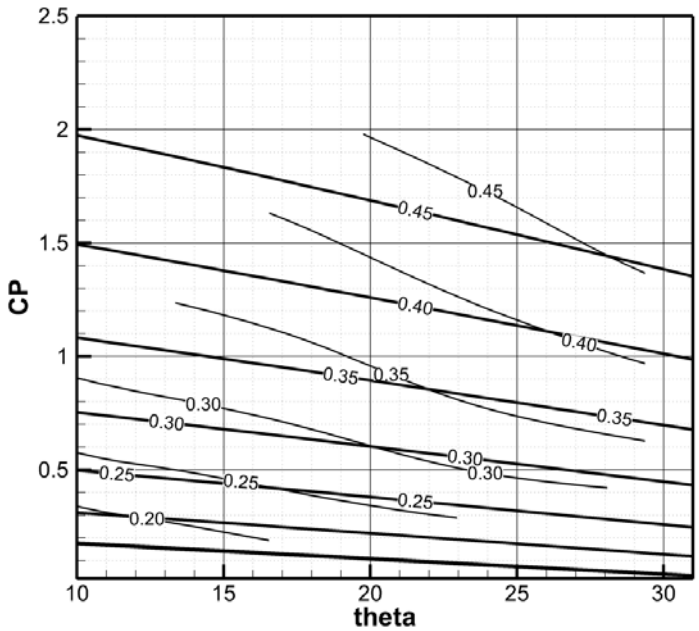

Figure II.1.3-18 $C_P - \theta_0$ **for** $s/c = 6, h_0/c = 0.75, b/c = 1/3$ **. Thicker lines are for calculated results and thinner, are for experimental, Schouveiler et al. (2005).**

II.1.4 Acceleration of programs used

As already mentioned, the major computational costs for the general unsteady case are (in order of higher to lower):

a) Calculation of the time evolution of the free shear layer surface S_F

b) The iterative solution of the nonlinear system.

c) The setup of the nonlinear system.

For the purpose of the acceleration of the computational method, the new technology of GPU computing was explored and implemented. More specifically, GPUs (Graphics Processing Units) are in effect processors with many (thousands) arithmetic units. Due to their original purpose of processing and rendering millions of vertices in real time the architecture of the GPU is different to the normal processors and is outstandingly fast, scalable and efficient at algorithms that need the repetition of the same set of instructions for a large range of points (or cases) that can run in parallel. This model is called Single Instruction Multi-Threading. Processes as matrix operations, or integrations, are the ones that are the most scalable and have been explored the most. More specifically, the well-known linear algebra LAPACK has been translated to CUDA (C Unified Development Architecture, developed by NVidia) and the CULA tools Package was created and optimized by EM Photonics. This tool provides a set of subroutines that allow the solution of linear systems at speedups of over 300x compared to solving on the CPU.

After the creation of a "wrapper" for the CULA routines, so they can be called by the existing programme, the solution accuracy, and the actual speedup can be evaluated. For the specific implementation, common commercial (gaming – low cost) GPUs were used in workstation grade pcs. The accuracy of solution, for single precision operations, is within the machine error margin that the solution on the CPU has, and the speedup for the solution of a 20000x20000 dense linear system is measured to be 800 to 900 times. This speedup, in the total time of the method, can mean a speedup of magnitude 9 up to 70, depending on whether a linear or on nonlinear Kutta condition is applied and on the amount of Newton iterations applied for the solution of the nonlinear system.

The calculation of the time evolution of the free wake, can also be broken down to the calculation of the induced velocities at each point, which can be done for each point separately (thus in parallel) and a series of matrix operations for the translation of the points. This means that this part of the algorithm is also parallelizable and possible to be run on a GPU. Even though it has not been implemented in the programs used for the purpose of this thesis, initial tests have been made and the potential for speedup of the subprocess is estimated to be at least 200x. This development will be discussed further in the Future Work part of the conclusion.

Part III SIMULATIONS WITH FULLY PRESCRIBED MOTIONS AND OPTIMUM DESIGN METHODOLOGY FOR FLAPPING WING PROPULSION

In the development of the work for the purposes of this thesis, prescribed motion simulations were considered to be the foundation for any other possible applications. As such, they were the first to be investigated and the ones to be thoroughly analysed.

In chronological order, most of cases were developed in parallel, as in Politis & Tsarsitalidis (2009) most wing configurations were introduced and some preliminary results of each case were presented and thereafter developed. In Politis & Tsarsitalidis (2010), simulations of bird flight were introduced, the concept propulsor FOD (Flexible Oscillating Duct) was introduced in Politis & Tsarsitalidis (2011) and analysed in detail in Politis & Tsarsitalidis (2012). FOD was further developed into FEOD (Flexible Elliptic Oscillating Duct) in Politis, Ioannou and Tsarsitalidis (2013). In the same time, systematic investigations for twin wing systems was shown in Politis & Tsarsitalidis (2013) and in Politis & Tsarsitalidis (2014) the first detailed series for single wing propulsors, along with a corresponding design method was presented.

Regardless of the chronological order of the publications and development of works, the methods, the simulations and the design applications for prescribed motions are going to be presented in a logical order that makes it easier for the reader to follow. The simulations grouped in order of similarity and complexity, are presented and discussed, along with their parameters, phenomenology analysis and systematic results (where applicable) which indicate the effects of parameters. Then, the design method for biomimetic propulsors of fully prescribed motion is presented and virtual applications on ships are presented and compared to conventional propellers.

III.1 Prescribed Motions Simulations

The fully prescribed motions can be considered to be of key importance, as through systematic variation of main motion and geometry parameters, observations on the governing mechanisms can be made and useful deductions can be obtained. Additionally, a thorough set of systematic simulations, can prove to be an extremely valuable input for those who attempt to make an advanced control system, as it can provide the data required for system identification, while it can also provide some initial insight, useful for the decisions required for the simulations of spring loaded wing, as will be discussed in Part III. Thus, extra gravity was given to the part of the systematic simulations of prescribed motions, in order to be as thorough and concise as time and compute capabilities would allow, in order to gain a wide coverage of parameters, which will lead to attaining a clearer insight of the effects of each parameter. . The accuracy of the simulation method in hand has already been examined in II.1.3. However, convergence and grid independence tests for each case are presented accordingly.

III.1.1 Single wing simulations - A systematic series for flapping wing propulsor design

The single foil configuration is the simplest, yet the most important, as all effects can be isolated and studied thoroughly. Additionally, it is the least computationally "expensive", thus making it the ideal starting point for a wide area of parameters analysis. Last but not least, it is the case where the most reliable experimental data exist, thus allowing for safer deductions, as they can be cross examined against experiments. The case of a single wing in pitching and heaving motion, was the first to be investigated in Politis & Tsarsitalidis (2009) and the first to be thoroughly investigated and published as a systematic series in Politis & Tsarsitalidis (2014). This series has been extended for a wider range of parameters and characteristic results are presented. Charts for the systematic series have been produced and the use of them is introduced. Finally, comparative diagrams are used for visualization of the effects of the parameters used.

III.1.1.1 Wing geometry, motion and panel generation.

The starting point for an unsteady BEM simulation is the generation of the time dependent paneling, describing the geometry of the system, Politis (2011). For the case of a moving wing, this can be done as follows:

The state of the system in question is defined uniquely by a set of independent variables, which can be decomposed into two groups: Group A containing the geometric variables and group B containing the motion related variables.

Group A: Wing geometry is defined by the wing outline (i.e.: span-wise distribution of chord, skewback and twist), camber and thickness distributions. Assuming geometrical similarity with respect to omitted variables, a minimum set of parameters defining wing geometry is its span s, the maximum chord c and the skewback angle $\hat{s}$.

Group B: Wing motion is defined by: (a) the amplitude h_0 of a sinusoidal heaving motion normal to the velocity of advance U, (b) the amplitude θ_0 (denoted as *theta* in some figures in the sequel) of a sinusoidal pitching motion, (c) the chordwise position b of pitching axis of the wing, (d) the frequency n (common for both heaving and pitching motions) and (e) the phase angle ψ between heaving and pitching motions.

Thus, assuming geometric similarity for the omitted variables, the geometry and motion of the flapping wing is completely defined by the variables: $(U, n, h_0, \theta_0, \psi, s, c, \hat{s}, b)$ or in non-dimensional form: $(\theta_0, Str, \psi, h_0/c, s/c, \hat{s}, b/c)$, where Str denotes the Strouhal number defined by:

$$Str = \frac{n \cdot h}{U}, h = 2h_0 \quad \text{(III.1)}$$

and h denotes the heave height.

The previous parameters define uniquely the instantaneous angle of attack $a(t)$ of the wing section with respect to the undisturbed flow through the equation:

$$a(t) = \theta_0 \sin(2\pi n \cdot t + \psi) - \tan^{-1}\left(\frac{h_0 2\pi n \cdot \cos(2\pi n \cdot t)}{U}\right) \quad \text{(III.2)}$$

or in non-dimensional form:

$$a(t) = \theta_0 \sin(2\pi n \cdot t + \psi) - \tan^{-1}(\pi \cdot Str \cdot \cos(2\pi n \cdot t)) \quad \text{(III.3)}$$

where t denotes time.

Having introduced the analytical description of both geometry and motion of the wing, the creation of a surface panel distribution describing the wing at consecutive time steps is straightforward. Figure III.1.1-1 shows animated flapping wing panel discretization for twenty four time instances, evenly distributed in two periods, for a wing of the series (to be introduced in III.1.1.3) with: $h_0 / c = 1.5, Str = 0.35, \theta_0 = 23.6^0, \psi = 90^0$. With the time evolution of the flapping wing paneling known, the code UBEM can be applied to calculate the resulting unsteady forces, energy requirements and free shear layer evolution.

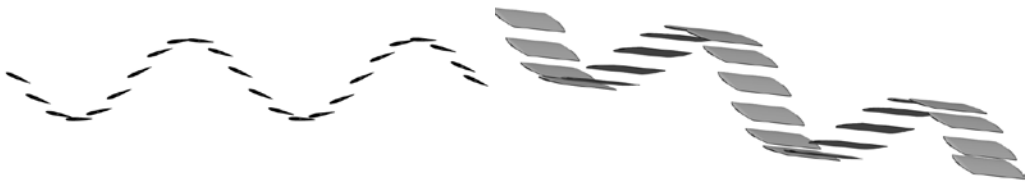

Figure III.1.1-1 Sequential positions of the flapping wing for $h_0 / c = 1.5, Str = 0.35, \theta_0 = 23.6^0, \psi = 90^0$

III.1.1.2 Transient flapping wing performance and selection of simulation period.

The main difference between a traditional propeller and a flapping wing is that the latter produces a period mean thrust as a result of a highly unsteady instantaneous thrust. The simulation method in hand can produce this time dependent thrust but, since it is a time stepping method, initial conditions on wing motion have to be imposed. A burst starting wing is used as the starting condition. In this case a transient phenomenon occurs. Thus the mean period values for thrust or power have to be calculated after the passage of this initial transient phenomenon. To care for this, time domain simulations have been performed for a time range extending to three periods and for several combinations of wing geometry and flow parameters, covering the range of the wing series (to be introduced in III.1.1.3), in order to decide about the proper simulation period which will produces mean forces free of transients. Indicatively, Figure III.1.1-2 to Figure III.1.1-6, show the variation of wing thrust coefficient $C_T(t)$ with time $t(\text{sec})$, where $C_T(t)=\dfrac{T(t)}{0.5\rho U^2 S}$ and $T(t)$ denotes the time dependent wing thrust, ρ denotes fluid density, U denotes the translational velocity of the wing and S denotes the wing swept surface ($S=s\cdot h$). A $\psi=90^0$ has been selected for these calculations.

From these figures it can be concluded that, for the examined family of wings and motions, the transient phenomenon is limited to the few initial time steps after the burst start. Thus it is safe to use the 2nd period of simulation, to calculate the mean thrust and power to be used as a representative of the mean open water performance of the family of simulations made.

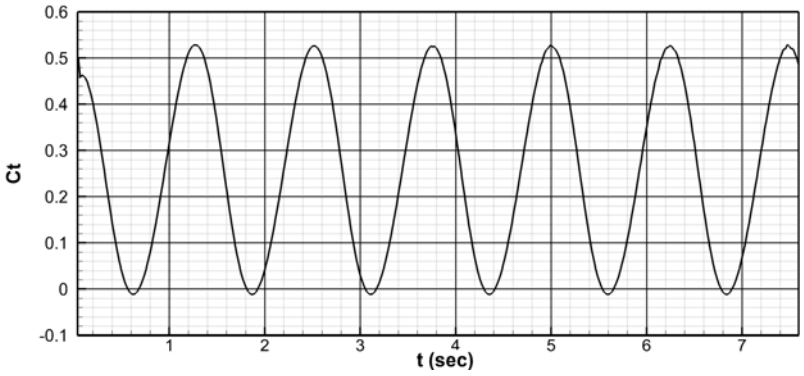

Figure III.1.1-2 $C_T(t)$ **for** $\{s/c=2, h_0/c=1, \text{Str}=0.35, \theta_0=23^0\}$ **timestep=0.026sec**

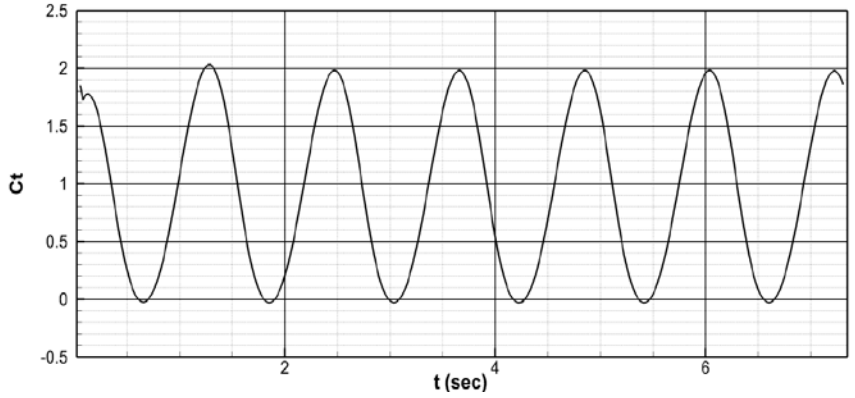

Figure III.1.1-3 $C_T(t)$ **for** $\{s/c=2, h_0/c=1.5, \mathrm{Str}=0.55, \theta_0=35^0\}$ **timestep=0.025sec**

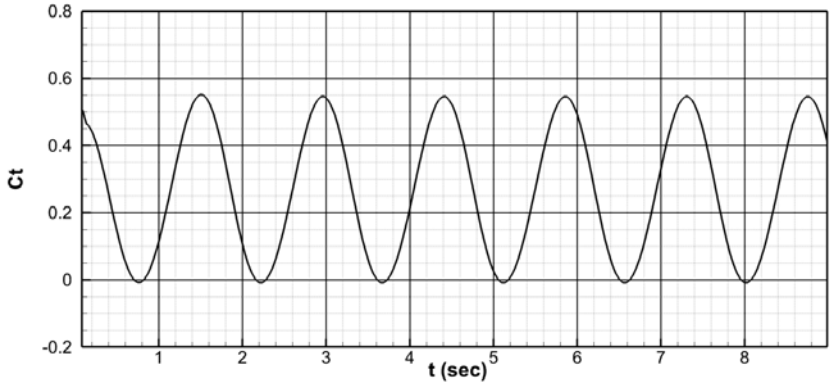

Figure III.1.1-4 $C_T(t)$ **for** $\{s/c=4, h_0/c=1, \mathrm{Str}=0.30, \theta_0=20^0\}$ **timestep=0.029sec**

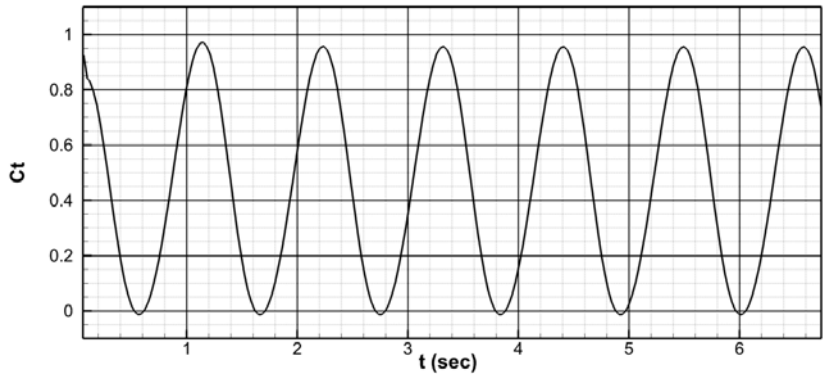

Figure III.1.1-5 $C_T(t)$ **for** $\{s/c=4, h_0/c=1, \mathrm{Str}=0.40, \theta_0=25^0\}$ **timestep=0.023sec**

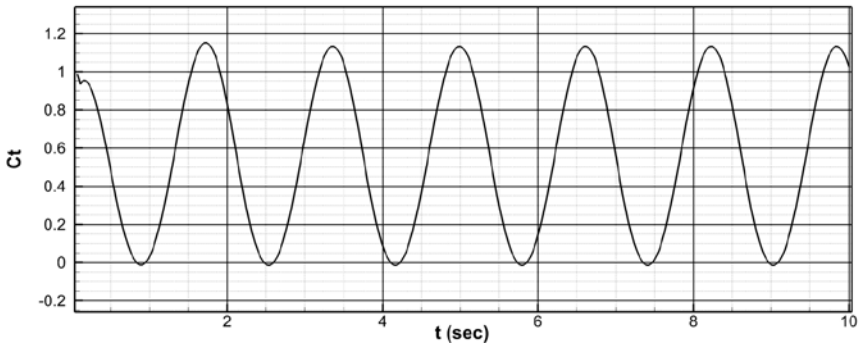

Figure III.1.1-6 $C_T(t)$ **for** $\{s/c=6, h_0/c=1.5, \text{Str}=0.40, \theta_0=25.6^0\}$ **timestep=0.031sec**

III.1.1.3 The flapping wing series

To proceed to a series based design process for flapping wings, decisions have to be taken, regarding the geometric and flow related parameters of the family. In this respect the following decisions have been taken:

- The wing outline is characterized by zero twist. For smoothening of the tip vortices the wing outline has rounded edges with the following detailed form: Starting from the wing tip and up to $c/2$ distance spanwisely, the chord changes from $c/4$ (at tip) to c (at $c/2$ from tip). The interpolation schema for the chord, for spanwise positions between tip and $c/2$, is a cubic spline with end conditions of $d^2c/ds^2=-5$ at tip and $dc/ds=0$ at $c/2$. A NACA 0012 thickness form has been selected for the whole span.
- Wing with span to chord ratio: $s/c=2,4,6$
- Sweep angles $\hat{s}$ = 0,15,30,45 degrees
- Heaving amplitude: $h_0/c=0.5,1.0,1.5,2.0$
- Position of the pitch axis (from leading edge): $b/c=0.1,0.33$
- Strouhal number: $Str=0.1\div0.7$
- Pitch angle θ_0 (*theta* in some diagrams): from 5 degrees to a maximum, corresponding to zero mean thrust.
- Phase angle between heaving and pitching motions: $\psi=90^0$.
- For selected cases, $s/c=8,10,12$, has also been tested
- For $s/c=6$ the following variation of phase angle was also tested $\psi=60^0,70^0,80^0,90^0,100^0,110^0,120^0$

The resulting wing geometry for the three selected values of s/c is seen in Figure III.1.1-7 and the additional swept wing geometries are shown in Figure III.1.1-8. The series was originally introduced in Politis & Tsarsitalidis (2014) and is extended with the addition of simulations for the swept wings, the variation of phase angle (for s/c=6) and the additional s/c values, in this work.

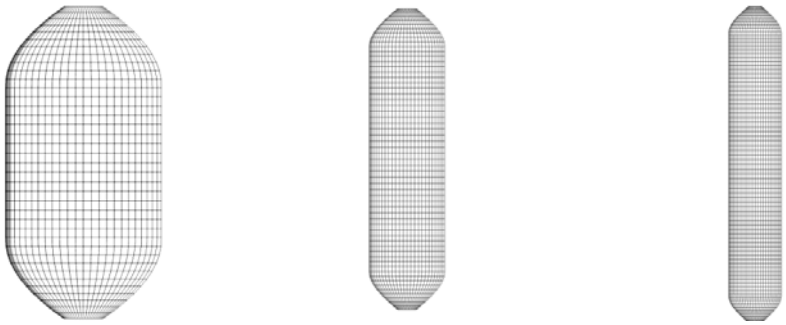

Figure III.1.1-7 Wing outline for $s/c = 2,4,6$ respectively.

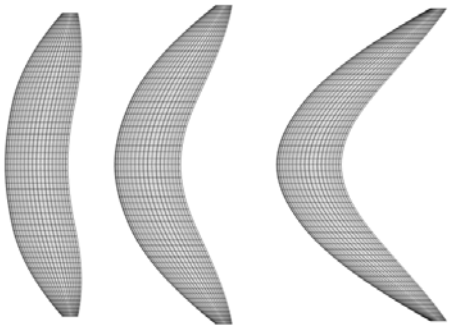

Figure III.1.1-8 Wing outline for $s/c = 4$ and $\hat{s} = 15^o, 30^o, 45^o$ respectively

Commenting on the previous selections, the wing span to chord ratio has been varied from 2 to 6 in order to include both a vertically orientated wing (lower aspect ratio) and a horizontal wing, extending along ship's breadth (higher aspect ratio). Larger aspect ratios were tested, in order to explore the 3D effects and their asymptotical tendency to a 2D result. Heave to chord amplitude has been selected from 0.5 to 2.0. This selection is related to the fact that optimum efficiency is usually observed in the range: $h_0/c = 0.75-1.0$, (Triantafyllou et al. (2005)). However it is interesting to investigate numerically the effect of greater values of h_0/c to the wing performance. The position of the pitching axis has been selected in the range $b/c = 0.1-0.33$. This decision is related to the fact that, in 2D inviscid linearized airfoil theory the center of pressures lays a quarter chords from leading edge, a value which is in-between the selected range. Regarding selection of Strouhal number previous simulation experience, as well as evidence from the literature, Triantafyllou et al. (2005), indicates that optimum hydrodynamic performance is achieved in the range: $Str = 0.15 \div 0.35$. The selection: $Str = 0.1 \div 0.7$ broadens the simulation to higher Strouhal numbers allowing quantitative estimation of the effect of propulsor loading (quantified by the Strouhal number) to its hydrodynamic efficiency. Notice that for greater ship speeds, the need of highly loaded flapping wings seems very probable. The range of the pitch angle θ_0 has been selected in order to cover the full thrust producing regime for each wing of the family. The selection of a minimum pitch angle of 5 degrees has to do with the fact that for lower values of θ_0, flapping wing flow is liable to leading edge separation, a phenomenon which is not modeled by UBEM.

Furthermore, as will be seen later on, this region of pitch angles is without practical interest due to the very low hydrodynamic efficiency observed. Finally, with the exception of s/c=6 where variation was tested, the phase angle between the heaving and pitching motions has been selected: $\psi = 90^0$, which is a nominal value providing good efficiencies, (Triantafyllou et al. (2005)).

With the previous discussion/decisions in mind, the wing family of existing simulations consists of 45 different sets of geometric/motion configurations (24 were created for Politis & Tsarsitalidis (2014)). Each configuration set has been set in motion using all combinations of Strouhal and pitch angle amplitudes in the selected range. The developed mean thrust and power is then represented in a number of charts with the maximum pitch angle θ_0 in the horizontal axis and the Strouhal number Str as parameter. Those charts are the analog of the 'open water performance charts' (where θ_0 plays the role of propeller pitch ratio and Str the role of the inverse of the propeller advance coefficient) used in propeller design, (Oosterveld & Oossannen (1975)), and are the subject of the next section.

III.1.1.4 The open water performance charts for the flapping wing series.]

Systematic unsteady BEM simulations have been performed with the selected flapping wing series. In all simulations a chord of $c = 1.0m$ has been selected. Variation of Strouhal number has been achieved by changing the frequency of the flapping wing oscillation, while the corresponding translational velocity has been held constant and equal to $V = 2.3m/s$. This results to an overcritical Reynolds number (based on translational velocity: $\mathrm{Re} = U \cdot c / \nu$) equal to $\mathrm{Re} = 2.02 \cdot 10^6$. Corresponding Reynolds numbers based on the maximum undisturbed flow velocity are Strouhal dependent according to the relation: $\mathrm{Re}_{Str} = \frac{U \cdot c}{\nu}\sqrt{1+(\pi \cdot Str)^2}$, or $\mathrm{Re}_{Str} = 2.12 \cdot 10^6$ at $Str = 0.10$ and $\mathrm{Re}_{Str} = 4.88 \cdot 10^6$ at $Str = 0.7$ (assumed kinematic viscosity $\nu = 1.139 \cdot 10^{-6} m^2/s$). Notice that UBEM incorporates a simplified viscous drag correction, as discussed in Politis (2004). Mean thrust and power have then been calculated by running UBEM for two time periods and calculating the mean values of the unsteady forces over the second period (as explained in III.1.1.2).

As it will be discussed in the next part and following previous experience, Politis & Tsarsitalidis (2012), the results are presented in the form of charts for the open water thrust and power loading coefficients (based on swept area) versus pitch angle: $C_T(\mathrm{Str}), C_P(Str) - \theta_0$ with parameter the Strouhal number (bold line), where:

$$C_T = \frac{T}{0.5\rho U^2 S}, C_P = \frac{P}{0.5\rho U^3 S} \qquad \text{(III.4)}$$

T, P denote the period-mean open water thrust and power of the flapping wing, ρ denotes fluid density, U denotes the translational velocity of the wing and S denotes the wing swept area ($S = sh = 2sh_0$).

Furthermore, the $C_T - \theta_0$ charts additionally contain, in parametric form, the open water efficiency η of the system:

$$\eta = \frac{T \cdot U}{P} = \frac{C_T}{C_P} \tag{III.5}$$

while the $C_P - \theta_0$ charts contain additionally in parametric form the $a_{\max}$ angle which is the maximum value of $a(t)$, relation (III.3), over one period. This last information is very useful for the designer in order to avoid maximum angles with a potential danger for separating flow (e.g. greater than 15-20deg), phenomenon which is not modeled by the current version of UBEM and consequently simulations can result in questionable and/or incorrect predictions in that region.

In addition, a new $Cp_P - \theta_0$ chart is introduced is this work, containing in non-dimensional form the energy required for the pitching of the wing:

$$Cp_p = \frac{\text{average pitching power}}{0.5\rho U^3 S} = \frac{(\int_t^{t+\mathrm{T}} M_p(t) \cdot \omega_p(t) dt) / \mathrm{T}}{0.5\rho U^3 S} \tag{III.6}$$

where $M_p(t)$ is the instantaneous moment around the pitching axis, $\omega_p(t)$ is the instantaneous rotational velocity around the pitching axis and T is the pitching period. Using the $Cp_P - \theta_0$ chart, the designer can estimate how, the total delivered power to the flapping wing system is distributed to the two different modes of motion (i.e. heaving motion & pitching motion).

P actually contains both pitching and heaving components of power, but as shown in the sequel, the pitching part is so small, that P is directly indicative of the power required for the heaving motion. Thus, no additional coefficient needs to be introduced. (if the user requires the heaving power precisely, all they have to do is subtract the pitching fraction)

An indicative set of open water performance charts for the flapping wing family, is shown in Figure III.1.1-9a,b,c and Figure III.1.1-10 a,b,c. In both figures a wing with $s/c = 6, h_0/c = 1.0, b/c = 0.33$ has been selected, while Figure III.1.1-9a,b,c shows results for $\psi = 90^0$ and Figure III.1.1-10a,b,c shows results for $\psi = 75^0$. A full collection of charts of this type is contained in the appendix, while the effects of parameters will be investigated in III.1.1.7.

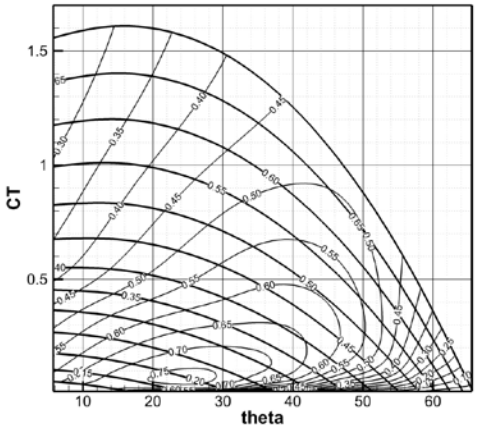

a

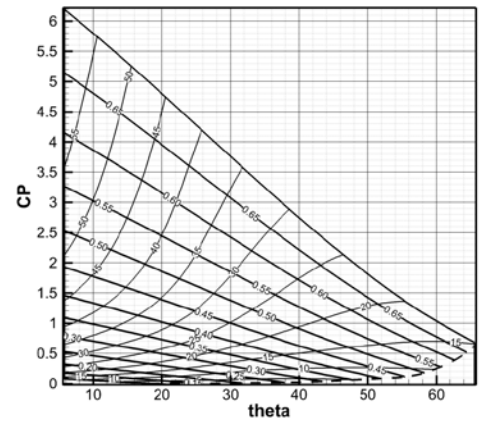

b

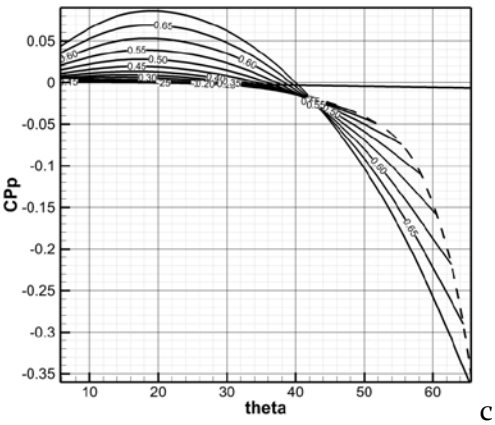

c

Figure III.1.1-9 a,b,c.

$s/c = 6, h_0/c = 1.0, b/c = 0.33, \psi = 90^0$

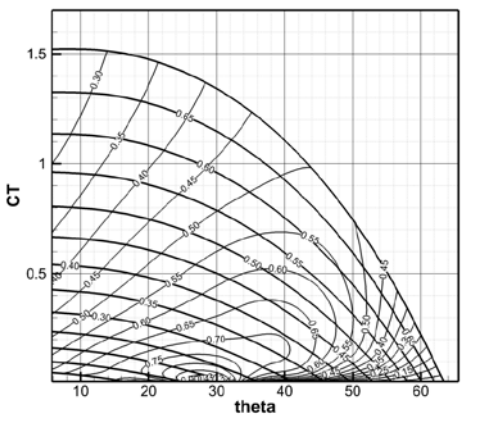

a

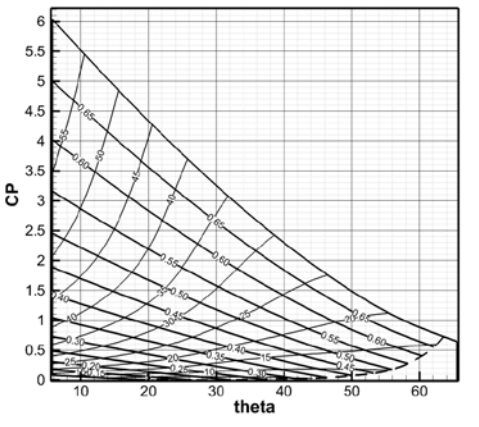

b

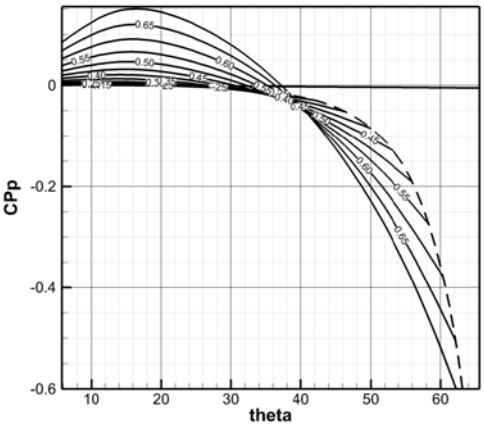

c

Figure III.1.1-10 a,b,c.

$s/c = 6, h_0/c = 1.0, b/c = 0.33, \psi = 75^0$

(a) Grid of constant Strouhal lines (bold) and constant efficiency lines, (b) Grid of constant Strouhal lines (bold) and maximum angle of attack and (c) Grid of constant Strouhal lines. Dashed lines in all figures are the zero thrust limits.

III.1.1.5 Grid independence of the UBEM predictions for the case.

In order to analyze the effect of the grid density to the calculated open water flapping wing performance, the systematic BEM calculations of the previous paragraph have been repeated with three different grid densities, according to Table II.1.3-3:

Table III.1.1-1. Grid densities.

name	No of chordwise elements (face + back)	No of spanwise elements		
		$s/c=2$	$s/c=4$	$s/c=6$
Grid1	**20**	**30**	**50**	**80**
Grid2	**35**	**45**	**80**	**120**
Grid3	**50**	**70**	**130**	**200**

The timestep is defined for each single simulation by calculating the maximum translation of the trailing edge (per step) and keeping it in comparable size to that of the used elements. For the comparison among grids, the following procedure has been used: For each one of the 24 configurations (introduced in section 4) and for each grid of table 1, figures like Figure III.1.1-9 can be produced. Considering the results (θ_0, Str, C_T) in figure III.1-9a, an alternative graphical representation is in the form of a 3D plot with θ_0, Str along the XY axis and C_T along Z axis. Thus a C_T surface can be created. Applying these procedures for all combinations of wing configurations and grids, a total of 24*3=72 surfaces for C_T are obtained. By inserting any two such surfaces in a plotting software, it is easy to obtain the mean and maximum deviation between them. Those data are shown on Table II**.1.3-4**, with the following convention: Above diagonal are overall mean of the %differences of mean thrust values and below diagonal are the maximum of the %differences of mean thrust values.

It can be seen that Grid2 (as well as Grid3) can be considered as a reliable discretization for systematic simulations. Nevertheless, Grid1 in spite of lacking accuracy, it is good enough to show trends and could be used for getting quick exploratory results.

Table III.1.1-2. Mean (above the diagonal) and maximum (below the diagonal) %deviations in mean thrust calculation.

	Grid1	**Grid2**	**Grid3**
Grid1	**0**	**4.50%**	**5.02%**
Grid2	**8.09%**	**0**	**0.52%**
Grid3	**10.45%**	**2.21%**	**0**

To verify the predictive ability of UBEM, experimental data was taken from the works of Prof. Triantafyllou and his team. More specifically figures 8 and 9 in Read et al. (2003), contain experimental measurements of mean thrust loading coefficient (based on wing plan form surface $S = sc$) and efficiency, for a rectangular wing with $s/c = 6$, for a range of Strouhal numbers and maximum angles of attack corresponding to the thrust producing regime. The wing has a rectangular outline with $c = 0.1m, s = 0.6m$ and it is equipped with endplates, to enforce 2D flow in most part of the wing surface. The pitch axis is located at $b/c = 1/3$ from leading edge, the heave to chord ratio has been selected as $h_0/c = 1.0$ and the phase angle has been selected as $\psi = 90^0$. Furthermore figures 5a,b in Schouveiler et al. (2005), contain analogous experimental results for the same wing but with different heave to chord ratio $h_0/c = 0.75$. Notice that the experimental data provided in the above papers are plotted in a different format than that used in the present work. More specifically instead of a $C_T(Str) - \theta_0$ plot used in the present work, they use a $a_{\max}(C_T) - Str$ plot, where $a_{\max}$ is the maximum angle of attack. Also instead of a $C_P(Str) - \theta_0$ plot used in the present work, they use a $a_{\max}(\eta) - Str$ plot, where η denotes the efficiency, equation (III.5). The previous experimental measurements have been digitized and transformed to the form $C_T, C_P - \theta_0$, consistent with the definitions used.

III.1.1.6 Wake visualizations – Understanding how the Flapping wing produces thrust.

For a better understanding of the underlying physical mechanisms of thrust production, the free shear layer of a flapping wing with $s/c = 6$ is plotted, for a representative case corresponding to: $h_0/c = 1.5, b/c = 0.33, \mathrm{Str} = 0.35, \theta_0 = 23.6^0 \quad \psi = 90^0$, Fig. 14. The wing surface and the free vortex sheet surface on those figures have been colored according to their surface dipole distribution intensity. Notice that constant dipole lines coincide with surface vortex lines. By using either the last property or the deformation patterns of the free vortex sheets, a number of strong ring vortices in the wake of the wing are easily visualized. Those ring vortices produce a series of oblique jet flows by which the flapping wing produces forces (thrust and lateral forces), through momentum conservation. Figure III.1.1-11 also contains artistic add-ons, showing the train of ring vortices and corresponding jets (straight arrows) by which the flapping wing produces forces. More specifically the straight arrows visualize the induced velocities produced by the ring vortices. This wake vortex system is the 3D analog of the well-known 'reverse Karman vortex street' pattern, appearing in aquatic animal and/or bird flapping wing propulsors, Schouveiler et al. (2005), Taylor et al. (2010). More extensive wake visualizations confirming the physical mechanism of systematic ring vortex creation, as the main mechanism for force production can be found in Politis & Tsarsitalidis (2009).

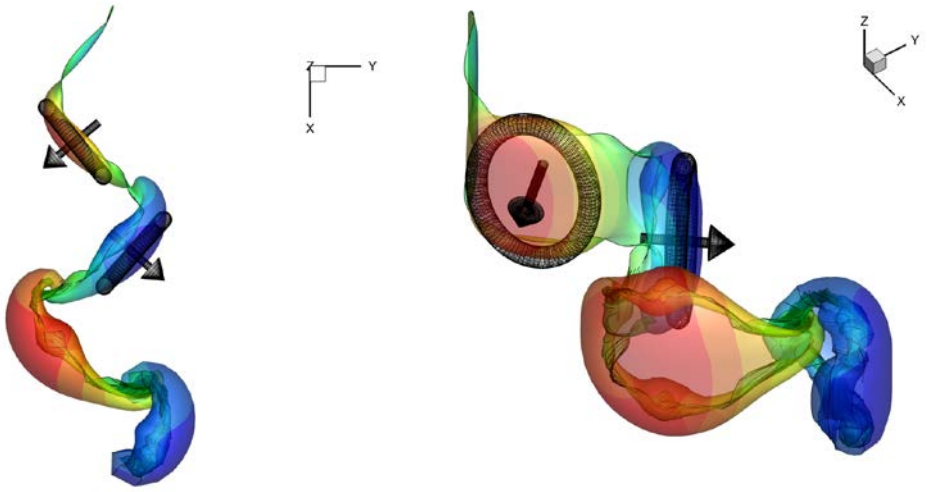

Figure III.1.1-11 Wake of a Flapping wing. Colors are for dipole potential. Artistic add-ons showing the train of ring vortices and corresponding jets by which the wing produces thrust.

III.1.1.7 Effects of parameters

By inspecting the results of the appendix as well as the comparative diagrams, in (Politis and Tsarsitalidis 2014) the following conclusions were deducted:

- The region of maximum hydrodynamic efficiency is achieved at a maximum angle of attack less than 20 degrees i.e. at the region of flow without serious unsteady separation;
- For constant s/c, increasing the heave to chord ratio h_0/c, the maximum hydrodynamic efficiency is increased. This result is consistent with what is observed for propellers, where the reduction of thrust loading coefficient C_T results in an increase of hydrodynamic efficiency, Reissner (1942). Notice that in Triantafyllou et al. (2005) an optimum in the range $0.75 \le h_0/c \le 1.0$ has been reported for 2D foils. Thus the effect of h_0/c on efficiency, is worth of further experimental investigation;
- Wings with higher s/c (i.e. higher aspect ratio) can produce higher hydrodynamic efficiencies. From the charts of the appendix the wing with $s/c = 6, h_0/c = 2$ results in maximum hydrodynamic efficiency of the order of 85%.
- Maximization of hydrodynamic efficiency is always achieved at lower values of the thrust loading coefficient. Thus, achievement of high hydrodynamic efficiencies with significant thrust is connected with our ability to maximize the swept area of the propulsor (recall the definition of the thrust and power loading coefficients used, where in the denominator of the corresponding formulas is the swept area).
- The position of the pitch axis point has a small effect on the hydrodynamic efficiency. By moving the pitch axis point towards wing leading edge (holding other non-dimensional parameters constant), the hydrodynamic efficiency is slightly reduced.
- The position of the pitch axis point affects the produced thrust loading coefficient. By moving the pitch axis point towards wing leading edge (holding other non-dimensional parameters constant), the thrust loading coefficient is increased.

- The mean power required for driving the pitching motion of the wing is an order of magnitude lower than the mean power required driving the heaving motion. The position of the pitch axis point as well as the selected pitch angle, affects seriously the required mean power for the pitching motion. This power can take both positive (i.e. the pitching power is provided by the user) or negative values. Thus with a proper selection of parameters, the pitching motion can be a mechanism of energy restoration.
- The selection of the phase angle ψ seems to play a secondary role in the powering performance of the flapping wing. For the considered case (Fig. 8,9), the change from $\psi = 90^0$ to $\psi = 75^0$ results in a small decrease of C_T with a corresponding increase in efficiency.

In order to examine the effect of each parameter, comparative diagrams for cases where only a selected parameter is varied follow (Figure III.1.1-12 up to Figure III.1.1-32), to enable the reader to see the effects clearly along with further discussion on each individual parameter. For each case, diagrams are made, where contours of the same parameter and value are plotted but a different value of the examined parameter are plotted (with different linetypes) against each other.

III.1.1.7.1 Effect of h/c

In Figure III.1.1-12 thru Figure III.1.1-20, iso-Strouhal and Iso-efficiency contours are plotted for varying h/c values, for all AR=s/c (2,4,6) and both pitching axis conditions (0.1c and 0.33c from le). A general conclusion is that with increasing h/c ratio, the loading gets lower and the efficiency increases, as noted previously. Another interesting remark is that the peak of efficiency (maximum thrust coefficient for the same efficiency) moves to larger values of theta (θ_o) which mean smaller maximum angle of attack, as the h/c increases, but also to larger values of thrust. This can be explained by the fact that the wing remains longer in angles of attack close to the maximum, when lateral travelling (heave) is increased, thus giving thrust for a larger part of the period (leading to increased average thrust). At the same time, since the swept area increases, the thrust coefficient is decreased, meaning lower loading, which leads to higher efficiency, an effect well explained by momentum theory. This effect is repeated for all cases, observation which solidifies the conclusion.

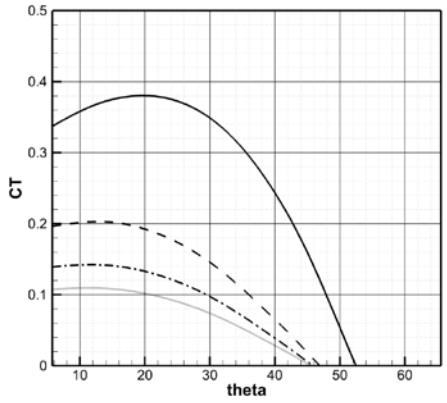

Figure III.1.1-12 Effect of h/c, iso-Strouhal contours (Str=0.3) for straight wing Ar2 pitch at 0.1c. Solid:0.5, Dashed:1.0, Dash-Dot:1.5, Dotted:2.0

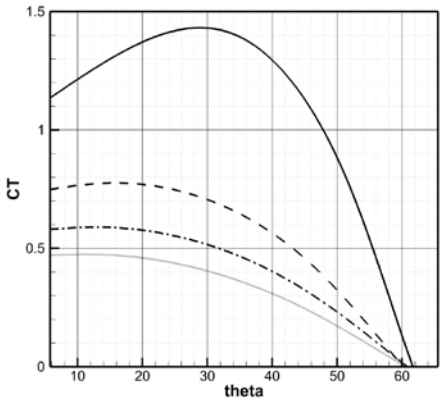

Figure III.1.1-13 Effect of h/c, iso-Strouhal contours (Str=0.5) for straight wing Ar2 pitch at 0.1c. Solid:0.5, Dashed:1.0, Dash-Dot:1.5, Dotted:2.0

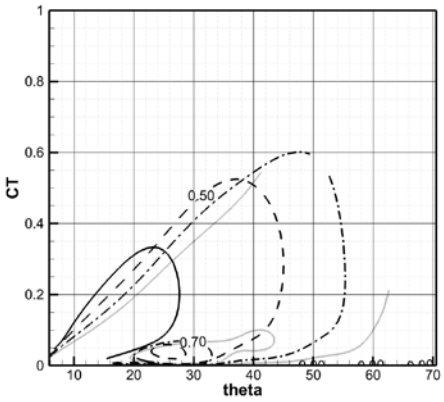

Figure III.1.1-14 Effect of h/c, iso-Efficiency contours for straight wing Ar2 pitch at 0.1c. Solid:0.5, Dashed:1.0, Dash-Dot:1.5, Dotted:2.0

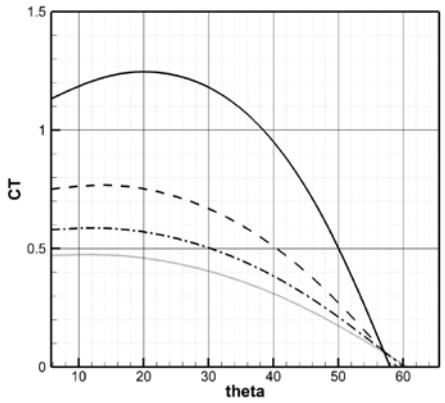

Figure III.1.1-15 Effect of h/c, iso-Strouhal contours (Str=0.5) for straight wing Ar4 pitch at 0.33c. Solid:0.5, Dashed:1.0, Dash-Dot:1.5, Dotted:2.0

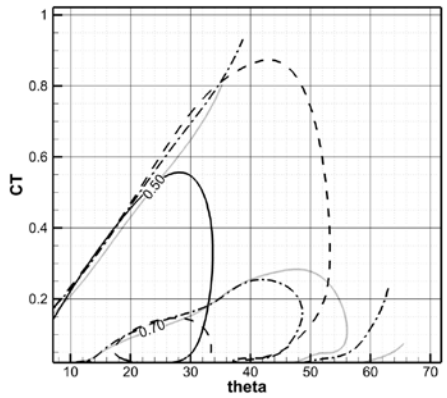

Figure III.1.1-16 Effect of h/c, iso-efficiency contours for straight wing Ar4 pitch at 0.33c. Solid:0.5, Dashed:1.0, Dash-Dot:1.5, Dotted:2.0

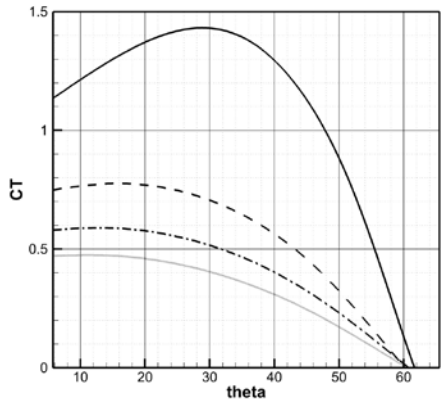

Figure III.1.1-17 Effect of h/c, iso-Strouhal contours (Str=0.5) for straight wing Ar4 pitch at 0.1c. Solid:0.5, Dashed:1.0, Dash-Dot:1.5, Dotted:2.0

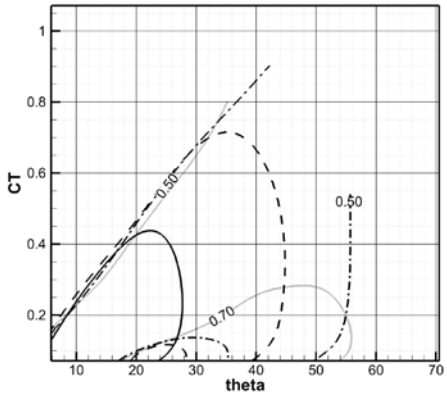

Figure III.1.1-18 Effect of h/c, iso-efficiency contours for straight wing Ar4 pitch at 0.1c. Solid:0.5, Dashed:1.0, Dash-Dot:1.5, Dotted:2.0

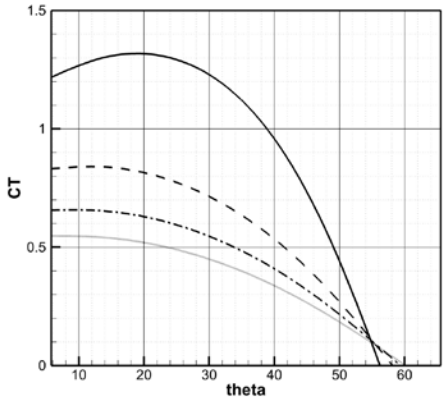

Figure III.1.1-19 Effect of h/c, iso-Strouhal contours (Str=0.5) for straight wing Ar6 pitch at 0.33c. Solid:0.5, Dashed:1.0, Dash-Dot:1.5, Dotted:2.0

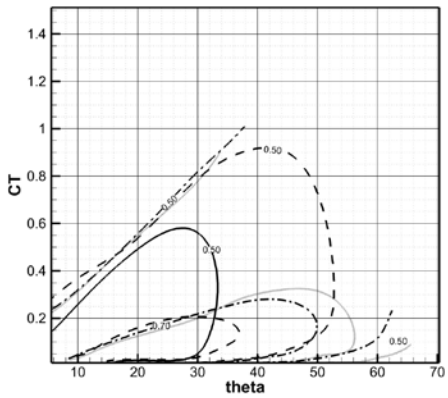

Figure III.1.1-20 Effect of h/c, iso-efficiency contours for straight wing Ar6 pitch at 0.33c. Solid:0.5, Dashed:1.0, Dash-Dot:1.5, Dotted:2.0

III.1.1.7.2 Effect of s/c

In Figure III.1.1-21 and Figure III.1.1-22 iso-Strouhal and Iso-efficiency contours are plotted for varying s/c values, for h/c=1 and pitching axis condition at 0.33c from le. Figure III.1.1-21 depicts Strouhal contour curves for the values of Str=0.5 and Str=0.3, with different linetypes for each value of s/c. In the same manner, Figure III.1.1-22 depicts efficiency contour curves for values n=0.5 and n=0.7. The general remark is that both thrust and efficiency increase when the s/c ratio increases and the slope of the iso Strouhal contours gets steeper, while the peak of efficiency remains at almost the same theta (and maximum angle of attack). The difference in slope can be attributed to the 3D effects (wake rollup) and the fact that they affect the total result less, as s/c increases. The results seem to converge to s/c=12, where 2D results seem to be reached. The observation that the iso-Strouhal curves cross at a single point, can be attributed to the fact that the 3D effects have a positive contribution to thrust, which is visible at near zero angles of attack.

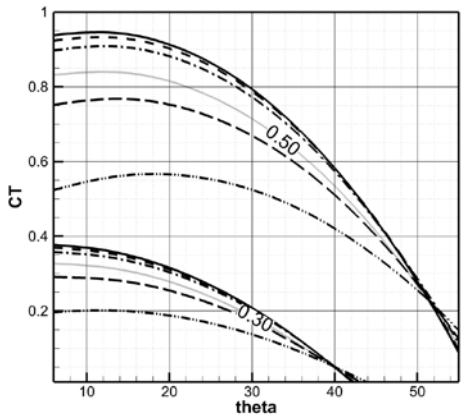

Figure III.1.1-21 Effect of S/c. Iso-Strouhal contours for straight wing, h/c=1, pitch at 0.33c. Dash dot dot: 2, Long dash: 4, Dotted: 6, Dash dot: 8, Dashed: 10, Solid: 12

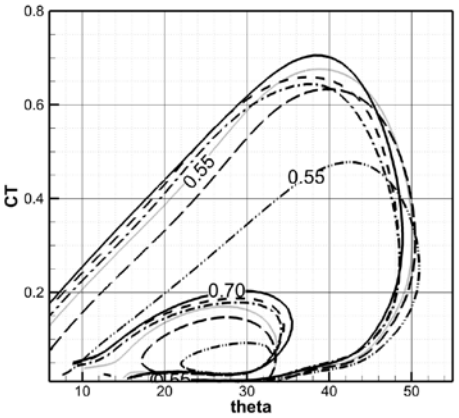

Figure III.1.1-22 Effect of S/c. Iso-efficiency contours for straight wing, h/c=1, pitch at 0.33c. Dash dot dot: 2, Long dash: 4, Dotted: 6, Dash dot: 8, Dashed: 10, Solid: 12

III.1.1.7.3 Effect of phase

In Figure III.1.1-23 thru Figure III.1.1-25, iso-Strouhal and Iso-efficiency contours are plotted for varying phase angle (60-120 degrees), for h/c=1 and pitching axis condition at 0.33c from le. Figure III.1.1-23 and Figure III.1.1-24 depict Strouhal contour curves for the indicated values, with different linetypes for each value of ψ. In the same manner, Figure III.1.1-25 depicts efficiency contour curves for values n=0.6. A general remark is that larger phase gives increased thrust, but at smaller efficiency, while smaller phase (compared to 90deg) gives smaller thrust at slightly better efficiency. To further observe the effect of phase, data form the point of highest efficiency for each set of simulations (one for each value of ψ), have been extracted and presented in Figure III.1.1-26 and Figure III.1.1-27 . These confirm the observations of Triantafyllou (1993), (2004), (2005) that the optimum phase angle is between 75 and 90 degrees. Additionally, it is observed that all the optimum points occur at Strouhal numbers between 0.1 and 0.22 and at maximum angles of attack below 10°.

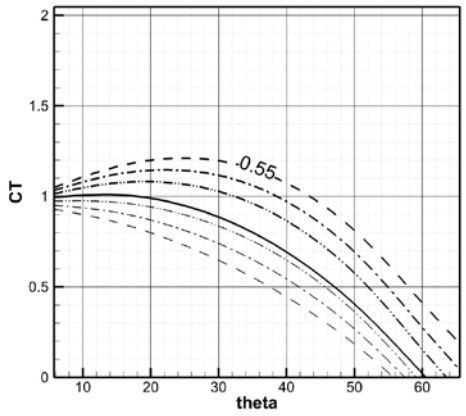

Figure III.1.1-23 Effect of Phase on performance. Iso- Strouhal curves. For straight wing, S/c=6, h/c=1.0, pitch at 0.33c. Thin dash: 60°, Thin dash dot: 70°, Thin dash dot dot: 80°, Solid: 90°, Thick dash dot dot: 100°, Thick dash dot: 110°, Thick dash: 120°.

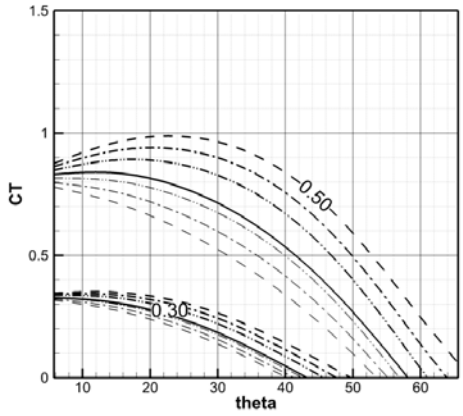

Figure III.1.1-24 Effect of Phase on performance. Iso- Strouhal curves. For straight wing, S/c=6, h/c=1.0, pitch at 0.33c. Thin dash: 60°, Thin dash dot: 70°, Thin dash dot dot: 80°, Solid: 90°, Thick dash dot dot: 100°, Thick dash dot: 110°, Thick dash: 120°.

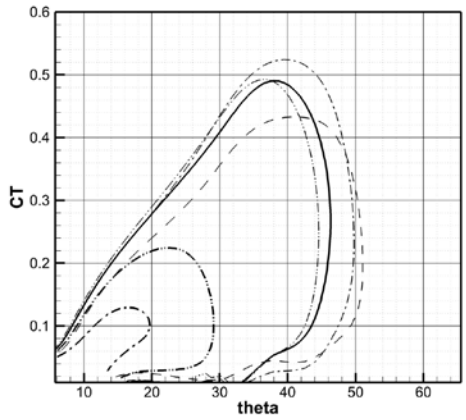

Figure III.1.1-25 Effect of Phase on performance. Iso- efficiency curves (n=0.6). For straight wing, S/c=6, h/c=1.0, pitch at 0.33c. Thin dash: 60°, Thin dash dot: 70°, Thin dash dot dot: 80°, Solid: 90°, Thick dash dot dot: 100°, Thick dash dot: 110°, Thick dash: 120°.

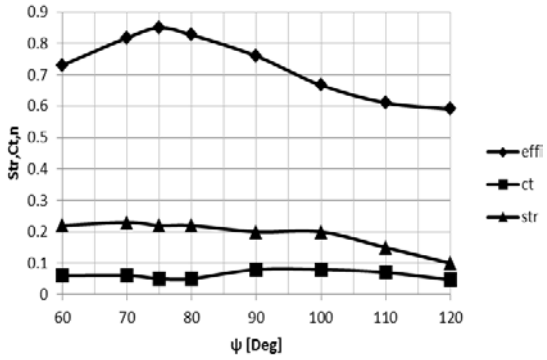

Figure III.1.1-26 Effect of Phase on points of maximum efficiency, for straight wing, S/c=6, h/c=1.0, pitch at 0.33c. Data are taken from the point of highest measured efficiency of each set ran for each value of ψ

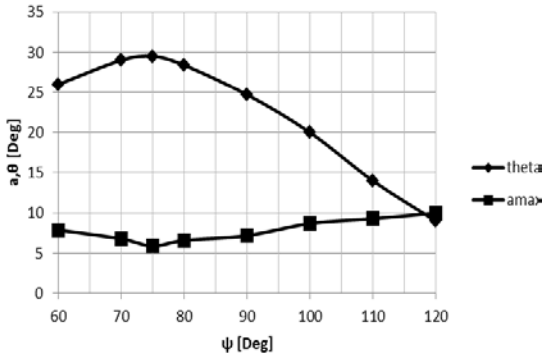

Figure III.1.1-27 Effect of Phase on points of maximum efficiency, for straight wing, S/c=6, h/c=1.0, pitch at 0.33c. Data are taken from the point of highest measured efficiency of each set ran for each value of ψ

III.1.1.7.4 Swept Wings

Iso-Strouhal and Iso-efficiency contours are plotted for varying skewback angle (0-45 degrees) for S/c=6 In Figure III.1.1-28 thru Figure III.1.1-30 and S/c=4 in Figure III.1.1-30 thru Figure III.1.1-32 for selections among h/c=1.0,1.5,2.0, and pitching axis at 0.33c of the midspan section. It can be observed, that the slope of iso Strouhal lines changes in a manner similar to a decreasing s/c ratio, but with a slight increase of thrust (instead of decrease that happens with the decrease of s/c for straight wings), but also at a significant decrease of efficiency. An initial deduction that can be made is that in the case of swept wings, the angle of attack is not the same for the whole span of the wing, but also the pitching axis is not at the same position relative to the center of each section. Thus, a further investigation of pitching axis position is necessary, before any conclusions are reached.

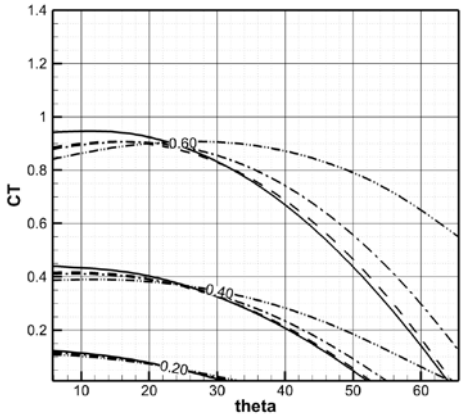

Figure III.1.1-28 Effect of sweptback wings. Iso-Strouhal lines for S/c=6, h/c=1.5, pitch at 0.33c of midspan. Solid: straight, Dashed: 15°, Dash dot: 30°, Dash dot dot: 45°

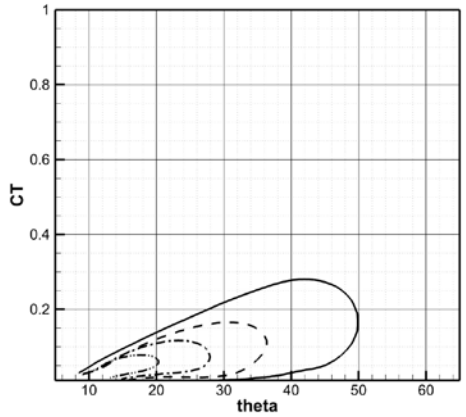

Figure III.1.1-29 Effect of sweptback wings. Iso-Efficiency lines (n=0.7) for S/c=6, h/c=1.5, pitch at 0.33c of midspan. Solid: straight, Dashed: 15°, Dash dot: 30°, Dash dot dot: 45°

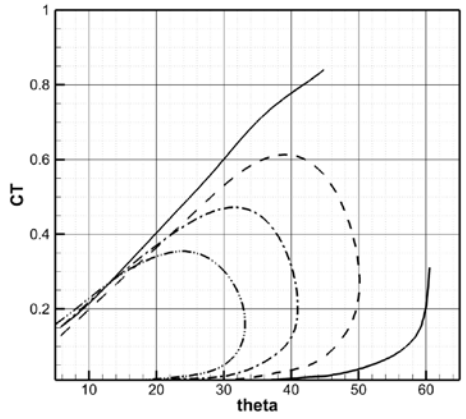

Figure III.1.1-30 Effect of sweptback wings. Iso-Efficiency lines (n=0.55) for S/c=6, h/c=1.5, pitch at 0.33c of midspan. Solid: straight, Dashed: 15°, Dash dot: 30°, Dash dot dot: 45°

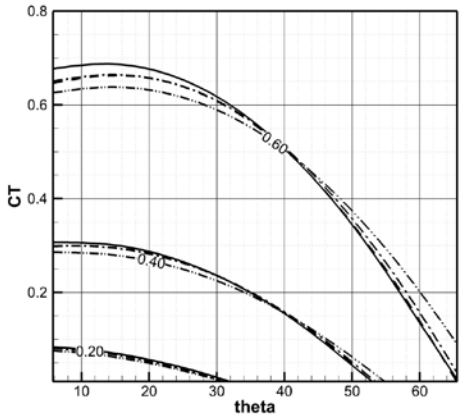

Figure III.1.1-31 Effect of sweptback wings. Iso-Strouhal lines for S/c=4, h/c=2.0, pitch at 0.33c of midspan. Solid: straight, Dashed: 15°, Dash dot: 30°, Dash dot dot: 45°

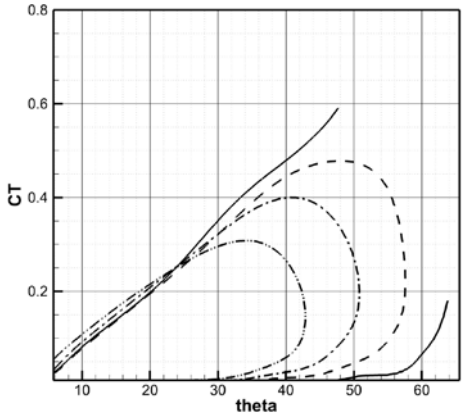

Figure III.1.1-32 Effect of sweptback wings. Iso-Efficiency lines (n=0.6) for S/c=4, h/c=2.0, pitch at 0.33c of midspan. Solid: straight, Dashed: 15°, Dash dot: 30°, Dash dot dot: 45°

III.1.2 Double (twin) wing configuration

Another promising configuration is that of a system of two wings in a biplane configuration moving symmetrically, thus producing no lateral forces. Aside of the lateral forces, a ground effect between the two wings is expected to produce some additional thrust, making the system even more appealing. Last but not least, changing the mean pitching angle (when in vertical position) gives thrust vectoring, giving improved manoeuvring characteristics.

III.1.2.1 Wing geometry, motion and panel generation.

For the case of a twin wing configuration, the independent variables which define the state of the system can be decomposed in two groups. Group A contains the geometric variables and group B contains the motion related variables.

Group A: Assuming zero skewback and twist the wing outline is fully described by its spanwise chord distribution $c(s)$, where $-span/2 < s < span/2$. The spanwise chord distribution has been selected as for the single wing as also shown in Figure III.1.2-1. Furthermore for a twin wing configuration a geometric parameter defining the distance between the mean positions of the two wings, has to be introduced. The aim is the development of a systematic series. Thus, the selection of this parameter should be done with care to be clear and repeatable. More specifically, from experience with extended twin wing simulations, a better variable characterizing the transverse position (measured along the heaving direction) of the wings, is the 'minimum distance' $h_{\min}$ between wing surface points, during a full cycle of wing oscillation. The appropriateness of this variable has to do with the following: (a) it is related to the mirroring flow effect produced by the twin wing configuration, and (b) it is the proper variable which controls/avoids the collisions of points of the twin oscillating wings in a direct manner. Thus, use of this minimum distance $h_{\min}$ (and not the distance between the mean positions of the wings) as the geometric parameter was chosen to describe the 'distance' between the twin wing configurations in hand. This selection introduces some complexity in the geometric description of our system, which shall be discussed after the introduction of the motion parameters.

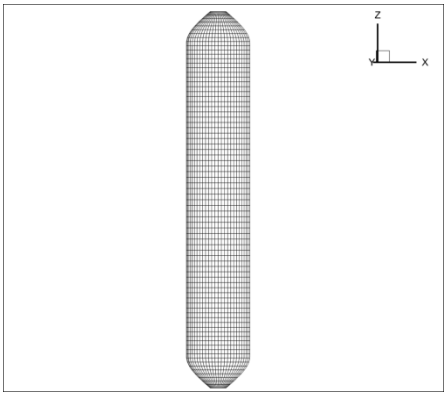

Figure III.1.2-1. Wing outline (s/c= 6).

Group B: Propulsor motion is defined by: (a) the amplitude h_0 of a sinusoidal heaving motion normal to the velocity of advance U, (b) the amplitude θ_0 of a sinusoidal pitching motion, (c) the frequency n (common for both heaving and pitching motions) and (d) the phase angle ψ between heaving and pitching motions.

Thus the state of the twin system is completely defined by the variables: $(U, n, \psi, h_0, b, \theta_0, h_{\min})$. The previous parameters define uniquely the instantaneous angle of attack $a(t)$ of each wing with respect to the undisturbed flow through the equation:

$$a(t) = \theta_0 \sin(2\pi n \cdot t + \psi) - \tan^{-1}\left(\frac{h_0 2\pi n \cdot \cos(2\pi n \cdot t)}{U}\right) \qquad \text{(III.7)}$$

or in non-dimensional form:

$$a(t) = \theta_0 \sin(2\pi n \cdot t + \psi) - \tan^{-1}(\pi \cdot Str \cdot \cos(2\pi n \cdot t)) \qquad \text{(III.8)}$$

where Str denotes the Strouhal number defined by:

$$St = \frac{n \cdot h}{U}, h = 2h_0 \qquad \text{(III.9)}$$

and h denotes the heave height.

The selection of $h_{\min}$ as the 'distance' parameter for the twin wing configuration, introduces a problem regarding calculation of the distance between the mean positions of the two wings. This distance is needed to define the thrust and power coefficients later on. For a resolution to this problem it is observed that for: (a) a symmetric wing outline around the mid-chord (span-wise) axis with a zero twist, (b) with the pitch axis in front of the mid-chord point and (c) with $h_{\min}$ greater than a multiple of the maximum thickness of the wing, the dangerous point for collision is the trailing edge of the wings. Furthermore, under the same conditions, the mid-span wing section is a representative of the whole wing. Taking those considerations into account, the distance of the wing trailing edge from the mean wing position, as a function of time, is given by the formula:

$$\mathrm{H}(t) = h_0 \sin 2\pi nt + (c-b)\sin(\theta_0 \sin(2\pi nt + \psi)) \qquad \text{(III.10)}$$

This is a nonlinear equation in t. Therefore, the maximum distance of the wing trailing edge from the mean wing position, can be found either numerically (i.e. by evaluating formula (III.10) in the range: $0 < t < T, T = 1/n$ and taking the maximum, T is the period of oscillation) or analytically. For the analytic prediction, the substitution: $2\pi nt = \pi/2 + eps$ together with the selection $\psi = \pi/2$ is used. A 3rd order series expansion in eps of formula (III.10) has then been derived and the value of eps which maximizes H has been analytically evaluated. The resulting equations are as follows:

$$eps = -\frac{-h_0 + \sqrt{h_0^2 + 2((c-b)\theta_0)^2 + 2(c-b)^2\theta_0^4}}{(c-b)\theta_0(1+\theta_0^2)} \qquad \text{(III.11)}$$

$$H_{\max} = h_0 - (c-b)\theta_0 eps - \frac{h_0}{2} eps^2 + \frac{(c-b)\theta_0}{6}(1+\theta_0{}^2) eps^3 \qquad \text{(III.12)}$$

Using $H_{\max}$, the distance of the mean wing position to the symmetry plane, of the twin wing system, is given by:

$$h_1 = H_{\max} + h_{\min} \qquad \text{(III.13)}$$

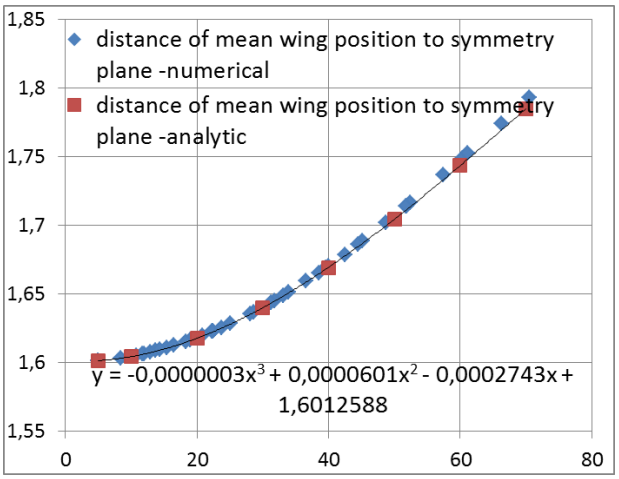

Figure III.1.2-2 Comparison of numerical vs. analytical prediction for the distance between the symmetry plane and the mean wing position for: $c = 1m$, $h_0 / c = 1.5$, $c - b = 2c/3$, $h_{\min} / c = 0.1$

Comparisons of analytical with numerical predictions for $h_1(m)$ vs $\theta_0(\text{deg})$ (horizontal axis) are shown in Figure III.1.2-2, together with a least square approximation for the analytic expression for h_1 .

Having introduced the analytical description of both geometry and motion of our wings, the creation of a surface panel distribution describing the systems at consecutive time steps is straight forward.

Figure III.1.2-3 shows the time instances of the twin wing mid-span section, evenly distributed in two periods. With the flapping wing paneling in time known, the code UBEM can be applied to calculate the resulting unsteady forces, energy requirements and free shear layer evolution.

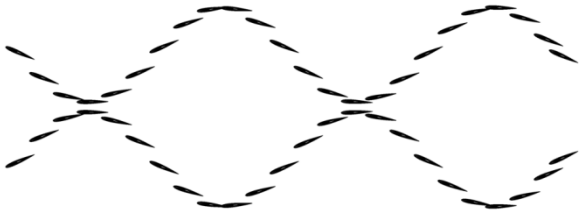

Figure III.1.2-3 Sequential positions of the twin wings for h_o/c=1.5, Str=0.35, θ_o=23.6,h_{min}/c=0.1

III.1.2.2 Decisions regarding Geometric and Flow/motion variables for the proposed twin wing series.

To proceed to a series based design process for a twin configuration, decisions have to be taken, on the corresponding geometric and flow related parameters. For the needs of the initial work on the subject, the series is limited in extent and consist of only a twin system geometry (span-wise chord distribution is discussed in previous paragraph) with $s/c = 2,4,6$, h_0/c=1.0,1.5,2.0, $b/c = 0.33$, $\psi = \pi/2$ and $h_{\min}/c = 0.1$. The Strouhal number has been selected in the range: $Str = 0.1 \div 0.7$. Using previous experience, this selection is expected to contain the region of maximum hydrodynamic efficiency. Finally the range of the pitch angle θ_0 has been selected from 5 deg to a maximum value, which depends on the Strouhal number. This maximum value of the pitch angle has been properly selected to include the full range of thrust producing wing motions. This investigation began with Politis & Tsarsitalidis (2013) where a single set for s/c=6 and h/c=1.5 was presented. In this work the series is extended to a total of 12 sets.

III.1.2.3 Transient twin wing performance and selection of simulation period.

The main difference between a traditional propeller and a flapping wing is that the latter produces a period mean thrust as a result of a highly unsteady instantaneous thrust. The simulation method in hand can predict this time dependent thrust but, since it is a time stepping method, initial conditions on motion have to be imposed. A burst starting twin wing is used as the starting condition. In this case a transient phenomenon occurs. Thus the mean period values for thrust or power have to be calculated after the passage of this initial transient phenomenon. To take care for this, time domain simulations have been performed for three periods and for several cases. Indicatively, Figure III.1.2-4and Figure III.1.2-5 are presented the unsteady thrust for two cases.

From these figures it can be concluded that, for the representative selected parameters, the transient phenomenon is limited to the few initial time steps after the burst start. Thus it is safe to use the 2nd period of simulation, to calculate the mean thrust and power to be used in the design charts.

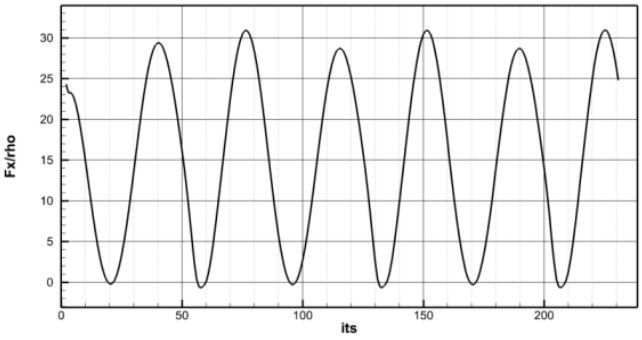

Figure III.1.2-4 Time evolution of thrust for (s/c =6, h_o/c=1.5,h_{min}/c=0.1, Str=0.34, Theta=20.6)

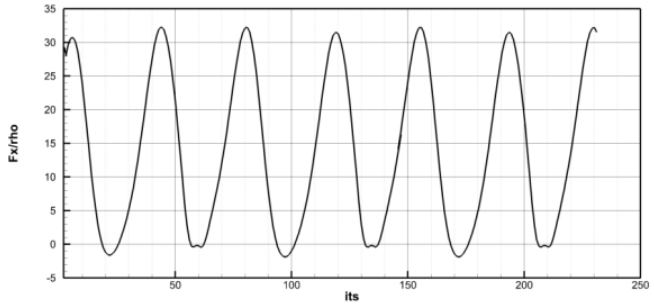

Figure III.1.2-5 Time evolution of thrust for (s/c =6, h_o/c=1.5, h_{min}/c=0.1, Str=0.46, Theta=44.5)

III.1.2.4 Open water performance diagrams and comparison with single wing systems.

Systematic unsteady BEM simulations have been performed with the selected flapping wing series described in section 5. In all simulations a chord of $c = 1.0m$ has been selected. Furthermore in all simulations a twin system was used with:

$$\frac{s}{c} = 6, \frac{h_0}{c} = 1.5, \frac{h_{\min}}{c} = 0.1, \frac{b}{c} = \frac{1}{3}, \psi = 90^0$$

Variation of Strouhal number has been achieved by changing the frequency of the flapping wing oscillation while the corresponding translational velocity has been held constant and equal to $U = 2.3m/s$. This results to a constant Reynolds number equal to $0.202 \cdot 10^7$, based on translational velocity ($\mathrm{Re} = U \cdot c / \nu$). Corresponding Reynolds numbers based on the maximum undisturbed flow velocity are Strouhal dependent, according to the relation: $\mathrm{Re}_{Str} = \frac{U \cdot c}{\nu}\sqrt{1 + (\pi \cdot Str)^2}$. Thus $\mathrm{Re}_{Str} = 0.22 \cdot 10^7$ at $Str = 0.10$ and $\mathrm{Re}_{Str} = 0.51 \cdot 10^7$ at $Str = 0.7$ (kinematic viscosity: $\nu = 1.139 \cdot 10^{-6} m^2/s$). Mean thrust and power have then been calculated by running the BEM code for two time periods and calculating the mean values of the unsteady forces over the second period. The results are presented in the form of $C_T - \theta_0$ diagrams (where $\theta_0 \rightarrow theta$ in diagrams), $C_P - \theta_0$ diagrams, and $Cp_P - \theta_0$ with parameter the Strouhal number (thick line in the diagrams), figures 6,7 and 8. Cp_P denotes the energy required for the pitching of the wing, given by:

$$Cp_p = \frac{\text{period mean pitching power}}{0.5\rho U^3 S} = \\ = \frac{1.}{0.5\rho U^3 S}\int_t^{t+T} M_p(t) \cdot \omega_p(t) dt \qquad \text{(III.14)}$$

where $M_p(t)$ is the instantaneous moment around the pitching axis and $\omega_p(t)$ is the instantaneous rotational velocity around the pitching axis.

$C_T - \theta_0$ diagrams contain additionally in parametric form the open water efficiency η of the system (thin lines):

$$\eta = \frac{T \cdot U}{DHP} = \frac{C_T}{C_P} \qquad \text{(III.15)}$$

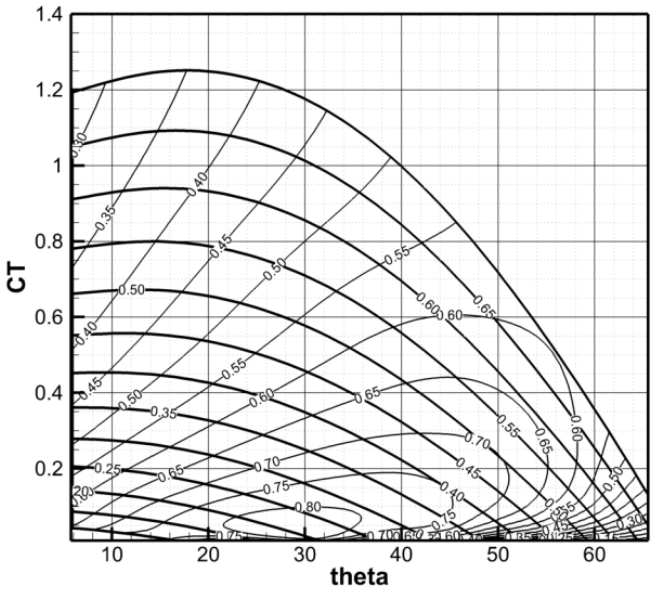

Figure III.1.2-6 Ct-theta chart for twin system. Thicker lines are for Strouhal number and thinner, are for efficiency.

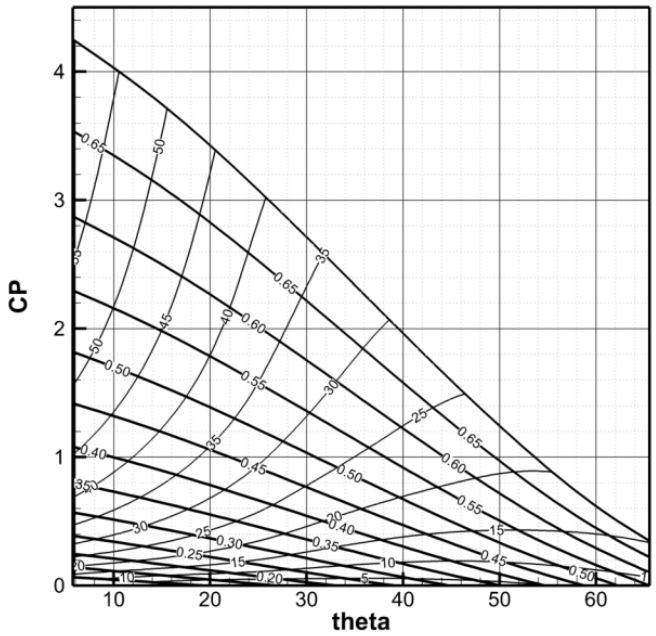

Figure III.1.2-7 CP-theta chart for twin system. Thicker lines are for Strouhal number and thinner, are for maximum angle of attack.

Also, $C_P - \theta_0$ diagrams contain additionally in parametric form the $a_{\max}$ angle (thin lines) defined as the maximum value of $a(t)$, relation (III.3), over one period. This last information is very useful for the designer in order to avoid maximum angles with a potential danger for separating flow (e.g. greater than 20deg), phenomenon which is not modeled by the used version of UBEM.

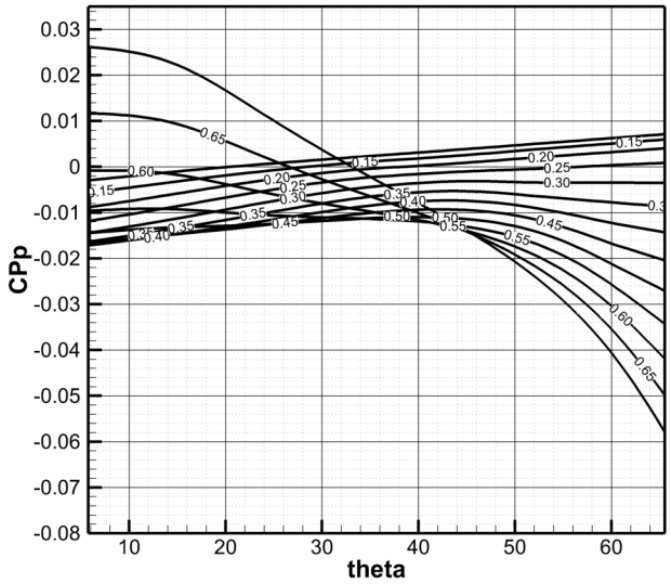

Figure III.1.2-8 CPp-theta chart for twin system with parameter the Strouhal number.

Interesting conclusions drawn from those figures are the following: (a) There is a relatively wide region of maximum hydrodynamic efficiency which is achieved at a maximum angle of attack less than 15degrees i.e. at the region of flow without expected separation, (b) The order of magnitude of the power required for pitching is approximately 1% of the corresponding total delivered power. It should be also noted that systematic inspections of the calculated pressure distributions gave no indication of local pressure less than the corresponding vapor pressure in the region around optimum performance. As a result no cavitation is expected at that region. For the comparison between the single wing and the twin wing system, it can be told, that the ground effect between the two wings seems to cause a very small difference in the resulting C_T, C_P values. After further examination of the efficiency curves, though, it can be seen, that the contours are narrower in the sense of theta, but slightly wider in the sense of C_T and Strouhal number. This difference will affect positively the design results produced later on. Commenting finally on the values of the power required for the pitch setting, it is observed that in the whole range of the pitch setting are small with a trend to approach zero for smaller Strouhal numbers.

These charts can be used to select an optimum twin wing configuration for a given ship very easily as follows: Assume that a ship is given, with a design speed of V knots. The problem of designing a s/c=6, h/c=1.5 twin wing (i.e., select its optimum geometry with the corresponding revolutions and required DHP) can be solved as follows: (a) with the design speed known, the ship resistance and, from equation (III.53), the propeller thrust and C_T can be calculated; (b) with this C_T draw a horizontal line on Figure 6 and find the intersection of this horizontal line with the various constant Strouhal lines, let $(\theta_0, Str)_i, i = 1, n_{str}$ denote the n_{str} intersection points; (c) from each Strouhal number the frequency of the propulsor motion can be found: $n_i = Str_i \cdot V / (2 \cdot h_0)$; (d) use Figure 7 to find $C_{P,i}$ for the points $(\theta_0, Str)_i, i = 1, n_{str}$, from the $C_{P,i}$ find the required open water power and use (III.50) to find $DHP_{B,i}$; (e) from the

calculated $DHP_{B,i}, i = 1, n_{str}$ select that with minimum required DHP_B. Finally use figure 8 to estimate the required power for the pitch mechanism.

III.1.2.5 Wake visualizations – Understanding how the twin wing configuration produces thrust.

For a better understanding of the underlying physical mechanisms of thrust production, the free shear layer produced by the twin wing system ($\frac{s}{c} = 6, \frac{h_0}{c} = 1.5, \frac{h_{\min}}{c} = 0.1, \frac{b}{c} = \frac{1}{3}, \psi = 90^0$) is plotted, Figure III.1.2-9. The wing surface and the free vortex sheet surface on those figures have been colored according to their surface dipole distribution intensity. Notice that constant dipole lines coincide with surface vortex lines. By using either the last property or the deformation patterns of the free vortex sheets, a number of strong ring vortices in the wake of the wing are made recognizable. Those ring vortices produce series of oblique jet flows by which the flapping wing produces thrust. Figure III.1.2-9 also contains artistic add-ons, showing the train of ring vortices (curved arrows) and corresponding jets (straight arrows) by which the flapping wing feeds with momentum the wake and produces thrust. More specifically the straight arrows are the results of the induced velocities produced by the ring vortices.

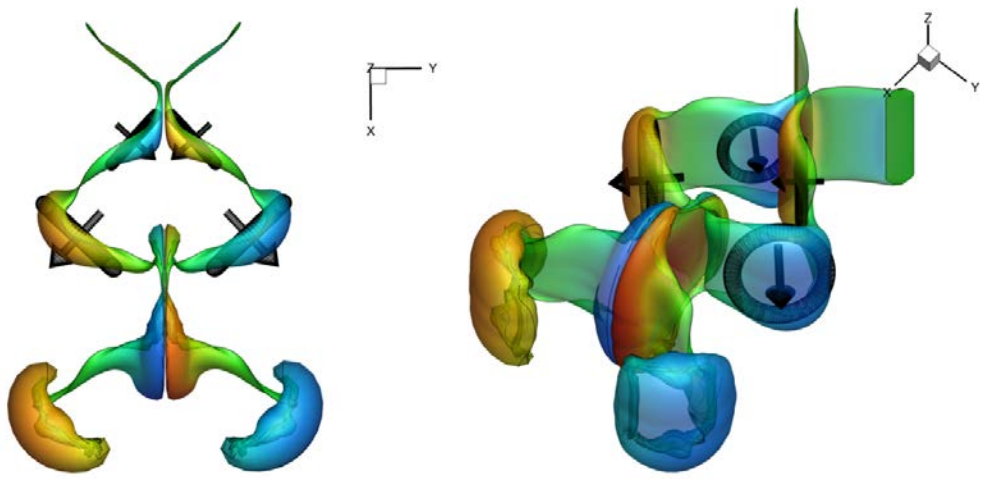

Figure III.1.2-9 Wake of a Flapping wing of s/c=6, h_o/c=1.5, h_{min}/c=0.1, Str=0.46, θ_o=44.5. Colors are for dipole potential. Artistic add-ons showing the train of ring vortices and corresponding jets by which the wing produces thrust.

III.1.2.6 Effects of parameters

As in the case of single wing, the effect of motion parameters is investigated. Most effects are similar to those for the single wing and probably amplified by the ground effect created between wings, especially in smaller s/c values, where 3d effects are more dominant.

III.1.2.6.1 Effect of s/c

In Figure III.1.2-10 and Figure III.1.2-11 iso-Strouhal and Iso-efficiency contours are plotted for varying s/c values, for h/c=1 and pitching axis condition at 0.33c from le. Figure III.1.2-10 depicts Strouhal contour curves for the value of Str=0.45, with different linetypes for each value of s/c. In the same manner, Figure III.1.2-11 depicts efficiency contour curves for value of n=0.7. The general remark is that both thrust and efficiency increase when the s/c ratio increases and the slope of the iso Strouhal contours gets steeper, while the peak of efficiency remains at almost the same theta (and maximum angle of attack). The difference in slope can be attributed to the 3D effects (wake rollup) and the fact that they affect the total result less, as s/c increases.

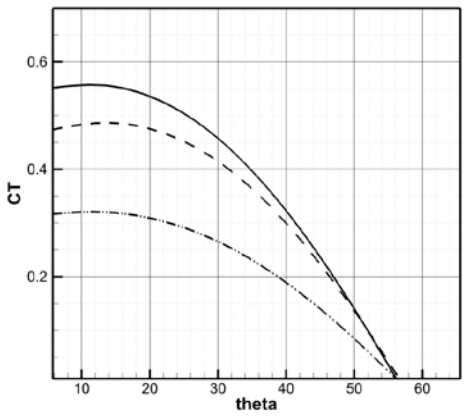

Figure III.1.2-10 Effect of S/c. Iso-Strouhal contours (Str 0.45) for straight wings, h/c=1.5, pitch at 0.33c. Lines: Dash dot dot: 2, dash: 4, solid: 6

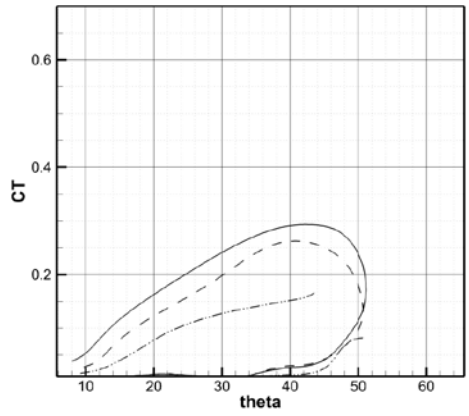

Figure III.1.2-11 Effect of S/c. Iso-efficiency contours (n=0.7) for straight wings, h/c=1.5, pitch at 0.33c. Lines: Dash dot dot: 2, dash: 4, solid: 6

III.1.2.6.2 Effect of h/c

In Figure III.1.2-12 thru Figure III.1.2-14, iso-Strouhal and Iso-efficiency contours are plotted for varying h/c values, for s/c=4 and pitching axis at 0.33c from le. A general conclusion is that with increasing h/c ratio, the loading gets lower and the efficiency increases, as noted previously. Another interesting remark is that the peak of efficiency (maximum thrust coefficient for the same efficiency) moves to larger values of theta (θ_o) which mean smaller maximum angle of attack, as the h/c increases, but also to larger values of thrust.

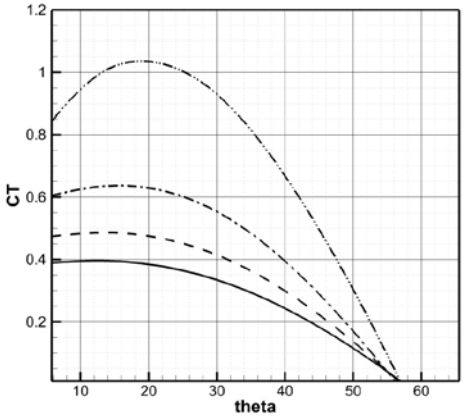

Figure III.1.2-12 Effect of h/c, iso-Strouhal contours (Str=0.45) for straight wings of s/c=4 pitch at 0.33c. Lines: dash dot dot: 0.5, dash dot: 1.0, dash: 1.5, solid: 2.0

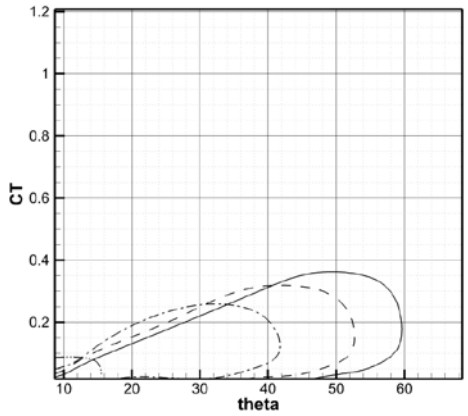

Figure III.1.2-13 Effect of h/c, iso-Efficiency contours (n=0.67) for straight wings s/c=4 pitch at 0.33c. Lines: dash dot dot: 0.5, dash dot: 1.0, dash: 1.5, solid: 2.0

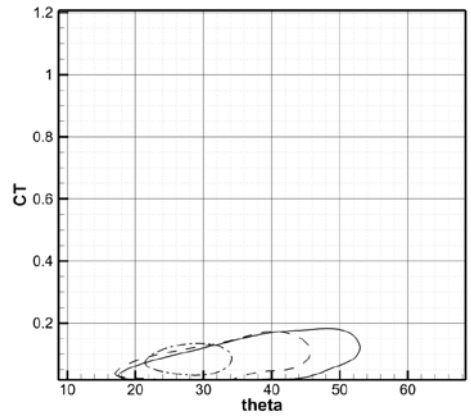

Figure III.1.2-14 Effect of h/c, iso-Efficiency contours (n=0.75) for straight wings s/c=4 pitch at 0.33c. Lines: dash dot: 1.0, dash: 1.5, solid: 2.0

III.1.3 Flexible Oscillating Duct (FOD)

Inspired by a jellyfish, where a bulk muscle oscillatory motion produces thrust, the initiative was taken to explore the propulsion capabilities of a new propulsor concept based on an oscillating/pulsating flexible duct. This device was named 'Flexible Oscillating Duct' (FOD).

III.1.3.1 FOD geometry, motion and panel generation.

The starting point for an unsteady BEM simulation of a flexible body is the generation of the time dependent paneling describing the geometry of the system (Politis 2011). The FOD time dependent geometry is produced as described below:

Starting from a conventional 2-D foil moving parallel to the X -axis with velocity U , which performs a heaving motion (along the vertical Y -axis) with amplitude h_0 and a pitching motion with amplitude θ_0 (measured from the X-direction) and a phase angle ψ with respect to the heaving motion. The pitching motion is performed around a pre-selected given pitching axis at distance b from the leading edge of the section. Both heaving and pitching motions are performed with angular velocity $\omega = 2\pi n$, where n is the corresponding frequency. Furthermore, the camber of the 2-D foil performs an unsteady motion with a chord-wise distribution $y_c(t,u)$ (u denotes the non-dimensional chord-wise position measured from leading edge and t denotes the time), taken e.g. from the NACA series, with an instantaneous maximum camber $m_c(t)$ (expressed as a fraction of chord). An oscillating camber motion can then be obtained by deciding about the form of the function $m_c(t)$. There are at least two possible reasonable selections for $m_c(t)$: (a) select $m_c(t)$ such that the instantaneous effective (defined with respect to the total undisturbed flow velocity) angle of attack of the section is a certain (time independent) fraction of the instantaneous ideal angle of attack of the section (i.e. the section operates in a percentage of its shock free entry at all times), (b) select $m_c(t)$ to oscillate harmonically with the same frequency and phase as that used for the pitching motion, and a maximum predetermined (user defined) value m_0 . It should be noted that in both cases unsteady motion of the camber surface has the same frequency and the same phase with that of the pitching motion. On the other hand, only case (b) results in pure harmonic motion for camber.

With the previous discussion in mind, at each time t , the foil geometry and position in the aforementioned XY plane has been defined. Taking an axis L parallel to the X axis, at a distance R along Y axis and rotating the foil by 360 deg around L , the FOD configuration at this time step is obtained. R defines the FOD radius and $D = 2 \cdot R$ the FOD diameter.

Quantifying the previous discussion, the instantaneous angle of attack $a(t)$ of a section (2-D foil) of the FOD, with respect to the undisturbed flow (resulting from the parallel movement along X-axis and the heaving motion of the pitch axis point), is given by the equation:

$$a(t) = \theta_0 \sin(2\pi n \cdot t + \psi) - \tan^{-1}\left(\frac{h_0 2\pi n \cdot \cos(2\pi n \cdot t)}{U}\right) \qquad \text{(III.16)}$$

or in non-dimensional form:

$$a(t) = \theta_0 \sin(2\pi n \cdot t + \psi) - \tan^{-1}(\pi \cdot Str \cdot \cos(2\pi n \cdot t)) \quad \text{(III.17)}$$

where Str denotes the Strouhal number defined by:

$$Str = \frac{n \cdot h}{U}, h = 2h_0 \quad \text{(III.18)}$$

and h denotes the heave height.

Furthermore, assuming a NACA four digit camber distribution, the camber motion is described by the following equations:

$$y_c(t,u) = m_c(t)\frac{c \cdot u}{p^2}(2p - u), 0 \le u \le p \quad \text{(III.19)}$$

$$y_c(t,u) = m_c(t)\left(\frac{c \cdot (1-u)}{(1-p)^2}\right) \cdot (1 + u - 2 \cdot p), p \le u \le 1 \quad \text{(III.20)}$$

where $m_c(t)$ is the maximum instantaneous camber as a fraction of chord, p is the location of maximum camber (as a fraction of the chord) and u is the non-dimensional chord-wise position, (Abbott I. & Doenhoff 1959). After this, it is possible to calculate the time evolution of maximum camber for the cases (a) and (b) discussed previously. For case (a) the instantaneous maximum camber is given by:

$$m_c(t) = \frac{f \cdot a(t) \cdot p^2(-p+1)^2\pi}{2(p - \frac{1}{2})(p^2\pi - 2p\vartheta + \vartheta - \sin(\vartheta))} \quad \text{(III.21)}$$
$$\vartheta = a\cos(1 - 2p)$$

where $a(t)$ is calculated from (III.3) and f is a time independent factor (estimated heuristically) by which the instantaneous camber partially represents the ideal camber. Relation (6) is produced by applying the formula for the ideal angle of attack to the camber line (III.19), (III.20) (Abbott I. & Doenhoff 1959). For case (b) the instantaneous maximum camber is given by:

$$m_c(t) = m_0 \sin(2\pi n \cdot t + \psi) \quad \text{(III.22)}$$

with m_0 heuristically selected by the designer.

Having introduced the analytical description of both geometry and motion of our FOD, the creation of a surface panel distribution describing the FOD at consecutive time steps is straight forward.

Figure III.1.3-1 shows the panel discretization of the FOD at nine time instances, corresponding to the maximum, minimum and inflection point positions of a FOD section in one period. Figure III.1.3-2 shows the section of the FOD with a plane containing the X axis for the same time instances.

With the FOD paneling in time known, the unsteady BEM code (Politis 2011) can be applied to calculate the FOD unsteady forces, energy requirements and free shear layer evolution.

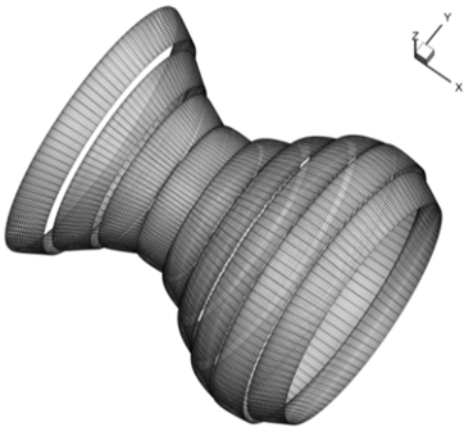

Figure III.1.3-1 Panel discretization at selected time steps

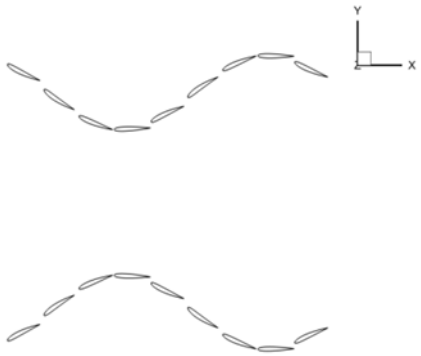

Figure III.1.3-2 XY section of the nine positions of the FOD

III.1.3.2 Decisions regarding Geometric and Flow/motion variables for the proposed FOD series.

To proceed to a series based design process for a FOD, decisions have to be taken, on the corresponding geometric and flow related parameters. In line with the discussion of the previous section, the series should consist of four different FOD geometries, termed in the sequel as Cases 1,2,3 and 4, as follows:

Case 1: $h_0 / c = 1.0$ with NACA 0012 section (no camber),

Case 2: $h_0 / c = 1.0$ with NACA 6412 section and time dependent maximum camber according to equation (III.22).

Case 3: $h_0 / c = 1.5$ with NACA 0012 section (no camber),

Case 4: $h_0 / c = 1.5$ with NACA 6412 section and time dependent maximum camber according to equation (III.22).

Other series geometric data have been selected constant, as follows: $m_o = 0.04$ in relation (III.22) and $R/c = 3$ (where R is the mean FOD radius measured at the position of pitching axis which have been selected at 1/3 chord from leading edge, i.e. $b/c = 1/3$).

Regarding flow/motion related variables the Strouhal number has been selected in the range: $Str = 0.15 \div 0.7$. Using our previous experience, gained from flapping wings, this selection is expected to contain the region of FOD maximum hydrodynamic efficiency. Finally the range of the pitch angle has been selected from 5 deg to a maximum value, which depends from the Strouhal number. This maximum value of the pitch angle has been properly selected to result in a thrust producing FOD.

III.1.3.3 Transient FOD performance and selection of simulation period.

The main difference between a traditional propeller and a FOD is that the FOD produces a period mean thrust as a result of a highly unsteady instantaneous thrust. The simulation method in hand can produce this time dependent thrust but, since it is a time stepping method, initial conditions on FOD motion have to be imposed. A burst starting FOD is used as the starting condition. In this case a transient phenomenon occurs. Thus the mean period values for thrust or power have to be calculated after the passage of this initial transient phenomenon. To care for this, time domain simulations have been performed for two periods and for the following selection of FOD state variables (geometry and motion):

I. [Case 1, Str=0.29, Theta=23.54]
II. [Case 1, Str=0.42, Theta=24.27]
III. [Case 2, Str=0.56, Theta=23.50]
IV. [Case 3, Str=0.42, Theta=24.27]

Results for the time dependent FOD thrust force Fx are shown on Figure III.1.3-3 through Figure III.1.3-6, where ρ denotes the fluid density. From those figures it is concluded that, for the selected parameters, the transient phenomenon is limited to the few initial time steps after the burst start. Thus the 2nd period of simulation can be safely used, to calculate the mean FOD thrust and power to be used in our design charts. Notice that according to the thrust sign conventions, a negative thrust force Fx is a propelling force, convention which is used in all future charts similar to Figure III.1.3-3.

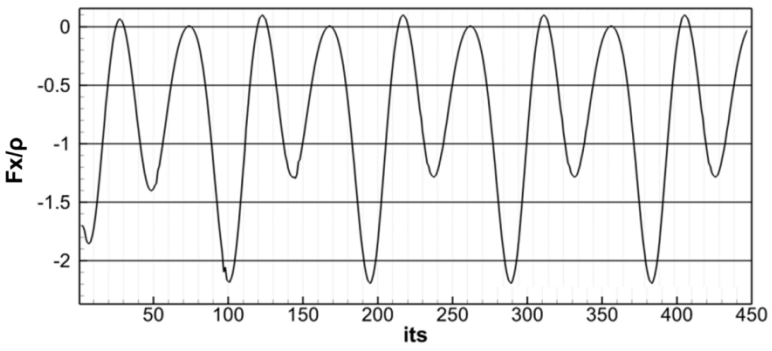

Figure III.1.3-3. Time evolution of thrust for [Case 1, Str=0.29 Theta=23.54]

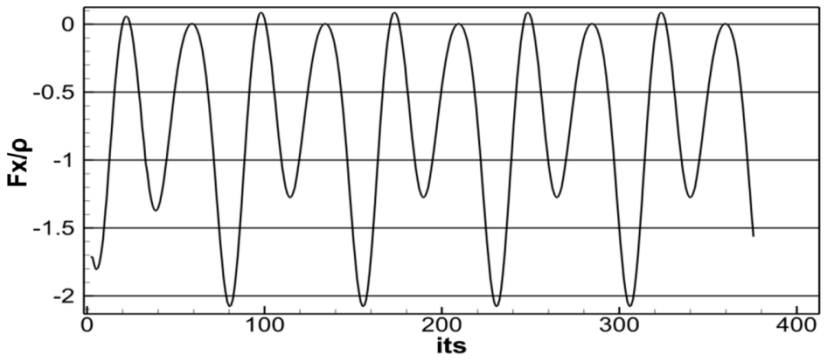

Figure III.1.3-4 Time evolution of thrust for [Case 1, Str=0.42 Theta=24.27]

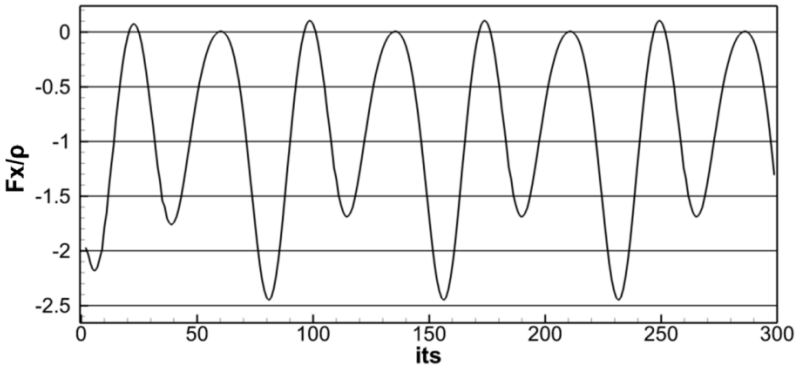

Figure III.1.3-5. Time evolution of thrust for [Case 2, Str=0.42 Theta=24.27]

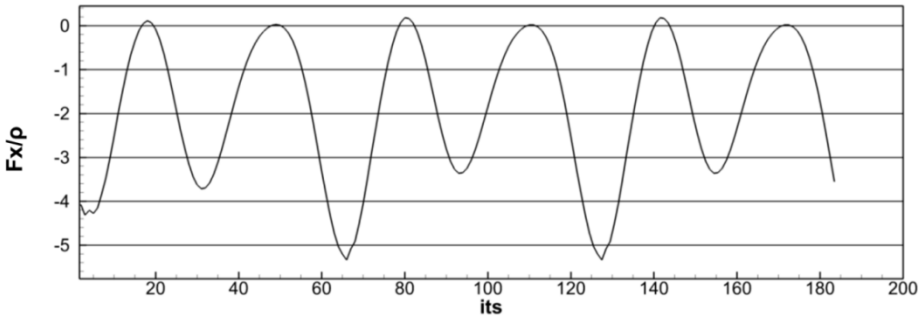

Figure III.1.3-6. Time evolution of thrust for [Case 3, Str=0.56 Theta=23.5]

III.1.3.4 Grid independence of the calculated open water diagrams.

In order to analyze the effect of the grid density to the calculated open water FOD performance, the systematic BEM calculations for the next paragraphs have been performed with three different grid densities, according Table III.1.3-1:

Table III.1.3-1. Grid densities.

name	No of chordwise elements (face + back)	No of circumferential elements
Grid1	20	55
Grid2	26	72
Grid3	32	80

For the comparison among grids, a measure for the maximum and mean deviation between the mean thrust forces produced by each grid, has been defined as follows: For each calculation case and each grid density, a mean value for thrust has been found. Thus a three dimensional surface has been created for each case. Then, mean and maximum deviation between surfaces can be easily calculated in any design software. The overall mean and maximum values are obtained (i.e. six more numbers are obtained). Those data are shown on Table III.1.3-2, with the following convention: Above diagonal are overall mean of the %differences of mean thrust values and below diagonal are the maximum of the %differences of mean thrust values.

It can be seen that Grid2 (as well as Grid3) can be considered as a reliable discretization for systematic simulations. Nevertheless, Grid1 in spite of lacking accuracy, it is good enough to show trends and could be used for getting quick exploratory results.

Table III.1.3-2. Mean (above the diagonal) and maximum (below the diagonal) %deviations in mean thrust calculation.

	Grid1	Grid2	Grid3
Grid1	0	5.1%	5.2%
Grid2	8%	0	0.7%
Grid3	10.1%	3.1%	0

Figure III.1.3-7 shows comparisons of calculated time dependent thrust for three different grids for the case: [Case 1, Str=0.70, theta=22.30], where the maximum difference of mean values was found. It should be noted, that even the coarser grid, produces results that follow the same trend in the time domain as well, while the difference is located at the peak values. It should be also noted that the differences in the calculated time dependent thrust are reduced as grid density increases, a fact which indicates the convergence of the results for finer grids.

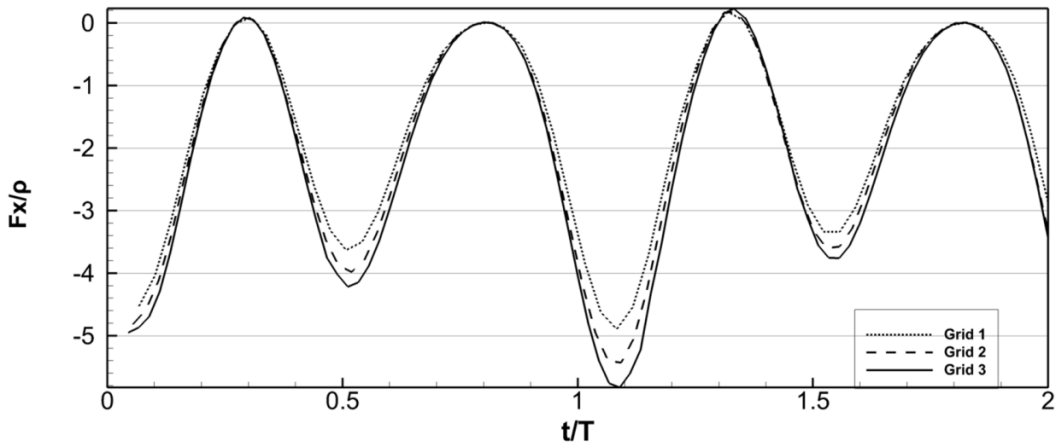

Figure III.1.3-7 : Effect of grid density to the calculated instantaneous thrust for the case: [Case 1, Str=0.70, theta=22.30].

III.1.3.5 Wake visualizations – Understanding how the FOD produces thrust.

For a better understanding of the underlying physical mechanisms of FOD's thrust production, the wake free shear layer is plotted, for a range of the FOD state variables, representative of our series described in section 5. More specifically two groups of results are presented. For the first group a definite combination of state variables has been selected: [Case 1, Str=0.42, theta=24.27] and present instances of the wake evolution at the following six consecutive time steps: [T/2, T, 3T/2, 2T, 5T/2, 3T] where T denotes the simulation period. Figure III.1.3-8 shows the FOD thrust as a function of time, with vertical bars at the points where wake snapshots have been taken. Figure III.1.3-9 (perspective view) and Figure III.1.3-10 (top view) show the FOD and corresponding wake snapshots, at the selected time steps. The FOD surface and the free vortex sheet surface on those figures have been colored according to their surface dipole distribution intensity. Notice that constant dipole lines coincide with surface vortex lines. By using either the last property or the deformation patterns of the free vortex sheets, a number of strong ring vortices in the wake of the FOD are made recognizable. Those ring vortices produce series of oblique jet flows by which the FOD produces thrust. Figure 10 shows a slice with a constant-Y plane of the FOD free vortex sheet for the six time steps considered, while figure 11 concentrates on the slice at t=3T. Figure III.1.3-11 also contains artistic add-ons, showing the train of ring vortices (curved arrows) and corresponding jets (straight arrows) by which the FOD produces thrust. More specifically the straight arrows are the results of the induced velocities produced by the ring vortices. Notice also the analogy of the vortex picture shown in the slice of Figure III.1.3-12 with the reverse Karman vortex street wake appearing in aquatic animal and/or bird flapping foil propulsors, Taylor (2010). By studying the evolution of the FOD at consecutive geometric positions, it is observed that the maximum angle of attack during FOD contraction and during FOD expansion occurs at asymmetric FOD geometries. More specifically, during the expansion phase of the FOD motion, the leading edge diameter is greater than the corresponding diameter during the

contraction phase. As a result the local maximum of thrust forces *Fx* during FOD expansion is greater than the corresponding local maximum during FOD contraction, Figure III.1.3-8.

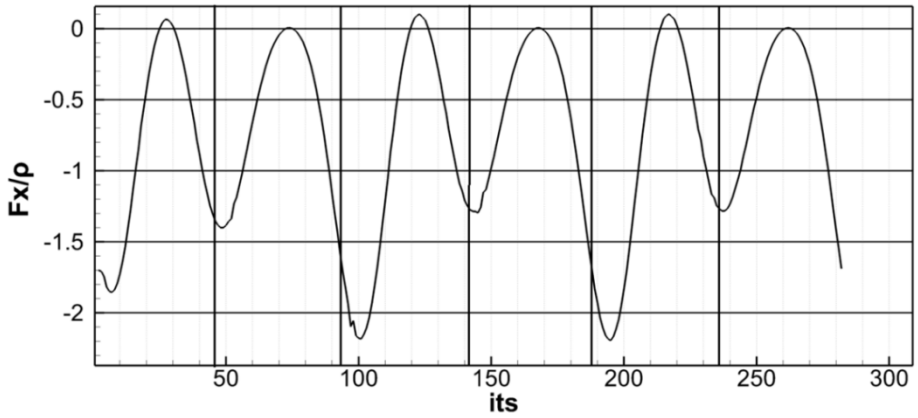

Figure III.1.3-8. Time evolution of FOD thrust for [Case 1, Str=0.42, theta=24.27]. The vertical lines indicate the times of the snapshots taken.

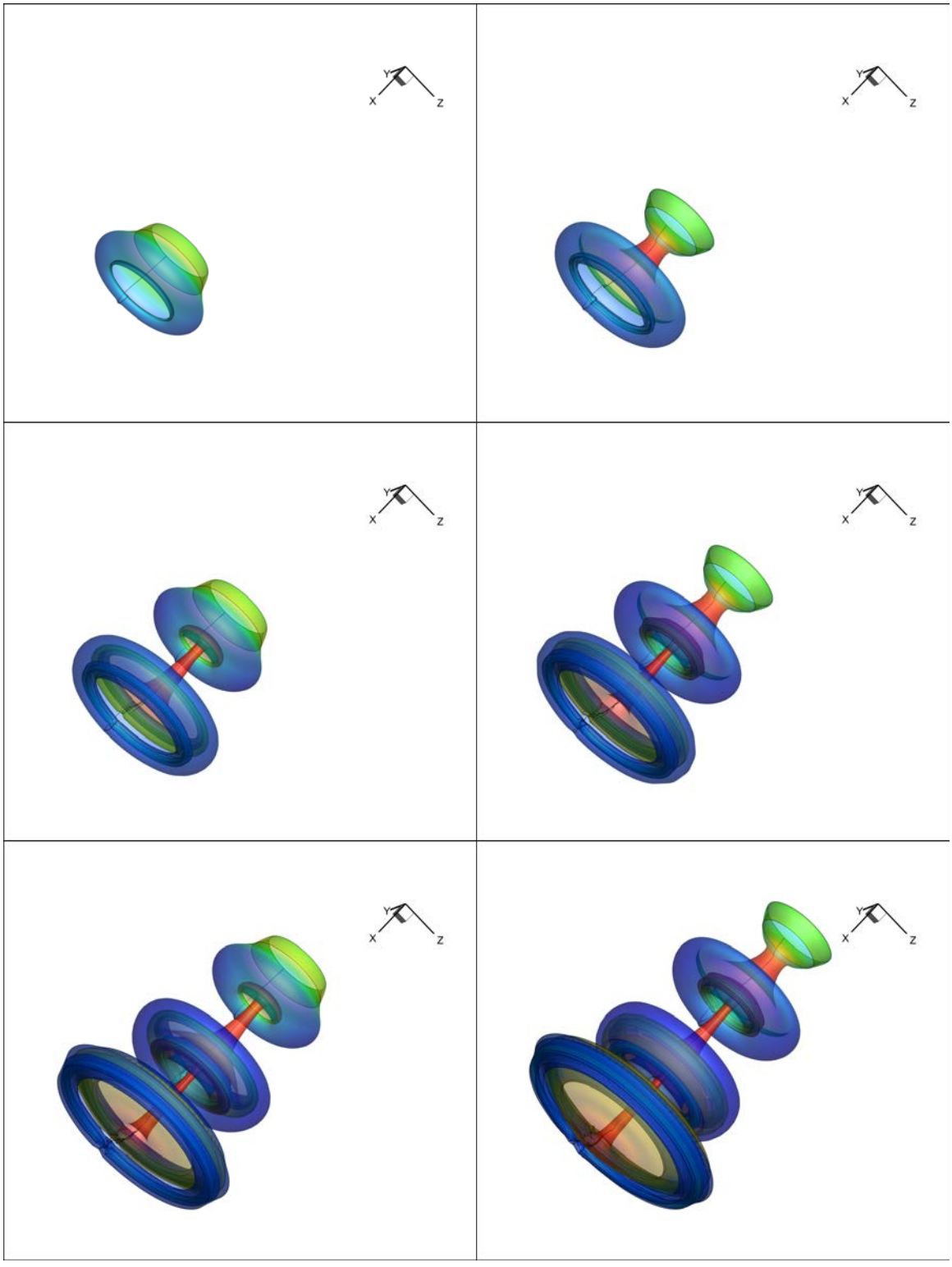

Figure III.1.3-9. Wake visualizations for [Case 1, Str=0.42, theta=24.27], at [T/2, T, 3T/2, 2T, 5T2, 3T] respectively. Perspective view

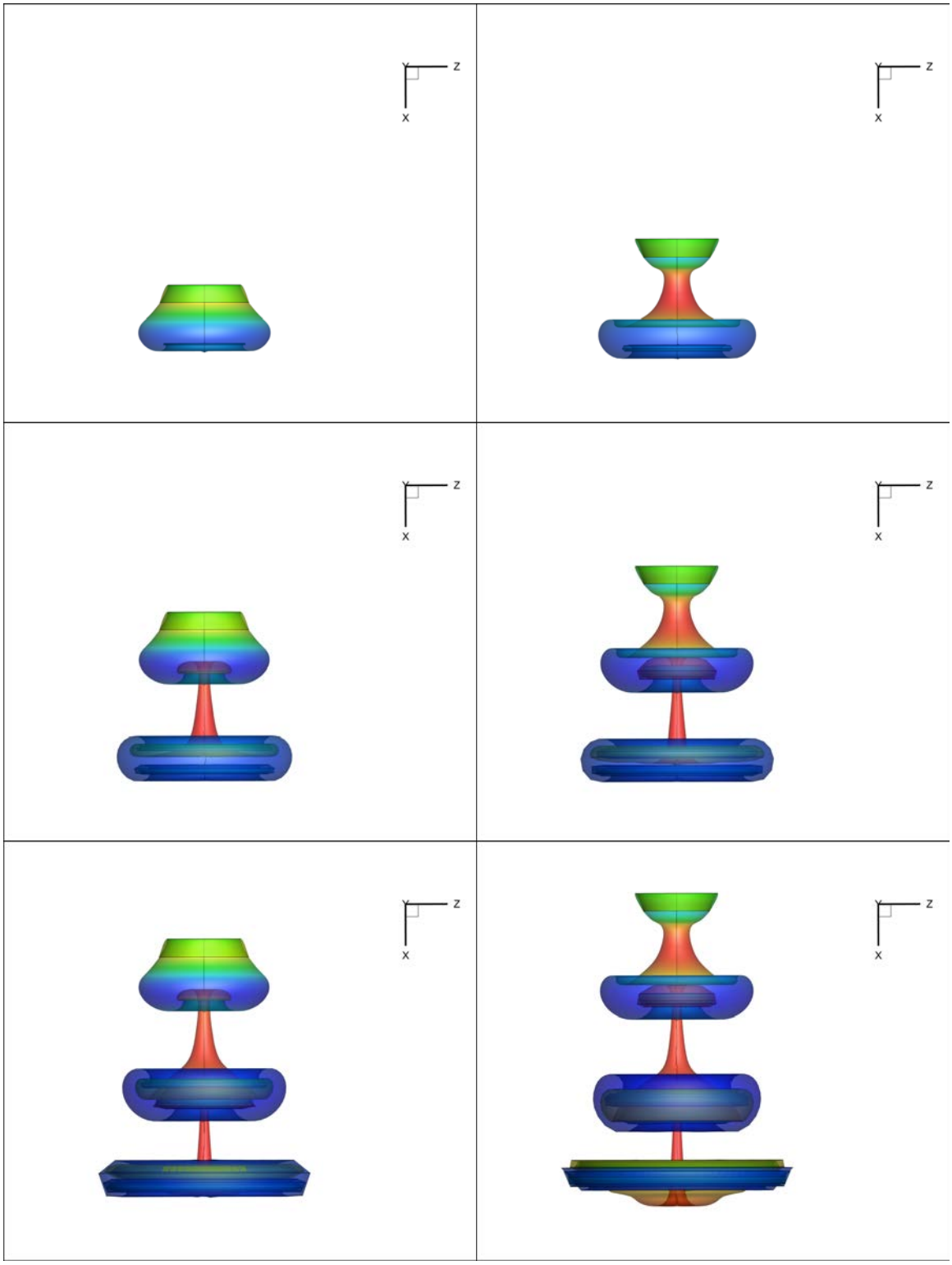

Figure III.1.3-10. Wake visualizations for [Case 1, Str=0.42, theta=24.27], at [T/2, T, 3T/2, 2T, 5T2, 3T] respectively. Top view.

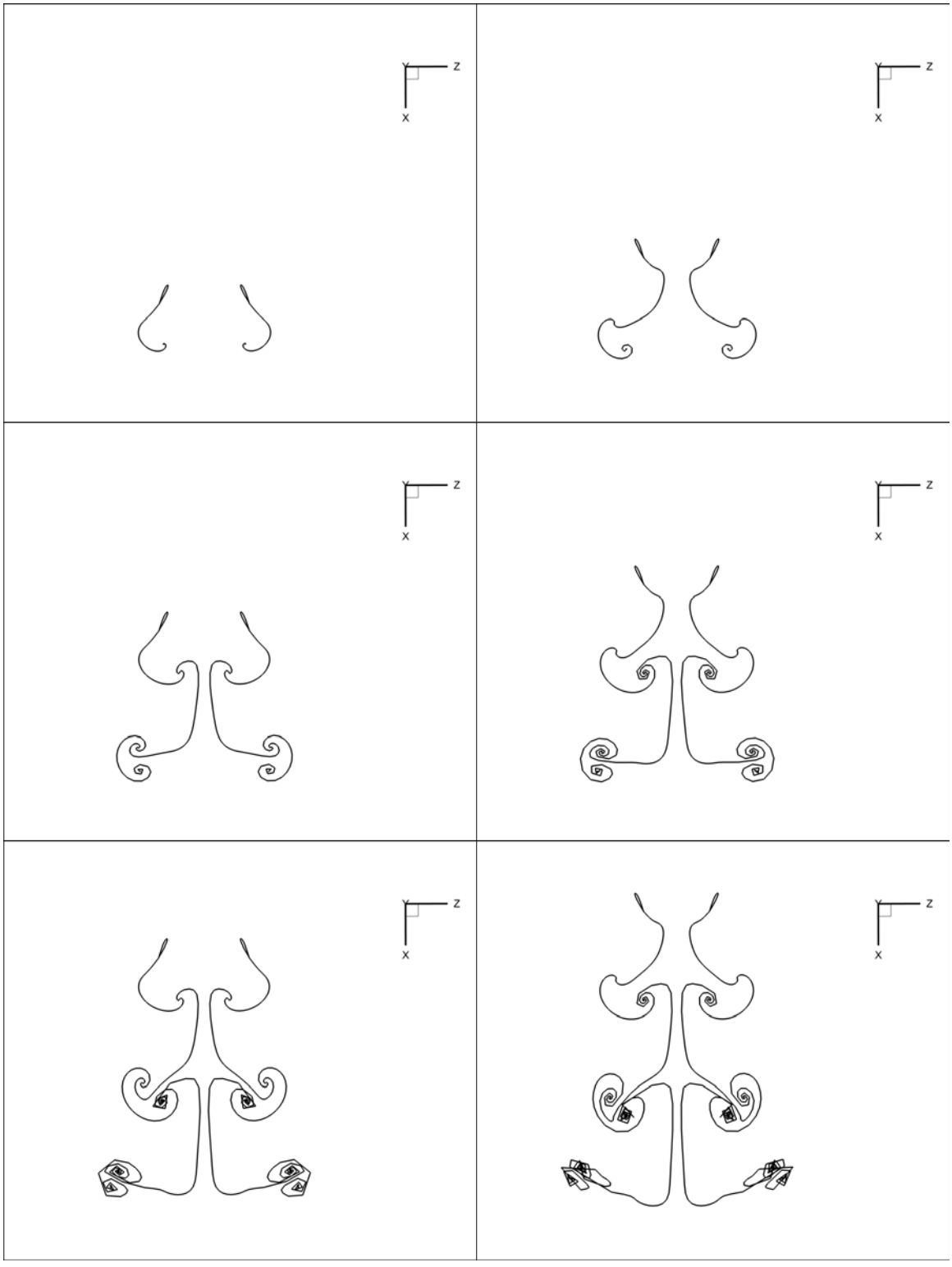

Figure III.1.3-11 . Wake visualizations for [Case 1, Str=0.42, theta=24.27], at [T/2, T, 3T/2, 2T, 5T2, 3T] respectively. Slice with the XZ plane

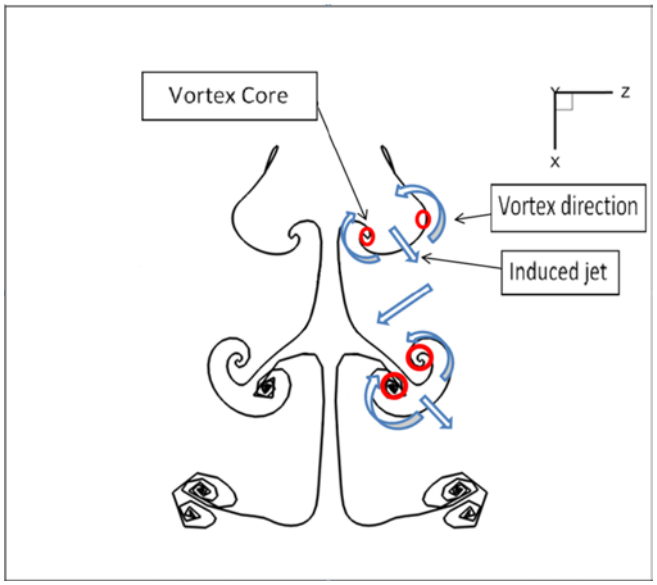

Figure III.1.3-12. Slice of the FOD wake at t=3T for [Case 1, Str=0.42, theta=24.27]. Artistic add-ons showing the train of ring vortices and corresponding jets by which the FOD produces thrust.

For the selection of the second group of wake visualizations, a decision was made to trace through the geometry of all four design cases (i.e. cases 1,2,3 and 4, section 5), selecting four different Strouhal numbers for each case: Str=[0.15, 0.29, 0.42, 0.56] and two different pitch-angles for each Strouhal number. The two selected pitch-angles are properly Strouhal dependent, in order to represent a lower FOD loading and a higher FOD loading for each given Strouhal. Figure III.1.3-13up to Figure III.1.3-28 present Y=0 slices of the free vortex sheet geometry at t=2T, for all the sixteen combinations of geometry and Strouhal. Each figure contains two wake slices, the first (dashed line) corresponds to the higher FOD loading (smaller pitch-angle) while the second (solid line) to the lighter loading (greater pitch angle).

From those figures it is observed that for a smaller θ_0 (which means a higher angle of attack) a wider wake is developed. This presumes stronger induced velocities and thus higher loading. Also, by a wake inspection between the figures, it is shown that increasing the Strouhal number the loading is increased. Regarding the effect of a non-zero camber (Cases 2 and 4) the wake survey/comparison shows only slight differences with the non-camber case for similar Strouhal and pitch angle conditions.

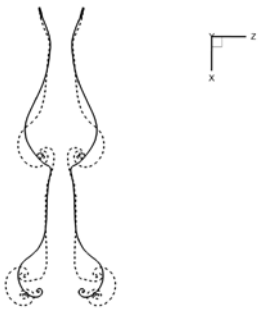

Figure III.1.3-13. Case 1, Wakes for Str=0.15 and theta=5 (dashed) and 18.49 (solid)

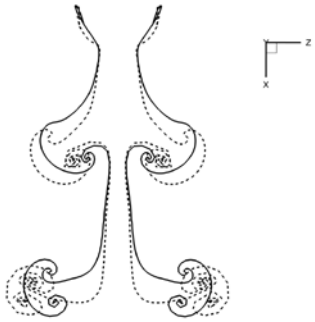

Figure III.1.3-14. Case 1, Wakes for Str=0.29 and theta=5 (dashed) and 23.54 (solid)

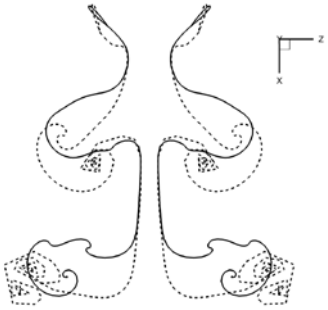

Figure III.1.3-15. Case 1, Wakes for Str=0.42 and theta=14.63 (solid) and 43.53 (dashed)

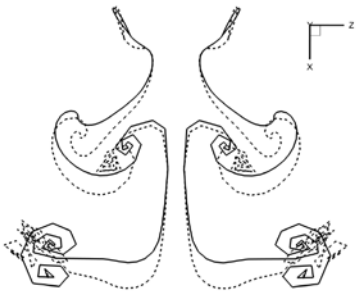

Figure III.1.3-16. Case 1, Wakes for Str=0.56 and theta=14.25 (dashed) and 32.75 (solid)

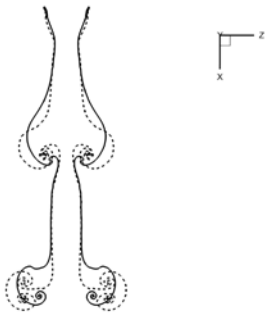

Figure III.1.3-17. Case 2, Wakes for Str=0.15 and theta=5 (dashed) and 18.49 (solid)

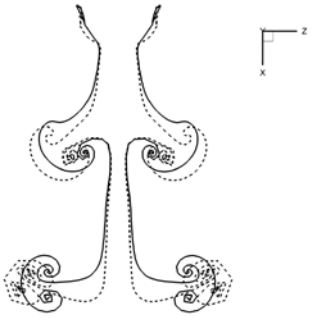

Figure III.1.3-18. Case 2, Wakes for Str=0.29 and theta=5 (dashed) and 23.54 (solid)

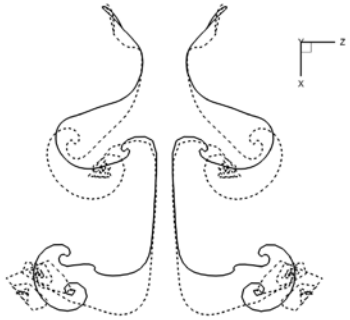

Figure III.1.3-19. Case 2, Wakes for Str=0.42 and theta=14.63 (dashed) and 43.53 (solid)

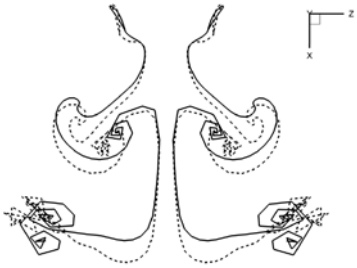

Figure III.1.3-20. Case 2, Wakes for Str=0.56 and theta=14.25 (dashed) and 32.75 (solid)

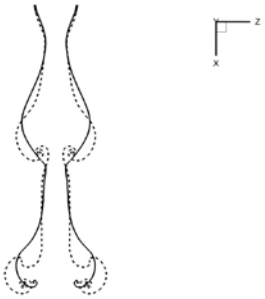

Figure III.1.3-21. Case 3, Wakes for Str=0.15 and theta=5 (dashed) and 18.49 (solid)

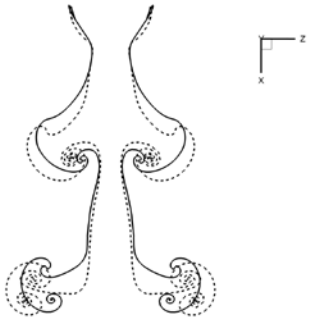

Figure III.1.3-22. Case 3, Wakes for Str=0.29 and theta=5 (dashed) and 23.54 (solid)

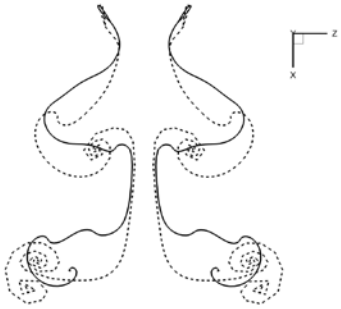

Figure III.1.3-23. Case 3, Wakes for Str=0.42 and theta=14.63 (dashed) and 43.53 (solid)

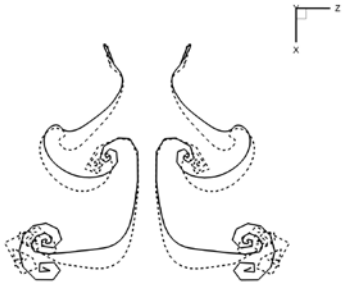

Figure III.1.3-24. Case 3, Wakes for Str=0.56 and theta=14.25 (dashed) and 32.75 (solid)

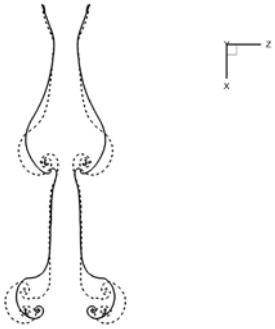

Figure III.1.3-25. Case 4, Wakes for Str=0.15 and theta=5 (dashed) and 18.49 (solid)

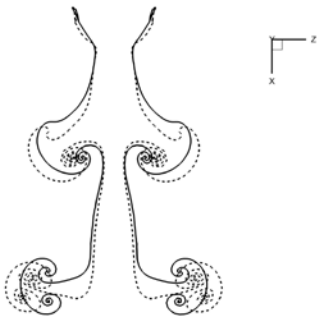

Figure III.1.3-26. Case 4, Wakes for Str=0.29 and theta=5 (dashed) and 23.54 (solid)

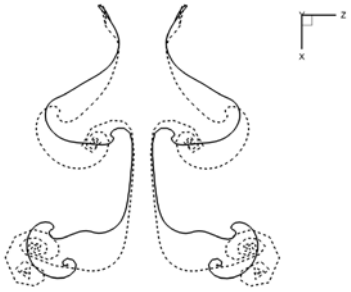

Figure III.1.3-27. Case 4, Wakes for Str=0.42 and theta=14.63 (dashed) and 43.53 (solid)

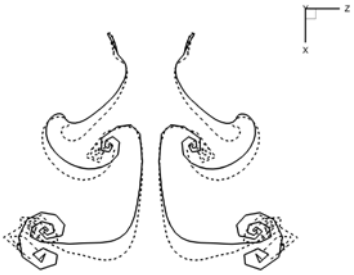

Figure III.1.3-28. Case 4, Wakes for Str=0.56 and theta=14.25 (dashed) and 32.75 (solid)

III.1.3.6 The open water performance diagrams for our FOD series.

Systematic unsteady BEM simulations have been performed with the selected FOD series described in section 5. In all simulations a chord of $c = 0.15m$ has been selected. Variation of Strouhal number has been achieved by changing the frequency of the FOD oscillation while the corresponding translational velocity has been held constant and equal to $V = 2.0m/s$. This results to a constant Reynolds number (based on translational velocity: $\mathrm{Re} = \frac{U \cdot c}{\nu}$) equal to $\mathrm{Re} = 0.263 \cdot 10^6$. Corresponding Reynolds numbers based on the maximum undisturbed flow velocity are Strouhal dependent according to the relation: $\mathrm{Re}_{Str} = \frac{U \cdot c}{\nu}\sqrt{1+(\pi \cdot Str)^2}$, or $\mathrm{Re}_{Str} = 0.291 \cdot 10^6$ at $Str = 0.15$ and $\mathrm{Re}_{Str} = 0.636 \cdot 10^6$ at $Str = 0.7$ (assumed kinematic viscosity $\nu = 1.139 \cdot 10^{-6} m^2/s$). Mean thrust and power have

then been calculated by running the BEM code for two time periods and calculating the mean values of the unsteady forces over the second period (see section 6). The results are presented in the form of $C_T - \theta_0$ diagrams (where $\theta_0 \rightarrow theta$ in diagrams), Figure III.1.3-29, Figure III.1.3-31, Figure III.1.3-33, Figure III.1.3-35, and $C_P - \theta_0$ diagrams, Figure III.1.3-30,Figure III.1.3-32,Figure III.1.3-34,Figure III.1.3-36, with parameter the Strouhal number (thick line in the diagrams).

The first set of figures contain additionally in parametric form (thin lines) the open water efficiency η of the FOD:

$$\eta = \frac{T \cdot U}{DHP} = \frac{C_T}{C_P} \qquad \text{(III.23)}$$

The second set contains additionally in parametric form the $a_{\max}$ angle (thin lines) defined as the maximum value of $a(t)$, relation (III.3), over one period. This last information is very useful for the designer in order to avoid maximum angles with a potential danger for separating flow (e.g. greater than 20deg), phenomenon which is not modeled by our method and consequently our BEM simulations can result in questionable and/or incorrect predictions in that region.

Interesting conclusions drawn from those figures are the following: (a) There is a relatively wide region of maximum hydrodynamic FOD efficiency which is achieved at a maximum angle of attack less than 15degrees i.e. at the region of flow without expected separation, (b) FODs with additional unsteady camber motion (cases 2, 4) increase both the produced thrust and the efficiency. It should be also noted that systematic inspections of the calculated pressure distributions gave no indication of local pressure less than the corresponding vapor pressure in the region around optimum performance. As a result no cavitation is expected in that region.

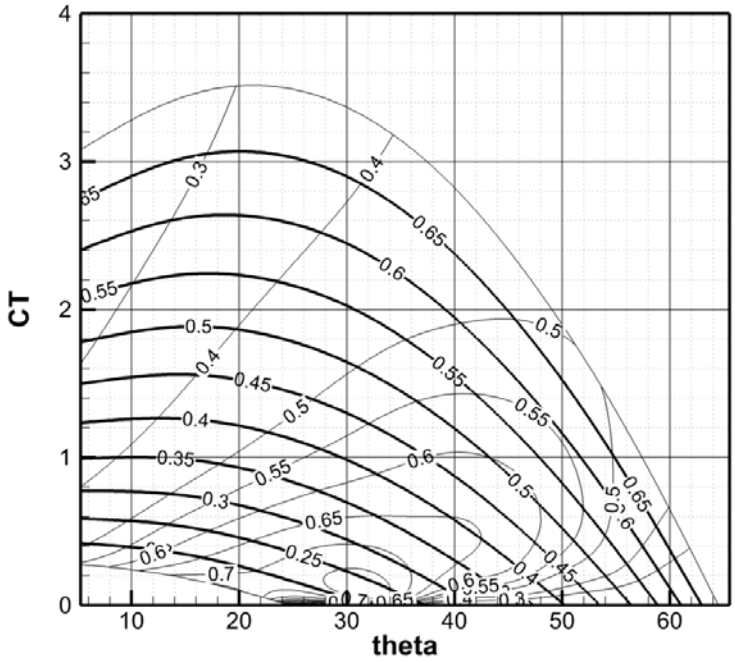

Figure III.1.3-29. Case1. Mean thrust coefficient, as function of θ_0. Thick lines stand for Str and thin lines for Efficiency.

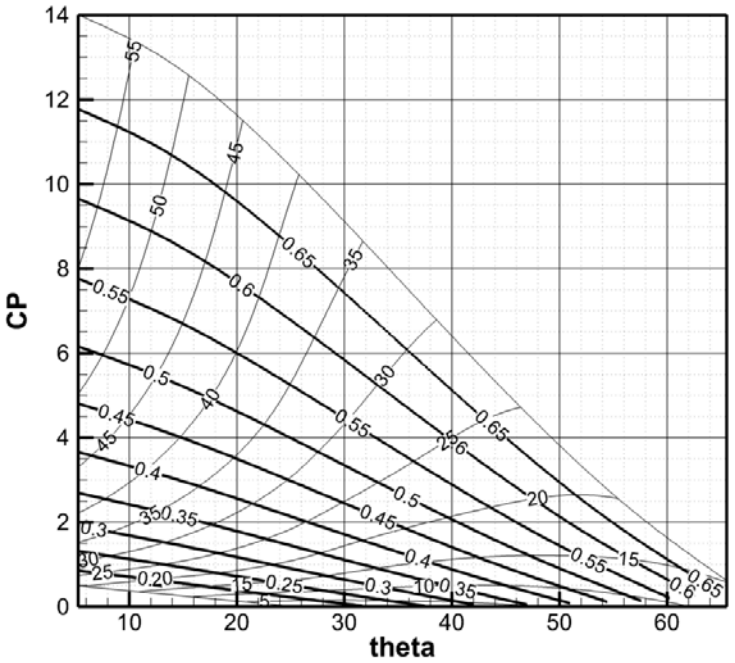

Figure III.1.3-30. Case 1. Mean Power coefficient, as function of θ_0. Thick lines stand for Str and thin for $a_{\max}$

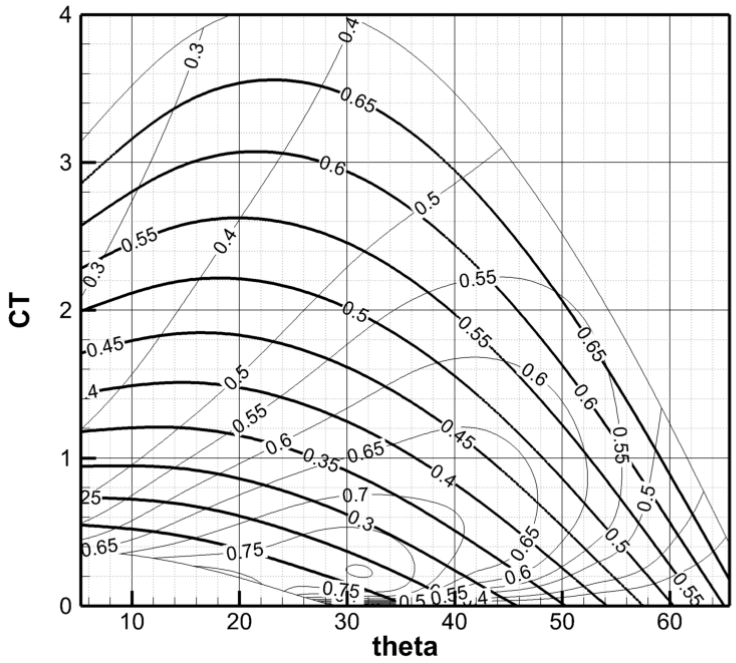

Figure III.1.3-31. Case 2. Mean thrust coefficient, as function of θ_0. Thick lines stand for Str and thin lines for Efficiency.

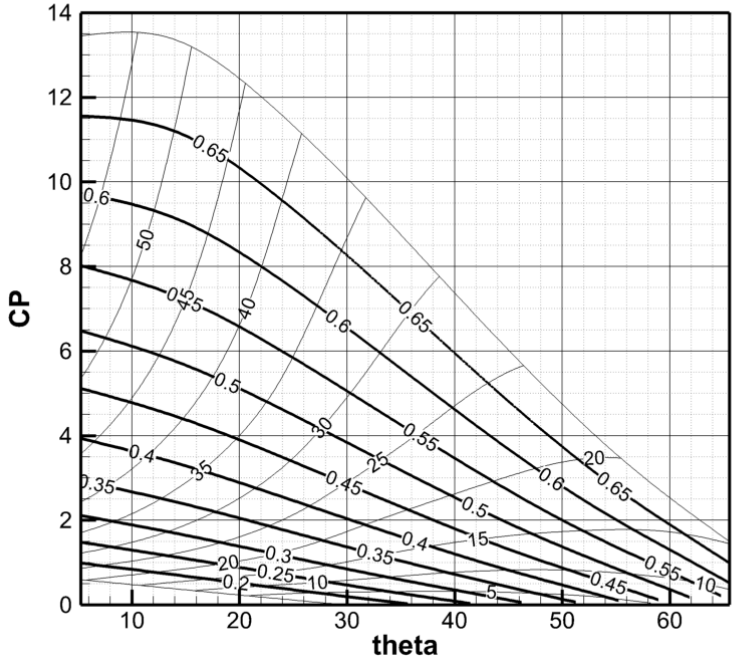

Figure III.1.3-32. Case 2. Mean Power coefficient, as function of θ_0. Thick lines stand for Str and thin for $a_{\max}$

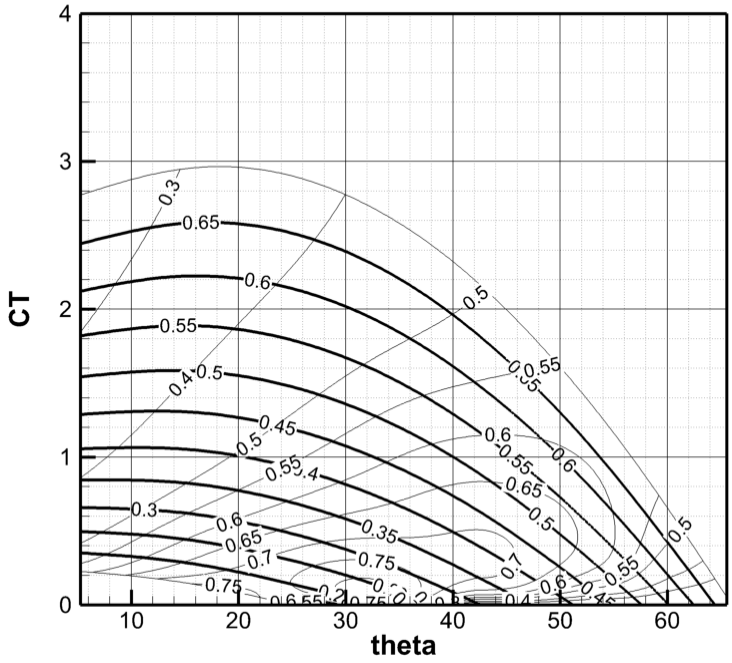

Figure III.1.3-33. Case 3. Mean thrust coefficient, as function of θ_0. Thick lines stand for Str and thin lines for Efficiency.

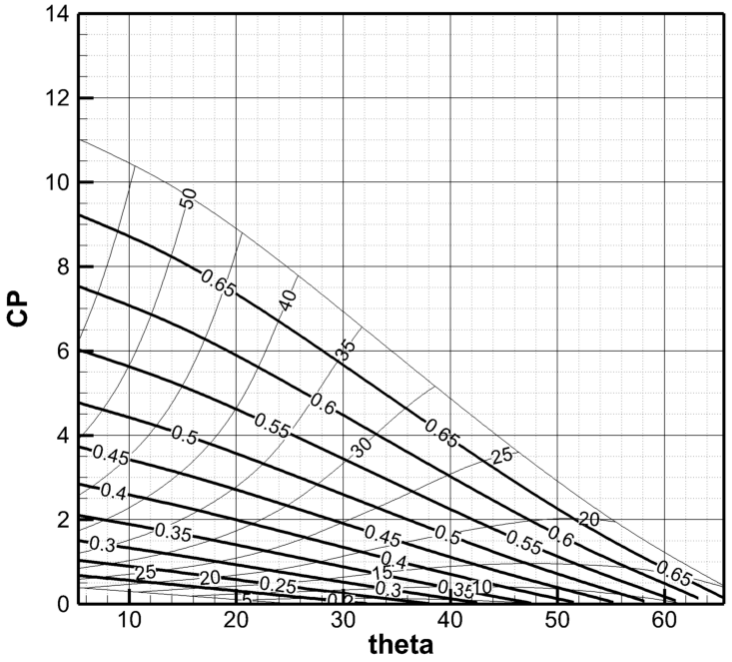

Figure III.1.3-34. Case 3. Mean Power coefficient, as function of θ_0. Thick lines stand for Str and thin for $a_{\max}$

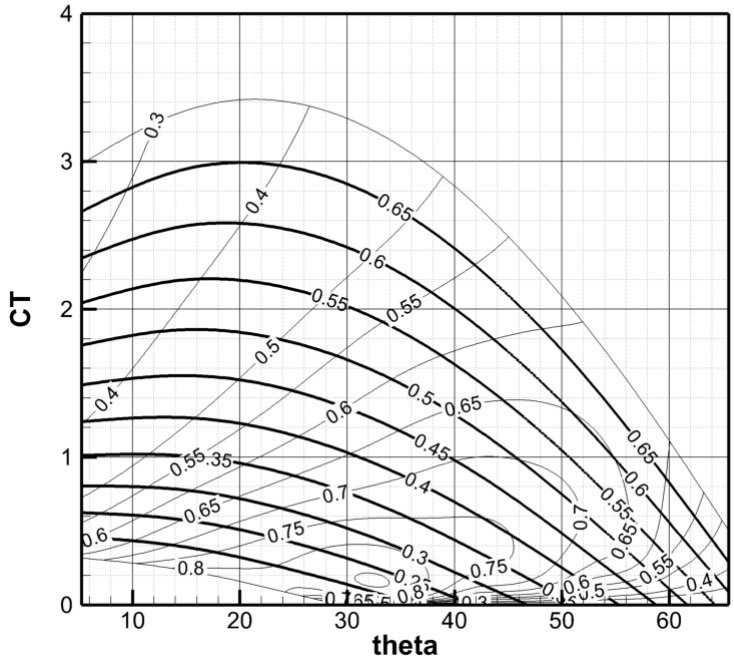

Figure III.1.3-35. Case 4. Mean thrust coefficient, as function of θ_0. Thick lines stand for Str and thin lines for Efficiency.

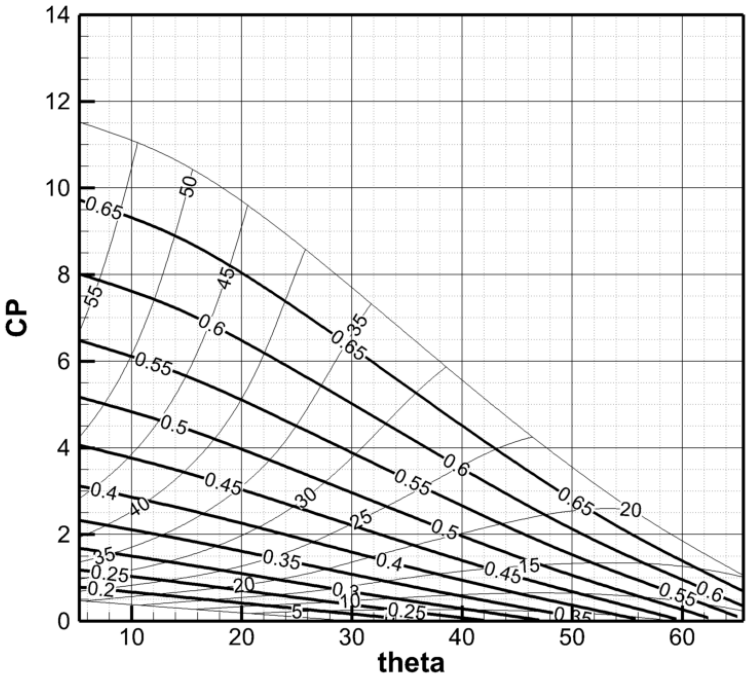

Figure III.1.3-36. Case 4. Mean Power coefficient, as function of θ_0. Thick lines stand for Str and thin for $a_{\max}$

III.1.4 Flexible Elliptic Oscillating Duct (FEOD)

The main conclusion from the previous case is that the FOD is a promissing propulsor with hydrodynamic efficiencies well over that of a convensional propeller, but also better than flapping wings. The main disadvantage of the FOD has to do with its support to the hull. More specifically it became obvious from the beginning that the completely circular geometry of the FOD makes its support onto the ship difficult, since every single point of the FOD would be in a constant motion. Towards resolution of this problem it was decided to expand/generalize the geometry of our propulsor allowing elliptical shapes. Thus the concept of a 'Flexible Elliptic Oscillating Duct' or simply, FEOD came up. An important difference between the FOD and the FEOD is that the latter can oscillate in both axis of the ellipse in a manner determined by the designer. This allows the designer to select one of the axis of the ellipse (for example the major axis) to be constant and the other to be oscillating. With this selection the major axis can be used for supporting the FEOD to the hull. Hence both ducts (FOD & FEOD) oscillate, but since the FEOD has two degrees of oscillation freedom (the two axis of the ellipse), deforms as an ellipse rather than as a circle in the general case.

III.1.4.1 FEOD geometry and motion – panel generation.

The starting point for an unsteady BEM simulation of a flexible body is the generation of the time dependent paneling describing the geometry of the system, Politis (2011). Thus, a discussion of the shape of the FEOD has to be made with a special consideration on the definition of the 'FEOD sections' and their 'pitch'.

Consider a plane Cartesian orthogonal coordinate system YZ, Figure III.1.4-1. There are three common descriptions for an elliptic shape with major and minor axis A, B as follows:

$$\frac{z^2}{A^2}+\frac{y^2}{B^2}=1 \tag{III.24}$$

$$z = A\cdot\cos(\tau) \tag{III.25}$$

$$y = B\cdot\sin(\tau) \tag{III.26}$$

$$z = r\cdot\cos(\varphi) \tag{III.27}$$

$$y = r\cdot\sin(\varphi) \tag{III.28}$$

where r, φ, τ are related by the equations:

$$r=\frac{1}{\sqrt{\frac{\cos^2\varphi}{A^2}+\frac{\sin^2\varphi}{B^2}}} \tag{III.29}$$

$$\tan\varphi=\frac{B}{A}\tan\tau \tag{III.30}$$

Equation (III.24) is the standard form, while equations (III.25),(III.26) and equations (III.27) ,(III.28) are parametric forms, with $\tau\in(0,2\pi)$ and $\varphi\in(0,2\pi)$ respectively. Form (III.25)

,(III.26) is termed 'concentric' in the sequel while form (III.27),(III.28) is termed 'polar'. The parameter φ in the description of the polar form has a very simple physical meaning. It denotes the angle of the line segment $\overline{OE}$ starting at the center of the ellipse O and ending at the point E belonging to the ellipse, figure 1. In the same figure the physical meaning of the parameter τ is shown.

The YZ system of Figure III.1.4-1, can now be completed to a right handed 3D Cartesian-orthogonal coordinate system, by adding the X-axis normal to YZ showing inwards. After that the FEOD can be described by 'building' the FEOD hydrodynamic sections around this ellipse. More specifically the ellipse of Figure III.1.4-1 is selected to be the locus of the pitch axis points of the FEOD sections. To complete the FEOD geometry, the position of the FEOD sections in space has to be defined. Figure 1 dictates two alternatives for this:

(a) *polar case*: the sections are placed in the plane defined by the X-axis and the line $\overline{OE}$ (angle φ from Z-axis), or

(b) *concentric case*: he sections are placed in a plane through E with orientation parallel to the plane defined by the X-axis and the line $\overline{OE''}$ (angle τ from Z-axis) .

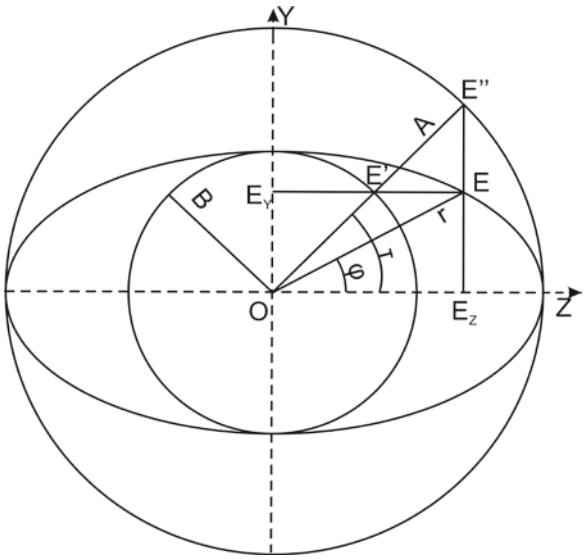

Figure III.1.4-1. Inscribed and outscribed circles of an ellipse. Points E, E', E_Y define a line parallel to Z-axis, while points E'', E, E_Z define a line parallel to Y-axis

Then the FEOD section is oriented, at either plane, to make an angle θ with the X-axis. In general θ can be a function of φ or τ i.e. $\theta(\varphi)$ or $\theta(\tau)$. Assuming further that the following variables are known functions: (i) the FEOD chord distribution $c(\varphi)$ $(c(\tau))$, (ii) the maximum camber distribution $f(\varphi)$ $(f(\tau))$, (iii) the maximum thickness distribution $T(\varphi)$ $(T(\tau))$, (iv) the thickness and camber forms, and (v) the chordwise position b for the sectional pitch axis from leading edge, the geometry of the FEOD is fully defined.

The two alternatives (a) and (b) lead to two different space grids which shall be termed as the 'polar grid' and the 'concentric grid' respectively, in accordance with the previous definitions regarding the parametric description of an ellipse.

Then, a heaving motion can be added to the pitch location (ellipse of Figure III.1.4-1), as follows. Assume:

$$A = A_0 + A_1 \cdot \sin\left(\omega \cdot t + \psi_A\right) \tag{III.31}$$

$$B = B_0 + B_1 \cdot \sin\left(\omega \cdot t + \psi_B\right) \tag{III.32}$$

where A_0, B_0 denote the mean major and minor axis positions and A_1, B_1 the corresponding oscillation amplitudes, ω denotes the angular velocity of oscillation which is common for both axis ($\omega = 2\pi n$ where n the frequency of oscillation) and ψ_A, ψ_B the phase angles.

With the previous considerations in mind, the points on the ellipse are identifiable through a certain value of the parameter φ (polar description/grid) or the parameter τ (concentric description/grid). Considering now the motion induced by relations (III.31),(III.32) to point E, it is observable that this depends on the parametric identification used for E i.e. it is different for the concentric and polar descriptions. Dividing the two sides of the polar equations (III.27) ,(III.28) gives: $\frac{y}{z} = \tan\varphi$ (III.33)

Relation (III.33) indicates that if the polar description is used to parameterize the points of the ellipse, then the $E(\varphi)$ moves along $\overline{OE}$ i.e. in-plane with the FEOD section. Denote by $dr(\varphi,t)/dt$ the 'heaving velocity' on the polar plane (r according to equation (III.29)). The total sectional undisturbed velocity due to the combined polar plane heaving and parallel translation V can then be calculated: $V^* = \sqrt{V^2 + \left(dr(\varphi,t)/dt\right)^2}$ and the angle $\phi(\varphi,t)$ between velocities V and V^* is given by the relation:

$$\phi(\varphi,t) = \tan^{-1}\left(\frac{dr(\varphi,t)/dt}{V}\right), \tag{III.34}$$

The sectional pitch angle $\theta(\varphi,t)$ can then be selected according to the formula:

$$\theta(\varphi,t) = w \cdot \phi(\varphi,t) = w \cdot \tan^{-1}\left(\frac{dr(\varphi,t)/dt}{V}\right) \tag{III.35}$$

where w denotes a weighting factor, independent of time, with values in the range: $0 < w < 1$. w is named '*the pitch control parameter*' after Politis & Politis (2012). An estimation of the angle of attack of the wing with respect to V^* is given by the following relation:

$$\alpha(\varphi,t) = \phi(\varphi,t) - \theta(\varphi,t) = (1-w) \cdot \tan^{-1}\left(\frac{dr(\varphi,t)/dt}{V}\right) \tag{III.36}$$

For this initial investigation, it was decided to use the polar description/grid for the FEOD discretization. In addition the major axis of the pitch loci ellipse is held constant in time i.e. $A_1 = 0$. Equation (III.29) applied for the minor axis (i.e. $\varphi = \pi/2$) becomes:

$$r(\pi/2,t) = B = B_0 + B_1 \cdot \sin\left(\omega \cdot t + \psi_B\right) \tag{III.37}$$

or introducing the substitutions: $B_0 = R, B_1 = h_0, \psi_B = \psi$ and $h(t) = h_0 \cdot \sin\left(\omega \cdot t + \psi\right)$:

$$r(\pi/2, t) = R + h(t) = R + h_0 \cdot \sin\left(\omega \cdot t + \psi\right) \quad \text{(III.38)}$$

The time derivative of (III.38) gives:

$$dr(\pi/2, t)/dt = dh(t)/dt = h_0 \omega \cos(\omega t + \psi) \quad \text{(III.39)}$$

and relation (III.36) for $\varphi = \pi/2$ becomes:

$$a(\pi/2, t) = (1 - w)\tan^{-1}(\pi \cdot Str \cdot \cos(\omega \cdot t + \psi)) \quad \text{(III.40)}$$

where Str denotes the Strouhal number defined by:

$$Str = \frac{n \cdot h}{V}, h = 2h_0 \quad \text{(III.41)}$$

Assuming given values for $w, B_0, R, h_0, V, \omega, \psi$ the motion of the FEOD is fully determined and equations (III.27),(III.28) and (III.29) can be used for the determination of the time dependent geometry and corresponding grid for the FEOD. In case of chord-wise flexibility the FEOD deforms in a similar manner to that discussed in Politis & Tsarsitalidis (2012).

Having introduced the analytical description of both geometry and motion of FEOD, the creation of a surface panel distribution at consecutive time steps is executed, describing the FEOD geometric evolution. Figure III.1.4-2 shows the panel discretization of the FEOD at a number of time instances, corresponding to the maximum, minimum and inflection point positions of a FEOD section in one period. With the FEOD paneling in time known, the code UBEM can be applied to calculate the FEOD unsteady forces, energy requirements and free shear layer evolution.

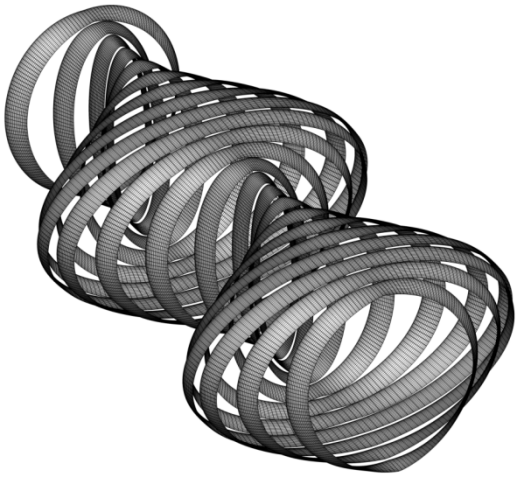

Figure III.1.4-2 Successive positions of the FEOD in two periods, R/c=B$_o$/c=4, h$_o$/c=3, Str=0.46.

III.1.4.2 Decisions regarding Geometric and Flow/motion variables for the proposed twin wing series.

To proceed to a series based design process for a FEOD, decisions have to be taken, on the corresponding geometric and flow related parameters. For the needs of the current pilot work on the subject, the series is limited in extent and consist of only one FEOD system, with $R/c = B_0/c = 4$, h_0/c=3.0 and $b/c = 0.33$. The Strouhal number has been selected in the range: $Str = 0.1 \div 0.7$. Using previous experience, this selection is expected to contain the region of maximum hydrodynamic efficiency. Finally the range of the pitch control parameter w has been selected between 0 and 1 which means a corresponding pitch angle $\theta(\varphi,t)$ which includes the full range of thrust producing motions for the various Strouhal numbers.

III.1.4.3 Transient FEOD performance and selection of simulation period.

The main difference between a traditional propeller and a biomimetic propulsor is that the latter produces a period mean thrust as a result of a highly unsteady instantaneous thrust. The simulation method in hand can predict this time dependent thrust but, since it is a time stepping method, initial conditions on motion have to be imposed. A burst starting FEOD is used as the starting condition. In this case a transient phenomenon occurs. Thus the mean period values for thrust or power have to be calculated after the passage of this initial transient phenomenon. To take care for this, time domain simulations have been performed for three periods and for several cases. Indicatively, Figure III.1.4-3, Figure III.1.4-4 present the unsteady thrust for two cases.

From these figures it can be concluded that, for the representative selected parameters, the transient phenomenon is limited to the few initial time steps after the burst start. Thus it is safe to use the 2nd period of simulation, to calculate the mean thrust and power to be used in the design charts.

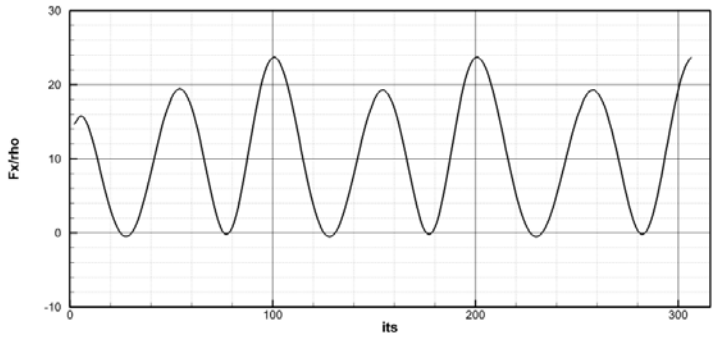

Figure III.1.4-3 Time evolution of thrust for (R/c=B$_o$/c=4, h$_o$/c=3, Str=0.22, Theta=13.3)

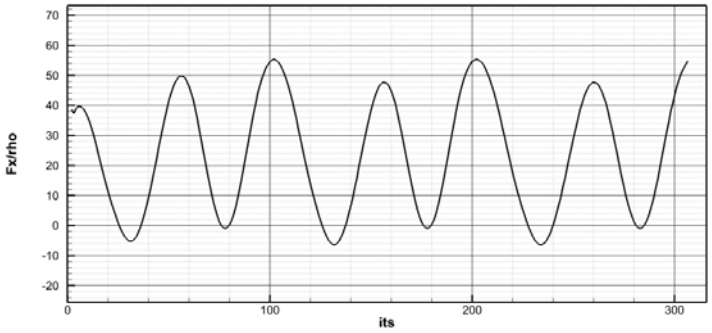

Figure III.1.4-4 Time evolution of thrust for (R/c=B$_o$/c=4, h$_o$/c=3, Str=0.46, Theta=34.4)

III.1.4.4 Open water performance diagrams and comparison with single wing systems.

Systematic simulations using UBEM have been performed with the selected FEOD series described in section 5. In all simulations a chord of $c = 1.0m$ has been selected. Furthermore in all simulations a FEOD system was used with: R/c=B$_o$/c==4, h$_o$/c=3,b/c=0.33.

Variation of Strouhal number has been achieved by changing the frequency of oscillation while the corresponding translational velocity has been held constant and equal to $V = 2.3m/s$. This results to a constant Reynolds number equal to $0.202 \cdot 10^7$, based on translational velocity ($\mathrm{Re} = V \cdot c / \nu$). Corresponding Reynolds numbers based on the maximum undisturbed flow velocity are Strouhal dependent, according to the relation: $\mathrm{Re}_{Str} = \frac{V \cdot c}{\nu}\sqrt{1+(\pi \cdot Str)^2}$. Thus $\mathrm{Re}_{Str} = 0.22 \cdot 10^7$ at $Str = 0.10$ and $\mathrm{Re}_{Str} = 0.51 \cdot 10^7$ at $Str = 0.7$ (kinematic viscosity: $\nu = 1.139 \cdot 10^{-6} m^2/s$). Mean thrust and power have then been calculated by running the UBEM code for two time periods and calculating the mean values of the unsteady forces over the second period. The results are presented in the form of $C_T - \theta_0$ diagrams, figure 5, (where $\theta_0 \rightarrow theta$ in diagrams) and $C_P - \theta_0$ diagrams, figure 6. Notice that the used θ_0 denotes the sectional pitch angle amplitude along the minor axis of the ellipse (equation (III.35) with $\varphi = \pi/2$). Notice also that for the FEOD the pitch angle is φ dependent.

$C_T - \theta_0$ diagrams contain additionally in parametric form the open water efficiency η of the system (thin lines):

$$\eta = \frac{T \cdot U}{DHP} = \frac{C_T}{C_P} \qquad \text{(III.42)}$$

Also, $C_P - \theta_0$ diagrams contain additionally in parametric form the $a_{\max}$ angle (thin lines) defined as the maximum value of $a(t)$, relation (III.40) with $\varphi = \pi / 2$, over one period. This last information is very useful for the designer in order to avoid maximum angles with a potential danger for flow separation (e.g. greater than 20deg), phenomenon which is not modeled by the used version of UBEM. For illustrative reasons, diagrams 7 and 8 contain similar results for a FOD with : R/c=4, h_o/c=2, so that comparisons are made easy. Note that the h_o/c ratio is not the same for the two cases, as the h_o/c ratio for the FEOD, refers to the maximum heave at the minor ellipse axis.

Interesting conclusions drawn from those figures are the following: (a) The region of maximum hydrodynamic efficiency is achieved at a maximum angle of attack less than 15degrees i.e. at the region of flow without expected separation, (b) The performance of the FEOD is diminished compared to that of the FOD, but it remains to be seen if such a compromise is acceptable for the sake of easier construction and proper fixing of the mechanism behind the boat. It should be also noted that systematic inspections of the calculated pressure distributions gave no indication of local pressure less than the corresponding vapor pressure in the region around optimum performance. As a result no cavitation is expected at that region. Finally notice that these charts can be used to select an optimum FEOD configuration for a given ship very easily as discussed in Politis & Tsarsitalidis (2012).

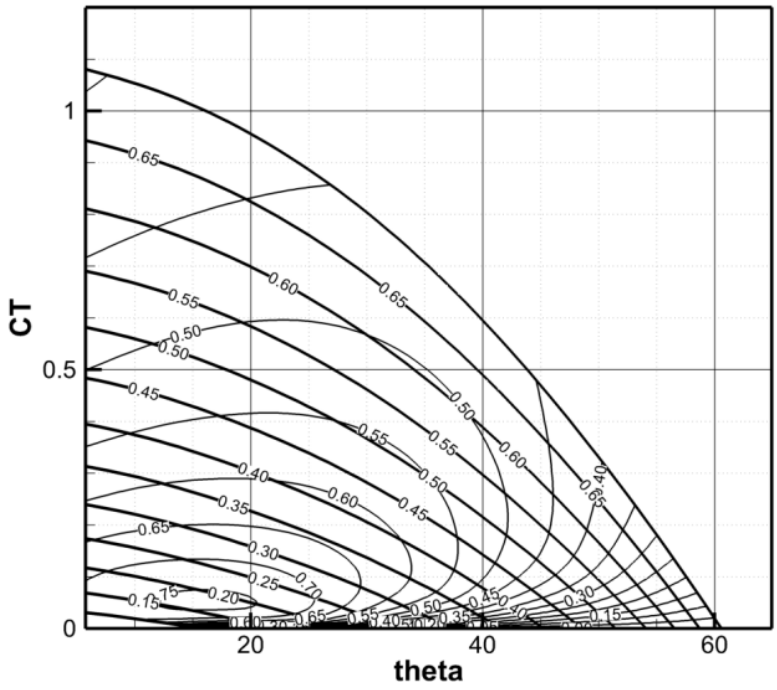

Figure III.1.4-5 $C_T - \theta_0$ **chart for FEOD. Thick lines stand for** Str **and thin lines for Efficiency.**

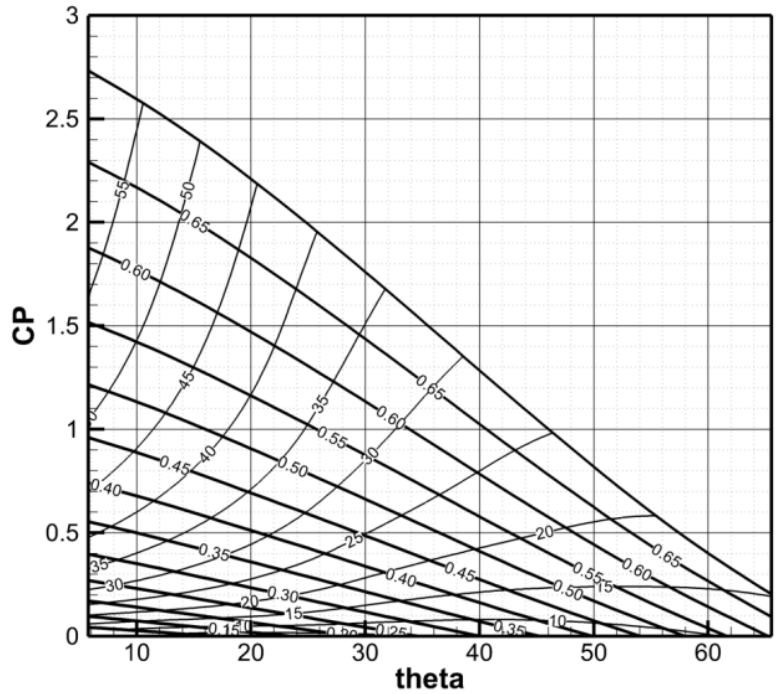

Figure III.1.4-6 $C_P - \theta_0$ **chart for FEOD. Thick lines stand for** Str **and thin for** $a_{\max}$

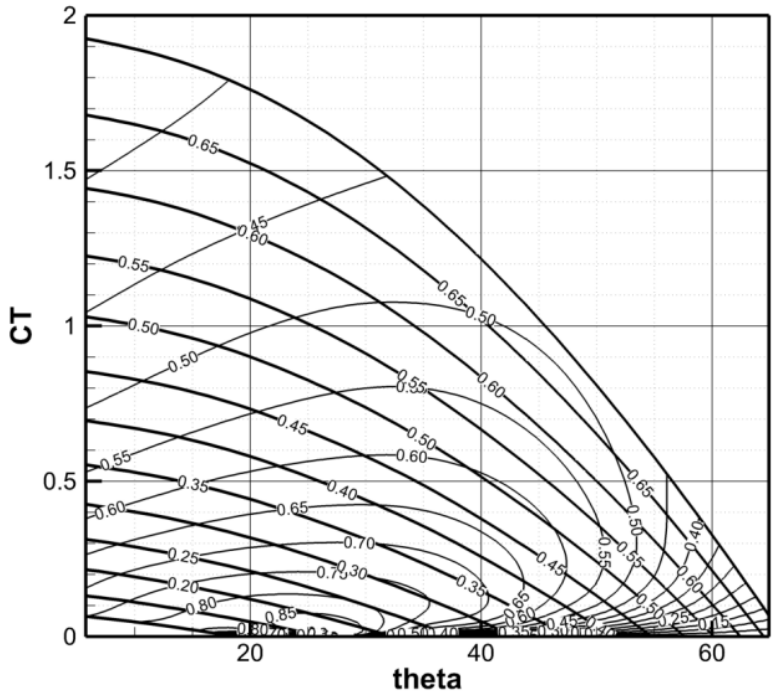

Figure III.1.4-7 $C_T - \theta_0$ **chart for FOD R/c=4 h$_o$/c=2.0. Thick lines stand for** Str **and thin lines for Efficiency.**

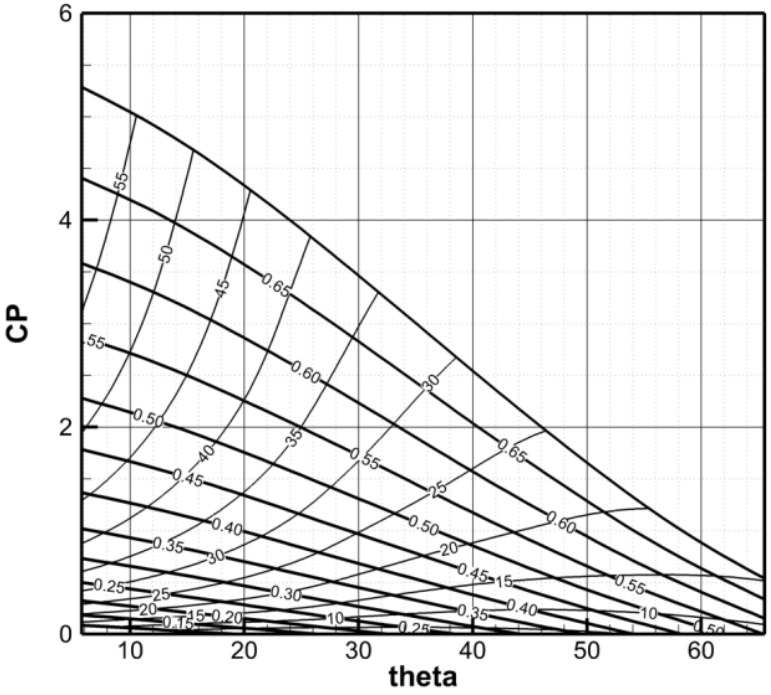

Figure III.1.4-8 $C_P - \theta_0$ **chart for FOD R/c=4 h$_o$/c=2.0. Thick lines stand for** Str **and thin for** $a_{\max}$

III.1.4.5 Wake visualizations – Understanding how the FEOD produces thrust**.**

For a better understanding of the underlying physical mechanisms of thrust production, the free shear layer produced by the FEOD system is plotted, Figure III.1.4-9. The FEOD surface and the free vortex sheet surface on those figures have been colored according to their surface dipole distribution intensity. Notice that constant dipole lines coincide with surface vortex lines. By using either the last property or the deformation patterns of the free vortex sheets, a number of strong ring vortices in the wake of the FEOD are made recognizable. Those ring vortices produce series of oblique jet flows by which the flapping wing produces thrust. Figure III.1.4-9 also contains artistic add-ons, showing the train of ring vortices (toroidal meshes) and corresponding jets (straight arrows) by which the flapping wing feeds with momentum the wake and produces thrust. More specifically the straight arrows are the results of the induced velocities produced by the ring vortices. What is important, is that the wake resembles more that of a twin wing system than that of the FOD (i.e. the homocentric rings have been replaced with couples of rings). From the shape of the rings, it is also noticeable that they resemble the rings produced by wings of small Aspect Ratio operating at lower Strouhal numbers (the rings are elongated in the axis of parallel translation, while in higher AR, they are elongated in the spanwise direction) This fact points to where further investigation is to be made (i.e. higher B_o/c ratios).

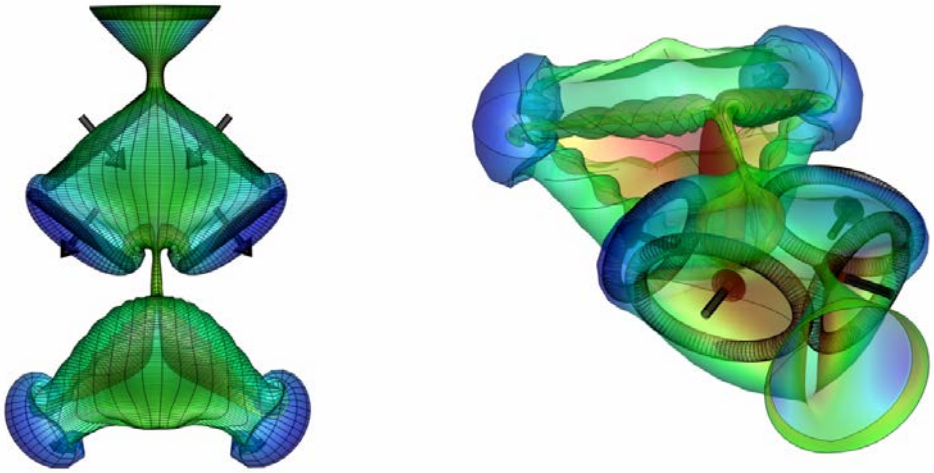

Figure III.1.4-9 Wake of a FEOD, Str=0.46, θ_o=34.4. Colors are for dipole potential. Artistic add-ons showing the train of ring vortices and corresponding jets by which the FEOD produces thrust.

III.1.5 Bird Flight

Among flapping wing types of motion, the flight of a bird is the most intriguing and astonishing, as the same wing works as a propulsor, a lifting surface and a control surface, enabling birds to achieve wondrous performance. Due to the complexity of the motions and geometry, both geometry and motions have been taken to an elemental level, where some initial deductions can be made. Thus, at this stage, there are no systematic simulations as made for the other cases.

III.1.5.1 Phenomenological considerations regarding geometry and motion of bird flight.

In order to simulate the motion of a bird's wings, advice has to be taken from biologist investigations. As seen in the picture below taken from biology clipart, the motion of a bird in flight is asymmetrical. Additionally, the wing outline and all other geometric/motion details are time dependent and in general allow for a large variety of alternatives.

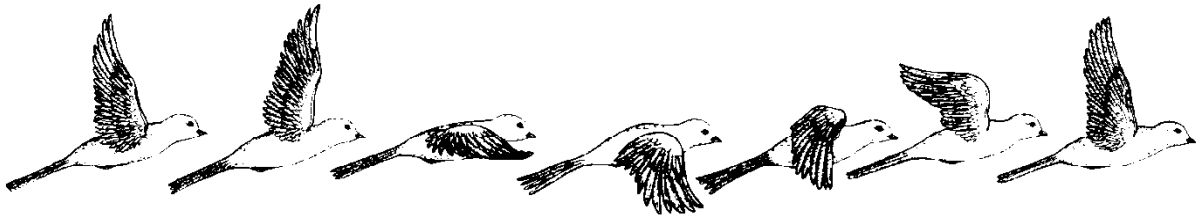

Figure III.1.5-1 A schematic view of a bird in flight (biology clipart)

This geometric complexity, which nature has introduced to the flying creatures by natural selection, is dependent from the creature operational objectives such as the ability of successful hunting, the ability to cope with their enemies or the peculiarities in the operational environment.

As a result, a multitude of flying creature wings can be met with different complexities. Simpler wing geometries are usually present in insects. For example a nearly elliptical wing is present in the case of a grasshopper. The grasshopper wing has not joints and is mainly stiff, allowing spanwise and chordwise deformations induced by the elastic properties of its construction. In many insects, wings are operating in tandem, allowing thus a balancing of developed aerodynamic forces. Birds are almost always equipped with wings of more complex motion capabilities and have joints. Not only can the wing as a whole change its position with time, but also its geometric details (such as the wing outline, the twist, the camber etc.) can be time dependent. This wing motion 'flexibility' is intimately connected with its physical anatomy and the existence of a spinal column with a muscle system. Biologists have systematically investigated the anatomy of bird wings and arrange them in groups according to their characteristics. From these investigations it is shown that there are species that employ a simpler wing outline and motion. For example the wing of a hummingbird is nearly elliptic without joints and its motion can be described by a combination of a flapping and a twisting motion. Unfortunately (for the scientists) the more complex wing motions are the rule for the flying creatures. For example a seagull's wing in simultaneous acceleration and

climbing condition (high thrust and lift) presents a highly asymmetric wing motion with very strong wing shape variations with time. This is connected with the existence of a 'joint' in seagull's wing, which allows independent control by the birds' brain, of the two parts of the wing.

A challenge for the scientist which attempts to numerically simulate the bird's flight is the introduction of a minimal, yet richly enough, group of geometric and motion parameters to control the variations of the geometric and kinematic characteristics of a birds wing in flight.

III.1.5.2 Handling birds' wing geometry and motion

Regarding simulation of geometry and kinematics of bird wings, our proposal is lent from the anatomy of the real wing that is the use of a spine-rail combination is proposed. Thus the instantaneous position of a birds' wing can be defined by: (a) a spine (a line tracing the wing in the span-wise direction), (b) the rails (a number of lines tracing the camber line in the chord-wise direction) and (c) a thickness distribution which is superimposed on the spine-rail surface (otherwise termed the 'reference wing surface'). The time dependent geometry of a birds' wing can then be reproduced by defining the successive positions of the reference surface as well as the thickness distribution which, if necessary, can also be time dependent.

More specifically the 'spine' is discretized by a variable (user determined and bird dependent) number of straight line spine segments of given length, not necessarily equally spaced. Each segment is connected to a 'next' and 'previous' one by a 'start' and 'end' joint respectively. Instantaneous spine geometry can then be defined by giving the position of the starting node of the first segment and the two rotation angles for each (and all) segments, defining their orientation in space with respect to a global XYZ coordinate system. Assuming the X axis to be along birds' instantaneous velocity and the XY plane as the plane of instantaneous flight symmetry (the investigation is currently limited to cases where bird wings are moving with a XY transverse plane of symmetry), the spine rotation around the X axis is termed Y-flapping while the spine rotation around the Y axis is termed the X-flapping. Figure III.1.5-1 shows schematically those notions.

The 'rail', which is attached to each end joint in a plane normal to the instantaneous position of the spine segment, is discretized similarly by a number of straight line segments tracking the local camber distribution. Rails obtain their position on this normal plane by determining a 'twist angle' relative to an initial position. By superimposing to this plane a thickness distribution, a section of the final wing surface has been constructed. Birds' wing camber and thickness distributions are lent from traditional 2-D data of the NACA family, which is characterized by analytic descriptions with a minimum number of defining free parameters. For example a camber/thickness distribution similar to the NACA four digits family of sections can be assumed(i.e. NACA 4412).

Then motion can be added to the bird wing by assuming that the spine joint X,Y flapping and twisting angles as well the rail maximum camber changes with time.

The previous methodology is entirely free to produce the most general flight patterns met in nature. Irrespective of this, for the needs of the current work, the previous methodology has been applied with the following simplified assumptions:

a) All joints perform harmonic flapping and twisting motions with a common (given) frequency. Similarly the maximum camber on joint positions varies harmonically with the same frequency.
b) Its joint flapping and/or twisting motion can have its own phase angle and mean value.

Thus, let $Q(t)$ denotes a motion defining parameter (for example a twist angle or a X,Y-flapping angle of the nth joint etc.), then:

$$Q(t) = Q_a \cdot \sin(\omega \cdot t + Q_{ph}) + Q_m \qquad \text{(III.43)}$$

where Q_a is the amplitude, Q_{ph} is the phase angle and Q_m is the mean value of the motion defining variable $Q(t)$ and ω the common to all motions circular frequency. Since the $Q(t)$'s are given at the joints of the spine as a function of time, an interpolation scheme is needed in order to produce the $Q(t)$'s at all points of the spine, necessary to calculate a dense boundary element grid for the description of kinematics of the birds wing. A linear interpolation is used between the values of the various $Q(t)$ parameters between joints. Thus $Q(t)$ is a C^0 function with support the spine length. Notice that in the case of X or Y flapping a C^0 continuity on spine angles results in a C^1 continuity in spine position. Thus a surface BEM grid with at least C^1 continuity is produced by our method.

With the previous considerations in mind the motion of a birds' wing is fully determined providing the:

a) X,Y flapping and twisting motions of the spine joints in the form of the set $(XF_a, XF_{ph}, XF_m)_{k=1,K}$, $(YF_a, YF_{ph}, YF_m)_{k=1,K}$, $(TW_a, TW_{ph}, TW_m)_{k=1,K}$ where XF denotes the X flapping angle, YF denotes the Y flapping angle and TW denotes the twisting angle at the kth joint and K denotes the number of joints of the spine,
b) Maximum camber motion $(MC_a, MC_{ph}, MC_m)_{k=1,K}$ where MC denotes the maximum camber of the kth joint,
c) The common circular frequency ω and
d) The parallel instantaneous bird velocity.

Before closing this section it is interesting to briefly discuss the motion of 2-D heaving and pitching wing in parallel flow. The interest of this simplified case has to do with the similarities it has with what a local observer, moving attached to the birds' wing surface, shows (strip theoretic approach). For a 2-D wing performing a harmonic heaving motion with amplitude h_0, a harmonic pitching motion with amplitude angle θ_0 and phase ψ, both at a frequency $n(=\omega/(2\pi))$, and moving with parallel velocity U, the instantaneous angle of attack $a(t)$ is given by:

$$a(t) = \theta_0 \sin(2\pi n \cdot t + \psi) - \tan^{-1}\left(\frac{h_0 2\pi n \cdot \cos(2\pi n \cdot t)}{U}\right) \qquad \text{(III.44)}$$

or in non-dimensional form:

$$a(t) = \theta_0 \sin(2\pi n \cdot t + \psi) - \tan^{-1}(\pi \cdot St \cdot \cos(2\pi n \cdot t)) \quad \text{(III.45)}$$

where St denotes the Strouhal number defined by:

$$St = \frac{n \cdot h}{U}, h = 2h_0 \quad \text{(III.46)}$$

From relation (III.45) it is observed that the combination (θ_0, ψ, St) determines fully the $a(t)$ and consequently the maximum angle of attack for the 2-D case. Since this is related to the maximum attainable lift as well as phenomena like viscous separation and stall, it is common to characterize an unsteady flight condition for a 2-D airfoil by the non-dimensional variables (θ_0, ψ, St). In the sequel, the previous non-dimensional variables shall be used, based on a single birds' wing section (for example in the first two cases the section at 70% of the birds wing semi-span is used) although it is clear that only a crude relation between the flow variables of the 3-D flow case with the 2-D case exists.

III.1.5.3 Cases simulated

Three different modes of flight have been investigated. The first is a motion where the wing flaps around the X-axis and twists harmonically. This is the simplest case of motion of a birds' wing and can be considered to resemble the motion of a hummingbird. The second case is an alteration of the first, with the difference that the flapping around X-axis has a non-zero mean value. Such a motion is employed by most birds when they maintain speed in steady flight (level flight). This type of asymmetry produces an additional amount of lift in level flight. The third case is a motion with strong deformations due to wing joints that simulates the motion of seagull's wings when accelerating and climbing at the same time (high thrust and lift). The wing outline is the same for all cases for reasons of comparison Figure III.1.5-2. Similarly a NACA 0012 section is used in all cases considered.

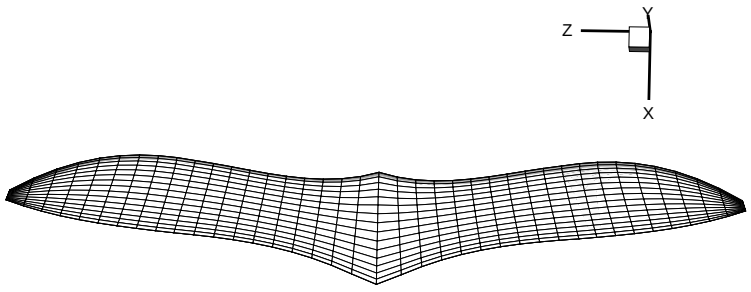

Figure III.1.5-2 Wing geometry for Bird Flight Simulations

III.1.5.3.1 Case 1 (hummingbird in vertical climb)

Figure III.1.5-3 shows the time evolution of the wing geometry over one period. The motion is characterized by a Strouhal number: $St = 0.15$ and $a_{\max} = 10^o$ ($a_{\max} = \max(a(t), t \in (0...T))$ at the spanwise section located at 70% of semi-span. Figure III.1.5-4 shows the 3-D pattern of the shear layer emanating from the wing trailing edge at various perspectives. By tracking the shear layer deformation it is possible to identify regions where well structured and intensive ring vortices evolve. For the non-experienced observer Figure III.1.5-5 presents an artistic addition which shows explicitly the shape and direction of such vortices. From those figures it is observed that in the considered flight a continuous strip of ring vortices is generated with axis inclined with respect to the axis of bird parallel movement. Four vortices are created in one period, two during upstroke, with axis inclined upward, and two other during downstroke, with axis inclined downward. In the case considered all the vortices have the same intensity and their vertical projection sums to zero in one period. This flight is realistic only when applied to a bird in entirely vertical hover. In level flights the bird needs both thrust and lift which is the subject of the next case. Figure III.1.5-6 presents the calculated thrust and lift. Notice the symmetry of the lift, by which its average value is zero. From the calculated unsteady thrust it is observed that there is a substantial average thrust. Finally the mean (one period) efficiency of the flapping wing for this case is 63%.

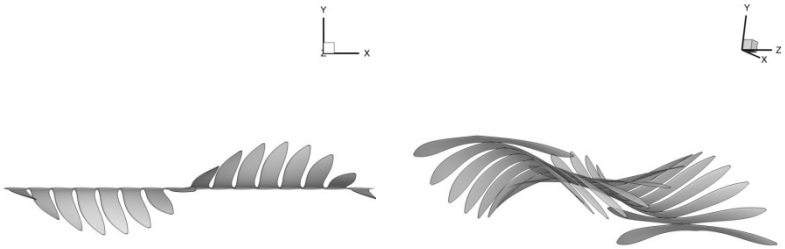

Figure III.1.5-3 Successive wing positions over one period

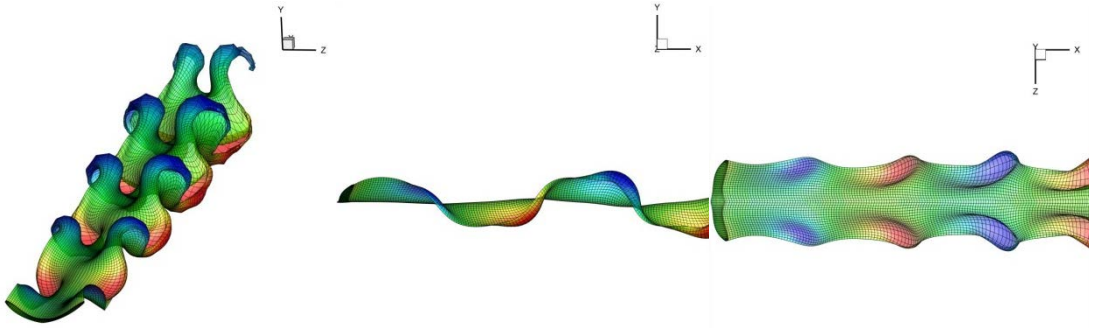

Figure III.1.5-4 Shear layer dynamics. Color represents dipole intensity.

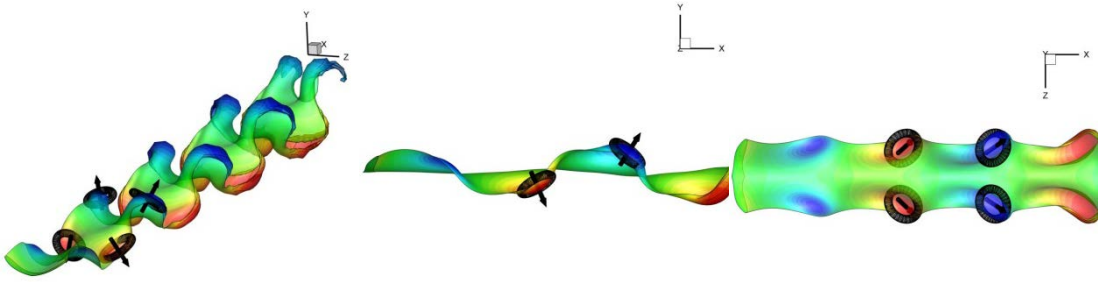

Figure III.1.5-5 Artistic addition of vortex rings and corresponding flow jets.

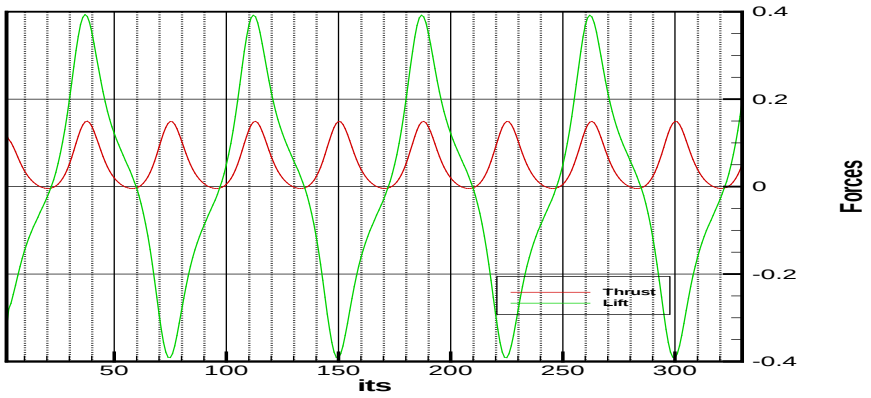

Figure III.1.5-6 Instantaneous thrust and lift as a function of time.

III.1.5.3.2 Case 2 (hummingbird maintaining steady level flight)

The next case considered is similar to the first in all aspects, with the exception of introducing a mean value in the Y-flapping angle. This introduces an asymmetry to the upstroke with respect to the down stroke motion of the wing which results in the development of a lift force useful for a level flight. Again $St = 0.15$ and $a_{\max} = 10^o$ at the spanwise section located at 70% of semi-span. Figure III.1.5-7 shows the time evolution of the wing geometry over one period. Figure III.1.5-8 shows the 3-D pattern of the shear layer emanating from the wing trailing edge at various perspectives. Figure III.1.5-9 presents an artistic addition which shows explicitly the shape and direction of created ring vortices. From those figures it is observed that the considered flight is maintained by a continues creation of ring vortices with inclined axis with respect to the axis of bird parallel movement. Four vortices are created in one period, two of them with axis inclined upward and two other with axis inclined downward. In opposition to the previous case, the vortices have not the same intensity and their vertical projection does not sum up to zero in one period. Thus a mean lift is obtained. This flight is realistic for a level flight, where the bird needs both thrust and lift. Figure III.1.5-10 presents the calculated thrust

and lift. Notice the asymmetry of the lift, by which its average value is different from zero. From the calculated unsteady thrust it is observed that there is a substantial average thrust. Finally the mean (one period) efficiency of the flapping wing for this case is 60%.

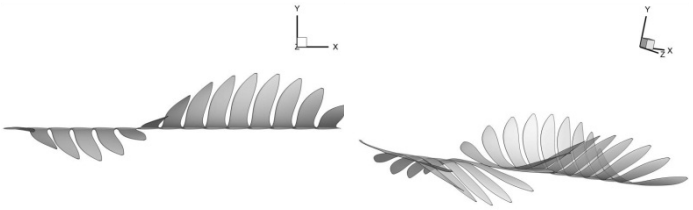

Figure III.1.5-7 Successive wing positions over one period

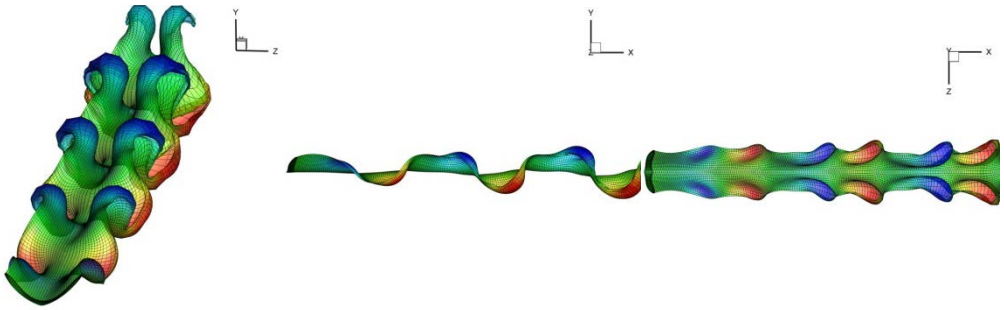

Figure III.1.5-8 Shear layer dynamics. Color represents dipole intensity.

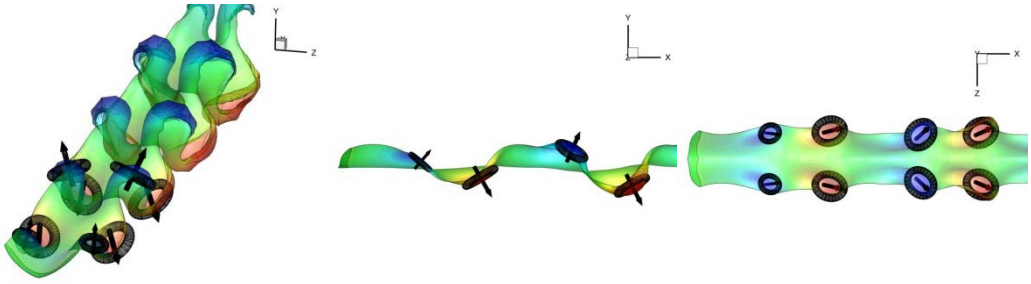

Figure III.1.5-9 Artistic addition of vortex rings and corresponding flow jets.

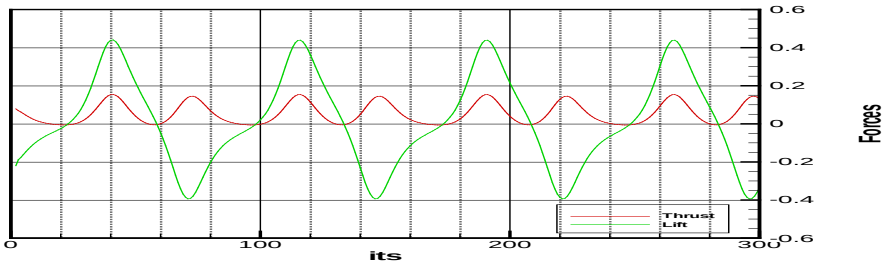

Figure III.1.5-10 Instantaneous thrust and lift as a function of time.

III.1.5.3.3 Case 3 (seagull's wings in highly deformed motion)

The next case considered is entirely different from the previous two cases. More specifically the inner part of the wing breaks harmonically with amplitude 35^{o} and mean value -25^{o} while the phase lapse between breaking and flapping is 90^{o} . This leads to breaking the wing during upstroke and extending it during downstroke. For this case $St = 0.4$ and $a_{\max} = 12^{o}$ at the spanwise section located at 55% of semi-span. Figure III.1.5-11and Figure III.1.5-12 show the time evolution of the wing geometry over one period for the upstroke and the downstroke movements respectively. Figure III.1.5-13 Figure III.1.5-14 and Figure III.1.5-15 show the 3-D pattern of the shear layer emanating from the wing trailing edge at various perspectives. More specifically the left side of the aforementioned figures present an artistic addition which shows explicitly the shape and direction of created ring vortices. From those figures it is observed that the considered flight is again characterized by a creation of ring vortices with inclined axis with respect to the axis of bird parallel movement. Notice that, the topology and number of vortices created by this flight in one period is different from that observed in the previous cases. There is also a ground effect between the wings during upstroke, the effect of which can be seen in the time evolution of shear layer geometry. Figure III.1.5-16 presents the calculated thrust and lift. Notice the effect of wing breaking in the instantaneous forces , which results in both serious lift and thrust forces. The mean thrust is 0.21N while the mean lift is 0.19N and the mean propulsive efficiency is 46%, lower than that of the cases considered previously.

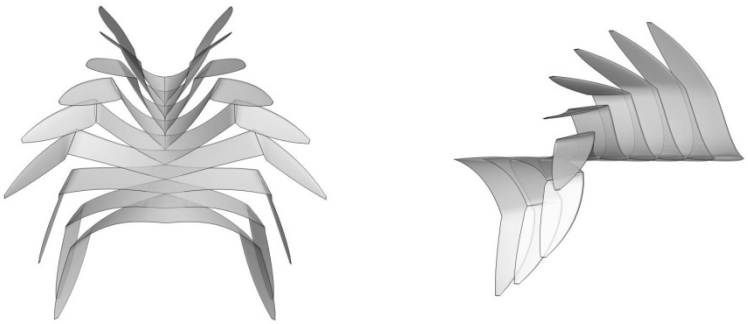

Figure III.1.5-11 Successive wing positions over one period – Upstroke

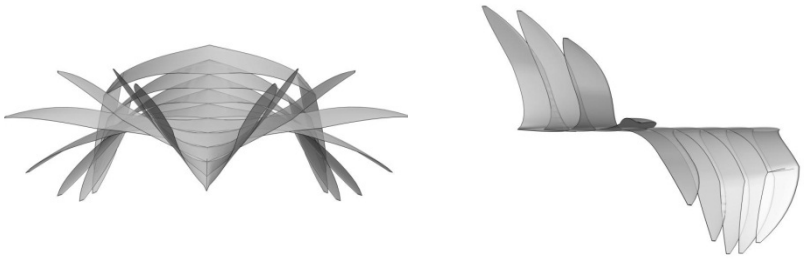

Figure III.1.5-12 Successive wing positions over one period - Downstroke

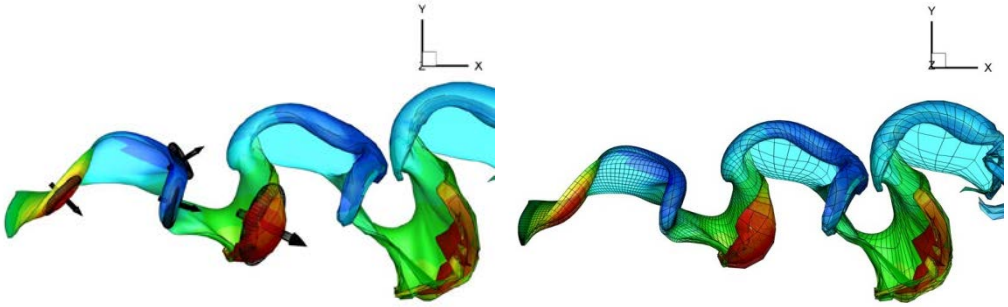

Figure III.1.5-13 Shear layer dynamics. Color represents dipole intensity - Side view

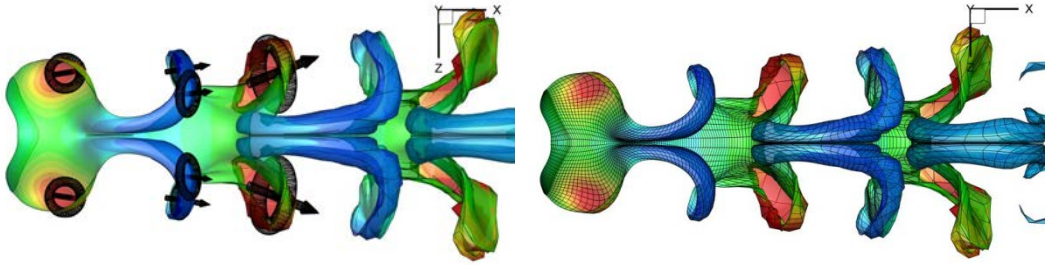

Figure III.1.5-14 . Shear layer dynamics. Top view

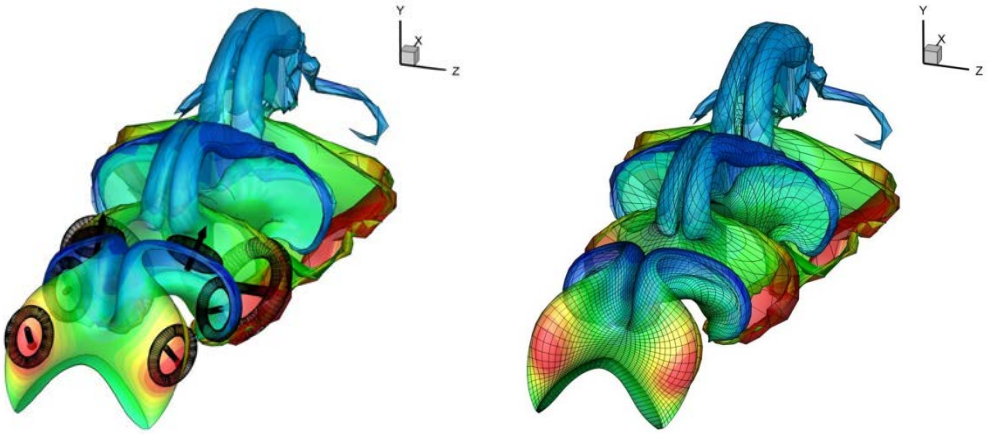

Figure III.1.5-15 Shear layer dynamics. Perspective view

Note that, except for the big difference in position and arrangement of vortex rings, there is also a ground effect between the wings during upstroke, the effect of which can be seen in the time evolution of results. The mean thrust is 0.21N while the mean lift is 0.19N and the mean propulsive efficiency is 46%, lower than cases before, but more than acceptable, as the lift is also very high.

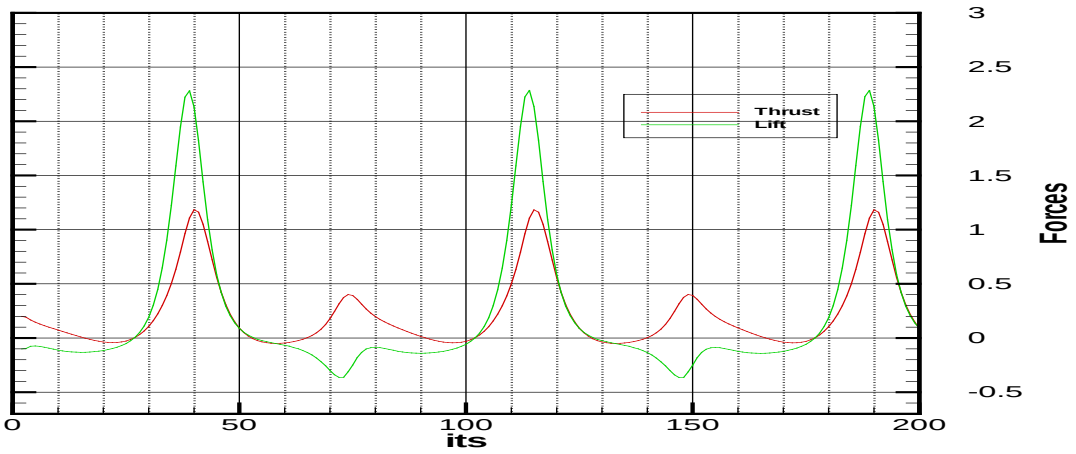

Figure III.1.5-16 Instantaneous thrust and lift as a function of time.

III.2 Optimum Design Methodology for Flapping Wing Propulsion and Applications

The purpose of making the tools and simulations discussed in the previous parts is to lead to designing optimal propulsors and/or energy saving systems. Working to this end, the data from the systematic simulations had to be presented in design charts and a design methodology had to be developed. First of all, a general concept of the proposed propulsor has to be introduced and decisions have to be made on the size and position of the system. Then, the problem of optimal design of a flapping wing propulsor is to be formulated, along with a solution method. This method is finally applied to virtual paradigms of ships equipped with such propulsors and comparisons are made with conventional propulsors.

III.2.1 Intro: Position and sizing of biomimetic propulsors

As already said in the first part, there have been several patents and designs of flapping wing propulsors and most of them have common characteristics based on their advantages and pointed towards the exploitation of their main differences to a conventional propulsor. The main advantage is that the swept area of a flapping wing is a box with width the span of the wing (if placed horizontally) and height the heave amplitude. On the other hand, a propeller, has a disk shaped swept area, which has to fit within the allowed size under the ship. As shown in Figure III.2.1-1, the conventional propellers take a considerably smaller area compared to a wing, which means that for the same ship and speed and under the same allowances, the wing will be loaded less, thus having higher efficiency. For wide and shallow vessels (like passenger ships or inland liners) this effect is even stronger. Another advantage of the flapping wing is that there is no asymmetric flow caused by its operation, thus having minimal hull interaction (for the rotational part). It should be noted, that for conventional propulsors, swirl handling (via appendages or hull deformation) has become a serious and costly energy saving issue.

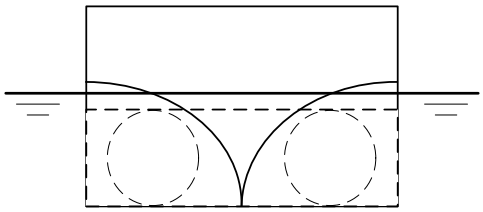

Figure III.2.1-1 Simplified stern view of a twin screw vessel. Dashed lines show the areas taken by propellers and a wing.

The examined case of a ship equipped with a flapping wing propulsor, follows the paradigm of Yamaguchi and Bose (1994), where a horizontal wing of the same span as the width of the ship is placed as shown in Figure III.2.1-2 and made to oscillate vertically, while most of the geometry of the ship is left unaltered. Bearing, also in mind, that (as seen in previous part) the larger span to chord ratios, but also the larger heave to chord ratios, have the greatest efficiency, usage of the maximum box that fits the stern is imperative and minimizing the chord length (within limitations, as a very small chord will lead to a smaller Reynolds number) leads to higher efficiency. This leads to the main trade off that the designer has to consider. For the same ship, a smaller chord will lead to a higher efficiency, but will also mean a structurally weaker wing, which will also have increased risk of cavitation. This is very similar to the expanded area ratio trade off that is made for conventional propellers, with the difference, that in the flapping wing case, the risk of cavitation can be smaller, while the structural problems may be serious. Thus, a decision on the wing chord has to be made, based on safety criteria and then the designer may use the design diagrams produced, to choose the operation parameters of the propulsor.

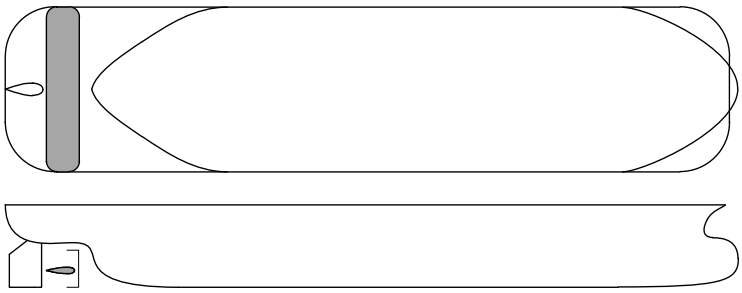

Figure III.2.1-2 Initial sketch of a vessel equipped with a flapping wing propulsor

For reasons of redundancy, support of the wings, motion and thrust transmission, but also for covering the need for larger rudder area, the proposed design of two independent wings supported by three struts equipped with flaps is presented in Figure III.2.1-3. The detailed design of the internal mechanism, is beyond the purposes of this thesis, but it can be assumed to follow the same principles as most existing patents for oscillating wings (i.e. O-Foil^{TM}).

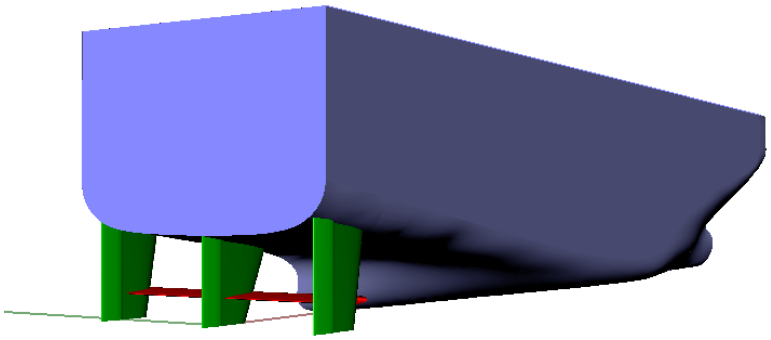

Figure III.2.1-3 Stern view of a ship equipped with a system of two wings, including supports-rudders.

III.2.2 Theoretical formulation and solution of the flapping wing propulsor design problem.

Propulsor design problem consists in finding the propulsor geometric and motion characteristics by which it can propel a given ship with a given ship speed. Among all possible design solutions, satisfying the constraint of a given ship speed; there is an optimum, which requires a minimum delivered power. Although the optimum propulsor problem is a problem of mutual propulsor/stern optimization, in most cases, the propulsor is optimized with the assumption of a given hull/stern geometry.

From the dimensional analysis of the problem, the following relations have been deducted, for the open water performance of a flapping wing propulsor:

$$C_T = \frac{T}{0.5\rho U^2 S} = C_T(\theta_0, Str, s/c, h_0/c, b/c,) \quad \text{(III.47)}$$

$$C_P = \frac{DHP}{0.5\rho U^3 S} = C_P(\theta_0, Str, s/c, h_0/c, b/c) \quad \text{(III.48)}$$

In self-propulsion conditions, a Taylor wake fraction w is assumed and defined by:

$$U = V(1-w) \quad \text{(III.49)}$$

where V is the ship's speed. Furthermore a relative rotative efficiency η_R and a shaft efficiency η_s are defined by:

$$\eta_R = \frac{DHP}{DHP_B}, \eta_s = \frac{DHP_B}{SHP} \quad \text{(III.50)}$$

where DHP_B denotes the (period-mean) power delivered to the flapping wing in self-propulsion conditions and SHP denotes the (period-mean) shaft horse power. Let t denote the thrust deduction factor: $R_0 = R_B(1-t)$ with R_0 denoting the hull towing resistance and R_B the resistance with the flapping wing in operation or 'behind resistance'. Assuming that a 'thrust equalization method' has been used for the determination of propulsor-hull interaction coefficients w, t, η_R, the flapping wing (mean) thrust and shaft power, in the self-propulsion conditions becomes:

$$T_B = T = 0.5\rho(V(1-w))^2 S \cdot C_T(\theta_0, \frac{n \cdot 2h_0}{V(1-w)}, \frac{s}{c}, \frac{h_0}{c}, \frac{b}{c}) \quad \text{(III.51)}$$

$$SHP \cdot \eta_R \cdot \eta_s = 0.5\rho(V(1-w))^3 S \cdot C_P(\theta_0, \frac{n \cdot 2h_0}{V(1-w)}, \frac{s}{c}, \frac{h_0}{c}, \frac{b}{c}) \quad \text{(III.52)}$$

For a self-propelled ship, moving with velocity V, the surrounding fluid interacts with the hull developing a resistance force: $R_B(V) = R_0(V)/(1-t)$. A hull can also pull an object with a force F (case of a tug-boat or a trawler). Then the thrust, under self-propulsion conditions, is given by:

$$T_B(V) = \frac{R_0(V)}{1-t(V)} + F(V) \qquad \text{(III.53)}$$

Assuming that $V, \theta_0, c, s, h_0, b, w, t, \eta_R$ are known parameters, equations (III.51), (III.52) and (III.53) become a non-linear system of three algebraic equations with three unknowns: (T, SHP, n). This system can be solved for a range of ship speeds: $V \in (V_1, V_2)$ and pitch angles: $\theta_0 \in (\theta_{0a}, \theta_{0b})$. Thus, the totality of design solutions for the given ship is obtained:

$$SHP(V,\theta_0), n(V,\theta_0) \leftarrow \left| given: \text{ ship}, c, s, h_0, w, t, \eta_R \right. \qquad \text{(III.54)}$$

The content of Equation (III.54) can be represented in a 2-D $SHP - n$ diagram in the form of parametric curves of constant V and constant θ_0. Notice that this presentation is similar to that used in conventional propellers, where the propeller pitch ratio P/D is taking the place of θ_0. Using this presentation of results, the required optimum flapping wing propulsor can be found by selecting the characteristics (geometric and motion) which require the minimum SHP for the given ship speed V.

III.2.2.1 Choices on the presentation layout of results

In order to arrive at the charts in the form they are produced and presented, a trial of alternative ways of presentation is necessary for the determination of the fittest. In this attempt, alternative definitions and representation schemes were tested.

The traditional (i.e. mostly used in literature so far) nondimensional factors are defied as:

$$C_T = \frac{T}{0.5\rho U^2 S} = C_T(\theta_0, St, R/c, h_0/c, b/c) \quad \text{and}$$

$$C_P = \frac{DHP}{0.5\rho U^3 S} = C_P(\theta_0, St, R/c, h_0/c, b/c)$$

Alternatively, the following can be also used:

$$K_T = \frac{T}{0.5\rho f^2 A^2 S} = K_T(\theta_0, St, R/c, h_0/c, b/c)$$

and

$$K_P = \frac{DHP}{0.5\rho f^3 A^3 S} = K_P(\theta_0, St, R/c, h_0/c, b/c)$$

The difference is that on the one case the speed is used for nondimensionalization, while on the other, it is the frequency times amplitude, as done with conventional marine propulsors. Eventually, the traditional ones (C_T, C_P).

The following alternative ways to present the data of a series were tested:

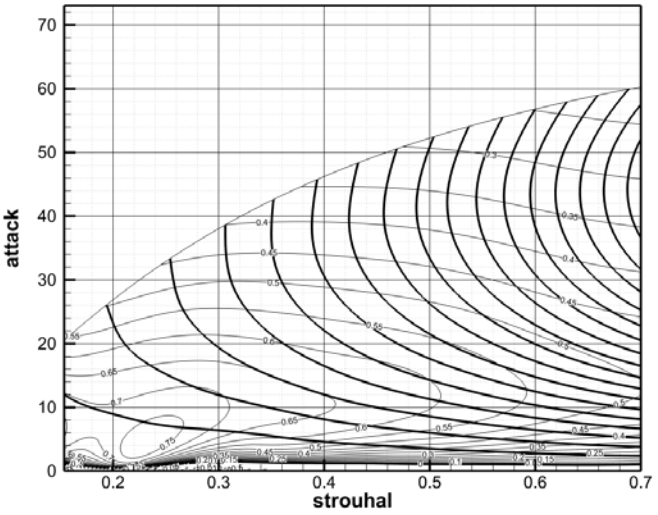

Figure III.2.2-1 "Traditional" Presentation as done in literature till present work (Triantafyllou 1996-2007). Thin line contours are for efficiency and thick ones, are for Thrust Coefficient C_T

In Figure III.2.2-1 the results are presented by defining the axes as Strouhal number and the maximum angle of attack (of the undisturbed flow). The contours are for the efficiency and the thrust coefficient. This type of presentation was introduced in the works of Prof. M. Triantafyllou and his colleagues (Triantafyllou, Triantafyllou et al. 1991). Even though these charts are clear and concise, issues arise on the definition of motion parameters for each case.

Alternative presentations are shown in Figure III.2.2-2,Figure III.2.2-3 and Figure III.2.2-4 . The use of C_T for the vertical axis and use of either the Strouhal number or the advance coefficient ($J = \frac{1}{Str}$), also present practical issues, especially with clarity and readability of charts for Small Strouhal number or large advance coefficient.

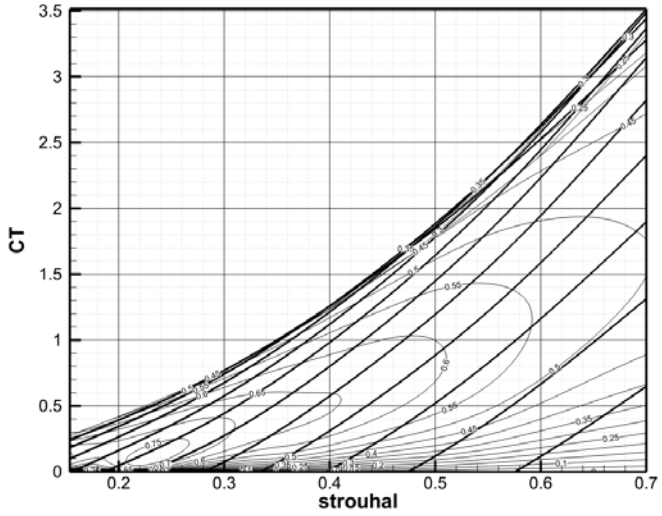

Figure III.2.2-2 Alternative presentation. Thin contour lines are for the efficiency and thick ones for the Maximum Pitching Angle.

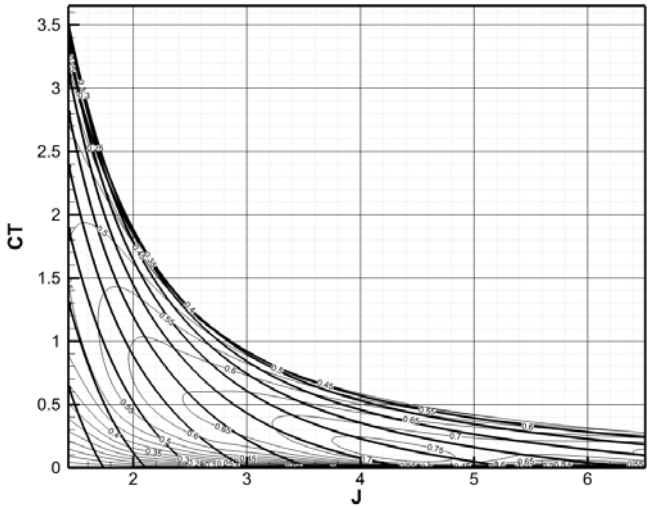

Figure III.2.2-3 Alternative presentation. Thin contour lines are for the efficiency and thick ones for the Maximum Pitching Angle.

In Figure III.2.2-4 a chart employing the use of K_T (as defined above) is presented. The chart is clear and readable, but the ease of use for design problems is not as good as for the final (and preferred) alternative of presentation

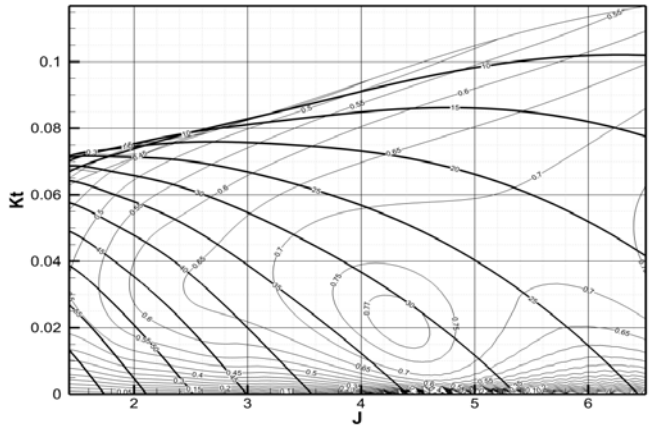

Figure III.2.2-4 Alternative presentation. Thin contour lines are for the efficiency and thick ones for the Maximum Pitching Angle.

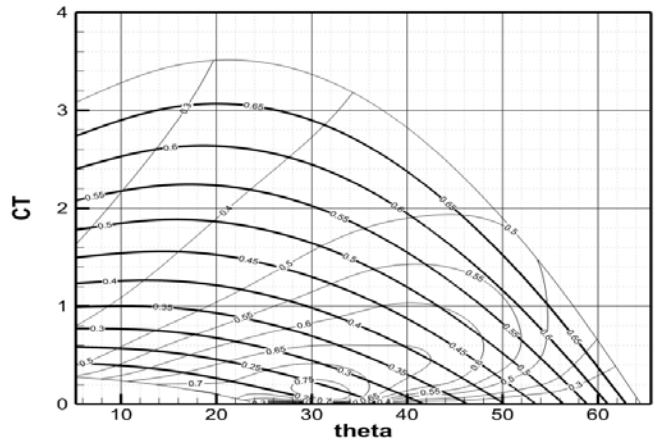

Figure III.2.2-5 Final Chosen Alternative Presentation. Thin contour lines are for Efficiency and thick ones are for Strouhal Number

III.2.2.2 Use of charts for the design of a biomimetic propulsor

Before closing this section a brief description is given, regarding how the charts can be used to select an optimum flapping wing propulsor for a given ship, using a hand calculator. Assume that a ship is given with a design speed of V knots. Assume further that a biomimetic wing with given $s/c=6, h_0/c=1.0, b/c=0.33, \psi=90^0$ has been selected. The problem of optimum (i.e. minimum SHP) selection of θ_0 and corresponding revolutions can be solved as follows: (a) with the design speed known and the corresponding ship resistance, the propeller thrust, equation (III.53), and C_T can be calculated; (b) with this C_T draw a horizontal line as on Figure III.2.2-6,a and find the intersection of this horizontal line with the various constant Strouhal lines, let $(\theta_0, Str)_i, i=1, n_{str}$ denote the n_{str} intersection points; (c) from each Strouhal number the frequency of the propulsor motion can be found: $n_i = Str_i \cdot V/(2\cdot h_0)$; (d) use Figure III.2.2-6,b to find $C_{P,i}$ for the known points $(\theta_0, Str)_i, i=1, n_{str}$, from the $C_{P,i}$ find the required open water power DHP and use equations (III.50) to find SHP_i; (e) from the calculated $SHP_{i,i=1,n_{str}}$ select that with minimum required SHP.

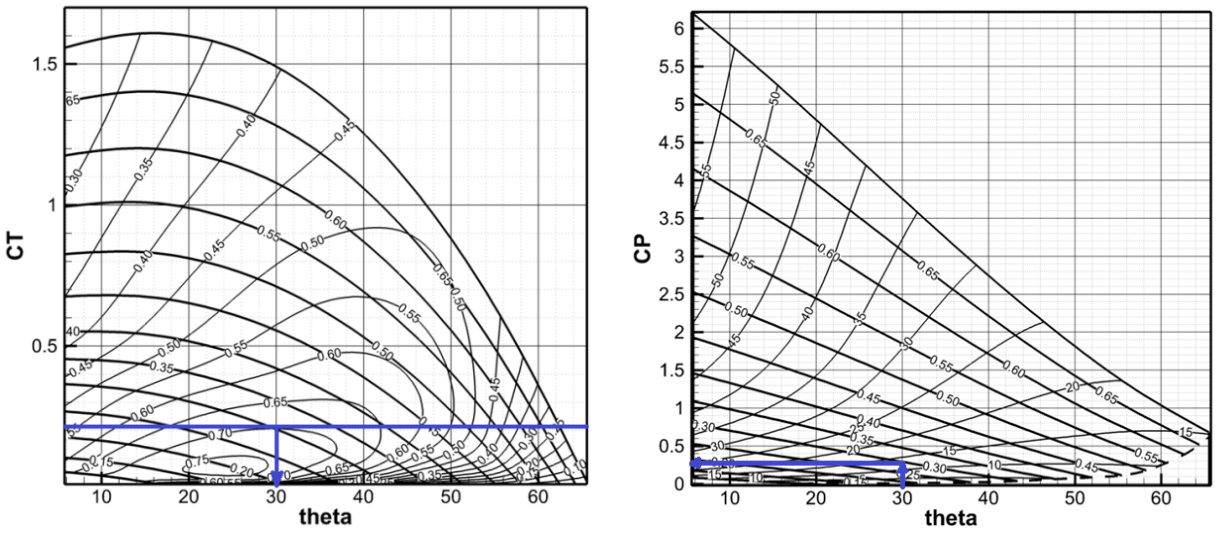

Figure III.2.2-6a,b. Application example, using $s/c=6, h_0/c=1.0, b/c=0.33, \psi=90^0$

III.2.3 Design applications

A large tanker, a passenger/car ferry and a speed boat are used in a feasibility study for the application of a Biomimetic Propulsor as an alternative to traditional propellers. The main characteristics of the ships are shown in Table III.2.3-1. More specifically the passenger/car ferry and a speed boat are based on prototypes taken from NTUA towing tank data base and the tanker has as prototype an AFRAMAX class tanker. In all cases a properly redesigned stern is assumed, capable of carrying one or more non-interacting biomimetic propulsors (non-interacting serial configuration). Having in mind the hydrodynamic behavior of a flapping wing system, maximization of both efficiency and corresponding thrust requires the maximization of the propulsor swept area. Furthermore, the designer should have in mind that maximization of either of $(h_0/c)_{des}$, $(s/c)_{des}$ results in better efficiency. Sizing of the flapping wing propulsor system for a given ship stern starts by inspecting the ratio of breadth to permitted vertical path $2h_0$ which in turn is a modulated by the design stern draft, taking into account propulsor-hull clearances and ventilation at dynamic conditions. For the considered cases it is assumed that the propeller diameter of the selected ships, is indicative of $2h_0$ (i.e. $2h_0 \approx D$), which results in a ratio of breadth to the permitted vertical path in the range $4.66 \div 5.00$. Thus two horizontal flapping wings (use: $\frac{s}{2h_0} = \frac{s/c}{2(h_0/c)}$ with: $s/c = 6, h_0/c = 1.5$, it is obvious that a large s/c, at given h_0/c, provides better efficiency) can be accommodated for all cases, with design particulars shown in table 3. The position of the pitch axis $(b/c)_{des}$ has been selected equal to 0.33 in all cases, since this selection results in slightly better efficiencies with corresponding reduction of the pitching moment required to adjust the pitch angle. Notice the relative merit of the flapping wing geometry in comparison to a conventional propeller. More specifically the former can better be adjusted to the stern area, allowing lower thrust loading coefficients and thus larger efficiencies for the same total thrust. In a real situation strength and vibration/noise issues have to be added to the previous optimum hydrodynamic efficiency criteria. In this respect the span to chord and the thickness to chord ratios of the wing has to be decided by using both hydrodynamic and structural considerations.

For comparison purposes, twin screw vessels have been selected for all cases. For the case of the large tanker, this selection results in a ship with propulsive efficiency much better than that of the corresponding single-screw. These paradigm ships are virtual and idealized, since its optimum propeller revolutions are outside the range (lower) of all existing marine engines but simulate the best possible performance a conventional system could produce. Thus presented comparisons of propulsive efficiency, underestimate the real efficiency gains.

The ship bare hull towing resistance data $R_0(V)$ are shown in Table III.2.3-2. They have been taken either from the database of the NTUA towing tank (ships no 2, 3) or calculated using systematic series (Holtrop method for ship no 1). With the bare hull resistance given, the nonlinear system of algebraic equations (III.51), (III.52) and (III.53) can be solved for a range of ship speeds V and pitch angles θ_0 and the totality of design solutions can be presented in a diagram, as dictated by Equation (III.54). For comparison purposes, it has been assumed that

in all cases (i.e. all ship types and either flapping-wing or propeller as propulsor): $w = 0.0, t = 0.0, \eta_R = 1.0, \eta_s = 1.0$. This is a reasonable assumption for twin screw vessels, which have small propulsor-hull interactions. Furthermore, the use of the same hull-interaction coefficients for the flapping-wing and the propeller can be considered with care, since interaction coefficients are (for the same stern geometry) mainly functions of propulsor diameter and the developed thrust, Harvald (1983) no inclined axis corrections were made for the conventional propellers. No correction of the bare hull resistance has been made for appendages. No corrections for full scale Reynolds number have been introduced for either type of propulsors.

It should be clarified, that hull propulsion interaction has been assumed negligible only for the sake of making a paradigm and due to the lack of any self propulsion experimental data, as also assumed by Yamaguchi and Bose (1994). Final conclusions on the actual performance of a ship operating with biomimetic propulsors, can only be made after the actual (experimentally determined) hull interaction factors (w, t, n_R) have been used.

Table III.2.3-1. Ship and propulsor particulars.

Ship no:	**1**	**2**	**3**
Ship Type:	**Large Tanker**	**Passenger/car ferry**	**Speedboat**
Propeller diameter $D(m)$	**9.00**	**4.10**	**1.40**
Stern Breadth $B(m)$	**42.**	**20.**	**7.**
Number of propulsors	**2**	**2**	**2**
$(s/c)_{des}$	**6**	**6**	**6**
$(h_0/c)_{des}$	**1.5**	**1.5**	**1.5**
$c_{des}(m)$	**3.00**	**1.37**	**0.47**
$s_{des}(m)$	**18.00**	**8.20**	**2.80**

Table III.2.3-2 Resistance curves of ships

Ship	1		2		3	
	$V(m/s)$	$R_0(kp)$	$V(m/s)$	$R_0(kp)$	$V(m/s)$	$R_0(kp)$
	4.11	30763	7.20	29055	9.25	9204
	4.63	38445	7.71	31056	10.27	10471
	5.14	46935	8.23	34528	11.32	11519
	5.66	56225	8.75	38374	11.83	11962
	6.17	66309	9.26	42755	12.35	12367
	6.69	77185	9.78	47292	12.87	12697
	7.20	88851	10.29	52301	13.38	13084
	7.72	101308	10.80	58153	13.88	13477
	8.23	114560	11.31	66426	14.40	13872
			11.83	78009	14.92	14306

III.2.3.1 Single wing

The totality of design solutions $SHP(V,\theta_0), n(V,\theta_0)$ (optimum and non-optimum) for the three vessels equipped with flapping-wings can be found in Figure III.2.3-1, Figure III.2.3-3 and Figure III.2.3-5 (where N in the horizontal axis denotes frequency in rounds per minute and SHP in the vertical axis denotes the total power in PS from both propulsors). The corresponding results $SHP(V,P/D), n(V,P/D)$ (where P/D denotes propeller pitch ratio) for the same ships equipped with B4-75 conventional propellers, Oosterveld & Oossannen (1975), can be found in Figure III.2.3-5, Figure III.2.3-2, Figure III.2.3-4, Figure III.2.3-6. On all the figures, the constant-velocity curves and the constant maximum pitch angle θ_0 curves or the constant P/D curves are shown and labeled accordingly. B-series results show that the optimum pitch ratio $P/D\big|_{opt}$ is greater than the maximum allowed by the systematic series, i.e. it is succeeded for a $P/D>1.4$. Since the constant velocity curves are relatively flat for $P/D>1.4$ the $P/D=1.4$ is considered to be representing the optimum point in a satisfactory manner.

Comparative propulsive performance, for the three ship types equipped with the different propulsion systems, is summarized in Table 5. In all cases the flapping wing shows superior efficiencies compared to that of the corresponding B-screw. More specifically gains in propulsive efficiency PC ($PC \overset{def}{=} R_0 \cdot V / SHP$) of the order of 5.49%, 3.99% and 4.72% over the B-screw are observed. The maximum improvement in propulsive efficiency is observed for the tanker (5.49%). It is also noticeable, that the optimum flapping wing revolutions are always significantly lower compared to that of a corresponding conventional optimum

propeller. This makes flapping wing propulsors friendlier to the environment with respect to aquatic animal life. Concluding, it should be stressed that the absolute values of power and overall efficiency, contained in Table III.2.3-3, are approximate to the extent of the uncertainty regarding values of full Reynolds scale effect and propulsor–hull interaction factors.

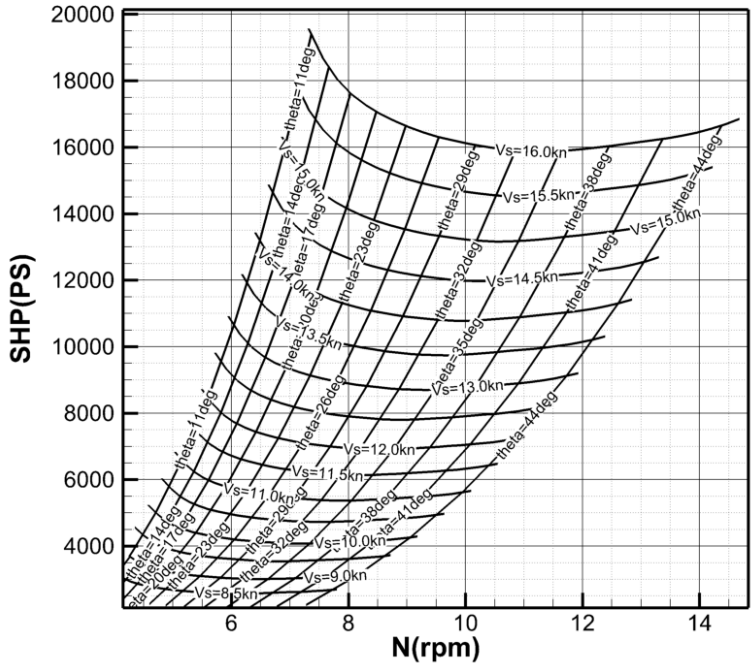

Figure III.2.3-1 Tanker (ship 1). Totality of design solutions in the form of Constant-V, constant-θ_0 grid. Flapping wing propulsor with: $(s/c)_{des}=6,(h_0/c)_{des}=1.5,(b/c)_{des}=0.33$.

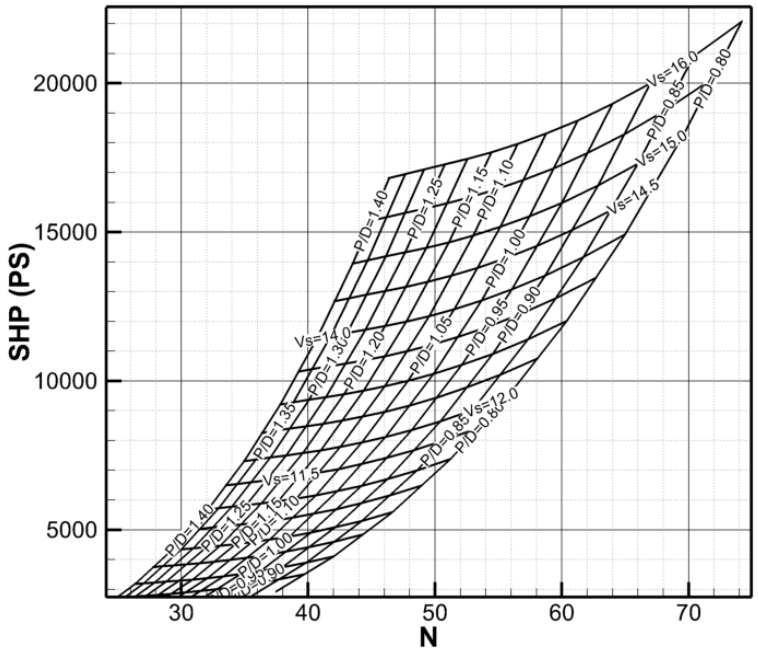

Figure III.2.3-2 Tanker (ship 1). Totality of design solutions in the form of Constant-V, constant-P/D grid, for B4.75 screw.

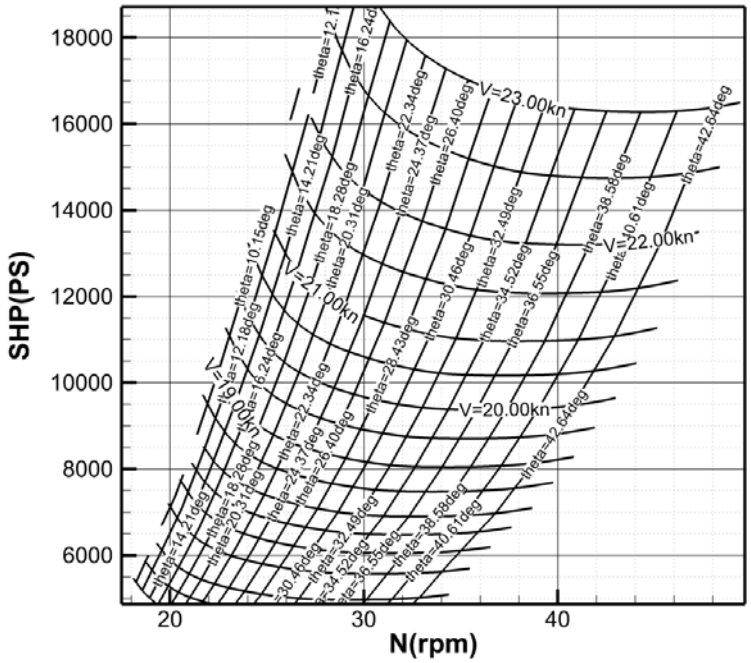

Figure III.2.3-3 Passenger Ferry (ship 2). Totality of design solutions in the form of Constant-V, constant-θ_0 grid. Flapping wing propulsor with: $(s/c)_{des} = 6, (h_0/c)_{des} = 1.5, (b/c)_{des} = 0.33$

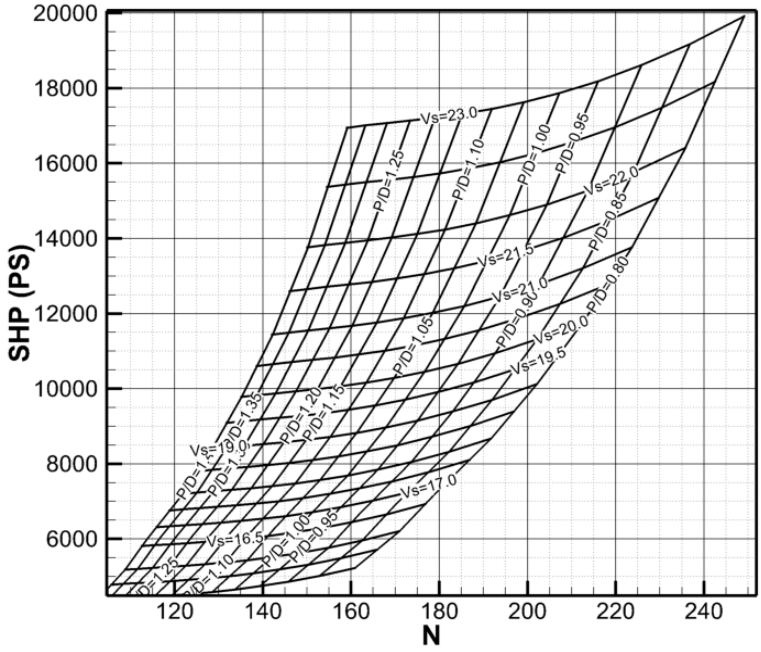

Figure III.2.3-4 Passenger Ferry (ship 2). Totality of design solutions in the form of Constant-V, constant-P/D grid, for B4.75 screw.

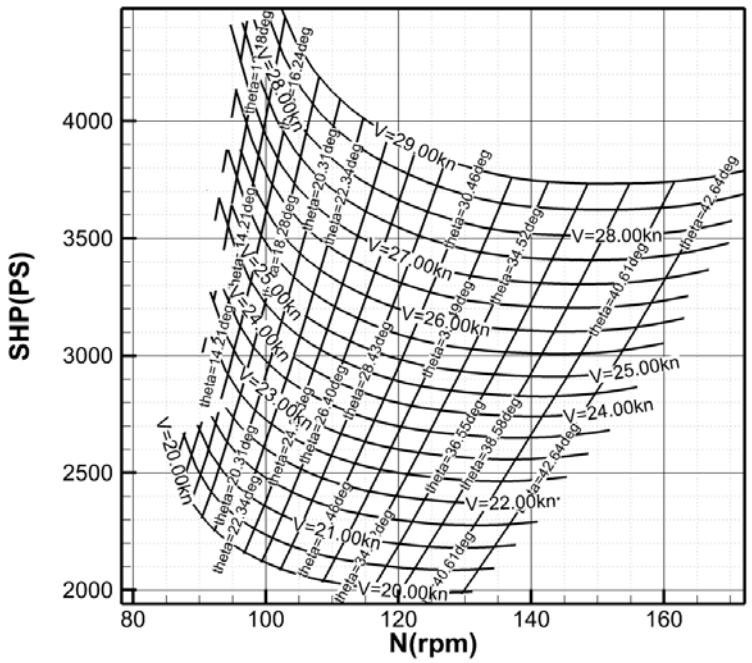

Figure III.2.3-5 Speedboat (ship 3). Passenger Ferry (ship 2). Totality of design solutions in the form of Constant-V, constant-θ_0 grid. Flapping wing propulsor with:

$$(s/c)_{des} = 6, (h_0/c)_{des} = 1.5, (b/c)_{des} = 0.33$$

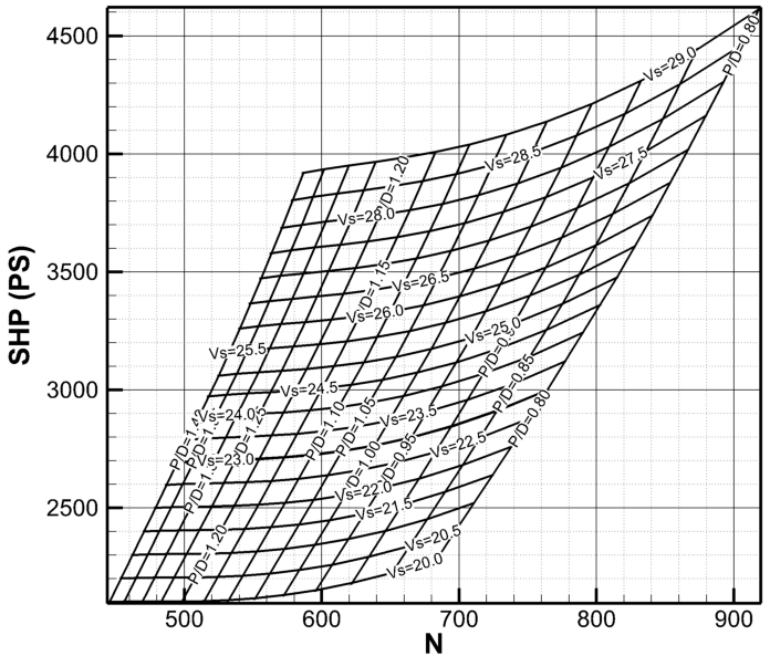

Figure III.2.3-6 Speedboat (ship 3). Totality of design solutions in the form of Constant-V, constant-P/D grid, for B4.75 screw.

Table III.2.3-3 Comparison of propulsors.

Ship	Design speed (kn)	Case	Revolutions (rpm)	Power (PS)	Propulsive Efficiency (%)	Power Gain (%)
1	16	$s/c=6$, $h_0/c=1.5$ ($C_T=0.126$)	11.49	15879.84	79.2	5.49
		B-screw	46.20	16803.60	74.8	
2	23	$s/c=6$, $h_0/c=1.5$ ($C_T=0.158$)	43.23	16289.72	75.5	3.99
		B-screw	158.80	16966.40	72.5	
3	29	$s/c=6$, $h_0/c=1.5$ ($C_T=0.146$)	154.26	3734.69	76.2	4.72
		B-screw	585.10	3919.60	72.6	

It can be said that the comparisons may be unfair against the conventional propellers, as the swept area of the Wing systems is far greater. Thus in an attempt to "help" the propellers, the expanded area ratio was reduced to the minimum A_E/A_o=0.55, in order to get the best possible efficiency. This leads to Figure III.2.3-7, Figure III.2.3-8 and Figure III.2.3-9 for the Iso-V / Iso-P/D charts and the comparison table for the optimal points is Table III.2.3-4

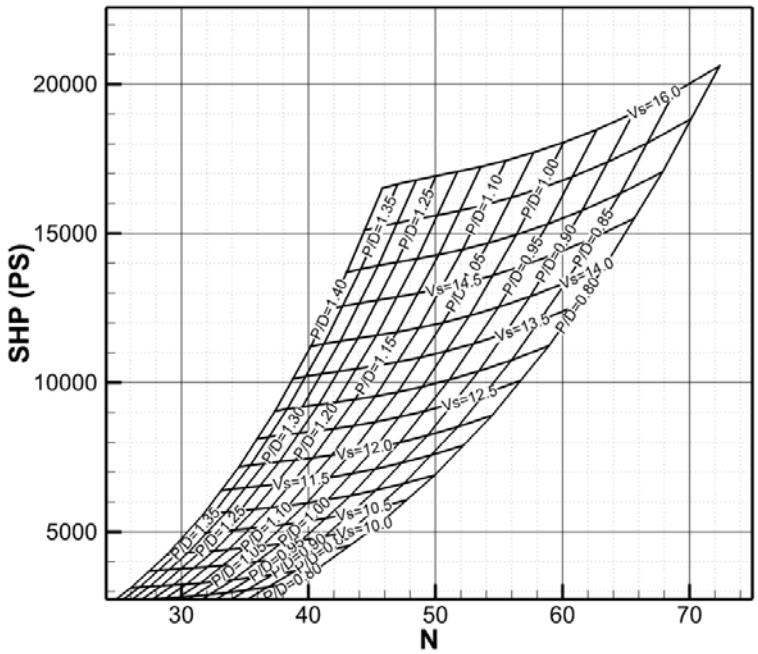

Figure III.2.3-7 Tanker (ship 1). Totality of design solutions in the form of Constant-V, constant-P/D grid, for B-4.55

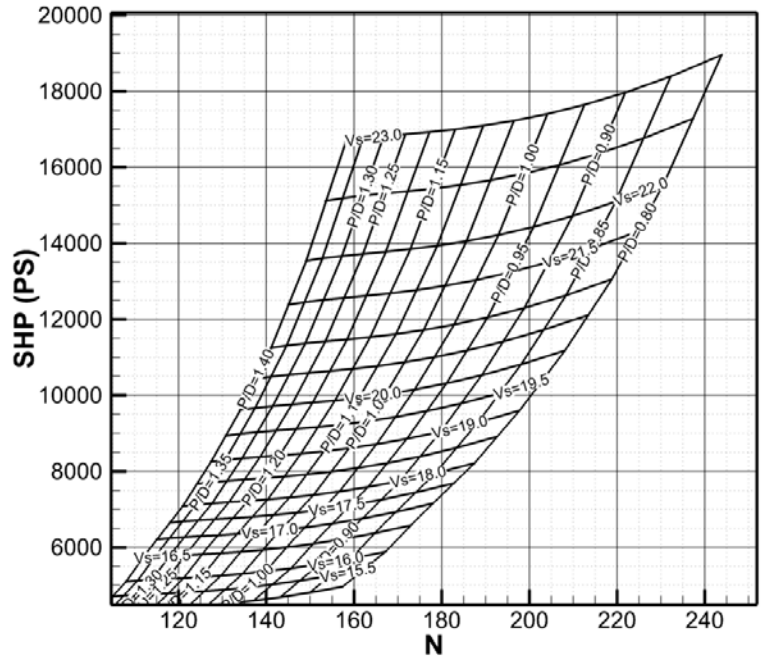

Figure III.2.3-8 Passenger Ferry (ship 2). Totality of design solutions in the form of Constant-V, constant-P/D grid, for B-4.55

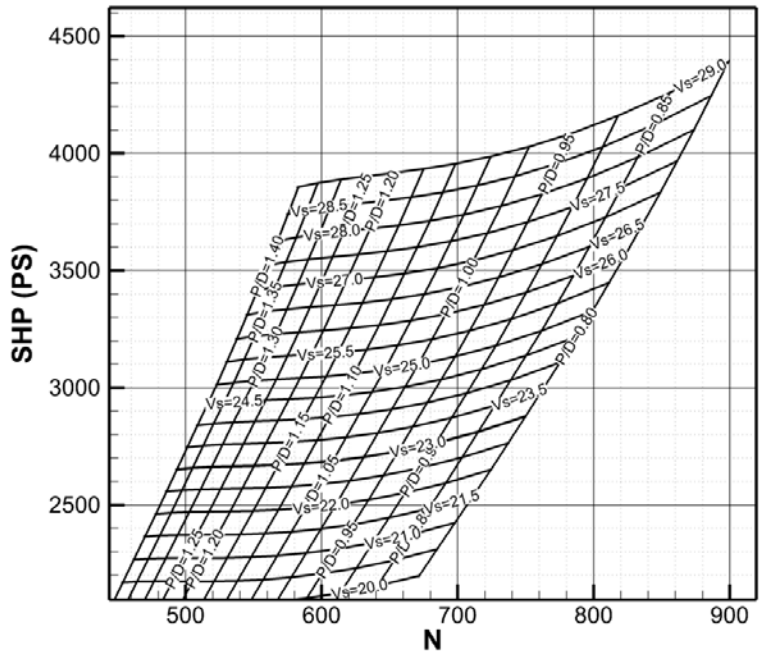

Figure III.2.3-9 Speedboat (ship 3). Totality of design solutions in the form of Constant-V, constant-P/D grid, for B-4.55

Table III.2.3-4 Overall comparison of propulsors.

Ship	Design speed (kn)	Case	Revolutions (rpm)	Power (PS)	Propulsive Efficiency (%)	Power Gain (%)
1	16	$s/c=6$, $h_0/c=1.5$ ($C_T=0.1$)	11.49	15879.84	79.2	3.76
		B-4.55	45.70	16500.40	76.2	
2	23	$s/c=6$, $h_0/c=1.5$ ($C_T=0.158$)	43.23	16289.72	75.5	2.38
		B-4.55	157.80	16687.00	73.7	
3	29	$s/c=6$, $h_0/c=1.5$ ($C_T=0.157$)	154.26	3734.69	76.2	3.11
		B-4.55	581.40	3854.80	73.8	

In cases 2 and 3 there is a high possibility for cavitation (especially 3, due to speed and high revolutions).

Additionally, on the matter of hullform, if a hull designed as in Bose (2008) (figure 11-9 (page 139) or similar to it is assumed, there is no serious difference to a podded ship. Especially if podded propulsion is assumed, minimal hull interaction is justified and comparison is more logical. The case of the tanker is considered unrealistic, due to the very large propeller and it is advantageous to the propeller. If the fact that b-series results are considered to be very optimistic compared to actual (off the shelf) propellers, is also taken into account, the expected gain for the flapping wing is even greater.

As far as the several uncertainties are concerned, grid independence tests have been made to all cases and since there is agreement with experimental results for small angles of attack, it is safe to deduce that the prediction is safe for the application cases as well. Hull interaction has not been determined, as there has been no self-propulsion test, but if the wing is at the AP, it can be expected that the wake of the wing will have minimal interaction with the hull.

III.2.3.2 Double wing

The case of a double (twin) wing propulsor is applied on the passenger ferry vessel (ship 2)in the same manner as in previous applications.

With the bare hull resistance given, the system of algebraic equations (III.51), (III.52) and (III.53) can be solved for a range of ship speeds V and θ_0 and the totality of design solutions can be presented in a diagram as dictated by Equation (III.54). For the need of the comparison, it has been assumed that in all cases: $w = 0.0, t = 0.0, \eta_R = 1.0$. This is a reasonable assumption for a twin screw vessel which has small propulsor-hull interactions. The use of the same hull-interaction coefficients for the flapping wing systems and the propeller can be considered reasonable since interaction coefficients are (for the same stern geometry) mainly functions of propulsor diameter and the developed thrust, Harvald (1983). No inclined axis corrections were made for the conventional propellers. No correction of the bare hull resistance for appendages has been made. A shaft efficiency equal to 1 has been used in the calculations. No corrections for full scale Reynolds number have been introduced for the propulsors.

Totality of design solutions in the form of Constant-V, constant-θ_0 grids for flapping wings and Constant-V, constant-P/D grids for propellers are illustrated for comparison in figures 14,15 and 16. The comparison of the optimum flapping wings (twin, single) vs. the optimum B-screw, for a ship speed equal to 23knots can be summarized in Table III.2.3-5.

Table III.2.3-5 Comparison of propulsors.

Case	Revolutions (rpm)	Power (PS)	Propulsive Efficiency (%)	Power Gain (%)
twin	64.97	16056.29	77	6.12
single	43.23	16289.72	75	4.75
B-screw	168.30	17103.40	72	

It is observed that a gain in propulsive efficiency of 4.75% is obtained for the case of a single biomimetic wing in comparison to a conventional propeller. The corresponding gain for a twin wing configuration is 6.12%. It is also noticeable, that the optimum flapping wing revolutions are always lower compared to that of corresponding conventional optimum propeller. It should be stretched that the absolute values of power and overall efficiency, contained in Table III.2.3-5, are approximate to the extent of our uncertainty regarding values of propulsor-

hull interaction factors. For the comparison between the single and twin wing, it is visible that the aforementioned small differences, has led to solutions with higher Strouhal numbers, meaning higher frequencies, but also an additional improvement in efficiency.

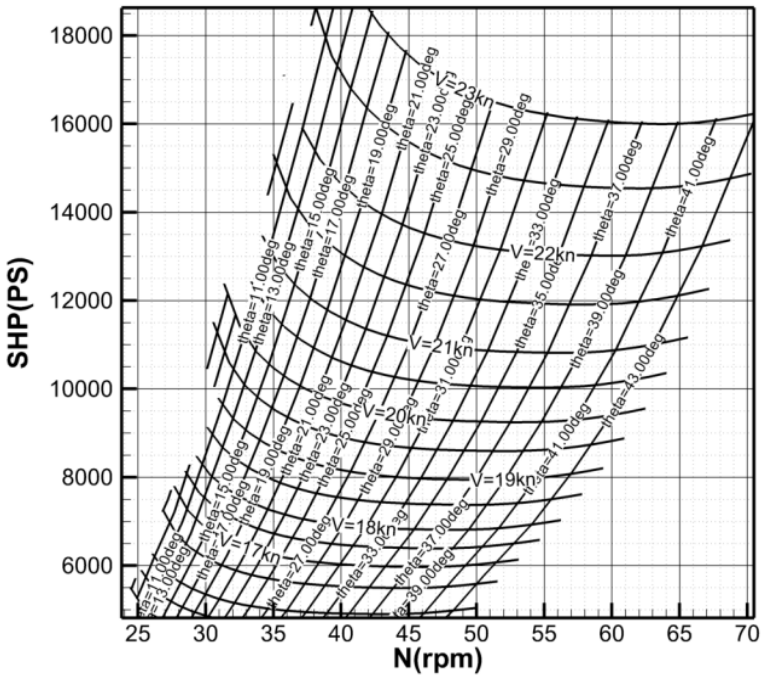

Figure III.2.3-10 Passenger Ferry-Twin wing: Totality of design solutions in the form of Constant-V, constant-θ_0 grid.

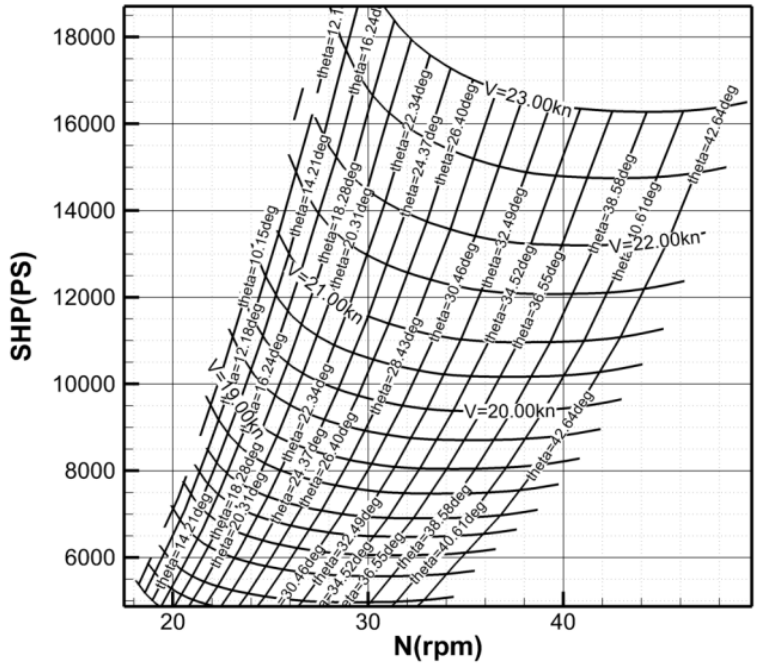

Figure III.2.3-11 Passenger Ferry-Single wing: Totality of design solutions in the form of Constant-V, constant-θ_0 grid.

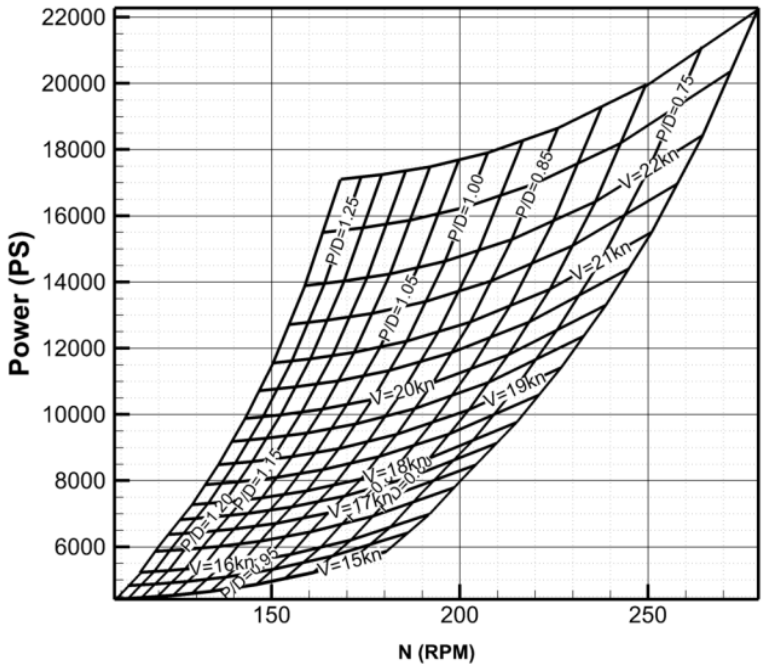

Figure III.2.3-12 Passenger Ferry- B4.75 screw: Totality of design solutions in the form of Constant-V, constant-P/D grid.

III.2.3.3 FOD

Three different vessels are used in a feasibility study for the application of a FOD as an alternative propulsor to traditional propellers. The main characteristics of the ships are shown in Table III.2.3-6 (D is the selected mean FOD diameter or the propeller diameter). The ship bare hull resistance data was taken from the database of the NTUA towing tank and are shown in Table III.2.3-7. With the bare hull resistance given, the system of algebraic equations (III.51), (III.52) and (III.53) can be solved for a range of ship speeds V and θ_0 and the totality of design solutions can be presented in a diagram as dictated by Equation (III.54). For the need of the comparison, it has been assumed that in all cases: $w = 0.0, t = 0.0, \eta_R = 1.0$. This is a reasonable assumption only for the two twin screw vessels which have small propulsor-hull interactions. For the single screw ship, this selection is sound solely for comparative purposes with the conventional propeller. The use of the same hull-interaction coefficients for the FOD and the propeller can be considered reasonable since interaction coefficients are (for the same stern geometry) mainly functions of propulsor diameter and the developed thrust, Harvald (1983). No inclined axis corrections were made for the conventional propellers. No correction of the bare hull resistance for appendages has been made. A shaft efficiency equal to 1 has been used in the calculations. No corrections for full scale Reynolds number have been introduced for either the FOD or the B-series propellers.

Table III.2.3-6 Ship particulars

Ship no:	**1**	**2**	**3**
type	**Bulk carrier**	**Passenger/car ferry**	**Speedboat**
Propulsor diameter (m)	**8.10**	**4.10**	**1.40**
Displacement (tons)	**37288.9**	**8917.66**	**160**
Number of propulsors	**1**	**2**	**2**

Table III.2.3-7 Resistance curves of ships

Ship	1		2		3	
V-R curve	V (m/s)	R(kp)	V (m/s)	R(kp)	V (m/s)	R(kp)
	3.05	09877	7.20	29055	9.25	09204
	3.56	14191	7.71	31056	10.27	10471
	4.06	18496	8.23	34528	11.32	11519
	4.58	23029	8.75	38374	11.83	11962
	5.08	27463	9.26	42755	12.35	12367
	5.59	34212	9.78	47292	12.87	12697
	6.10	40134	10.29	52301	13.38	13084
	6.61	48142	10.80	58153	13.88	13477
	7.12	61364	11.31	66426	14.40	13872
	7.63	75358	11.83	78009	14.92	14306

The totality of design solutions DHP-N (optimum and non-optimum) for the three vessels equipped with a Case 4-FOD can be found in Figure III.2.3-13, Figure III.2.3-15 and Figure III.2.3-17. Similarly, the totality of design solutions DHP-N (optimum and non-optimum) for the same ships equipped with B5-70 conventional propellers (Oosterveld & Oossannen 1975), can be found in Figure III.2.3-14, Figure III.2.3-16 and Figure III.2.3-18. On the figures, the constant-velocity curves and the constant maximum pitch angle θ_0 curves or the constant P/D curves are shown and labeled accordingly.

The comparisons of the optimum FOD over the optimum B-screw for the three ship types at corresponding selected design speeds can be summarized in Table III.2.3-8. In all cases the FOD shows efficiencies of the order of 80% and the gain compared to the B-screw, ranges from 9.81% to 13.21%. It is also noticeable, that the optimum FOD revolutions are always lower compared to that of corresponding conventional optimum propeller. For illustrative reasons, Figure III.2.3-17 includes propulsive efficiency contours shown with dashed lines. It should be stretched that the absolute values of power and overall efficiency, contained in table 5, are approximate to the extent of our uncertainty regarding values of propulsor-hull interaction factors.

Table III.2.3-8 Overall comparison of propulsors

Ship	speed (kn)	Case	Revolutions (rpm)	Power (PS)	Overall Efficiency (%)	Power Gain (%)
1	15	FOD ($CT = 0.480$)	29.6	9650	79.4	9.81
		B-screw	47.0	10700	71.6	
2	23	FOD ($CT = 0.403$)	87.5	7550	81.4	13.21
		B-screw	145.0	8700	70.7	
3	29	FOD($CT = 0.401$)	305.0	1735	82.0	10.70
		B-screw	552.0	1943	73.2	

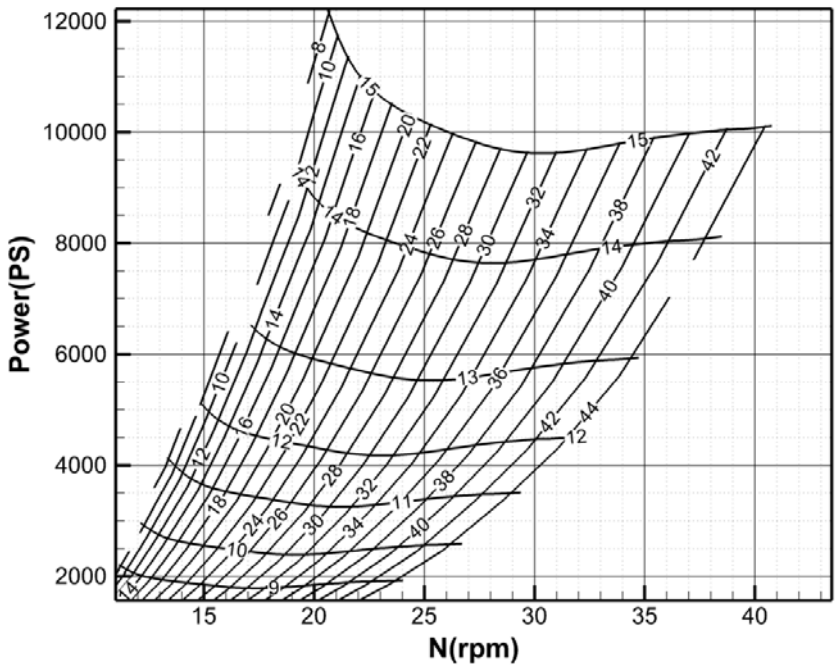

Figure III.2.3-13 Bulk Carrier (ship 1) – FOD: Totality of design solutions in the form of Constant-V, constant-θ_0 grid.

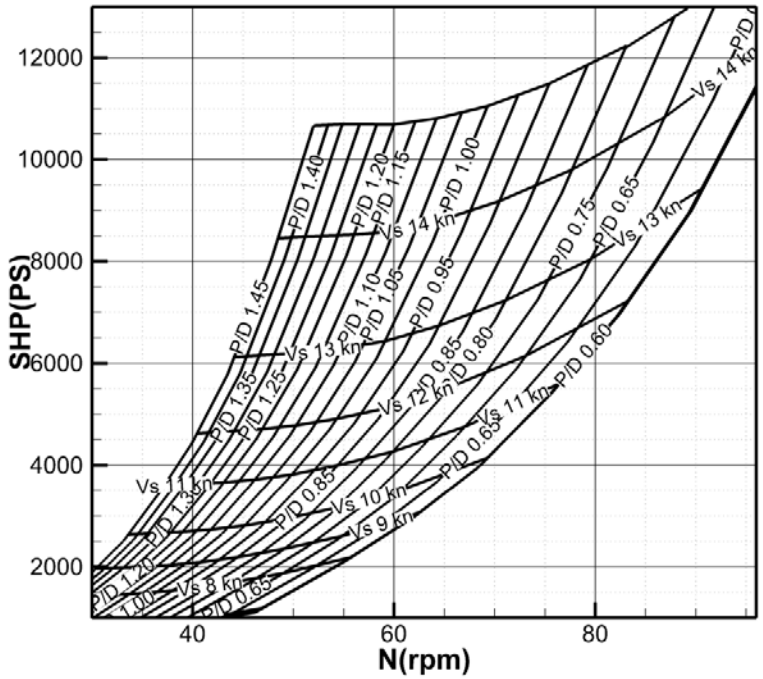

Figure III.2.3-14. Bulk Carrier (ship 1)-B5.70 screw: Totality of design solutions in the form of Constant-V, constant-P/D grid.

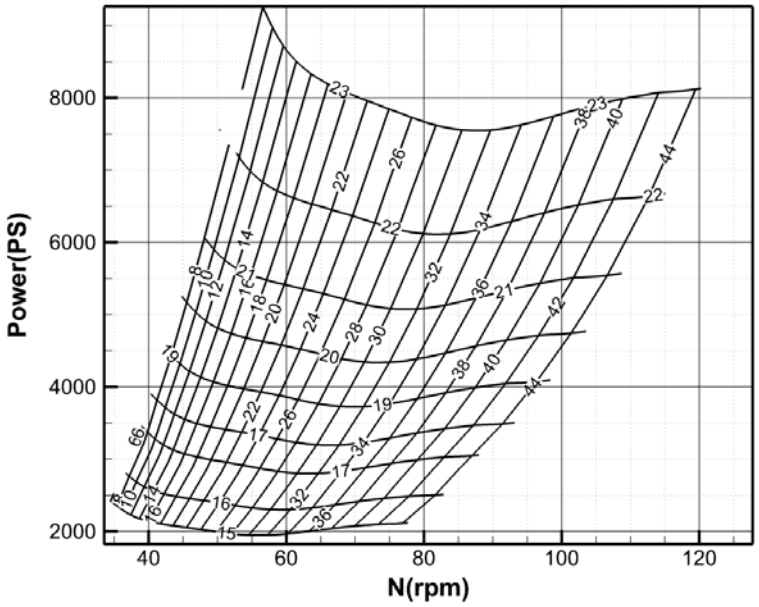

Figure III.2.3-15. Passenger Ferry (ship 2)-FOD: Totality of design solutions in the form of Constant-V, constant-θ_0 grid.

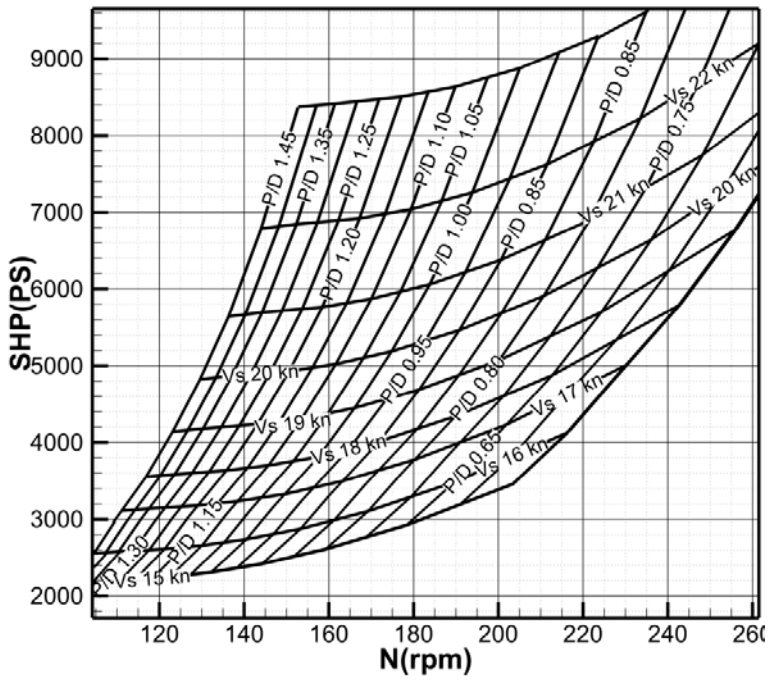

Figure III.2.3-16. Passenger Ferry (ship 2)- B5.70 screw: Totality of design solutions in the form of Constant-V, constant-P/D grid. Results for one of the two propulsor units.

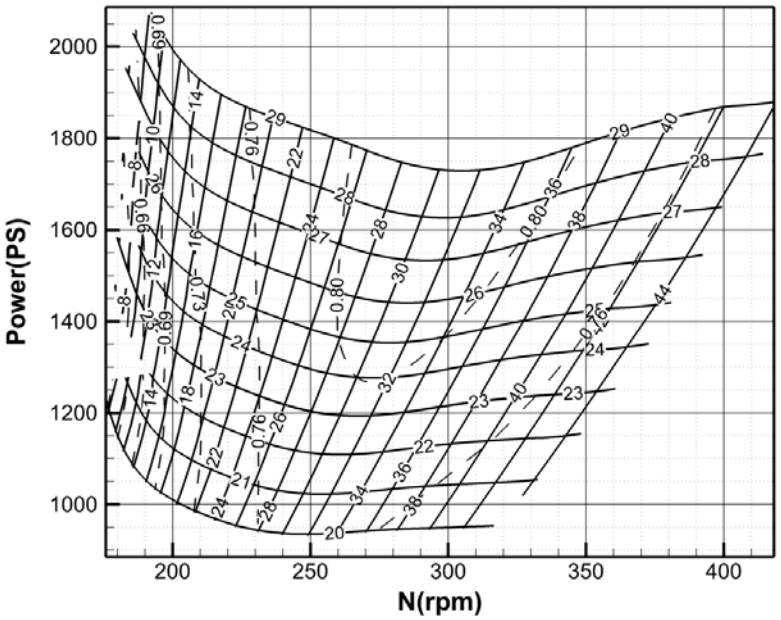

Figure III.2.3-17. Speedboat (ship 3)-FOD: Totality of design solutions in the form of Constant-V, constant-θ_0 grid. Efficiency contours (dashed) are also plotted. Results for one of the two propulsor units.

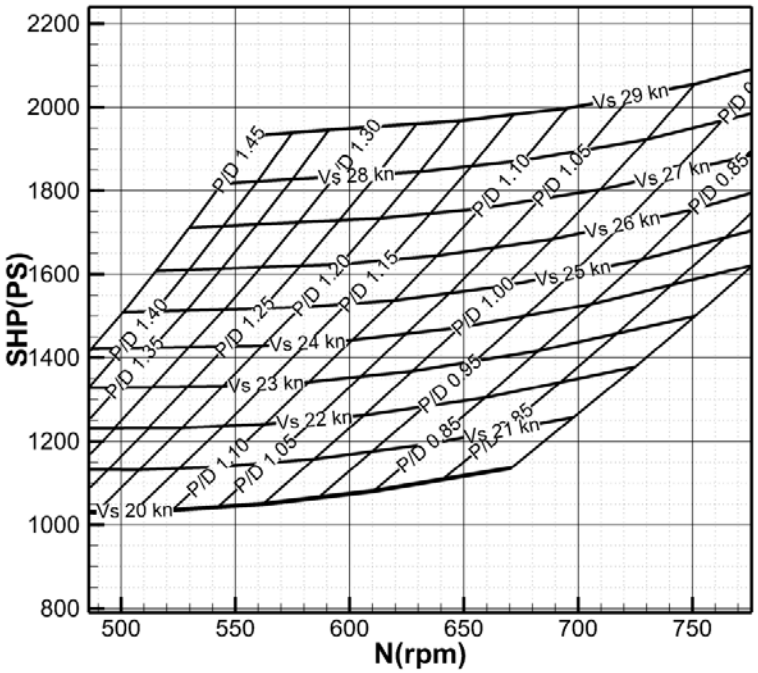

Figure III.2.3-18. Speedboat (ship 3)- B5.70 screw: Totality of design solutions in the form of Constant-V, constant-P/D grid. Results for one of the two propulsor units.

III.2.3.4 FEOD

A passenger ferry is used in a feasibility study for the application of the FEOD, the FOD and a traditional propeller as alternative propulsors, by applying the method explained in Politis & Tsarsitalidis (2012), as expanded in section 4. The passenger ferry is a twin screw vessel with displacement of 8917.66 tons and a maximum allowed propeller diameter of 4.1 meters. The bare hull resistance curve of the ship, taken from the database of the NTUA towing tank, is given in Table III.2.3-9.

With the bare hull resistance given, the system of algebraic equations (III.51), (III.52) and (III.53) can be solved for a range of ship speeds V and θ_0 and the totality of design solutions can be presented in a diagram as dictated by Equation (III.54). For the need of the comparison, it has been assumed that in all cases: $w=0.0, t=0.0, \eta_R=1.0$. This is a reasonable assumption for a twin screw vessel which has small propulsor-hull interactions. The use of the same hull-interaction coefficients for the FEOD/FOD systems and the propeller can be considered reasonable, since interaction coefficients are (for the same stern geometry) mainly functions of propulsor diameter and the developed thrust, Harvald (1983). No inclined axis corrections were made for the conventional propellers. No correction of the bare hull resistance for appendages has been made. A shaft efficiency equal to 1 has been used in the calculations. No corrections for full scale Reynolds number have been introduced for the propulsors.

Totality of design solutions in the form of Constant-V, constant-θ_0 grids for flapping wings and Constant-V, constant-P/D grids for propellers are illustrated for comparison in figures Figure III.2.3-19, Figure III.2.3-20 and Figure III.2.3-21. The comparison of the optimum FEOD and FOD vs the optimum B-screw, for a ship speed equal to 23knots can be summarized in Table III.2.3-10. In all cases, the ship is equipped with two propulsors.

Table III.2.3-9. Resistance curve.

V (m/s)	R(kp)
7.71	31056
8.23	34528
8.75	38374
9.26	42755
9.78	47292
10.29	52301
10.80	58153
11.31	66426
11.83	78009

Table III.2.3-10. Comparison of propulsors.

Case	Revolutions (rpm)	Power (PS)	Propulsive Efficiency (%)	Power Gain (%)
FEOD	**9.81**	**16211.83**	**76**	**5.21**
FOD	**29.55**	**14961.13**	**82**	**12.52**
B-screw	**168.30**	**17103.40**	**72**	

Note, that while the propeller and the FOD, use the maximum allowed (by tolerances) diameter, the FEOD, as it does not move at the upper and lower point, it uses a larger diameter, which in this case, is the maximum diameter the FOD will take (i.e. $D+2h_o$), thus the required Thrust coefficient is lower and the diminished performance of the FEOD is compensated.

It is observed that a gain in propulsive efficiency of 5.21% is obtained for the case of a FEOD in comparison to a conventional propeller. The corresponding gain for a FOD is 12.52%. It is also noticeable, that the optimum flapping wing revolutions are always lower compared to that of corresponding conventional optimum propeller. It should be stretched that the absolute values of power and overall efficiency, contained in table 2, are approximate to the extent of our uncertainty regarding values of propulsor-hull interaction factors.

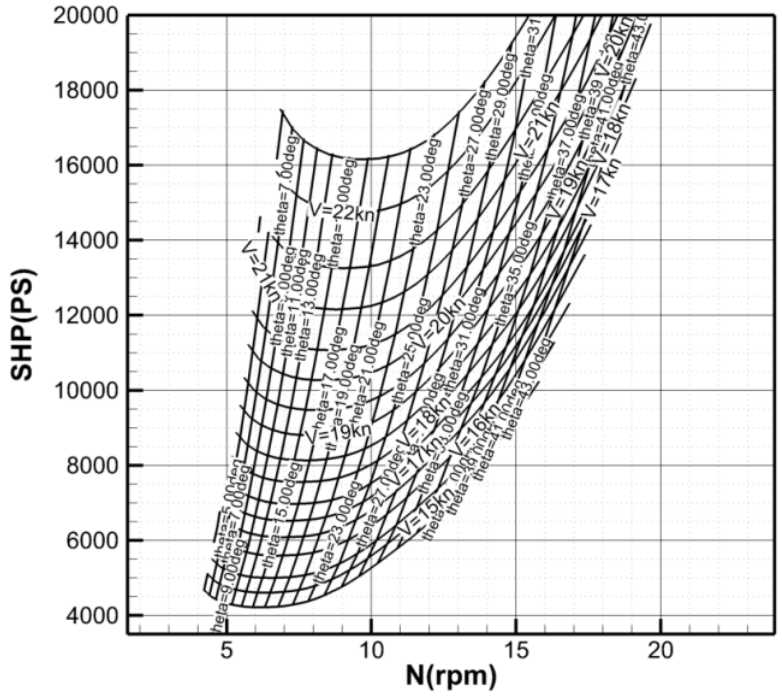

Figure III.2.3-19 Passenger Ferry-FEOD: Totality of design solutions in the form of Constant-V, constant-θ_0 grid.

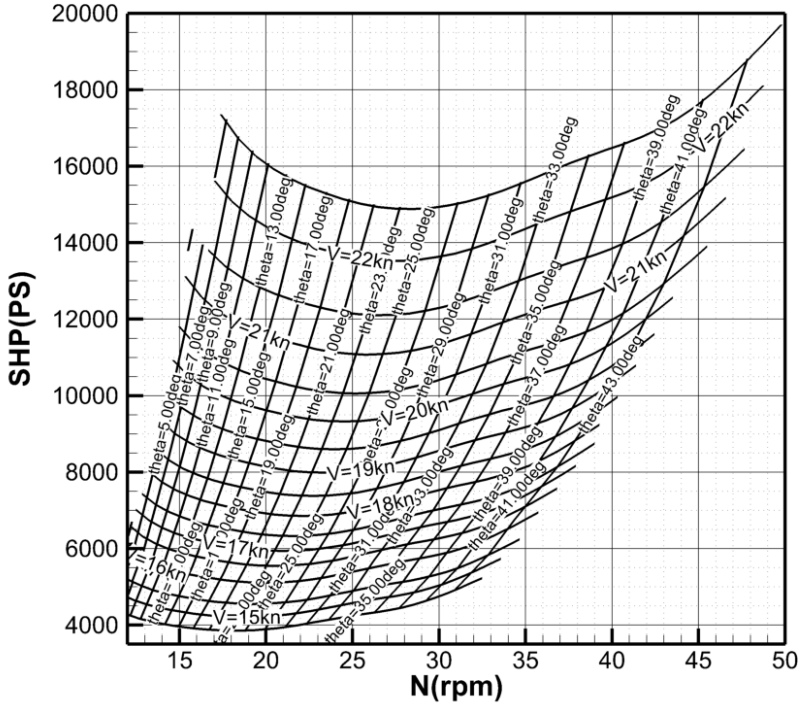

Figure III.2.3-20 Passenger Ferry-FOD: Totality of design solutions in the form of Constant-V, constant-θ_0 grid.

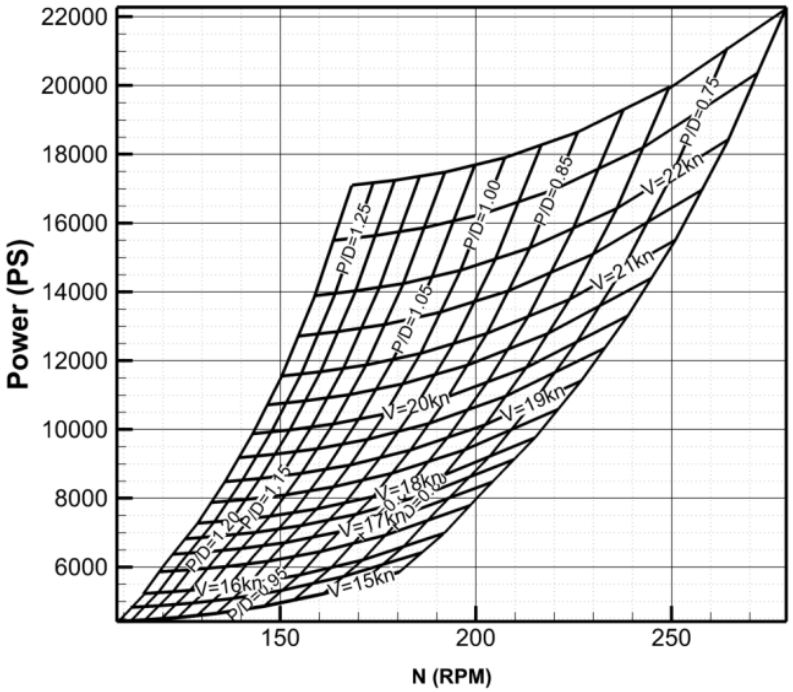

Figure III.2.3-21 Passenger Ferry- B4.75 screw: Totality of design solutions in the form of Constant-V, constant-P/D grid.

Part IV SIMULATIONS UNDER GIVEN HEAVING CONDITIONS

In the previous part the flapping wing propulsor has been investigated performing fully prescribed motions. The undertaking of simulations for properly selected ranges of the physical and geometric parameters (independent variables of the system) enabled the production of a design methodology which can be applied for the selection of optimum flapping wing propulsor for a given ship. In this case the designer has to provide to the flapping wing the required power for the two different modes of its motions i.e. (a) the heaving motion and (b) the pitching motion. From the analysis of the previous chapters it is also observed that with the proper position of the pitching axis the powering requirements of the pitching motion are minimal compared to that of the heaving motion. This observation explains why natural selection has chosen flapping wings as propulsors for living creatures. More specifically, if the heaving motion can be 'provided by the environment the living creature can be propelled at the expense of a very small amount of energy.

For the case of a ship large amounts of wave energy are stored in the form of heaving and pitching motions. If those motions are used to provide the necessary heaving energy for the flapping wing, then at the very small cost for provide the pitching motion, propulsive power will be produced at almost no cost.

With the previous considerations in mind, in this part two mechanisms / procedures shall be examined, which allow provision of the pitching motion when the heaving motion is given (this includes also the case of random heaving motions of a given spectrum). The first mechanism for pitching determination is through the use of a given spring/damper configuration. This case is discussed in IV.1.1 (theoretical setup) and IV.2 (results) and requires the integration of the dynamical equations of the system in the time domain (single degree of freedom hydro-elastic problem). This case is termed ‘spring loaded wing’. The second mechanism does not require the dynamical equations to be solved, but in this case the pitch at each instant is decided by the history of the heaving motion. This case is termed as 'actively pitch controlled wing'. This case is discussed in IV.1.2 (theory) and IV.3 (results). In general, all cases where the pitching motion is not fully prescribed, can be termed as 'event driven pitch control', or ‘flow driven pitch control’

IV.1.1 Formulation of spring loaded wing problem

The problem of a spring loaded wing in unsteady motion, is a one degree of freedom hydroelasticity problem. A wealth of literature can be found in the aerospace engineering sector, such as Bisplinghoff (1996), Dowell (####), Hodges and Pierce (2002), Wright and Cooper (2007) and Geradin and Rixen (1994). However, aerospace applications have the primary objective of minimizing instabilities and resonances. Thus, there are little or no experimental data on the specific case. This means that the models produced can be verified in parts and/ or for simpler cases, as it will be discussed in the sequel.

IV.1.1.1 Governing equations of a 1DOF hydroelastic model.

The generalized aero/hydroelastic problem of a spring loaded wing is presented in Figure IV.1.1-1. Wing of chord length c , has the aerodynamic centre at ac and centre of gravity at cg and has mass m and is free to rotate about the elastic axis ea and has moment of inertia I_a . A spring of stiffness K and damper C , govern the pitching motion.

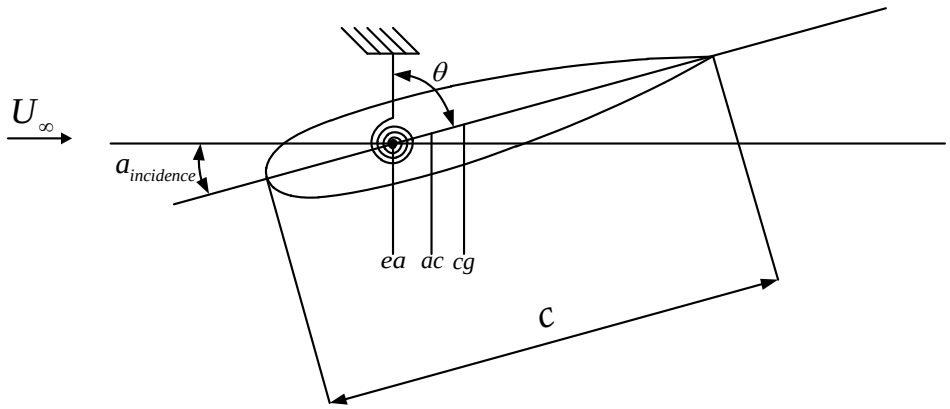

Figure IV.1.1-1 1DOF airfoil section. ea is the elastic axis, ac is the aerodynamic center, and cg is the center of gravity.

The balance of forces is

$$M_{ext}(t) = I_a\ddot{\theta}(\mathrm{t}) + C\dot{\theta}(\mathrm{t}) + K\theta(\mathrm{t}) \qquad \text{(IV.1)}$$

Where M_{ext} is the external moment (in the specific case, the hydrodynamic moment).

The solution of the problem is done in an explicit scheme, where the hydrodynamic forces calculated in each step are used as $M_{ext}(t)$ in order to find the deflections for the next. As long as the timestep is small enough and deflections are also small, this scheme is expected to be robust and accurate, as long as time integrations (solution of (IV.1) for constant $M_{ext}(t)$ and given timestep) are made correctly. It should be noted, that the time integration of the

inertia/spring/damper system can be done via either explicit or implicit methods. The connection of the Inertia/spring/damper system with the hydrodynamic loads is termed hydroelastic coupling and it can also be done either explicitly or implicitly, as long as stability and consistency are checked. Thorough discussion on the matter has been made by Baxevanou, Chaviaropoulos et al. (2008). Coupling was selected to be explicit, in order to keep the modular architecture of the software used, while time integration of the inertia/spring/damper system can be either implicit or explicit. Detailed review of most time integration methods, including mixed schemes, can be found in Dokainish (1989)

IV.1.1.2 Time integration Methods

For the solution of (IV.1) two alternative time integration schemes are employed, for comparison as well as freedom to the user.

IV.1.1.2.1 Newmark family of methods

The Newmark method is a method of numerical integration used to solve differential equations. It is widely used in numerical evaluation of the dynamic response of structures and solids such as in finite element analysis to model dynamic systems. The method is named after Nathan M. Newmark, former Professor of Civil Engineering at the University of Illinois, who developed it in 1959 for use in Structural dynamics.

Numerical Evaluation of Dynamic Response is made following the algorithm as produced by Chopra (1995) (page 188 of 2007 print).

- ***Algorithm: Newmark's Method for Nonlinear Systems***

Special cases:

(1) Average acceleration method $\left(\gamma=\frac{1}{2},\beta=\frac{1}{4}\right)$

(2) Linear acceleration method $\left(\gamma=\frac{1}{2},\beta=\frac{1}{6}\right)$

1.0 Initial calculations

1. 1 State determination: $(\mathrm{M}_S)_0$ and $(k_T)_0$

1.2 $\ddot{\theta}_0=\dfrac{M-C\dot{\theta}_0-\left(M_S\right)_0}{I}$

1.3 Select Δt.

1.4 $a_1=\dfrac{1}{\beta(\Delta t)^2}I+\dfrac{\gamma}{\beta\Delta t}C$; $a_2=\dfrac{1}{\beta\Delta t}I+\left(\dfrac{\gamma}{\beta}-1\right)C$ and

$$a_3 = \left(\frac{1}{2\beta} - 1\right) I + \Delta t \left(\frac{\gamma}{2\beta} - 1\right) C$$

2.0 Calculations for each time instant, i=0, 1, 2, …

2.1 Initialize $j = 1$, $\theta_{i+1}^{(j)} = \theta_i$ $(M_S)_{i+1}^{(j)} = (M_S)_i$, and $(k_T)_{i+1}^{(j)} = (k_T)_i$

2.2 $\hat{P}_{i+1} = M + a_1\theta_i + a_2\dot{\theta}_i + a_3\ddot{\theta}_i$

3.0 For each iteration, $j = 1, 2, 3$ …

3.1 $\hat{R}_{i+1}^{(j)} = \hat{P}_{i+1} - (M_S)_{i+1}^{(j)} - a_1\theta_{i+1}^{(j)}$

3.2 Check convergence; If the acceptance criteria are not met, implement step 3.3 to 3.7 otherwise, skip these steps and go to step 4.0

3.3 $(\hat{k}_T)_{i+1}^{(j)} = (k_T)_{i+t}^{(j)} + a_1$

3.4 $\Delta\theta^{(j)} = \hat{R}_{i+1}^{(j)} \div (\hat{k}_T)_{i+1}^{(j)}$.

3.5 $\theta_{i+1}^{(j+1)} = \theta_{i+1}^{(j)} + \Delta\theta^{(j)}$

3.6 State determination: $(M_S)_{i+1}^{(j+1)}$ and $(k_T)_{i+1}^{(i+1)}$

Replace j by $j+1$ and repeat steps 3.1 to 3.6; denote final value as θ_{i+1}

4.0 Calculations for velocity and acceleration

4.1 $\dot{\theta}_{i+1} = \frac{\gamma}{\beta\Delta t}\left(\theta_{i+1} - \theta_i\right) + \left(1 - \frac{\gamma}{\beta}\right)\dot{\theta}_t + \Delta t\left(1 - \frac{\gamma}{2\beta}\right)\ddot{\theta}_i$

4.2 $\ddot{\theta}_{i+1} = \frac{1}{\beta(\Delta t)^2}\left(\theta_{i+1} - \theta_i\right) - \frac{1}{\beta\Delta t}\dot{\theta}_t - \left(\frac{1}{2\beta} - 1\right)\ddot{\theta}_i$

5.0 *Repetition for next time step*. Replace i by $i+1$ and implement steps 2.0 to 4.0 for the next time step.

It should be noted that step 3 (3.1 to 3.6) are actually a Newton iteration for the non-linearity of K. M_S is the resisting moment (in this case spring moment) and k_T is the tangent stiffness defined as $k_{Ti}^{\ j} = \left.\frac{\partial M_S}{\partial\theta}\right|_{\theta_i^j}$. It is clear, that for a linear spring, the iterations will converge immediately, thus it is not necessary to activate and deactivate according to the case. In the current implementation, the method is applied between timesteps of the hydrodynamic solver, estimating the deflection for the next step by integrating in a given number of steps and keeping the moment from the current step.

IV.1.1.2.2 Crank Nicolson (trapezoidal rule)

Crank Nicolson is an unconditionally stable implicit one-step method, which is second order accurate in time and relates the displacements, velocities, and accelerations as

$$\begin{aligned}\theta_{n+1} &= \theta_n + \frac{\Delta t}{2}\left(\dot{\theta}_n + \dot{\theta}_{n+1}\right)\\ \dot{\theta}_{n+1} &= \dot{\theta}_n + \frac{\Delta t}{2}\left(\ddot{\theta}_n + \ddot{\theta}_{n+1}\right)\end{aligned} \qquad \text{(IV.2)}$$

n corresponds to the old time step and $n+1$ is the new time step. Δt is the time step size. Rearranging equations (IV.2) gives

$$\begin{aligned}\ddot{\theta}_{n+1} &= \frac{2}{\Delta t}\left(\theta_{n+1} - \theta_n\right) - \dot{\theta}_n\\ \ddot{\theta}_{n+1} &= \frac{4}{\Delta t^2}\left(\theta_{n+1} - \theta_n\right) - \frac{4}{\Delta t}\dot{\theta}_n - \ddot{\theta}_n\end{aligned} \qquad \text{(IV.3)}$$

By combining equations (IV.3) with the equations of motion, equation (IV.1) at step $n+1$, one finds

$$K^{eff}\theta_{n+1} = R^{eff}{}_{n+1} \qquad \text{(IV.4)}$$

Where the effective stiffness, K^{eff}, and the effective load $R^{eff}{}_{n+1}$ are respectively

$$K^{eff} = \frac{4}{\Delta t^2} I + \frac{2}{\Delta t} C + K \qquad \text{(IV.5)}$$

$$R^{eff}{}_{n+1} = R^{ext}{}_{n+1} + M_{ext}\left(\frac{4}{\Delta t^2}\theta_n + \frac{4}{\Delta t}\dot{\theta}_n + \ddot{\theta}_n\right) + C\left(\frac{2}{\Delta t}\theta_n + \dot{\theta}_n\right) \qquad \text{(IV.6)}$$

- ***Algorithm: Crank Nicolson***

The solution algorithm is as follows:

1. Get mass, stiffness, and damping parameters.
2. Set initial conditions for displacements, velocities and accelerations from previous step.
3. Find effective stiffness, K^{eff} from equation (IV.5).
4. Find effective load vector, $R^{eff}{}_{n+1}$ from equation (IV.6).
5. Solve equation (IV.4) for θ_{n+1} .
6. Update velocities and accelerations to step $n+1$ using equations (IV.3)
7. Output if desired or go to 4.

IV.1.1.3 Implementation of the explicit coupling scheme

As already discussed, an explicit scheme is used for the coupling of the inertia/spring/damper system and the hydrodynamic solver for the simulation of spring loaded wings. According to this, After the UBEM solver has made calculations for a given step, the calculated pressure distribution is integrated appropriately, in order to calculate the moment on the axis of rotation, which is fed to the time integration subprogram, along with the timestep size. Then, either the (one step) Krank Nicolson method is applied, or the timestep is divided into substeps (number given by user) and the Newmark method is applied. The resultant deflection angle for the next step is given to the Geometry Generation subprogram, which will create the geometry (using $\theta(i+1)$, along with all other geometry and motion descriptive data) to be fed back to the main solver. This process is graphically presented in Figure IV.1.1-2. This procedure, when integrated to the architecture of the existing software, may appear to complicate things, but in fact, it is a self-contained module that can be modified independently, as well as allow the rest of the software be modified, as long as the interface for data exchange remains the same. In this application, this interface is a file containing the geometry and the pressure distribution on the elements of the body written in a specific format.

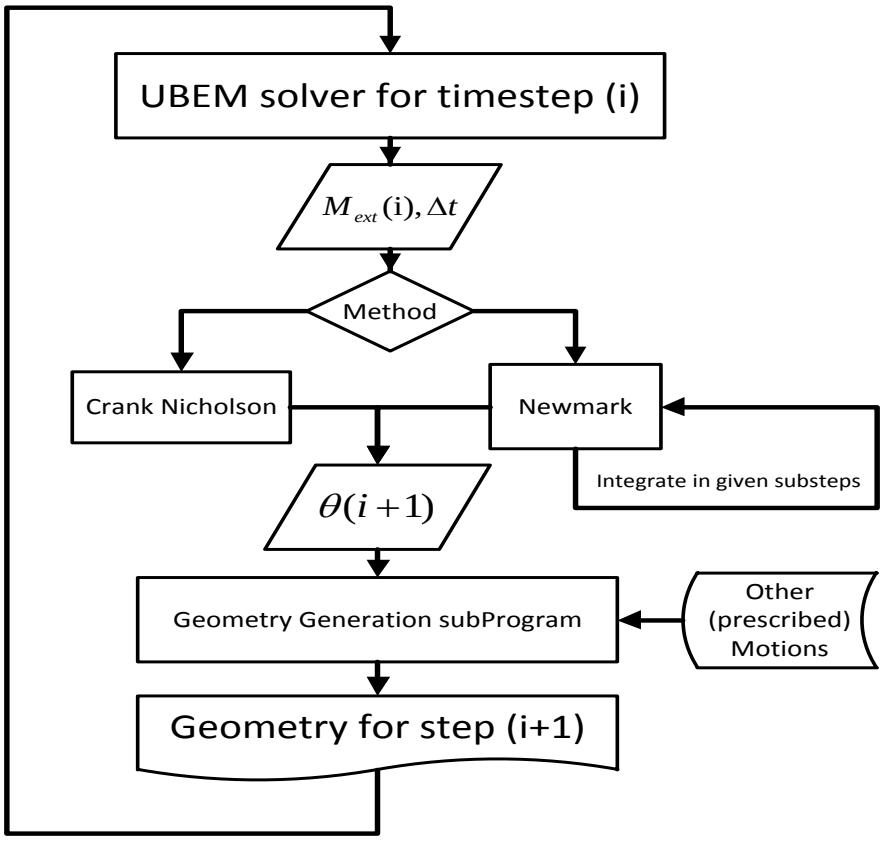

Figure IV.1.1-2 Logical diagram of the explicit scheme used for the solution of the spring loaded wing problem.

IV.1.2 Active Pitch Control

One last feature of the developed code, regarding pitching motion is the addition of the capability to use an active pitch control algorithm. For the specific application in hand, the simple open loop algorithm presented by (Politis and Politis 2012), (Belibassakis and Politis 2013) is employed and evolved as follows.

From the original of (Politis and Politis 2012), the pitch angle at each step is defined as:

$$\theta(t) = w\tan^{-1}\left(\frac{dh/dt}{U}\right) \tag{IV.7}$$

Where w, a control parameter ranging from zero to one that is set beforehand. Knowing the expected heave amplitude, frequency and speed of advance, and knowing that:

$$a(t) = (1-w)\tan^{-1}\left(\frac{dh/dt}{U}\right) \tag{IV.8}$$

the parameter w can be set to a number that the maximum angle of attack does not exceed a defined value.

Closer examination of (IV.8), and Figure IV.1.2-1 gives the understanding that $\tan^{-1}(dh/dt/U)$ gives the angle of the undisturbed flow and that the decrease of the value of w, increases the angle of attack. In the previous method, the desired angle of attack is attained momentarily. On the other hand, (as also seen in Figure IV.1.2-1,) it is understandable that, at points where the heaving velocity is zero, it is impossible to have a nonzero thrust producing angle of attack. Thus, the goal is to attain the desired angle of attack for as long as possible. With all the above taken into consideration, the variable $w(t)$ is introduced in the place of w. Keeping in mind the objective of keeping the angle of attack below a given value, a new law can be obtained for $w(t)$, by finding the minimum value of $w(t)$ that satisfies

$$A \geq (1-w(t))\tan^{-1}\left(\frac{dh/dt}{U}\right), A = given \tag{IV.9}$$

The value found is then substituted in (IV.7), to give the pitching angle.

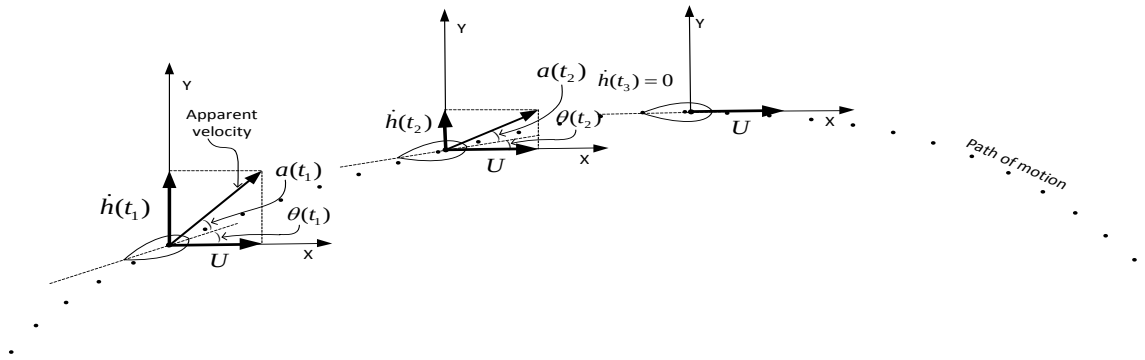

Figure IV.1.2-1 Three successive positions of a wing in pitching and heaving motion.

The algorithm can be summarized as follows:

a) Find the translation velocity of the pitching axis after all possible motions have been applied (from previous step)

b) break the velocity to the x,y components of the local (axis built) system

c) start with $w(t)=1$

d) Decrease $w(t)$ by a given step (required accuracy)

e) evaluate $a(t)=(1-w)\tan^{-1}\left(\frac{dh/dt}{U}\right)$, if $a(t)<A\max$, back to d)

f) exit with $w(t)$ and apply to (IV.7) to get $\theta(t)$

This method gives at a minimal addition of computational cost, a different, non-harmonic profile of pitching motion, where the angle of attack is kept below the given value, but also equal to it for a longer time. It should be noted, that when the angle of the undisturbed flow is smaller than the desired angle of attack (and when it changes from the positive to negative – one side of wing to the other-) it is better to keep the wing at a zero pitch angle, something that this algorithm follows very well. As shown in the testing of the methods part, the angle profiles can be very different to the known patterns so far, producing interesting results. As it can be seen in the algorithm, the method is sensitive to the simulation timestep, as it actually gets the proper angle of attack for the previous step, and to the step of required accuracy. Since the computational cost for the evaluation of (IV.8) is very low compared to the overall computations, this internal step can be brought to such a small size that it is does not affect the solution. It should be noted, that getting the velocities from the previous timestep, is a realistic choice, as in any control system there is a considerable time between sampling and acting. However, the effect of timestep (or sampling rate) has to be explored, in order to validate the method.

IV.1.3 New architecture of code

The aforementioned explicit scheme of passing the hydrodynamic solution of each step to the calculation of the next position of geometry to be passed in turn to the hydrodynamic solver, dictates a serious change in the structure of the program in hand. In order to allow for further developments, the modular aspect of architecture is evolved even more.

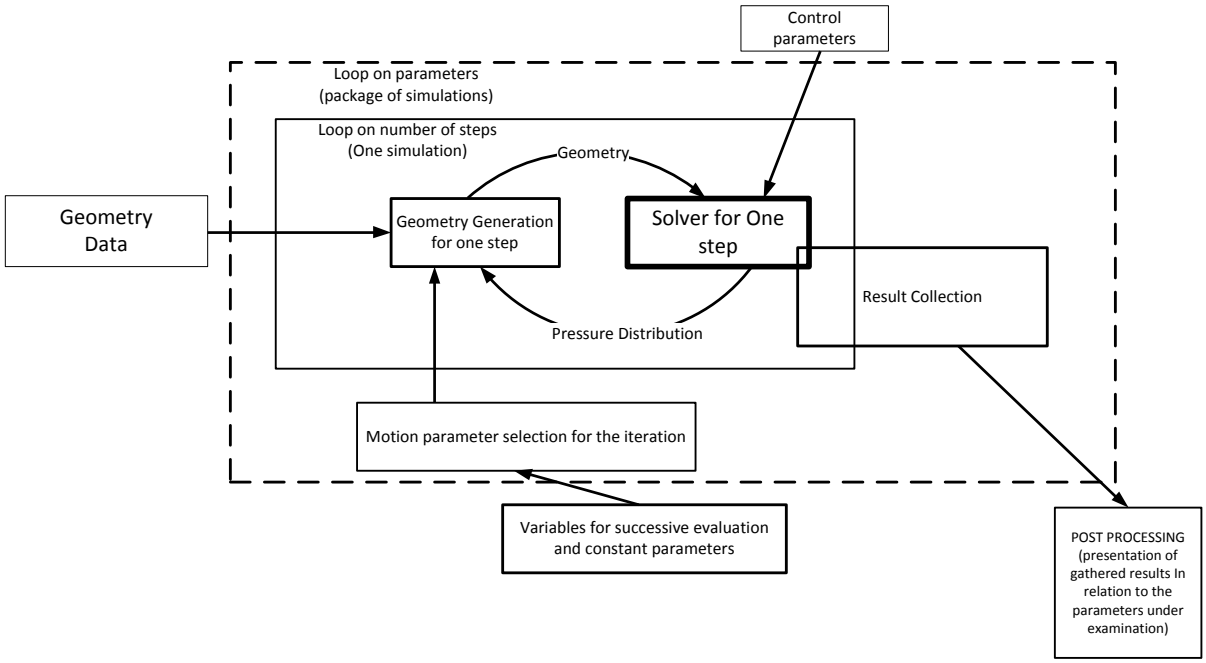

Figure IV.1.3-1 Reviewed architecture of the program in hand

As shown in Figure IV.1.3-1, the hydrodynamic solver code has to be run at each step and send data to the program that generates the geometry for the next step. In order to allow for further upgrades, an interface is made, through which the solver sends the pressure distribution for all simulated bodies and receives the geometry for the next step. The geometry generation subprogram will choose what will be integrated (forces, moments on selected points and axes) and how (method of integration) and what will be deformed and how. Thus, it is possible to change the simple spring loaded wing with a finite element method of whatever complexity, without having to change anything more than the corresponding subprogram.

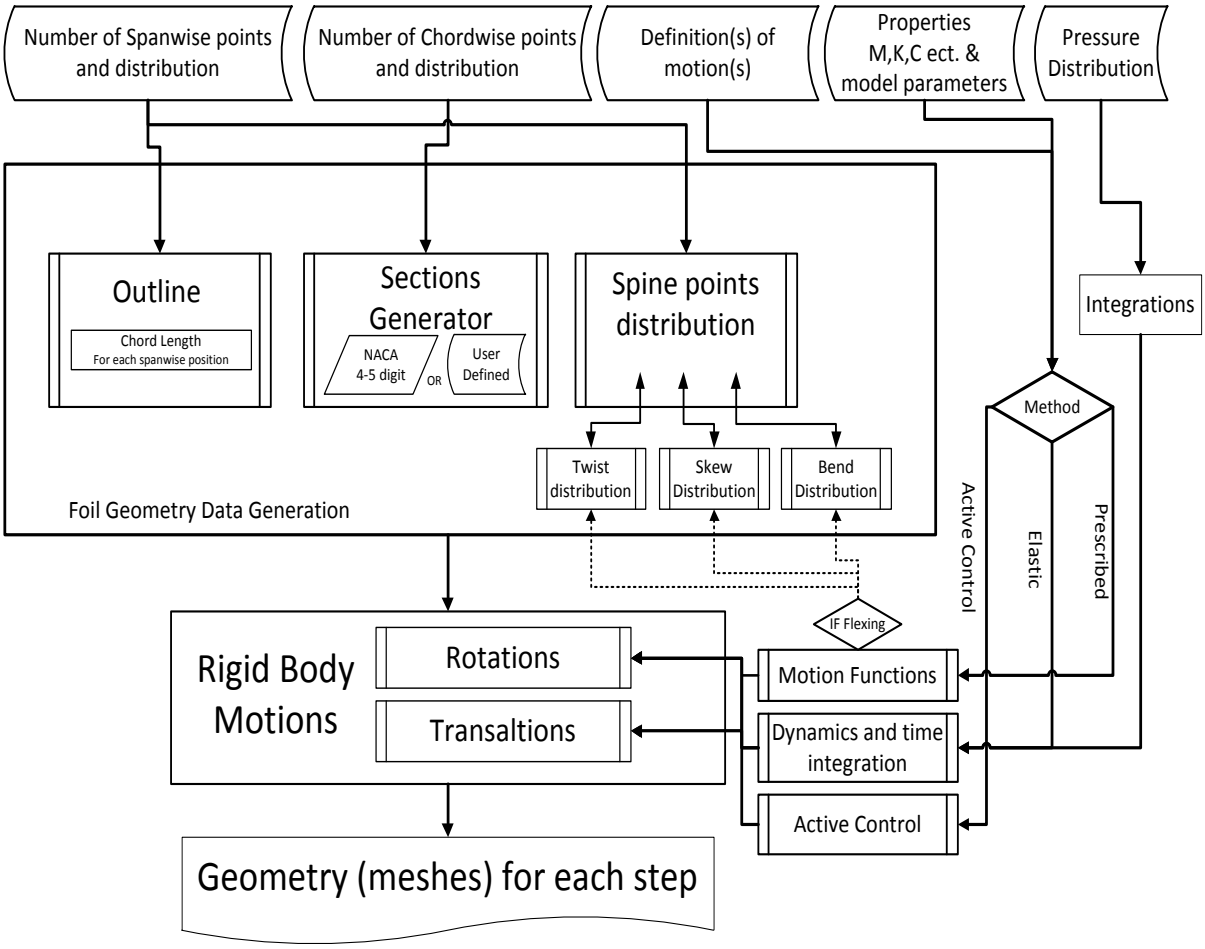

Figure IV.1.3-2 Detail of the Architecture of the wing geometry generation subprogram.

IV.1.4 Selection of parameters of the time integration schemes

The problem of a spring loaded wing under heaving motion is very different from what has been simulated in the past and most hydroelastic and aeroelastic problems tested in literature, have been set with the goal of avoiding resonance or predicting steady deflections. This means that there is virtually no experimental data for the case in hand and there is no reference point for direct validation of the code. Nevertheless, the components of the code can be verified independently and the coupled problem can be tested by simpler benchmark cases. Additionally, the active pitch control method has to be checked for stability and consistency.

The hydrodynamic solver has been proven to be accurate enough for most cases, with the exception of very high loads, as already shown in II.1.3.2.2 where it has been systematically compared to experimental results.

Thus, the need for verification remains for the time integration schemes and for the fully coupled problem, either with elasticity, or with control.

IV.1.4.1 Stability and accuracy of time integration schemes

The Newmark family of time integration methods, has been thoroughly investigated in the existing literature for its stability, depending on the values of γ and β.As shown by M. Geradin and D. Rixen, in "Mechanical Vibrations: Theory and Applications to Structural Dynamics", Figure IV.1.4-1 depicts this dependency. When $\gamma < 1/2$, the scheme is unconditionally unstable. For $\gamma \geq 1/2$ the scheme is unconditionally stable when

$$\beta \geq 1/4\left(\gamma + \frac{1}{2}\right)^2 \tag{IV.10}$$

and for smaller β the the stability limit of the scheme is

$$\left(\gamma + 1/2\right)^2 - 4\beta \leq 4/\omega^2 h^2 \tag{IV.11}$$

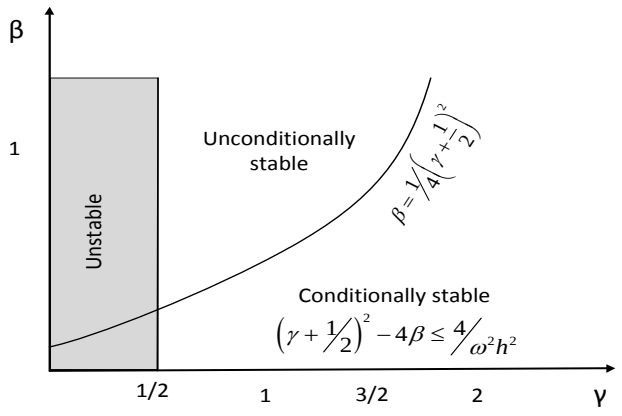

Figure IV.1.4-1 Stability of the Newmark method

However, the use of the parameters γ and β, imposes a numerical damping to the solution. The most noted selections of these parameters, along with their stability limit and the expected Amplitude and Periodicity errors are shown in Table IV.1.4-1. From that it can be seen that the purely explicit scheme ($\gamma = 0$, $\beta = 0$) is unstable and also has an amplitude error (mostly amplifying instabilities), rendering it useless. The Fox & Godwin scheme has asymptotically the smallest phase error but is only conditionally stable, while the average constant acceleration is the unconditionally stable scheme with asymptotically the highest accuracy. Thus, the last three methods are to be used (within restrictions) in order to find the best suited for the case. The Krank Nicolson scheme is unconditionally stable and its error can be found in literature.

Table IV.1.4-1 Schemes of the Newmark family

Algorithm	γ	β	Stability limit ωh	Amplitude error $\rho - 1$	Periodicity error $\frac{\Delta T}{T}$
Purely explicit	0	0	0	$\frac{\omega^2 h^2}{4}$	—
Central difference	$\frac{1}{2}$	0	2	0	$-\frac{\omega^2 h^2}{24}$
Fox & Goodwin	$\frac{1}{2}$	$\frac{1}{12}$	2.45	0	$\mathcal{O}(h^3)$
Linear acceleration	$\frac{1}{2}$	$\frac{1}{6}$	3.46	0	$\frac{\omega^2 h^2}{24}$
Average constant acceleration	$\frac{1}{2}$	$\frac{1}{4}$	∞	0	$\frac{\omega^2 h^2}{12}$

IV.1.4.2 Stability and accuracy of the solution of coupled hydroelastic problem

No experimental data can be found on the fully unsteady case. Thus, simpler benchmark cases of steady problems and grid and timestep independence tests are conducted for the unsteady case. The simplest problem is that of a wing in a flow at an angle and allowing it to align with the flow. With the behaviour characteristics of the wing and the spring stiffness known, the point of equilibrium can be estimated. Thus, with varying stiffness, damping factors and time integration scheme parameters, the stability limits can be explored, along with the speed of convergence to the position of balance.

As known from literature, the factors of the time integration scheme, while stabilizing the solution, they also act as numerical dampers. In Figure IV.1.4-2 results (rotational response history in rad) of the coupled hydroelastic problem are compared for different schemes. From this figure it is clear that the smallest possible factors are desirable, in order to get the smallest damping effect possible. Of course, this comes at a cost, as for $\beta < 1/4$ the schemes are conditionally stable and care has to be given in order to keep the timestep small enough. The effect of timestep is explored and presented in Figure IV.1.4-3. In the figure, the responses

(rotation in rad) is plotted over time for different time discretizations. As it is shown, the scheme is unstable for 35 steps per second, while for 50 and 70, it gives almost identical solutions making the curves almost indistinguishable.

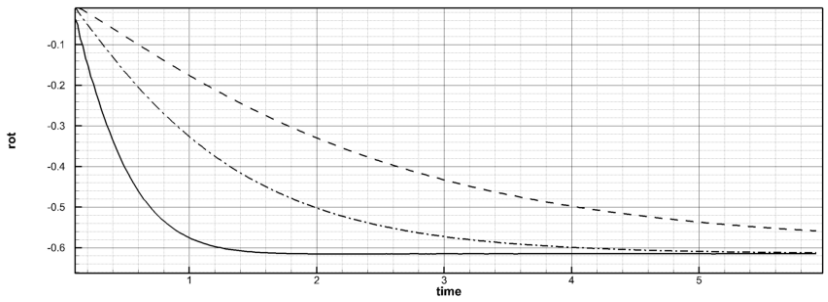

Figure IV.1.4-2 Effect of time integration scheme on speed of convergence to solution. Straight wing AR=4 K/ρ=12 . Dashed: Average constant acceleration, Dash-dot: Linear acceleration, Solid: Fox & Goodwin.

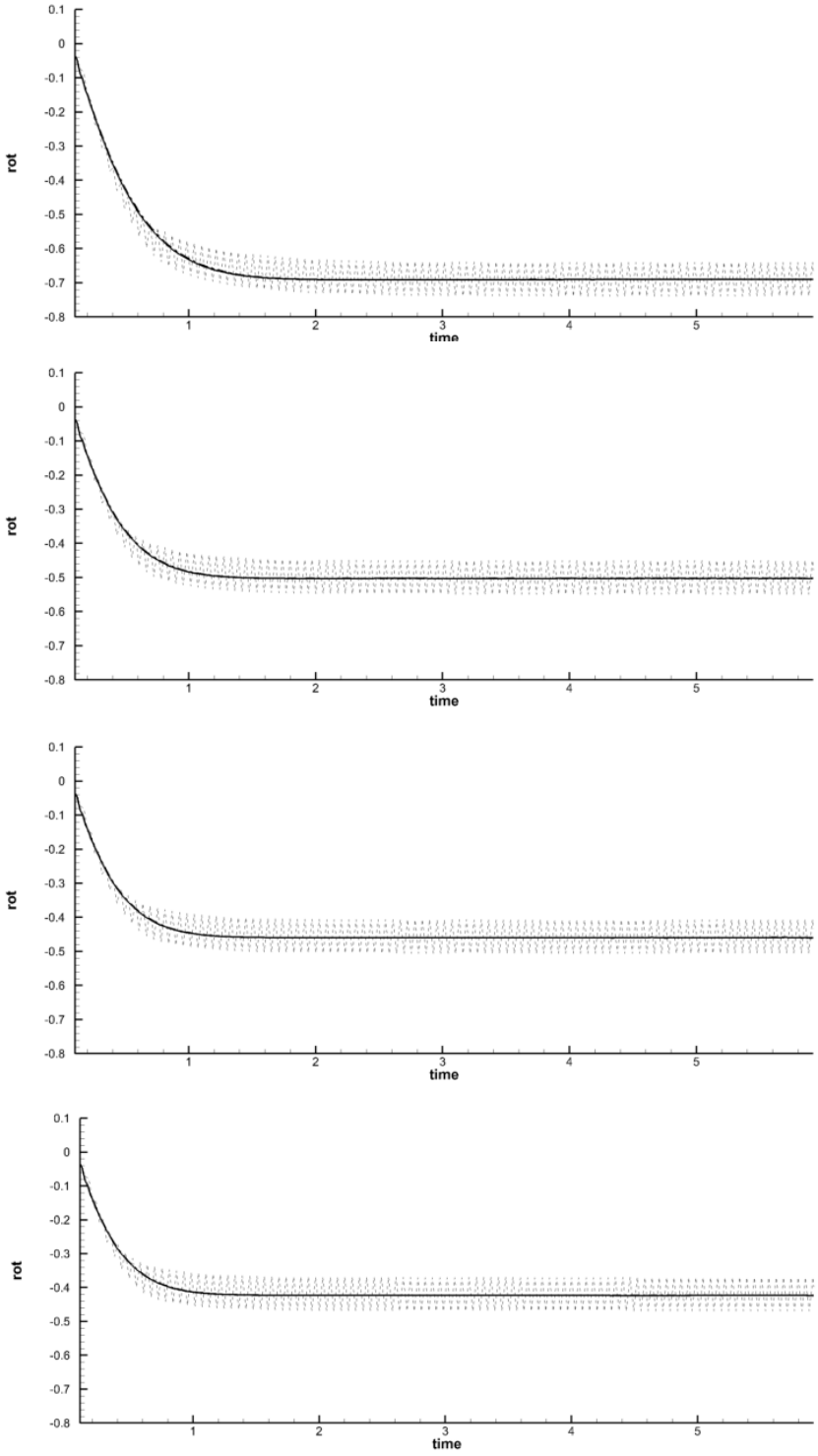

Figure IV.1.4-3 Effect of timestep on speed of convergence to solution (Straight wing, AR=4, K/ρ=10,20,30,40 from top respectively, Flow at 45deg, Fox & Goodwin scheme). Dotted 35 steps per second solid 50 steps per second Dash-dot 70 steps per second

In order to explore the effect of time integration scheme on the phase of response (periodicity error), harmonic heave motions are also tested. Since there are no experimental data on the

case, the effect of timestep and integration scheme can be explored in the same manner as grid independence tests, since all are supposed to converge to the same solution. In Figure IV.1.4-4 through Figure IV.1.4-6, some additional effects are observed. For the smaller Strouhal number (lower frequency), the instability due to the small timestep is expressed as oscillation around the expected solution, while at larger Strouhal numbers, the solution looks stable, but the response amplitude is larger, which is unclear if it happens due to smaller damping or instability. It is also observed, that smaller timesteps, meaning more steps per period, lead to amplification of the damping effect of the time integration schemes. This is shown in all three figures, as a delay and reduction of amplitude of the response.

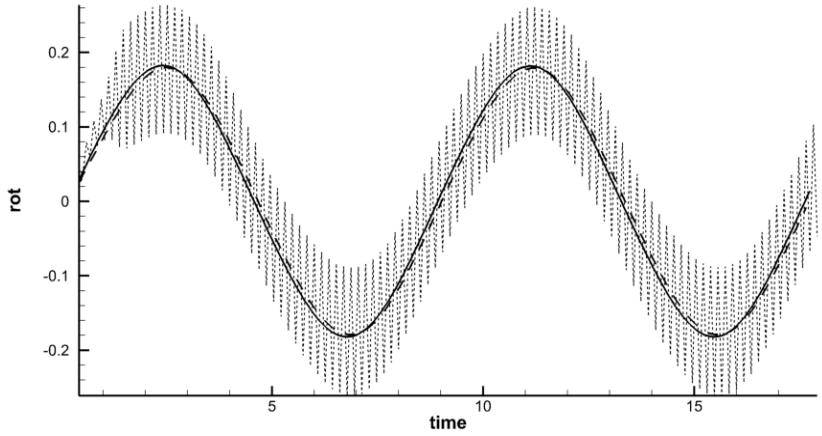

Figure IV.1.4-4 Plot of rotation response (in radians) over time for different time discretizations. Dotted: 100 steps per period, Solid: 150 steps per period, Dashed: 200 steps per period. All plots for h/c=2, Str=0.2, K/ρ=26, γ=0.5, β=0.16

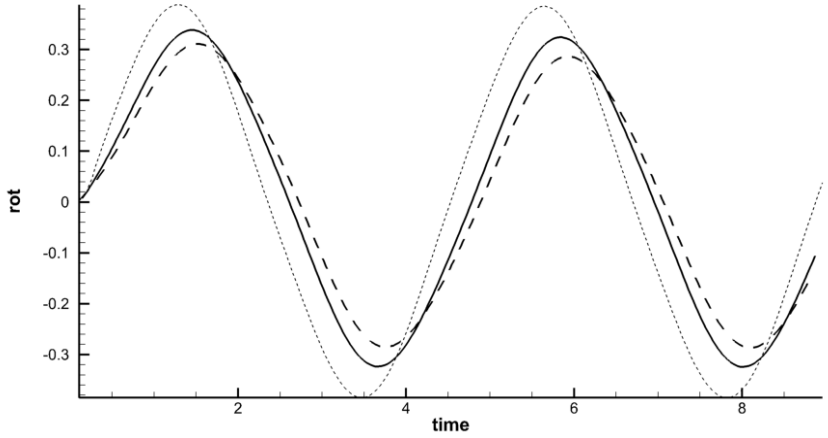

Figure IV.1.4-5 Plot of rotation response (in radians) over time for different time discretizations. Dotted: 100 steps per period, Solid: 150 steps per period, Dashed: 200 steps per period. All plots for h/c=2, Str=0.4, K/ρ=26, γ=0.5, β=0.16

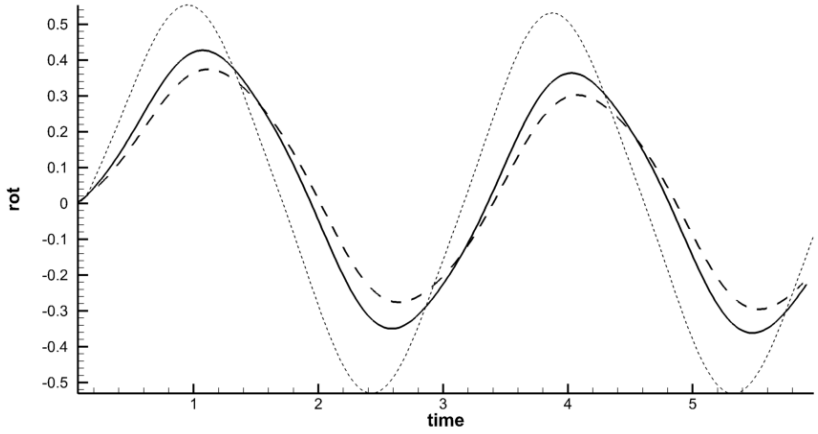

Figure IV.1.4-6 Plot of rotation response (in radians) over time for different time discretizations. Dotted: 100 steps per period, Solid: 150 steps per period, Dashed: 200 steps per period. All plots for h/c=2, Str=0.6, K/ρ=26, γ=0.5, β=0.16

IV.1.4.3 Stability and consistency of the active pitch control algorithm

The active pitch control algorithm is not a simulation of a physical phenomenon. Thus, all verification there is to be made, regards the sensitivity of the method to timestep and magnitude of motions. Since the objective is to maintain the angle of attack below a selected level, the primary evaluation of the method has to be the level of success at maintaining this goal. It is understandable, that since the sampling rate is finite and also the timesteps of the simulations have to be finite, a phase error is expected which will lead to an error at the achieved angles of attack. Such error is acceptable, as long as it is consistent, can be quantified and can be kept at a magnitude that gives improved (and realistic) results. It should be noted that improved (i.e. more efficient) results, produced by a simulated experiment with low sampling rate (which means slower response), can be expected to be more achievable in actual application. As seen in Figure IV.1.4-7 and Figure IV.1.4-8, the method works as expected for harmonic motions and even though the maximum angle of attack is missed in absolute, the difference is consistent and shows the same pattern for all cases. The different profile is considered to be caused by the offset between excitation and response and is dependent on the timestep. However, small changes in the timestep size make little or no effect (thus, no comparative figures were made). The new angle of attack profile and whether it is beneficial or not, as well as the behaviour with more complex excitations, will be discussed thoroughly in the Conducted simulations (Part III)

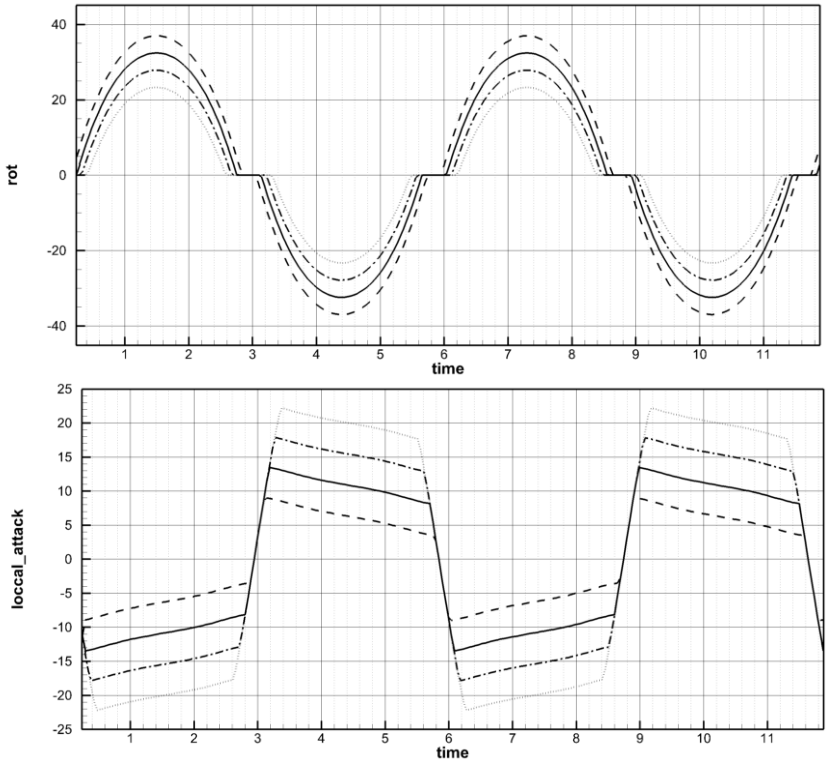

Figure IV.1.4-7 Rotation after control and achieved attack angles for a wing moving at str=0.3 h/c=2. Dashed line is for A_{target}=6.3, Solid for 10.9, Dash-dot for 15.4 and dotted for A_{target}=20.0

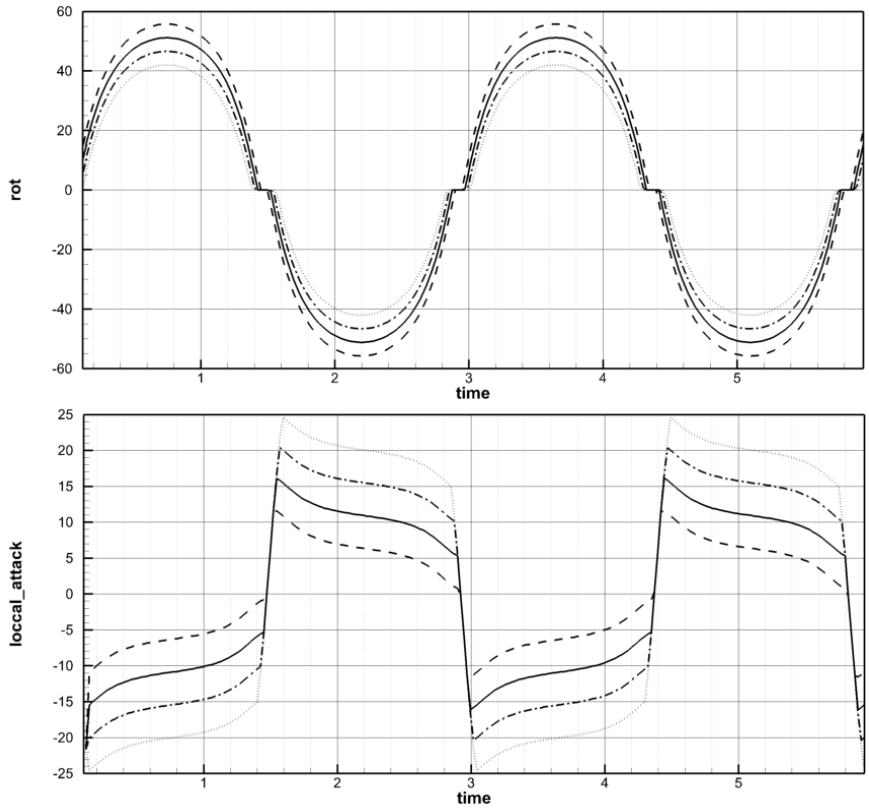

Figure IV.1.4-8 Rotation after control and achieved attack angles for a wing moving at str=0.6 h/c=2. Dashed line is for A_{target}=6.3, Solid for 10.9, Dash-dot for 15.4 and dotted for A_{target}=20.0

IV.2 Motions of spring loaded wings

As discussed in the previous paragraphs, the program developed has the ability to simulate the hydroelastic behavior of a spring loaded wing. Spring loaded wings have been well documented and tried for many years, with contradicting results. Even though there have been many patents, designs and full scale attempts (Rozhdestvensky and Ryzhov 2003) and for specific conditions the systems have shown amazing gains (the Russian trawler achieved a 40% reduction in fuel consumption), the performance seems to be inconsistent and/or troublesome to maintain. Thus, it is necessary to explore the case systematically and thoroughly, in order to understand the underlying phenomena. Adding one degree of freedom alone, adds at least three additional parameters (spring stiffness, damper factor and moment of inertia of the wing). Possible non linearities add even higher complexity to the system, making the cost of experiments forbidding and even the computational cost very high. Investigation of different geometries, increases the complexity even further. At this stage, it is necessary to employ existing knowledge in order to set up a starting point and conduct initial investigations that will show the way to more detailed future work.

IV.2.1 Initial assumptions

In order to proceed with the simulations, initial assumptions/decisions have to be made regarding the properties of the wing (shape, mass, moment of inertia) and the spring-damper system, along with the position of the pitching axis. For the properties of the wing, an initial simple geometry is chosen and conventional materials were assumed. For the spring and damper, choices have been made through knowledge of the dynamics of a harmonic oscillator and the position of the pitching axis was selected by employing knowledge gained from prescribed motions simulations as explained below.

IV.2.1.1 Wing properties

For the wing, an initial geometry is selected to be that of a straight wing of s/c=4.0 and a mass distribution resembling that of solid wood or an aluminium shell of the same shape was assumed. Then, the mass, centre of mass and moment of inertia can be calculated by employing a CAD software, numerical integrations or empirical rules (found in textbooks) for simple geometries. Figure IV.2.1-1, shows the selected wing. For such a wing of c=1.0m (s=4.0m) the calculated useful data are:

- Surface area= 7.5818m^2
- Volume = 0.2823m^3
- Centre of volume at 0.4188m from le
- Volume moment of inertia about centroid Iz=0.0151326m^5

(it is reminded that mass moment of inertia is taken by multiplying the volume moment of inertia with density, when density is constant and should not be confused with the second moments used for analysis of sections)

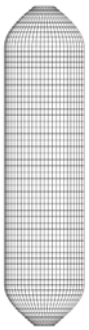

Figure IV.2.1-1 Geometry of a straight wing of s/c=4.0

IV.2.1.2 Spring – Damper system

As it is known from the dynamics of harmonic oscillators,

$$\zeta = \frac{c}{2\sqrt{Ik}} \qquad \text{(IV.12)}$$

is called the 'damping ratio'.

The value of the damping ratio ζ critically determines the behavior of the system. A damped harmonic oscillator can be:

Overdamped ($\zeta > 1$): The system returns (exponentially decays) to steady state without oscillating. Larger values of the damping ratio ζ make the system return to equilibrium slower.

Critically damped ($\zeta = 1$): The system returns to steady state as quickly as possible without oscillating.

Underdamped ($\zeta < 1$): The system oscillates (with a slightly different frequency than the undamped case) with the amplitude gradually decreasing to zero. The angular frequency of the underdamped harmonic oscillator is given by $\omega_1 = \omega_0\sqrt{1-\zeta^2}$ (it is reminded that $\omega_0 = \sqrt{\frac{k}{m}}$; for the specific case $\omega_0 = \sqrt{\frac{k}{I}}$)

It is desirable that the system is not allowed to resonate with the excitation, but also that it does not delay to respond. Thus, the logical initial setting, is to choose $\zeta=1$ as a parameter for the initial explorations. From a known ζ, the corresponding damping factor c can be calculated for each setting of k, which will be chosen to vary for the systematic simulations.

IV.2.1.3 Selection of Pitching Axis Position

For the selection of the pitching axis position, the decision was made that it should be at a position in front (closer to the leading edge) of the centre of pressure of the wing throughout the duration of motion, in order to have a stable case. Thus, this decision depends on the determination of the hydrodynamic centre of the wing. To this end, the following procedure was followed.

The hydrodynamic centre of the wing is the axis around which the total moment is zero. At any other point, the moment will be $M_z = F_y \cdot d$, where d is the distance between the centre and the different point. Solving for d, gives $d = M_z / F_y$. Then, by analysing the results from existing (prescribed motion) simulations and applying $d(\mathrm{t}) = M_z(\mathrm{t}) / F_y(t)$ for each selected simulation, the position of the hydrodynamic centre is estimated at each instant. In Figure IV.2.1-2 thru Figure IV.2.1-6 these calculations are shown for whole packages of simulations (one curve for each simulation) for varying pitching axis position from the middle of the chord to 0.1c from the leading edge. The peaks of the lines should be disregarded, as they are result of the very small F_y at the upper and lower points of the oscillation. From the main part of the

curves, it can be concluded that the hydrodynamic centre resides slightly ahead of 0.3c from le for most of the time for all cases. Figure IV.2.1-7 is the result of an additional package of simulations made to verify this, and it can be confirmed that the hydrodynamic centre of the wing of s/c=4 with naca0012 section resides between 0.25c and 0.3c from the Leading Edge for most of the time for all cases, while the position of the pitching axis has a secondary effect on its position. After this analysis, the logical starting point for simulations of spring loaded wings is to have the pitching axis at 0.25c from le, or closer to the leading edge. It should be noted that a position much closer to the le, could mean large moments, which could lead to strong responses and instabilities, difficult for the program to solve, if all parameters are not set correctly.

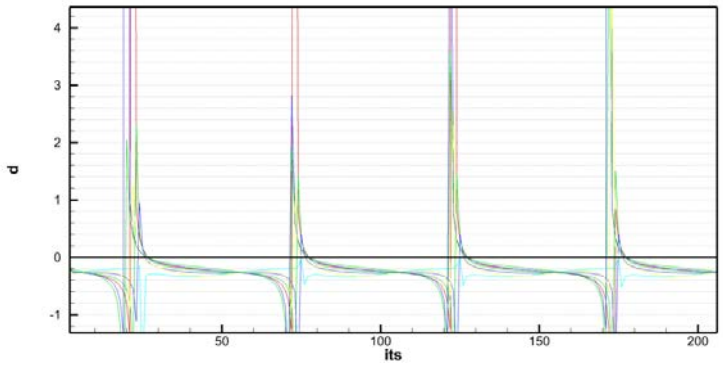

Figure IV.2.1-2 Histories of position of the hydrodynamic center, relative to the pitching axis, for pitch axis at 0.5c from le. (negative is for forward)

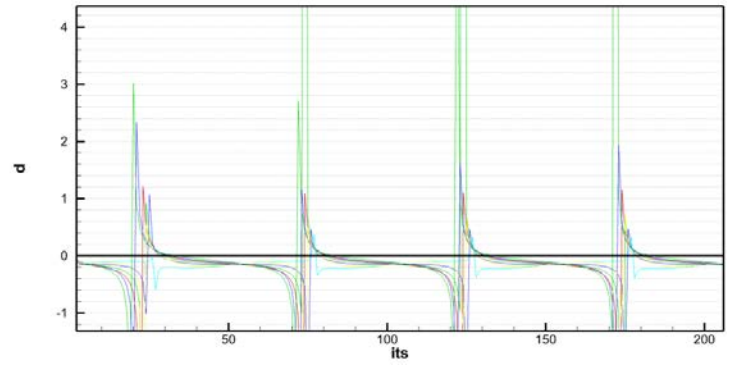

Figure IV.2.1-3 Histories of position of the hydrodynamic center, relative to the pitching axis, for pitch axis at 0.4c from le. (negative is for forward)

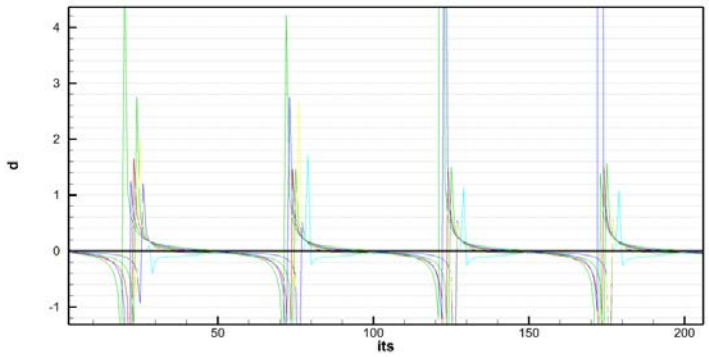

Figure IV.2.1-4 Histories of position of the hydrodynamic center, relative to the pitching axis, for pitch axis at 0.3c from le. (negative is for forward)

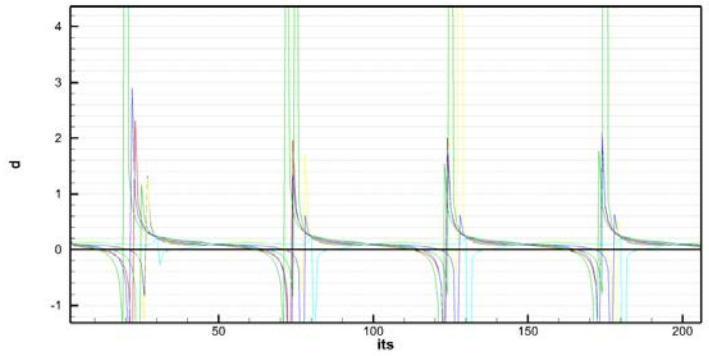

Figure IV.2.1-5 Histories of position of the hydrodynamic center, relative to the pitching axis, for pitch axis at 0.2c from le. (negative is for forward)

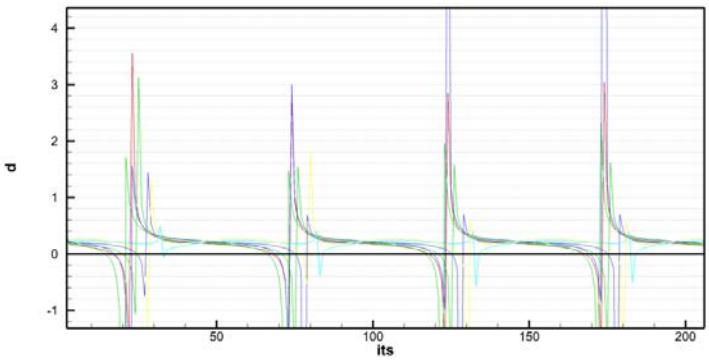

Figure IV.2.1-6 Histories of position of the hydrodynamic center, relative to the pitching axis, for pitch axis at 0.1c from le. (negative is for forward)

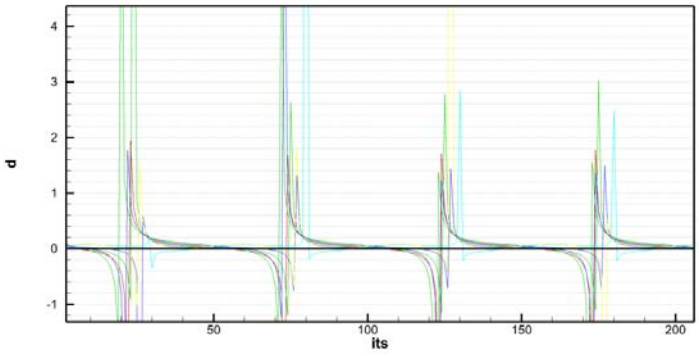

Figure IV.2.1-7 Histories of position of the hydrodynamic center, relative to the pitching axis, for pitch axis at 0.25c from le. (negative is for forward)

IV.2.2 Simulations with spring – loaded Straight wings

Taking all the previous into consideration, Exploratory simulations were made for the straight s/c=4 wing with pitching axis at 0.25c from le and Strouhal number varying from 0.2 to 0.7 and K varying from 1 to 20Nm/rad. It was also set that ζ=1, thus C is calculated accordingly.

In Figure IV.2.2-1 thru Figure IV.2.2-4, the deflection responses of the wing are recorded for varying K and the same Strouhal number in each diagram. The y oscillation is also recorded (dashed line), in order to aid the reader in seeing the phase between motion and response, as well as the influence of parameter K (and C) on deflection amplitude and phase. It is observable, that for the smaller Strouhal numbers, the variation of K between 1Nm/rad and 25Nm/rad produces an even spread of responses (obviously larger deflections for smaller K and vice versa), while for larger Strouhal numbers, the response has much smaller variation. This indicates that the stiffer springs are required for higher Strouhal numbers. Additionally, a difference in phase is observed with the variation of K, as it appears that the phase between pitch and heave decreases for increasing K. This cannot be attributed to the variation of C that happens along, as the increase of C is expected to delay motions. Additionally, the increase of heave amplitude, appears to cause increase of deflections for the same K and Str. Last but not least, in the same manner Ct-theta diagrams were produced for prescribed motions, Ct-K diagrams are presented in Figure IV.2.2-5 and Figure IV.2.2-6. Even in these very first exploratory simulations, efficiency of the order of 70% is calculated, but for a very narrow area of parameters.

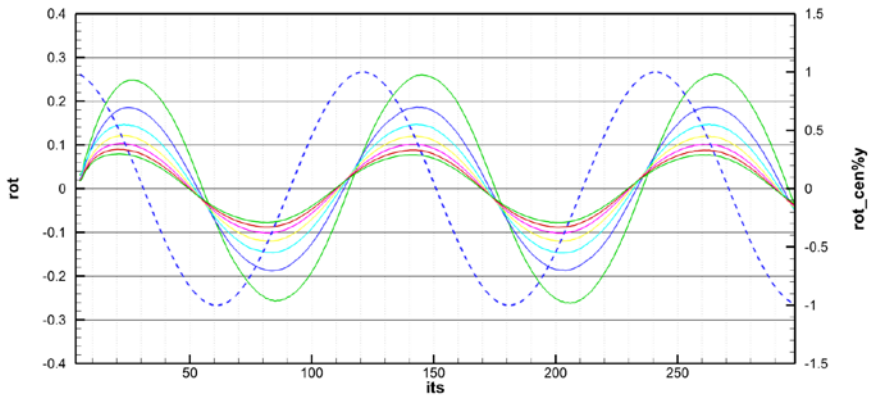

Figure IV.2.2-1 Responses (rot) in radians, for varying K(1-25Nm/rad, increment=4, largest amplitude for smallest K) for straight wing s/c=4 at Str=0.2 h/c=1 Dashed line is for the y position of the rotation center (pitching axis)

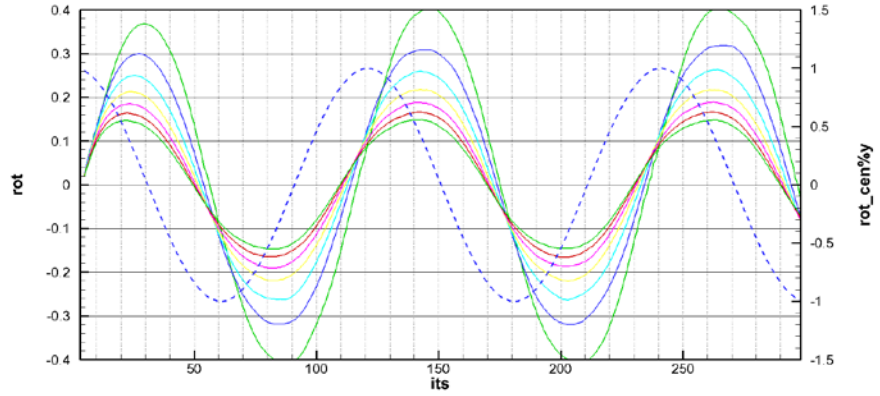

Figure IV.2.2-2 Responses (rot) in radians, for varying K(1-25Nm/rad, increment=4, largest amplitude for smallest K) for straight wing s/c=4 at Str=0.3 h/c=1 Dashed line is for the y position of the rotation center (pitching axis)

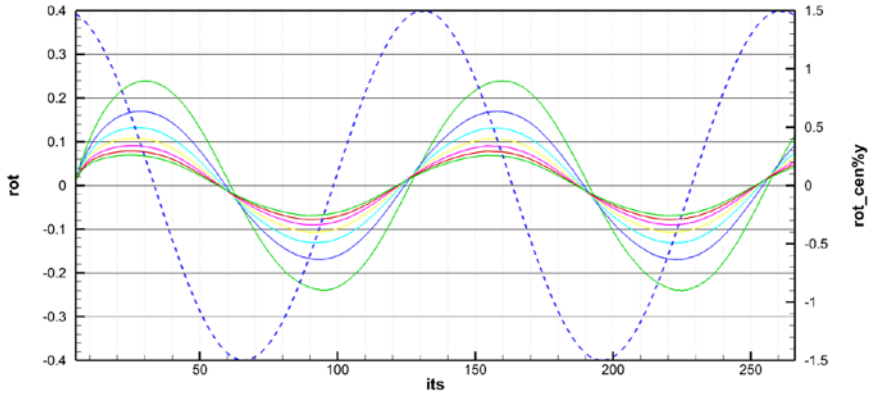

Figure IV.2.2-3 Responses (rot) in radians, for varying K(1-25Nm/rad, increment=4, largest amplitude for smallest K) for straight wing s/c=4 at Str=0.2 h/c=1.5 Dashed line is for the y position of the rotation center (pitching axis)

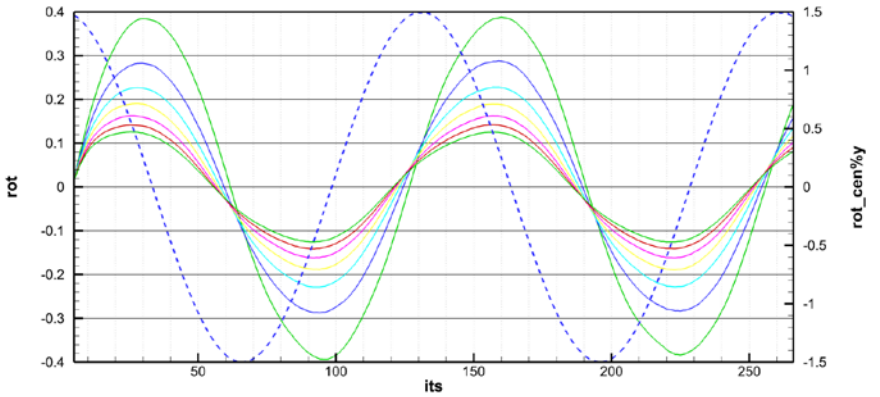

Figure IV.2.2-4 Responses (rot) in radians, for varying K(1-25Nm/rad, increment=4, largest amplitude for smallest K) for straight wing s/c=4 at Str=0.3 h/c=1.5 Dashed line is for the y position of the rotation center (pitching axis)

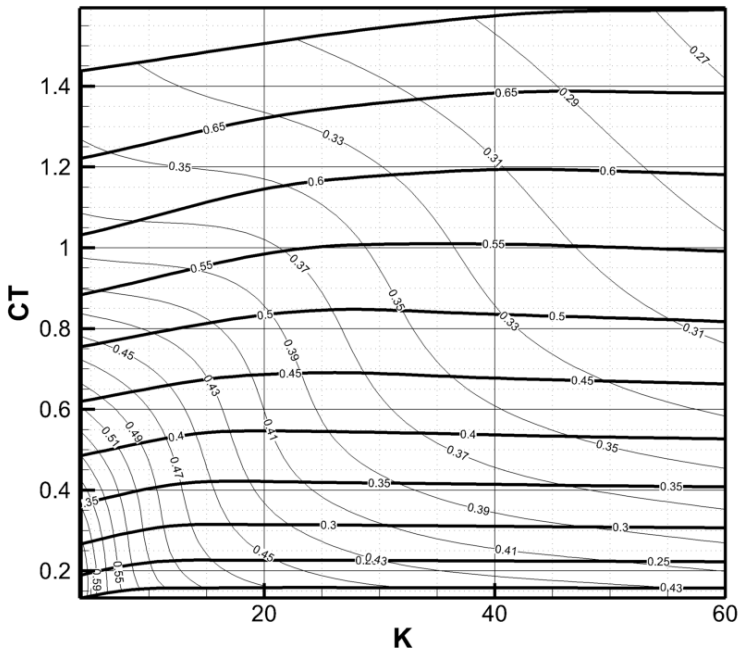

Figure IV.2.2-5 Ct-K chart for a straight wing S/c=4, h_o/c=1, under simple harmonic motion. Thicker lines are for Strouhal number and thinner, are for efficiency.

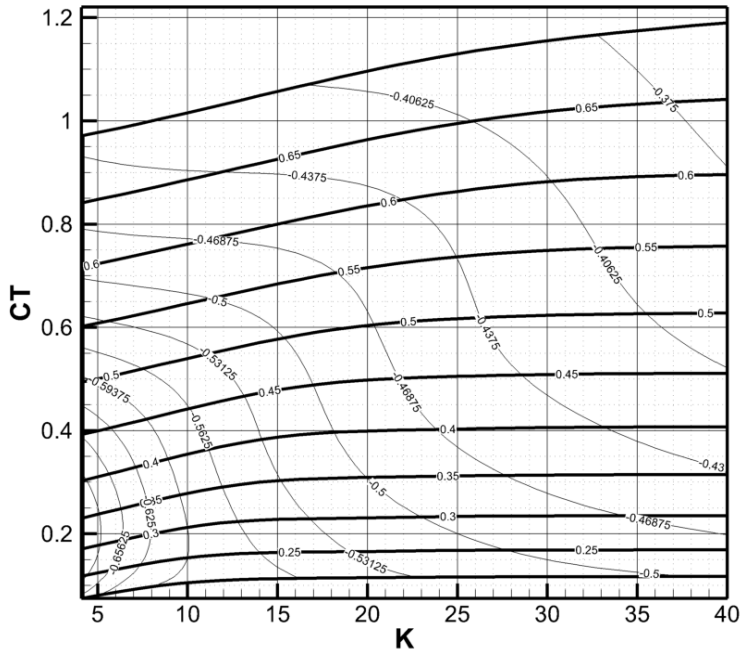

Figure IV.2.2-6 Ct-K chart for a straight wing S/c=4, h_o/c=1.5, under simple harmonic motion. Thicker lines are for Strouhal number and thinner, are for efficiency.

IV.3 Motions through Active Pitch Control

As discussed in IV.1.2, the program was developed to have the ability of executing a wing pitching motion that is result of active pitch control. Initial exploratory results are presented for both straight and swept wings and the effects of parameters are explored for harmonic and pseudo-random motions.

As expected and discussed in the previous paragraph, a spring loaded wing, will respond well in a very narrow area of parameters and will most likely respond only to the main frequency of a random excitation. Thus, an Actively Pitch Controlled (APC) wing is considered to be more promising for an open sea application, as it would adapt to the environment better. The same principle can be extended to the case of an energy saving device (heave motion taken from ship motions (Belibassakis and Politis 2013, Bøckmann and Steen 2014, Filippas and Belibassakis 2014, Politis and Politis 2014)).

IV.3.1 Time domain results for wings with APC

In Figure IV.3.1-1 thru Figure IV.3.1-3 time domain results for select cases of Actively Pitch Controlled wings are presented. The heave motion is plotted in dashed line (rot_cen%y –y motion of the rotation center-), along with the rotation response (rot), the instantaneous angle of attack (local_attack) and the instantaneous value of w(t) (ww). The solid line shows the produced thrust (fx). As it can be seen, the Target A_{max} is achieved for the most of the time and substantial thrust is produced throughout the evolution of the simulation. Even in pseudo-random motions, the same behavior is achieved, showing the worthiness of the algorithm for further investigation

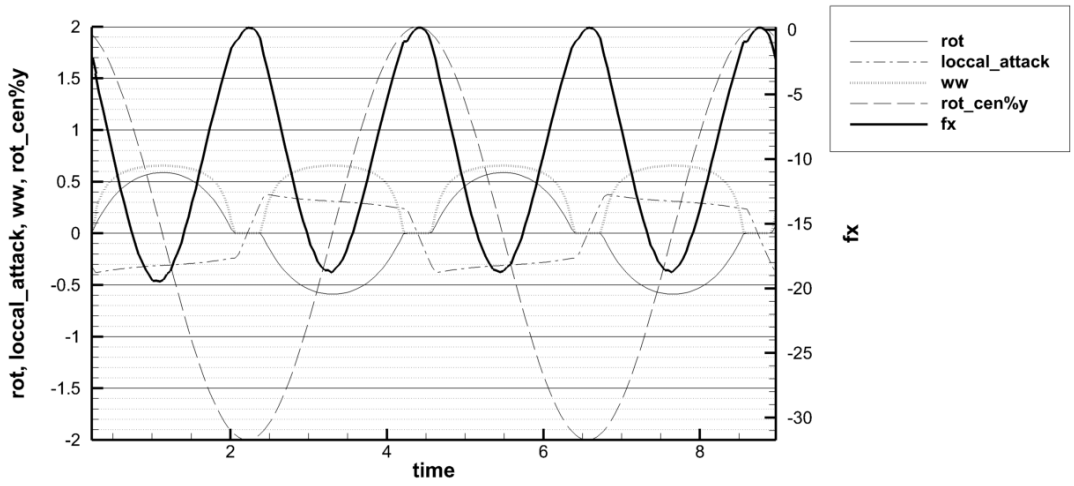

Figure IV.3.1-1 Time series of simulation of a Controlled wing of S/c=4 at Str=0.4 and Target A_{max}=17°. Thin solid: selected pitch of wing (rad), Dash dot: instantaneous angle of attack (rad), Dotted: selected instantaneous w factor, Dashed: heave motion of the wing, Thick solid: Instantaneous Fx/ρ (negative is thrust)

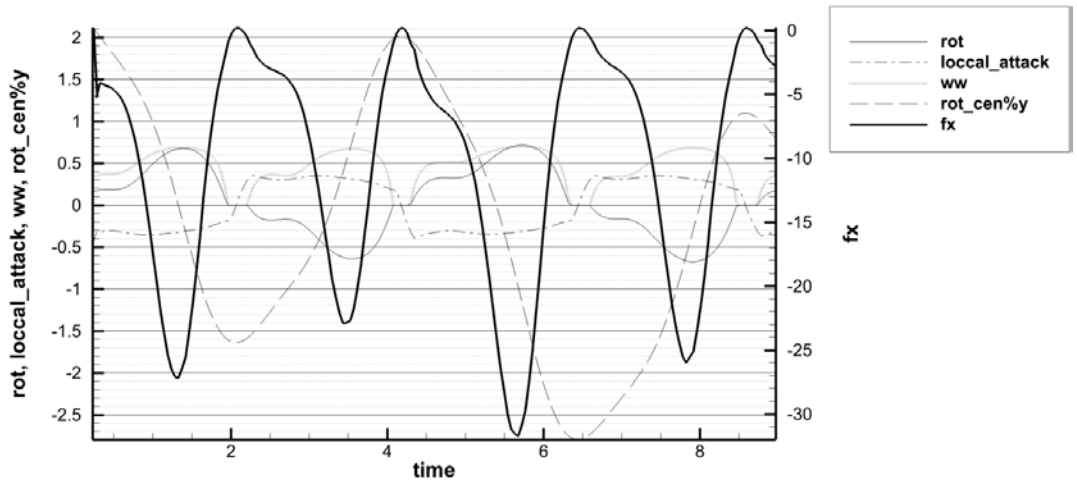

Figure IV.3.1-2 Time series of simulation of a Controlled wing of S/c=4 at Str=0.4 plus four random sinusoidal motions and Target $A_{max}=17^{o}$. Thin solid: selected pitch of wing (rad), Dash dot: instantaneous angle of attack (rad), Dotted: selected instantaneous w factor, Dashed: heave motion of the wing, Thick solid: Instantaneous Fx/ρ (negative is thrust)

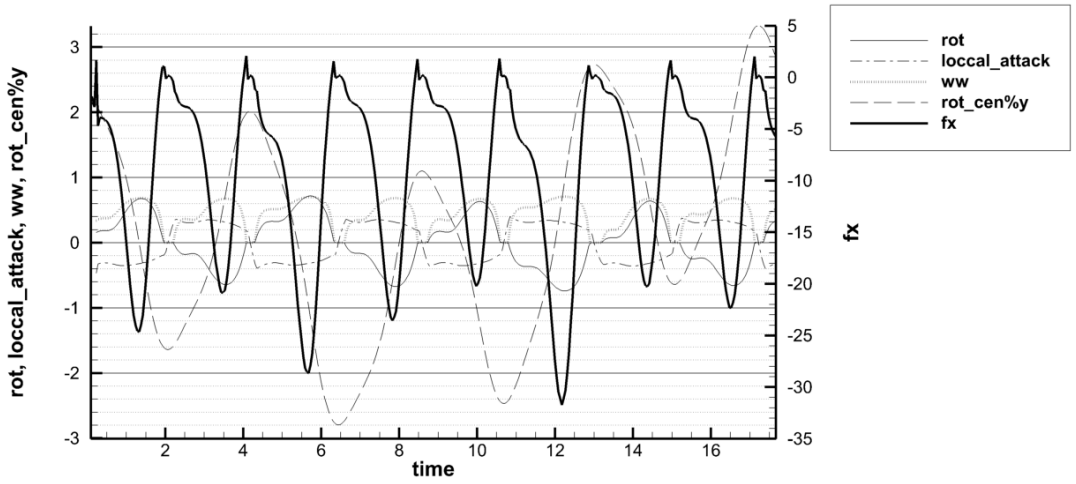

Figure IV.3.1-3 Time series of simulation of a Controlled wing of S/c=4 at Str=0.4 plus four random sinusoidal motions and Target $A_{max}=17^{o}$. Thin solid: selected pitch of wing (rad), Dash dot: instantaneous angle of attack (rad), Dotted: selected instantaneous w factor, Dashed: heave motion of the wing, Thick solid: Instantaneous Fx/ρ (negative is thrust)

IV.3.2 Time averaged results for Straight Wings with APC

Systematic simulations have been conducted for both spimple harmonic heave and pseudo – random heave added to the harmonic. From the time averaged results, systematic diagrams have been produced in the same spirit as previous ones, but with the value of Target A_{max} as the horizontal axis parameter. Substantial thrust and high efficiency (over 74%) are observed.

For the pseudo-random cases (Figure IV.3.2-3, Figure IV.3.2-4), the curves of the maximum angle of attack, appear erratic, but it is understandable, as there may be moments when angles of attack are much higher than desired. The standrard deviation of the angle of attack might be a better evaluator for such cases.

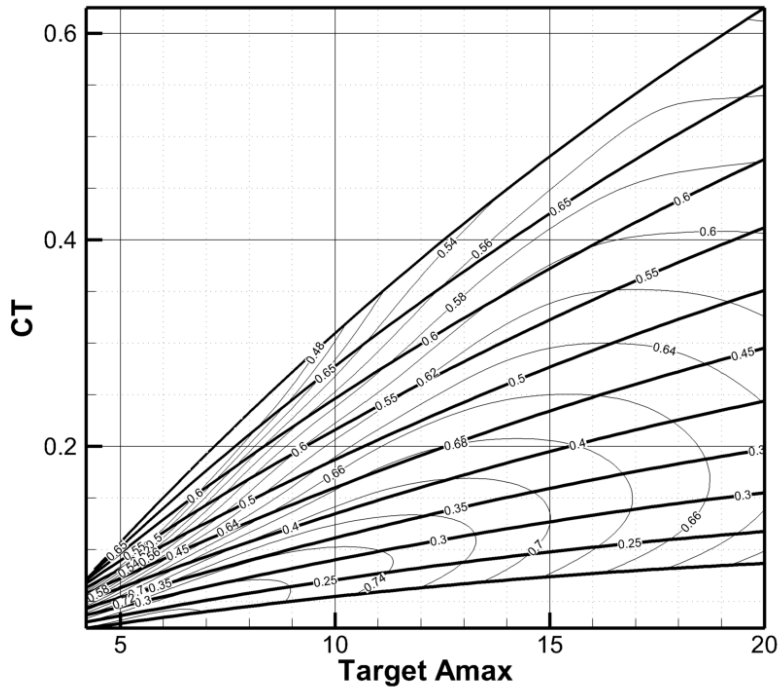

Figure IV.3.2-1 Ct-Target A_{max} chart for a straight wing S/c=4, h_o/c=2, under simple harmonic motion. Thicker lines are for Strouhal number and thinner, are for efficiency.

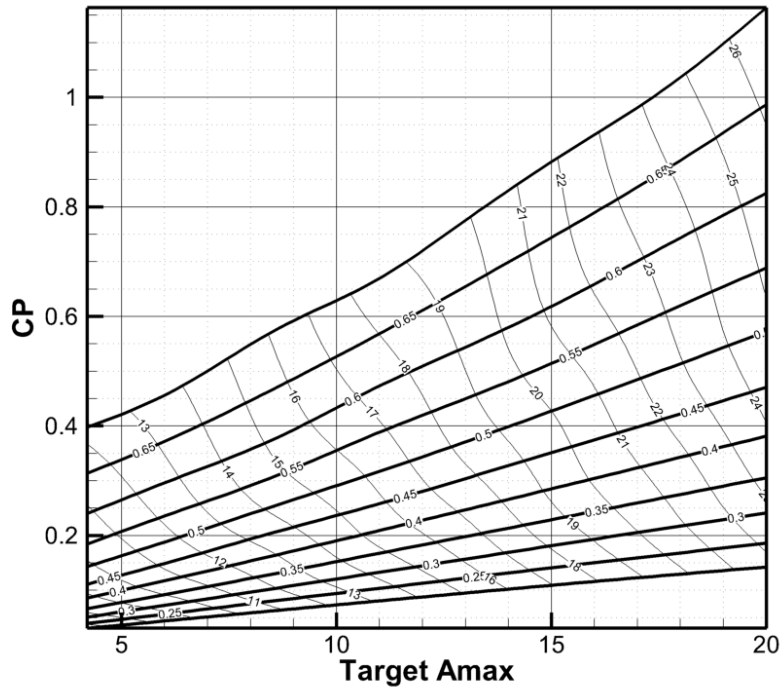

Figure IV.3.2-2 Cp-Target A_{max} chart for a straight wing S/c=4, h_o/c=2 under simple harmonic motion. Thicker lines are for Strouhal number and thinner, are for achieved maximum angle of attack

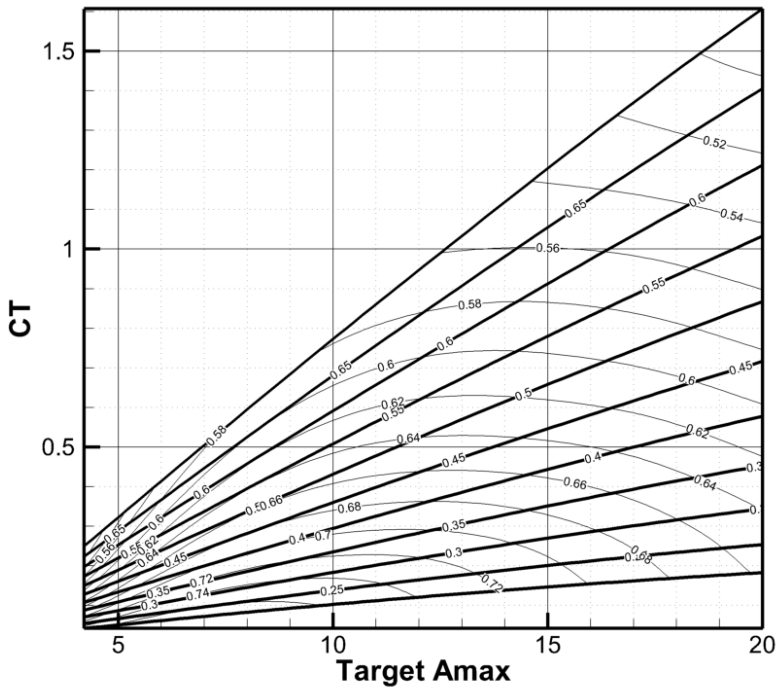

Figure IV.3.2-3 Ct-Target A_{max} chart for a straight wing S/c=4, h_o/c=2, under pseudo-random motion. Thicker lines are for Strouhal number and thinner, are for efficiency.

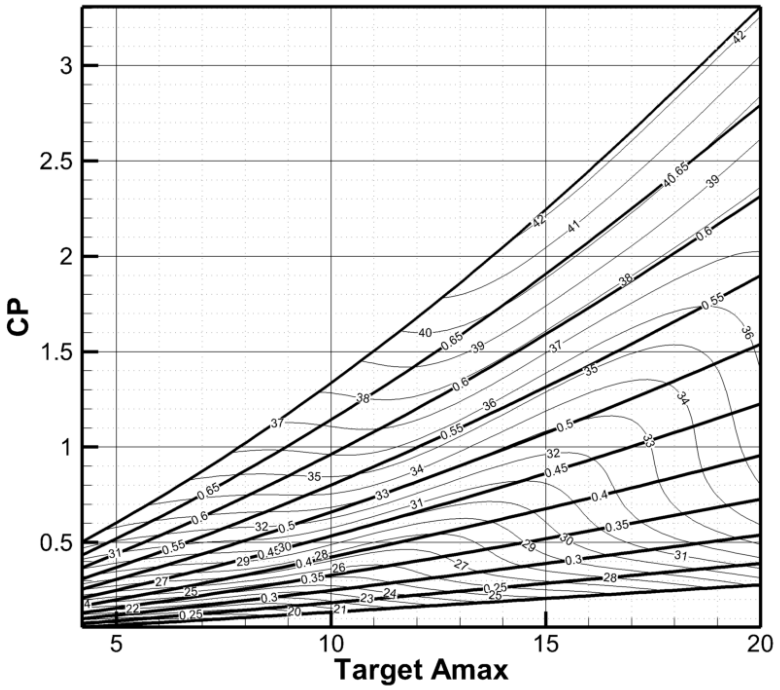

Figure IV.3.2-4 Cp-Target A_{max} chart for a straight wing S/c=4, h_o/c=2 under pseudo-random motion. Thicker lines are for Strouhal number and thinner, are for achieved maximum angle of attack

IV.3.3 Time averaged results for Swept Wings with APC

As in the previous paragraph, Systematic simulations have been conducted for the same parameters of motion, but for a 30 degree swept wing. Similar behaviors are observed, but with smaller thrust and larger efficiency (over 78%). This difference can be attributed to the fact that the angle of attack is not the same for the whole span of the wing, and the mechanism behind this effect is to be ivestigated further.

Last but not least, it should be noted, that the same charts can also be used in the case of an energy saving device (wavepropulsor) in a slightly different context. Power coefficient indicates the energy extracted from motions (motion reduction) and the efficiency is the efficiency of the process of conversion of kinetic energy to thrust.

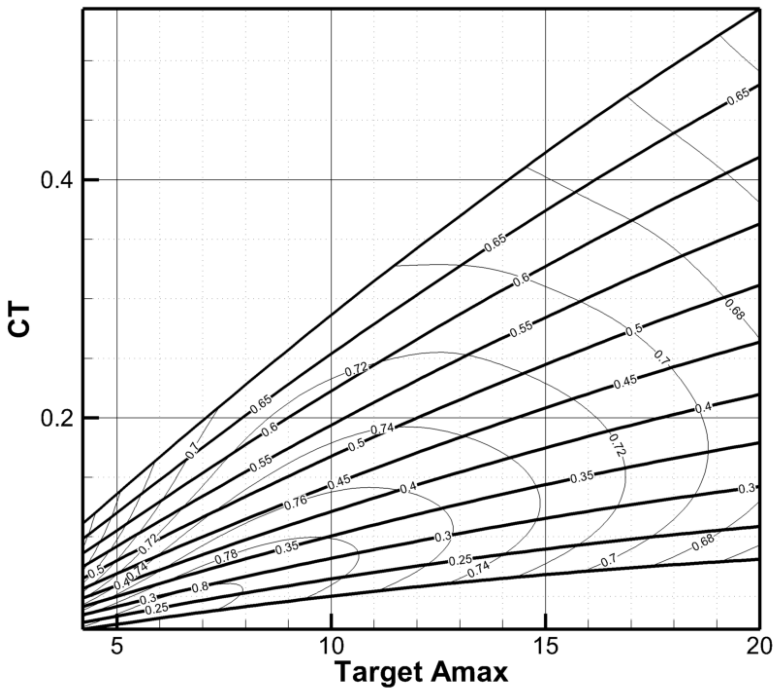

Figure IV.3.3-1 Ct-Target A_{max} chart for a 30° swept wing, S/c=4, h_o/c=2, under simple harmonic motion. Thicker lines are for Strouhal number and thinner, are for efficiency.

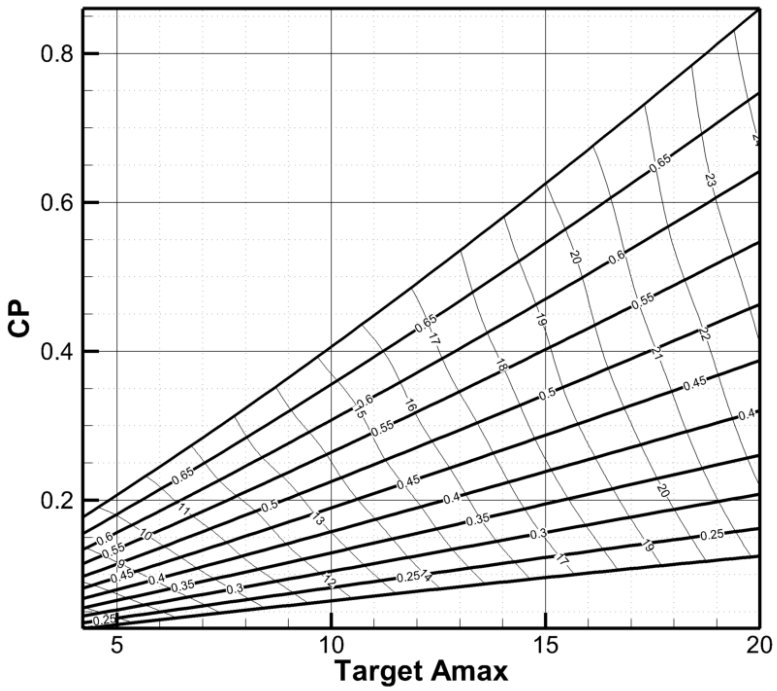

Figure IV.3.3-2 Cp-Target A_{max} chart for a 30° swept wing S/c=4, h_o/c=2 under simple harmonic motion. Thicker lines are for Strouhal number and thinner, are for achieved maximum angle of attack

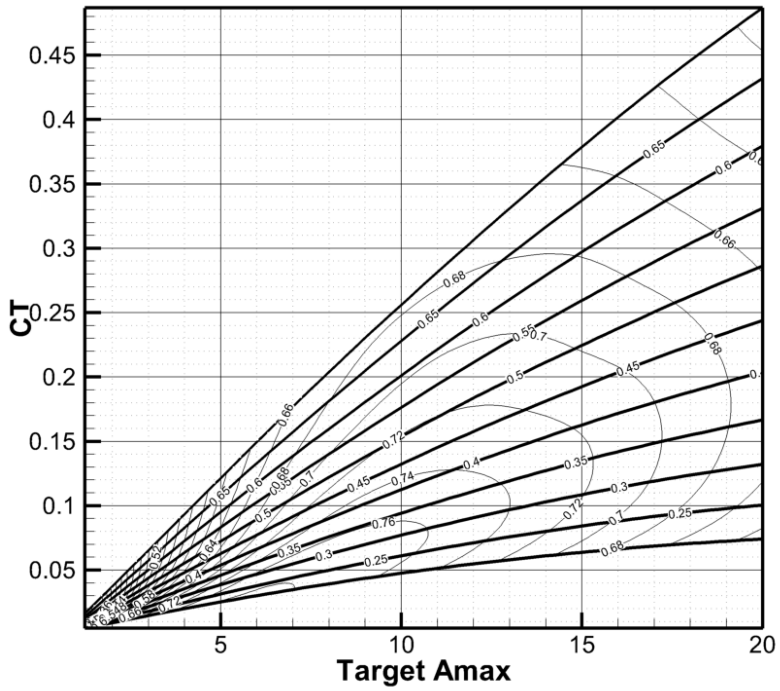

Figure IV.3.3-3 Ct-Target A_{max} chart for a 30° swept wing S/c=4, h_o/c=2, under pseudo-random motion. Thicker lines are for Strouhal number and thinner, are for efficiency.

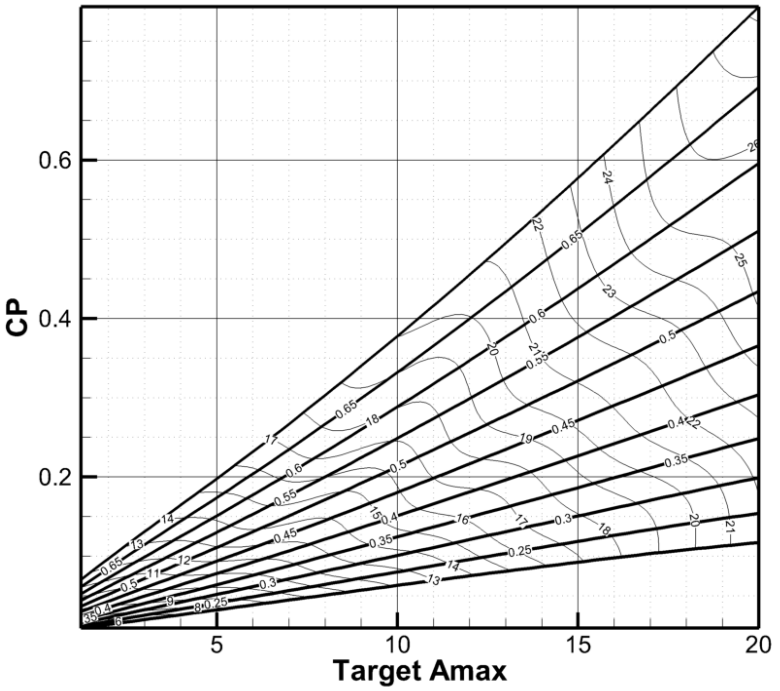

Figure IV.3.3-4 Cp-Target A_{max} chart for a 30° swept wing S/c=4, h_o/c=2 under pseudo-random motion. Thicker lines are for Strouhal number and thinner, are for achieved maximum angle of attack

Part V CONCLUSION

Closing a package of work is among the most difficult tasks, as answers bring up new questions and solutions open the possibility of new explorations, which in turn lead to new problems. In this part, a review of the previously analysed work is made, discussing its key points and their contribution to the goal of producing optimal marine propulsors and/or energy saving systems. Proof of thesis is presented and concept designs of ships operating under Biomimetic propulsion are proposed. Last but not least, the open questions and new areas of exploration are acknowledged and future work is proposed in the area of development of the simulation methods, of extending the existing investigations and of pushing the development of a biomimetic marine propulsor / energy saving system as an actual, realizable device.

V.1 Review of content

In order to start the investigations on the subject of biomimetic marine propulsion, a thorough investigation of the existing literature was made. A collection of more than 3000 papers was made, from a wide spectrum of fields, ranging from biology, to marine engineering, and from numerical simulations to robotics. The larger part of the literature concerns biology, which may provide with inspiration, but is not very helpful in explaining the reasons and the underlying phenomena. Additionally, almost all robotic applications are made for micro air vehicles or autonomous underwater vehicles, which operate at a much smaller scale and take advantage of different phenomena. From the limited useful literature, inspiration was taken and data for comparison and verification of the developed tools were extracted.

The CFD program UBEM, originally developed by Professor Politis for simulating unsteady propeller motions (Politis 2004) and extended to simulating any given body in unsteady motion (Politis 2009, 2011), was employed, and data generation (geometry generation and animation) programs were created in order to be able to simulate any given wing/body (or more than one) under any harmonic flapping motion given by the user, as well as any other prescribed motion, as a sequence of many simple motions. UBEM was accelerated by using GPU computing for the solution of linear systems, thus allowing for the use of nonlinear boundary condition (pressure kutta). All the above were used as modular parts of a larger program, which can apply systematic variation to problem parameters and produce results of systematic simulations.

Using the aforementioned programs, systematic simulations were conducted and series were produced for Single wing, double (twin) wing, the Flexible Oscillating Duct and the Flexible Elliptic Oscillating Duct, while initial investigations of bird flight cases were made. The systematic investigations showed efficiencies of magnitude significantly greater than that of a conventional propulsor for all configurations. A design method, that uses diagrams produced from the systematic simulations, was developed and applied for virtual paradigms of ships. The results were compared to conventional propulsor design applications for the same vessels, and the advantage of biomimetic propulsors is clear. Single wing propulsors were estimated to be in the order of 5% better than conventional, while double was at 6%. FOD was at 11% and FEOD at 6% better than the best performance of an ideal conventional propeller.

After the systematic investigation of prescribed motions, the ability to simulate the behavior of a wing on spring loaded mountings was also added to the programs used along with an active control method for the pitch. Initial investigations show that spring loaded wings have considerable efficiency and thrust at a very limited range of parameters, while the actively controlled wings produce increased thrust for almost the same (better than conventional) efficiency. Both cases are not proving to be much better than wings of fully prescribed motion, but the prospective of operating and adapting in a wavy environment, where the motion of the wing through water is not a pure sinusoidal one, makes the applications very promising and worth to be investigated further. Especially in passenger vessels and multihulls, which suffer from motions and always require speed, such a mechanism that absorbs energy from the motions and turns it into thrust, is most desirable.

V.2 Proof of thesis

As already stated in the introduction, thesis of this work is that production of a propulsor that employs biomimetic characteristics is feasible and more efficient, compared to conventional systems, at a level that it can also be cost effective. As it has been proven with the design paradigms, all examined systems are advantageous compared to conventional propulsors. Considering the cost, the construction and maintenance of a simple wing is considerably smaller than that of a propeller, while it can also operate in shallow water and has minimal risk of rope entanglement or marine animal injury.

To the existing statement that a driving mechanism for an oscillating wing would be inefficient or have strength issues, it can be argued that even with traditional mechanisms like a crankshaft or a scotch yoke, when operating at low frequencies and have large size, mechanical losses are minimal. Additionally, applications like the O-Foil™, prove that construction is not an issue, but the operation is. More specifically, with almost the same mechanism, it is possible to give great efficiency or small, depending on the determination of the pitching motion and the pitching axis. The energy required for the pitching part of the motion, is an order of magnitude smaller than the total energy, while for some cases, it is even negative (energy has to be extracted), making the control of the pitching motion an issue solvable with existing technologies. Furthermore, with proper control of the pitching motion, it is possible to produce additional thrust in waves, by absorbing energy from the ship motions. Considering this prospect even further, a passive system could operate as an energy saving device. Last but not least, new technologies like linear motors, may lead to further simplification of construction, while exotic materials like electroactive polymers, can lead to deformable wings like the bird cases studied which could be an interesting application for hydrofoiling crafts or the FOD propulsor.

V.3 Proposed designs and considerations

After design applications on virtual paradigms have been presented and proven to be worthy of consideration, presentation of proposed designs for full scale application, (either as a propulsor, or as an energy saving system or as a part of a greater "zero emissions" design), is in order. Alternative applications are presented and considerations, both on hydrodynamic and structural aspects are discussed. The feasibility of each system, regarding existing and under development technologies is also taken into consideration. It should be cleared out, that detailed designs and analysis of a final system spans well beyond the purposes (and available means) of this work. Thus, only concept designs enriched with the knowledge gathered so far are to be discussed and considerations are to be discussed, in order to open the way for future work.

V.3.1 Biomimetic system as Main Propulsor

As previously discussed, the most promising configuration for a propulsor, is that of a horizontal wing. For reasons of redundancy and increased manoeuvrability, two such wings supported by three wing shaped vertical struts are proposed. The supporting wings can be equipped with flaps, in order to serve as rudders. In Figure V.3.1-1 and Figure V.3.1-2 a ship equipped with flapping wing propulsors as main drive, along with energy saving bow and bottom wings is illustrated. With red colour are the thrust producing surfaces, while with green are control and auxiliary surfaces. The added energy saving wings, are producing additional stability and manoeuvrability, while reducing consumption even further.

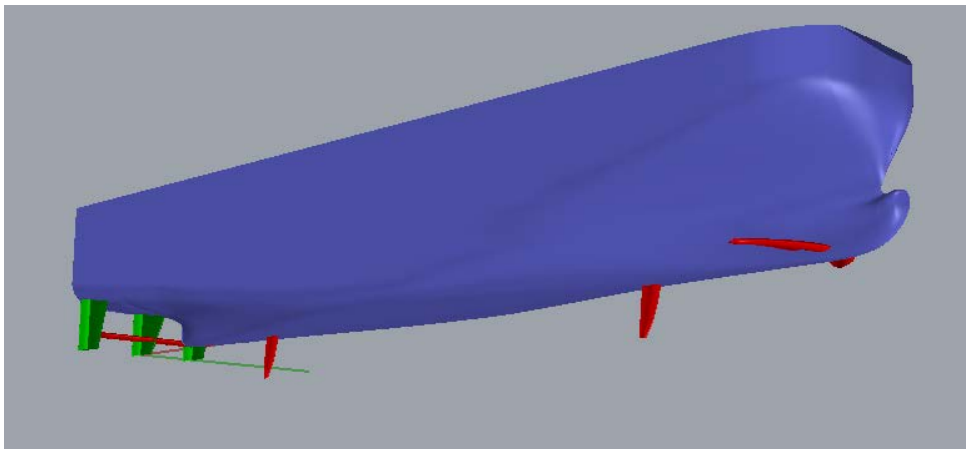

Figure V.3.1-1 Ship equipped with flapping wing propulsors as main drive, along with energy saving bow and bottom wings. Bow view

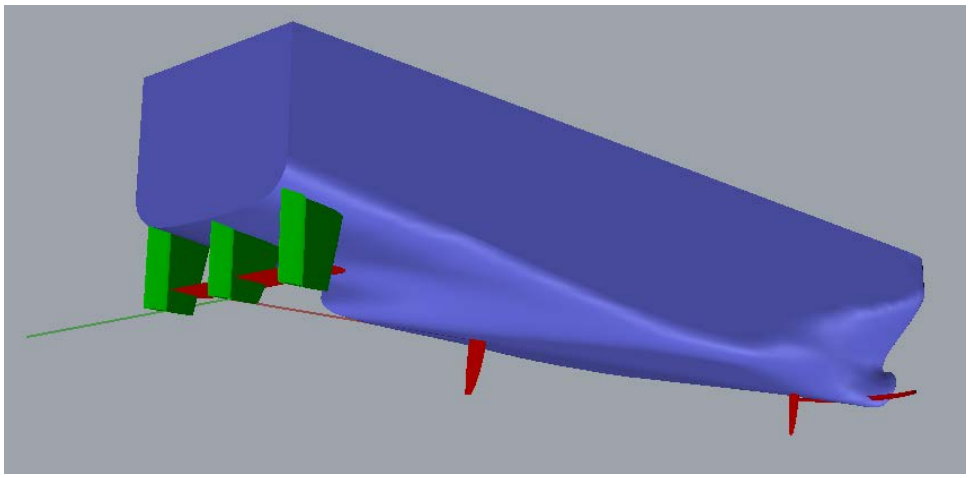

Figure V.3.1-2 Ship equipped with flapping wing propulsors as main drive, along with energy saving bow and bottom wings. Stern view

V.3.2 Biomimetic System as Energy saving device

The idea of employing the characteristics of an oscillating wing for the production as an energy saving device, has been introduced in the past as described by Nikolaev et al (1995) and Jakobsen (1983). Such designs are being reviewed and reconsidered under the light of new technologies and experience. Figure V.3.2-1 and Figure V.3.2-2 present a conventional ship, equipped with (passive) wings, acting as energy saving systems. Horizontal wings fore and aft are for energy extraction from heaving and pitching motions, while the vertical is for extraction of energy from rolling motions. The horizontal wings are located as close to the baseline as possible and the longitudinal position has to be investigated in order to maximize effects, while minimizing the risk of damage from slamming.

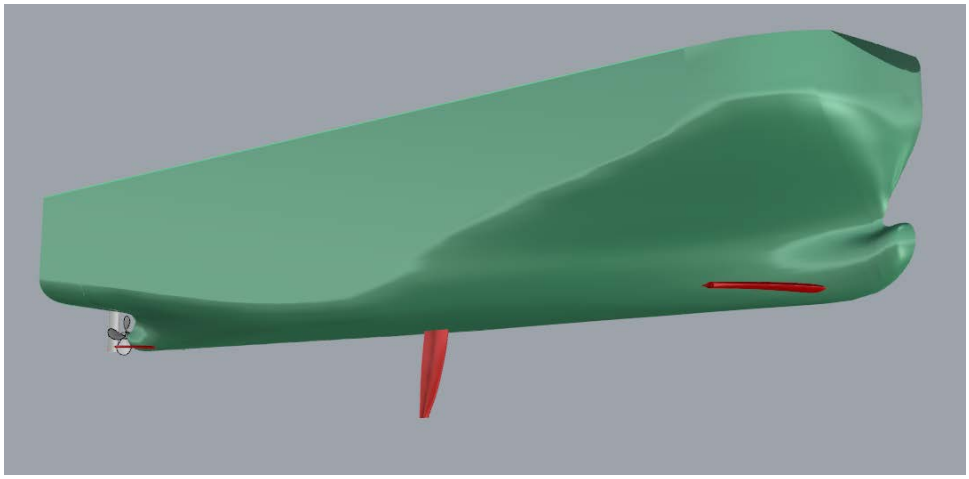

Figure V.3.2-1 Conventional ship equipped with wings working as energy saving systems Bow View

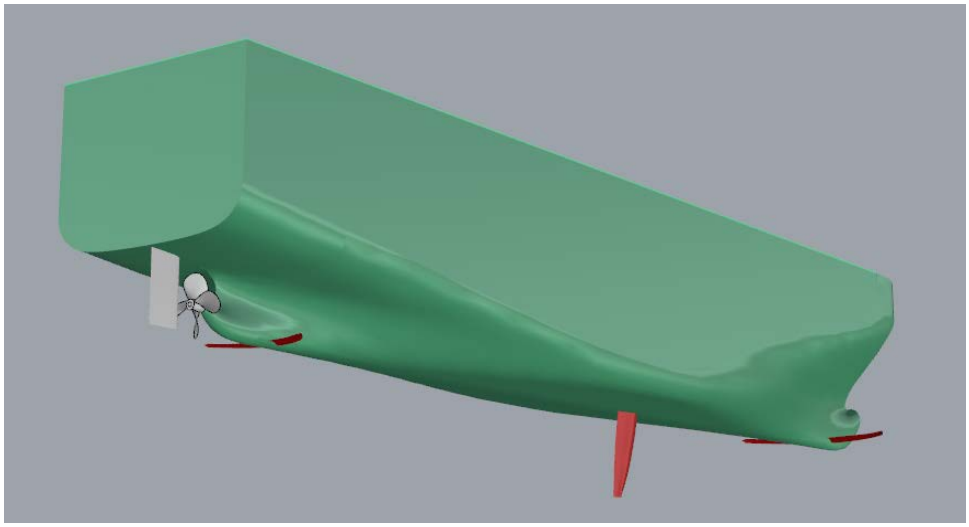

Figure V.3.2-2 Conventional ship equipped with wings working as energy saving systems Stern View

V.3.3 Multihull Applications

Multihulls are a special case, for which wing propulsors and/or energy saving systems show increased advantages, as multihulls are much wider allowing for larger wings, while operating at higher speeds. Additionally, the void between hulls allows for much more undisturbed flow to the wing and protects the wing from collisions. Last but not least, multihulls are known for suffering from motions in rough seas, which means that there is a large potential for the energy saving application.

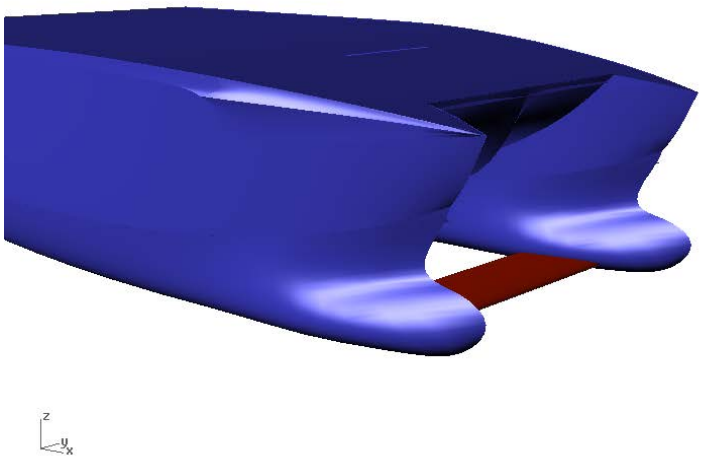

Figure V.3.3-1 Catamaran equipped with wings working as energy saving systems Bow View

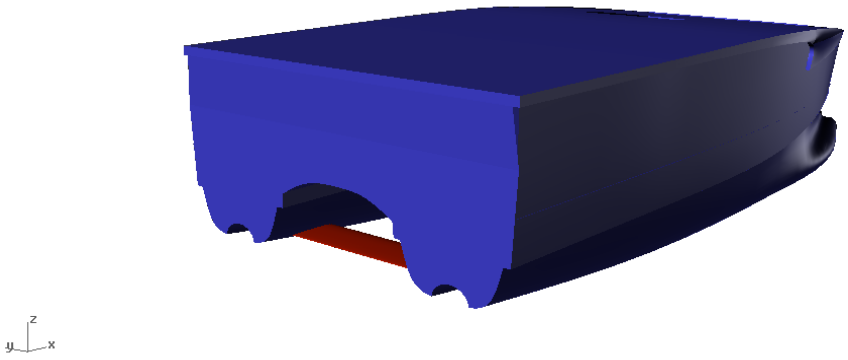

Figure V.3.3-2 Catamaran equipped with wings working as energy saving systems Stern View

V.3.4 Zero emissions application

A last design, in the quest for a more efficient ship, is a wind/wave powered ship, equipped with wingsails (green wings) which will drive the ship using wind power as sails. Horizontal wings fore and on the aft keel turn energy from ship motions to thrust, while a fore wing, acts as an additional keel but also takes energy from rolling motions. The angled wings aft, can take energy both from roll and heave-pitch, while also working as rudders. The modified bow, can allow for the wing to be lower and further in front, while reducing bow slamming effects. The middle part is exactly the same as a common "boxy" big ship like a bulk carrier or tanker. Of course, these concept designs are not of a detailed design, but combine the knowledge produced in this work with existing technologies in a feasible manner, giving a starting point for further discussion and investigation.

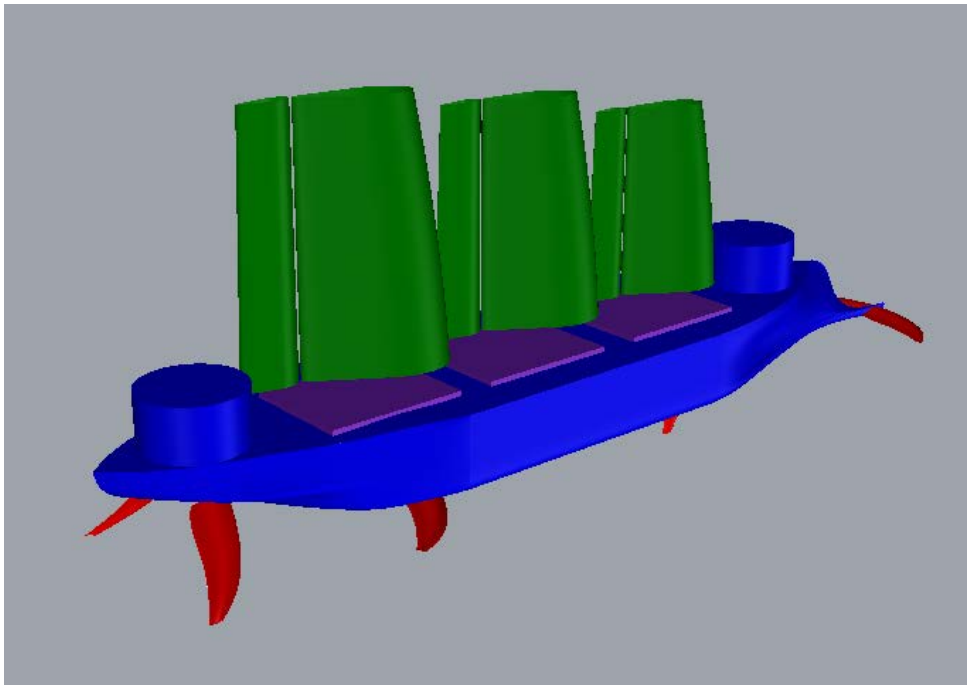

Figure V.3.4-1 Zero emissions concept. Stern View

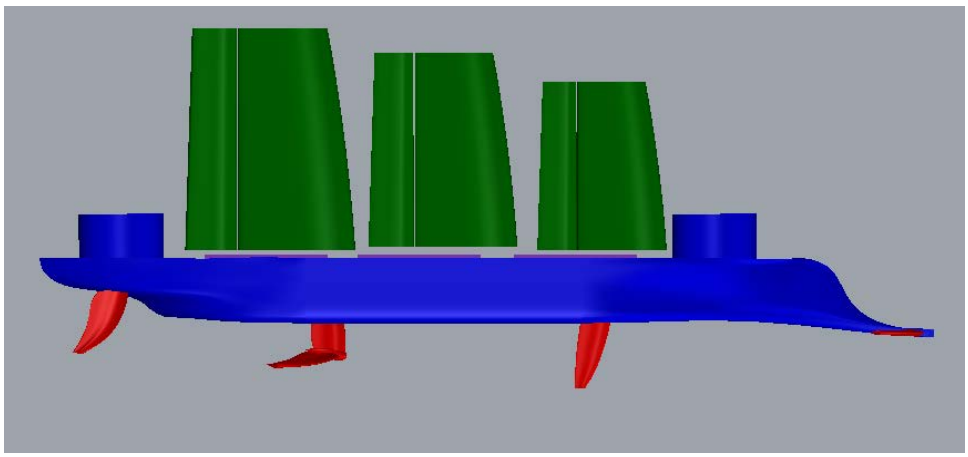

Figure V.3.4-2 Zero emissions concept. Side View

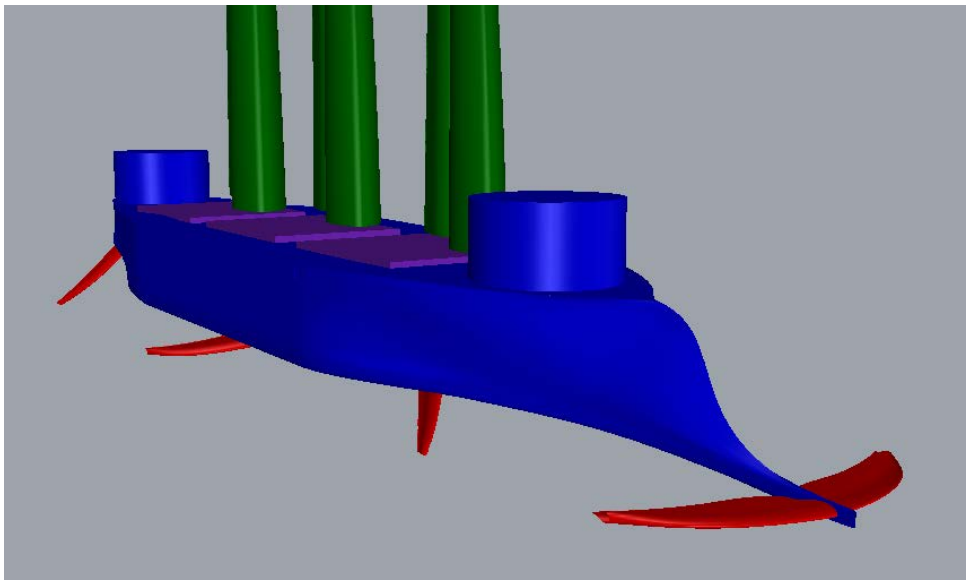

Figure V.3.4-3 Zero emissions concept. Bow View

V.4 Future work

With the thesis of this work proven and proposed concept designs set, the road is shown for additional investigations and further development. Future work can be categorized into the further development of simulation methods, extension of the existing investigations or new investigations via application of the existing or proposed tools and the development of a fully functional biomimetic marine propulsor/energy saving system. In the following last paragraphs, each category is analysed.

V.4.1.1 Development of methods

The solver code UBEM has been accelerated by using GPU for the solution of linear systems. Such acceleration can be extended to the free wake deformation calculations, which is the second most demanding part of the code. Such acceleration is necessary when long simulations (more than three periods) are made and would bring the ability of making more, larger in size and longer in time and more complex simulations in less time.

Even though the simulations for spring loaded wings appear to be working properly, alternative methods for the solution of dynamics would allow for comparisons, while coupling the programs with a Finite Element Method for the simulation of elastic wings, will open the road for even more investigations. Additional to coupling the wing dynamics with the solver, it is possible to couple all the programs with a subprogram that would solve the ship dynamics and attempt the solution of the fully coupled problem.

Last but not least, in this whole work, there has been no simulation of any free surface effects, as the wing(s) was assumed to be deeply submerged. However, it is not necessary that a biomimetic propulsor will always operate (relatively) far from the free surface and it is not clear that the free surface interaction will not be beneficial for energy extraction from waves.

V.4.1.2 Extended investigations

Regardless of the size of the developed series, there are still several areas not covered in the area of systematic investigations; even for the prescribed motion simulations, there are several open problems. The series for double wings have to be extended to the detail of the single wing series, while, even for the single wing, the outline has not been examined closely and different shapes, resembling whale tails are definitely worthy of investigation. With the examination of swept and other shapes of wing, the position of the pitching axis and its effects is also an issue to be addressed, while the effect of bending is also of major interest. Systematic investigations of bird flight, either with prescribed motion of wings or with controlled or flexing motions, could prove useful for hydrofoiling applications or added manoeuvrability.

For the case of spring loaded wings, only the starting point was shown in this work. A wider systematic variation of parameters is needed, while also investigating the effect of the pitch

axis position and the damping factor. The effects of different shapes are another big issue, while the use of springs of nonlinear stiffness may show a great potential.

Almost the same apply for the case of actively controlled wings. Variation of the position of pitching axis is to be investigated, but also it is interesting to see its performance for different wing shapes. Different methods of control need to be applied, as well as more sophisticated systems, which would use the data from the existing simulations for system recognition that would lead to the creation of a state-space controller for thrust production in random motions.

V.4.1.3 Biomimetic Propulsor Application Development

To the final objective of producing an actual biomimetic propulsor, several key steps have to be taken. From the design point of view, strength criteria have to be developed, in order to determine the required thickness for each application. The same applies with cavitation criteria, for the determination of the wing surface area (thus leading to chord length definition).

For the creation of a final product of biomimetic propulsor, experiments have to be conducted, for proof of concept, of propulsor and self-propelled ship, in order to determine hull interaction parameters which will allow for actual and undisputed applications and comparisons to be conducted.

Last but not least, serious work needs to be done on the detailed design of such systems, from the mechanical engineering part, to the structural of the wing and supports, up to the retrofit required for the application on an existing ship. The experience form old patents and the latest full scale applications can prove fertile ground, but original thinking may also be necessary to overcome obstacles the previous found.

V.5 Acknowledgements

This research has been co-financed by the European Union (European Social Fund – ESF) and Greek national funds through the Operational Program "Education and Lifelong Learning" of the National Strategic Reference Framework (NSRF) - Research Funding Program: Heraclitus II. Investing in knowledge society through the European Social Fund.

The author of this thesis would also like to express his gratitude to his supervising professor and the committee for the knowledge, advice and cooperation they offered. Additional thanks are to be given to the neighboring office researchers and PhD Candidates, P. Hasapogiannis, J. Prospathopoulos, V. Papakonstantinou, J Georgiou, K. Politis, S. Polyzos, K. Sfakianaki, G Papadakis, D. Manolas, M. Manolesos, I. Tsantili, E. Filippas, Z. Kapelonis, C. Papoutselis, P. Sxinas for their valuable help, advice, remarks and tolerance.

Additional thanks are to be given to the Greek Section of SNAME and especially to Mr. P. Lalangas, P. Dimitriadis, N. Dionyssopoulos, K. Maounis and Dr. J. Kokkarakis for their support, and sharing of Knowledge.

Last but not least, the author wants to express his utmost gratitude to his family for doing more than what they could to help during this effort.

REFERENCES

Abbott I. & Doenhoff, H. (1959). Theory of Wing Sections, Dover.

Anderson, J. M. and N. K. Chhabra (2002). "Maneuvering and stability performance of a robotic tuna." Integrative and Comparative Biology **42**(1): 118-126.

Anderson, J. M., K. Streitlien, D. S. Barrett and M. S. Triantafyllou (1998). "Oscillating foils of high propulsive efficiency." Journal of Fluid Mechanics **360**: 41-72.

Basu, B. C. and G. J. Hancock (1978). "UNSTEADY MOTION OF A TWO-DIMENSIONAL AEROFOIL IN INCOMPRESSIBLE INVISCID FLOW." Journal of Fluid Mechanics **87**(pt 1): 159-178.

Baxevanou, C. A., P. K. Chaviaropoulos, S. G. Voutsinas and N. S. Vlachos (2008). "Evaluation study of a Navier–Stokes CFD aeroelastic model of wind turbine airfoils in classical flutter." Journal of Wind Engineering and Industrial Aerodynamics **96**(8–9): 1425-1443.

Belibasakis, K. A. and G. K. Politis (1998). "A nonlinear velocity based boundary element method for the analysis of marine propellers in unsteady flow." International Shipbuilding Progress **45**(442): 93-133.

Belibassakis, K. A. and G. K. Politis (2013). "Hydrodynamic performance of flapping wings for augmenting ship propulsion in waves." Ocean Engineering **72**: 227-240.

Betz, A. (1912). "Ein Beitrag zur Erklaerung des Segelfluges." Zeitschrift fur Flugtechnik und Motorluftschiffahrt **3**(21): 269-272.

Bisplinghoff, R. L., H. Ashley and R. L. Halfman (1955). Aeroelasticity.

Blevins, R. D. (1992). Applied Fluid Dynamics Handbook.

Blondeaux, P., F. Fornarelli, L. Guglielmini, M. S. Triantafyllou and R. Verzicco (2005). "Numerical experiments on flapping foils mimicking fish-like locomotion." Physics of Fluids **17**(11): 1-12.

Blondeaux, P., F. Fornarelli, L. Guglielmini, M. S. Triantafyllou and R. Verzicco (2005). Vortex structures generated by a finite-span oscillating foil, Reno, NV.

Blondeaux, P., L. Guglielmini and M. S. Triantafyllou (2005). "Chaotic flow generated by an oscillating foil." AIAA Journal **43**(4): 918-921.

Bøckmann, E. and S. Steen (2014). "Experiments with actively pitch-controlled and spring-loaded oscillating foils." Applied Ocean Research **48**: 227-235.

Borazjani, I. and F. Sotiropoulos (2008). "Numerical investigation of the hydrodynamics of carangiform swimming in the transitional and inertial flow regimes." Journal of Experimental Biology **211**(10): 1541-1558.

Borazjani, I. and F. Sotiropoulos (2009). "Numerical investigation of the hydrodynamics of anguilliform swimming in the transitional and inertial flow regimes." Journal of Experimental Biology **212**(4): 576-592.

Bose, N. (1992). "A time-domain panel method for analysis of foils in unsteady motion as oscillating propulsors." 11th Australasian Fluid Mechanics Conference.

Bose, N. (1993). "Propulsive performance of chordwise flexible oscillating foils using a time-domain panel method." Second Canadian Marine Dynamics Conference: 150-156.

Bose, N. (2008). Marine Powering Prediction and Propulsors, SNAME.

Brackenbury, J. (2002). "Kinematics and hydrodynamics of an invertebrate undulatory swimmer: The damsel-fly larva." Journal of Experimental Biology **205**(5): 627-639.

Bratt, J. B. (1953). "Flow patterns in the wake of an oscillating airfoil." Aeronautical Research Council.

Chopra, A. K. (1995). Dynamics of Structures: Theory and Applications to Earthquake Engineering.

Chopra, A. K. (2007). Structural Dynamics.

Chopra, M. G. (1976). "LARGE AMPLITUDE LUNATE-TAIL THEORY OF FISH LOCOMOTION." Journal of Fluid Mechanics **74**(pt 1): 161-182.

Coene, R. (1975). "SWIMMING OF FLEXIBLE SLENDER BODIES IN WAVES." Journal of Fluid Mechanics **72**(pt 2): 289-303.

Combes, S. A. and T. L. Daniel (2003). "Flexural stiffness in insect wings I. Scaling and the influence of wing venation." Journal of Experimental Biology **206**(17): 2979-2987.

Daniel, T. L. and S. A. Combes (2002). "Flexible wings and fins: Bending by inertial or fluid-dynamic forces?" Integrative and Comparative Biology **42**(5): 1044-1049.

Dickinson, M. H., F. O. Lehmann and S. P. Sane (1999). "Wing rotation and the aerodynamic basis of insect right." Science **284**(5422): 1954-1960.

Dokainish, M. A. and K. Subbaraj (1989). "A survey of direct time-integration methods in computational structural dynamics-I. Explicit methods." Computers and Structures **32**(6): 1371-1386.

Dokainish, M. A. and K. Subbaraj (1989). "A survey of direct time-integration methods in computational structural dynamics—II. Implicit methods." Computers & Structures **32**(6): 1371-1386.

Dokainish, M. A. and K. Subbaraj (1989). "A survey of direct time-integration methods in computational structural dynamics—III. Recent developments in Implicit methods." Computers & Structures **32**(6): 1371-1386.

Dokainish, M. A. and K. Subbaraj (1989). "A survey of direct time-integration methods in computational structural dynamics—IV. Mixed Implicit -Explicit Methods." Computers & Structures **32**(6): 1371-1386.

Dong, H., R. Mittal and F. M. Najjar (2006). "Wake topology and hydrodynamic performance of low-aspect-ratio flapping foils." Journal of Fluid Mechanics **566**: 309-343.

Drucker, E. G. (1996). "The use of gait transition speed in comparative studies of fish locomotion." American Zoologist **36**(6): 555-566.

Drucker, E. G. and G. V. Lauder (2002). "Experimental hydrodynamics of fish locomotion: Functional insights from wake visualization." Integrative and Comparative Biology **42**(2): 243-257.

Dudley, R., G. Byrnes, S. P. Yanoviak, B. Borrell, R. M. Brown and J. A. McGuire (2007). Gliding and the functional origins of flight: Biomechanical novelty or necessity? **38:** 179-201.

Ellington, C. P., C. D. Van Berg, A. P. Willmott and A. L. R. Thomas (1996). "Leading-edge vortices in insect flight." Nature **384**(6610): 626-630.

Eloy, C. (2012). "Optimal Strouhal number for swimming animals." Journal of Fluids and Structures **30**: 205-218.

Filippas, E. S. and K. A. Belibassakis (2013). Free surface effects on hydrodynamic analysis of flapping foil thrusters in waves, Nantes.

Filippas, E. S. and K. A. Belibassakis (2014). A boundary element method for the hydrodynamic analysis of flapping-foil thrusters operating beneath the free surface and in waves, A Coruna.

Filippas, E. S. and K. A. Belibassakis (2014). "Hydrodynamic analysis of flapping-foil thrusters operating beneath the free surface and in waves." Engineering Analysis with Boundary Elements **41**: 47-59.

Fish, F. E. (1984). "Mechanics, power output and efficiency of the swimming muskrat (Ondatra zibethicus)." Journal of Experimental Biology **110**: 183-201.

Floc'h, F., S. Phoemsapthawee, J. M. Laurens and J. B. Leroux (2012). "Porpoising foil as a propulsion system." Ocean Engineering **39**(0): 53-61.

Freymuth, P. (1988). "Propulsive vortical signatures of plunging and pitcing airfoils." AIAA Paper(323).

Garrick, I. E. (1936). "Propulsion of a flapping and oscillating airfoil." Propulsion of a Flapping and Oscillating Airfoil.

Geradin, M. and D. Rixen (1994). "Mechanical vibrations. Theory and application to structural dynamics." Mechanical Vibrations: Theory and Application to Structural Dynamics.

Godoy-Diana, R., J. L. Aider and J. E. Wesfreid (2008). "Transitions in the wake of a flapping foil." Physical Review E - Statistical, Nonlinear, and Soft Matter Physics **77**(1).

Godoy-Diana, R., C. Marais, J. L. Aider and J. E. Wesfreid (2009). "A model for the symmetry breaking of the reverse Bénard-von Kármán vortex street produced by a flapping foil." Journal of Fluid Mechanics **622**: 23-32.

Golubev, V. V. (1944). "Mechanics of thrust generation by a flapping wing." Trudy Nauchnoteknichtskoi Konferentsii VVIA im. Prof. N.E. Zhukovskogo **3**: 7-19.

Golubev, V. V. (1946). "Thrust of a flapping wing." Otdelenie Tekhnicheskikh Nauk **5**: 46-58.

Guglielmini, L., P. Blondeaux and G. Vittori (2004). "A simple model of propulsive oscillating foils." Ocean Engineering **31**(7): 883-899.

He, M., B. Veitch, N. Bose, B. Colbourne and P. Liu (2007). "A three-dimensional wake impingement model and applications on tandem oscillating foils." Ocean Engineering **34**(8-9): 1197-1210.

Hodges, D. H. and G. A. Pierce (2002). "Introduction to structural dynamics and aeroelasticity." Introduction to Structural Dynamics and Aeroelasticity.

Hover, F. S., Ø. Haugsdal and M. S. Triantafyllou (2004). "Effect of angle of attack profiles in flapping foil propulsion." Journal of Fluids and Structures **19**(1): 37-47.

Hover, F. S., D. A. Read and M. S. Triantafyllou (2001). "Experiments with a 2D oscillating foil for propulsion and maneuvering." 12th International Symposium on Unmanned Untethered Submersible Technology (UUST01).

James, E. C. (1975). "LIFTING-LINE THEORY FOR AN UNSTEADY WING AS A SINGULAR PERTURBATION PROBLEM." Journal of Fluid Mechanics **70**(pt 4): 753-771.

Katz, J. and D. Weihs (1978). "HYDRODYNAMIC PROPULSION BY LARGE AMPLITUDE OSCILLATION OF AN AIRFOIL WITH CHORDWISE FLEXIBILITY." Journal of Fluid Mechanics **88**(pt 3): 485-497.

Katzmayr, R. (1922). "Effect of periodic changes of angle of attack on behavior of airfoils." NACA TM No. 147(147).

Keldysh, M. V. and M. A. Lavrentiev (1935). "On the theory of the oscillating wing." Tekhnicheskiye Zametki TsAGI im. Prof. N.E. Zhukovskogo(35): 48-52.

Kim, E. and Y. Youm (2004). Design and dynamic analysis of fish robot: PoTuna, New Orleans, LA.

Knoller, R. (1909). "Die Gesetze des Luftwiderstandes." Flug-und Motortechnik (Wien) **3**(21): 1-7.

La Mantia, M. and P. Dabnichki (2008). "Unsteady 3D boundary element method for oscillating wing." CMES - Computer Modeling in Engineering and Sciences **33**(2): 131-153.

La Mantia, M. and P. Dabnichki (2009). "Unsteady panel method for flapping foil." Engineering Analysis with Boundary Elements **33**(4): 572-580.

La Mantia, M. and P. Dabnichki (2012). "Added mass effect on flapping foil." Engineering Analysis with Boundary Elements **36**(4): 579-590.

Lauder, G. V. and E. G. Drucker (2004). "Morphology and experimental hydrodynamics of fish fin control surfaces." IEEE Journal of Oceanic Engineering **29**(3): 556-571.

Lauder, G. V., B. Flammang and S. Alben (2012). "Passive robotic models of propulsion by the bodies and caudal fins of fish." Integrative and Comparative Biology **52**(5): 576-587.

Lauder, G. V. and E. D. Tytell (2005). Hydrodynamics of Undulatory Propulsion. Fish Physiology. **23:** 425-468.

Levi, E. (1983). "UNIVERSAL STROUHAL LAW." Journal of Engineering Mechanics **109**(3): 718-727.

Lewin, G. C. and H. Haj-Hariri (2003). "Modelling thrust generation of a two-dimensional heaving airfoil in a viscous flow." Journal of Fluid Mechanics(492): 339-362.

Lian, Y., W. Shyy, D. Viieru and B. Zhang (2003). "Membrane wing aerodynamics for micro air vehicles." Progress in Aerospace Sciences **39**(6-7): 425-465.

Lighthill, J. (1977). "Aquatic animal locomotion." TRANS. N.E. COAST INST. ENGRS. & SHIPBUILD. **93**(6 , Jul. 1977): 127-135.

Lighthill, M. J. (1969). "Hydromechanics of aquatic animal propulsion." Annu. Rev. Fluid Mech. **1**: 413-446.

Liu, H. (2009). "Integrated modeling of insect flight: From morphology, kinematics to aerodynamics." Journal of Computational Physics **228**(2): 439-459.

Liu, H., R. Wassersug and K. Kawachi (1997). "The three-dimensional hydrodynamics of tadpole locomotion." Journal of Experimental Biology **200**(22): 2807-2819.

Liu, P. and N. Bose (1997). "Propulsive performance from oscillating propulsors with spanwise flexibility." Proceedings of the Royal Society A: Mathematical, Physical and Engineering Sciences **453**(1963): 1763-1770.

Liu, P. and N. Bose (1999). "Hydrodynamic characteristics of a lunate shape oscillating propulsor." Ocean Engineering **26**(6): 519-529.

Low, K. H. (2006). Maneuvering and buoyancy control of robotic fish integrating with modular undulating fins, Kunming.

Low, K. H. (2007). "Design, development and locomotion control of bio-fish robot with undulating anal fins." International Journal of Robotics and Automation **22**(1): 88-99.

Low, K. H. (2009). "Modelling and parametric study of modular undulating fin rays for fish robots." Mechanism and Machine Theory **44**(3): 615-632.

Luznik, L. and N. Bose (1998). "Propulsive thrust of an oscillating foil at large angles of attack: Experimental study." Am. Towing Tank Conf.: 1-8.

Mason, R. and J. W. Burdick (2000). Experiments in Carangiform robotic fish locomotion, San Francisco, CA, USA.

McGovern, S. T., G. M. Spinks, B. Xi, G. Alici, V. Truong and G. G. Wallace (2008). Fast bender actuators for fish-like aquatic robots, San Diego, CA.

McLetchie, K. M. W. (2003). Drag reduction of an elastic fish model, San Diego, CA.

Menozzi, A., P. Bandyopadhyay and S. Warren (2005). Interfacing olivo-cerebellar neuron hardware to FIN actuators of a Biorobotic Autonomous Underwater Vehicle, Cambridge, MA.

Menozzi, A. and H. Leinhos (2007). Synthesis and coordination of the motion of multiple flapping foils for control of a biorobotic AUV.

Ming, A., Y. Huang, Y. Fukushima and M. Shimojo (2008). Development of an active flapping wing using piezoelectric fiber composites, Bangkok.

Mojarrad, M. (2000). AUV biomimetic propulsion, Providence, RI, USA, IEEE.

Mojarrad, M. and M. Shahinpoor (1997). Biomimetic robotic propulsion using polymeric artificial muscles, Albuquerque, NM, USA, IEEE.

Morgansen, K. A., V. Duindam, R. J. Mason, J. W. Burdick and R. M. Murray (2001). Nonlinear control methods for planar carangiform robot fish locomotion, Seoul.

Morikawa, H. and N. Isshiki (1980). "The study on a propulsion system by fin stroke." Bulletin of M.E.S.J **8**(1): 71-79.

Muramatsu, K., M. Watanabe and N. Kobayashi (2001). Aquatic mobile robot using waving motion of a flexible fin, Pittsburgh, PA.

Nakabayashi, M., R. Kobayashi, S. Kobayashi and H. Morikawa (2008). A novel propulsion mechanism using a fin with a variable-effective-length spring, Bangkok.

Nakabayashi, M., R. Kobayashi, S. Kobayashi and H. Morikawa (2009). "Bioinspired propulsion mechanism using a fin with a dynamic variable-effective-length spring: Evaluation of thrust characteristics and flow around a fin in a uniform flow." Journal of Biomechanical Science and Engineering **4**(1): 82-93.

Nakadoi, H., D. Sobey, M. Yamakita and T. Mukai (2008). Liquid environment-adaptive IPMC fish-like robot using extremum seeking feedback, Nice.

Narasimhan, M., H. Dong, R. Mittal and S. N. Singh (2006). "Optimal yaw regulation and trajectory control of biorobotic AUV using mechanical fins based on CFD parametrization." Journal of Fluids Engineering, Transactions of the ASME **128**(4): 687-698.

Newman, J. N. and T. Y. Wu (1973). "GENERALIZED SLENDER-BODY THEORY FOR FISH-LIKE FORMS." Journal of Fluid Mechanics **57**(Part 4): 673-693.

Nikolaev, M. N., A. I. Savitskiy and Y. U. F. Senkin (1995). "Basics of calculation of the efficiency of a ship was propulsor of the wing type." Sudostroenie **4**: 7-10.

Norberg, U. M. (1986). "Evolutionary convergence in foraging niche and flight morphology in insectivorous aerial-hawking birds and bats." Ornis Scandinavica **17**(3): 253-260.

Pavlenko, G. E. (1936). "Energy extraction in the course of the ship motion in waves." Sudostroenie **6**: 394-401.

Pines, D. J. and F. Bohorquez (2006). "Challenges facing future micro-air-vehicle development." Journal of Aircraft **43**(2): 290-305.

Platzer, M. F., K. D. Jones, J. Young and J. C. S. Lai (2008). "Flapping-wing aerodynamics: Progress and challenges." AIAA Journal **46**(9): 2136-2149.

Poling, D. R. and D. P. Telionis (1986). "RESPONSE OF AIRFOILS TO PERIODIC DISTURBANCES - THE UNSTEADY KUTTA CONDITION." AIAA journal **24**(2): 193-199.

Politis, G. and K. Politis (2012). "Biomimetic propulsion under random heaving conditions, using active pitch control." Journal of Fluids and Structures.

Politis, G. and K. Politis (2014). "Biomimetic propulsion under random heaving conditions, using active pitch control." Journal of Fluids and Structures **47**: 139-149.

Politis, G. and V. Tsarsitalidis (2012). "Flexible Oscillating Duct: An approach to a novel propulsor." Applied Ocean Research **36**: 36-50.

Politis, G. K. (2004). "Simulation of unsteady motion of a propeller in a fluid including free wake modeling." Engineering Analysis with Boundary Elements **28**(6): 633-653.

Politis, G. K. (2005). "Unsteady rollup modeling for wake-adapted propellers using a time-stepping method." Journal of Ship Research **49**(3): 216-231.

Politis, G. K. (2009). A BEM Code for the Calculation of Flow Around Systems of Independently Moving Bodies Including Free Shear Layer Dynamics, In: Sapountzakis, E.J., Aliabadi, M.H. (Eds.): 381-388.

Politis, G. K. (2011). "Application of a BEM time stepping algorithm in understanding complex unsteady propulsion hydrodynamic phenomena." Ocean Engineering **38**(4): 699-711.

Politis, G. K. (2011). The BEM as a tool for analysing unsteady propulsor motions, with applications to maneuvering propellers and biomimetic flows, Lisbon.

Politis, G. K., T. Ioannou and V. T. Tsarsitalidis (2013). "Flexible elliptic oscillating duct. Taking the FOD one step further." Third International Symposium on Marine Propulsors, SMP13.

Politis, G. K., Tsarsitalidis V. T. (2009). Simulating Biomimetic (Flapping Foil) Flows for Comprehension, Reverse Engineering and Design. First International Symposium on Marine Propulsors, SMP'09. Trondheim Norway.

Politis, G. K. and V. T. Tsarsitalidis (2009). Simulating Biomimetic (Flapping Foil) Flows for Comprehension, Reverse Engineering and Design. First International Symposium on Marine Propulsors, smp'09. Trondheim, Norway.

Politis, G. K. and V. T. Tsarsitalidis (2010). UNDERSTANDING BIRD'S FLIGHT, USING A 3-D BEM METHOD AND A TIME STEPPING ALGORITHM. 4th IC-SCCE 2010. Athens, Greece.

Politis, G. K. and V. T. Tsarsitalidis (2013). "Biomimetic propulsion using twin oscillating wings." Third International Symposium on Marine Propulsors, SMP13.

Politis, G. K. and V. T. Tsarsitalidis (2014). "Flapping wing propulsor design: An approach based on systematic 3D-BEM simulations." Ocean Engineering **84**: 98-123.

Prempraneerach, P., F. S. Hover and M. S. Triantafyllou (2003). "The effect of chordwise flexibility on the thrust and efficiency of a flapping foil." International Symposium on Unmanned Untethered Submersible Technology.

Ramamurti, R. and W. C. Sandberg (2002). "A three-dimensional computational study of the aerodynamic mechanisms of insect flight." Journal of Experimental Biology **205**(10): 1507-1518.

Ramamurti, R. and W. C. Sandberg (2007). A computational study of the aerodynamics of hovering and maneuvering in Drosophila, Reno, NV.

Riziotis, V. A., P. K. Chaviaropoulos and S. G. Voutsinas (1996). "Develpoment of a state-of-the art aeroelastic simulator for horizontal axis wind turbines. Part 2: Aerodynamic aspects and application." Wind Engineering **20**(6): 423-440.

Rozhdestvensky, K. V. and V. A. Ryzhov (2003). "Aerohydrodynamics of flapping-wing propulsors." Progress in Aerospace Sciences **39**(8): 585-633.

Sandberg, W. C., R. Ramamurti and R. Lohner (2001). "Pectorial fin flapping with and without deformations in the bird wrasse; 2-D unsteady computations." 12th International Symposium on Unmanned Untethered Submersible Technology (UUST01).

Sane, S. P. (2003). "The aerodynamics of insect flight." Journal of Experimental Biology **206**(23): 4191-4208.

Sane, S. P. and M. H. Dickinson (2001). "The control of flight force by a flapping wing: Lift and drag production." Journal of Experimental Biology **204**(15): 2607-2626.

Sane, S. P. and M. H. Dickinson (2002). "The aerodynamic effects of wing rotation and a revised quasi-steady model of flapping flight." Journal of Experimental Biology **205**(8): 1087-1096.

Sane, S. P., A. Dieudonné, M. A. Willis and T. L. Daniel (2007). "Antennal mechanosensors mediate flight control in moths." Science **315**(5813): 863-866.

Sarpkaya, T. (1975). "AN INVISCID MODEL OF TWO-DIMENSIONAL VORTEX SHEDDING FOR TRANSIENT AND ASYMPTOTICALLY STEADY SEPARATED FLOW OVER AN INCLINED PLATE." Journal of Fluid Mechanics **68**(1).

Schmidt, W. (1965). "Der Wellpropeller, ein neuer Antrieb fuer Wasser-, Land-, und Luftfahrzeuge." Zeitschrift für Flugwissenschaften **13**(12): 472-479.

Sfakiotakis, M., D. M. Lane and J. B. C. Davies (1999). "Review of fish swimming modes for aquatic locomotion." IEEE Journal of Oceanic Engineering **24**(2): 237-252.

Shyy, W., H. Aono, S. K. Chimakurthi, P. Trizila, C. K. Kang, C. E. S. Cesnik and H. Liu (2010). "Recent progress in flapping wing aerodynamics and aeroelasticity." Progress in Aerospace Sciences **46**(7): 284-327.

Shyy, W., P. Ifju and D. Viieru (2005). "Membrane wing-based micro air vehicles." Applied Mechanics Reviews **58**(1-6): 283-301.

Singh, S. N., A. Simha and R. Mittal (2004). "Biorobotic AUV maneuvering by pectoral fins: Inverse control design based on CFD parameterization." IEEE Journal of Oceanic Engineering **29**(3): 777-785.

Sparenberg, J. A. (2002). "Survey of the mathematical theory of fish locomotion." Journal of Engineering Mathematics **44**(4): 395-448.

Stanford, B., P. Ifju, R. Albertani and W. Shyy (2008). "Fixed membrane wings for micro air vehicles: Experimental characterization, numerical modeling, and tailoring." Progress in Aerospace Sciences **44**(4): 258-294.

Streitlien, K. and G. S. Triantafyllou (1998). "On thrust estimates for flapping foils." Journal of Fluids and Structures **12**(1): 47-55.

Streitlien, K., G. S. Triantafyllou and M. S. Triantafyllou (1996). "Efficient foil propulsion through vortex control." AIAA Journal **34**(11): 2315-2319.

Streitlien, K. and M. S. Triantafyllou (1995). "Force and moment on a Joukowski profile in the presence of point vortices." AIAA journal **33**(4): 603-610.

Su, Y., Z. Wang, Y. Li, Z. Qin and W. Chen (2009). Study on hydrodynamics of a bionic flapping hydrofoil, Guilin.

Sun, M. and J. Wu (2003). "Unsteady lift mechanisms and energetic in flying insects." Beijing Hangkong Hangtian Daxue Xuebao/Journal of Beijing University of Aeronautics and Astronautics **29**(11): 970-977.

Sun, M. and J. H. Wu (2002). "Biomimetic aerodynamics of micro-air vehicles - Aerodynamic force and power requirements in forward flight of insect." Hangkong Xuebao/Acta Aeronautica et Astronautica Sinica **23**(5): 385-393.

Tang, J., S. Chimakurthi, R. Palacios, C. E. S. Cesnik and W. Shyy (2008). Computational fluid-structure interaction of a deformable flapping wing for micro air vehicle applications, Reno, NV.

Tang, J. and M. Sun (2001). "Force and flow structures of a wing performing flapping motion at low Reynolds number." Acta Mechanica **152**(1-4): 35-48.

Taylor, G. K., M. S. Triantafyllou and C. Tropea (2010). "Animal locomotion." Proc. 26th Springer Verlag.

Techet, A. H. (2008). "Propulsive performance of biologically inspired flapping foils at high Reynolds numbers." Journal of Experimental Biology **211**(2): 274-279.

Techet, A. H. and M. S. Triantafyllou (1999). "Boundary layer relaminarization in swimming fish." Proceedings of the 1999 Ninth International Offshore and Polar Engineering Conference: 415-418.

Tobalske, B. W. (2001). "Morphology, velocity, and intermittent flight in birds'." American Zoologist **41**(2): 177-187.

Tobalske, B. W. (2007). "Biomechanics of bird flight." Journal of Experimental Biology **210**(18): 3135-3146.

Tobalske, B. W. (2009). "Evolution: Symmetry in turns." Science **324**(5924): 190-191.

Tobalske, B. W., J. W. D. Hearn and D. R. Warrick (2009). "Aerodynamics of intermittent bounds in flying birds." Experiments in Fluids **46**(5): 963-973.

Tobalske, B. W., T. L. Hedrick, K. P. Dial and A. A. Biewener (2003). "Comparative power curves in bird flight." Nature **421**(6921): 363-366.

Tobalske, B. W., D. R. Warrick, C. J. Clark, D. R. Powers, T. L. Hedrick, G. A. Hyder and A. A. Biewener (2007). "Three-dimensional kinematics of hummingbird flight." Journal of Experimental Biology **210**(13): 2368-2382.

Triantafyllou, G. S., M. S. Triantafyllou and M. A. Grosenbaugh (1993). "Optimal Thrust Development in Oscillating Foils with Application to Fish Propulsion." Journal of Fluids and Structures **7**(2): 205-224.

Triantafyllou, M. S., D. S. Barrett, D. K. P. Yue, J. M. Anderson, M. A. Grosenbaugh, K. Streitlien and G. S. Triantafyllou (1996). New paradigm of propulsion and maneuvering for marine vehicles, New York, NY, USA, Soc of Naval Architects & Marine Engineers.

Triantafyllou, M. S., F. S. Hover, A. H. Techet and D. K. P. Yue (2005). "Review of hydrodynamic scaling laws in aquatic locomotion and fishlike swimming." Applied Mechanics Reviews **58**(1-6): 226-236.

Triantafyllou, M. S., A. H. Techet and F. S. Hover (2004). "Review of experimental work in biomimetic foils." IEEE Journal of Oceanic Engineering **29**(3): 585-594.

Triantafyllou, M. S. and G. S. Triantafyllou (1995). "An efficient swimming machine." Scientific American **272**(3): 40-48.

Triantafyllou, M. S., G. S. Triantafyllou and R. Gopalkrishnan (1991). "Wake mechanics for thrust generation in oscillating foils." Physics of Fluids A **3**(12): 2835-2837.

Tuncer, I. H., J. Lai, M. A. Ortiz and M. F. Platzer (1997). "Unsteady aerodynamics of stationary/flapping airfoil." AIAA Paper, No. 97-0659 **659**.

Tuncer, I. H. and M. F. Platzer (1996). "Thrust generation due to airfoil flapping." AIAA Journal **34**(2): 324-331.

Tuncer, I. H. and M. F. Platzer (1999). "A computational study of flow separation characteristics and wake profiles behind a flapping airfoil." AIAA Paper, No. 99-0648 **648**.

Tuncer, I. H. and M. F. Platzer (2000). "Computational study of flapping airfoil aerodynamics." Journal of Aircraft **37**(3): 514-520.

Tuncer, I. H., M. F. Platzer and J. A. Ekaterinaris (1994). Computational analysis of flapping airfoil aerodynamics. American Society of Mechanical Engineers, Fluids Engineering Division (Publication) FED.

Usherwood, J. R. and C. P. Ellington (2002). "The aerodynamics of revolving wings I. Model hawkmoth wings." Journal of Experimental Biology **205**(11): 1547-1564.

Vezza, M. and R. A. M. Galbraith (1985). "INVISCID MODEL OF UNSTEADY AEROFOIL FLOW WITH FIXED UPPER SURFACE SEPARATION." International Journal for Numerical Methods in Fluids **5**(6): 577-592.

Vezza, M. and R. A. M. Galbraith (1985). "METHOD FOR PREDICTING UNSTEADY POTENTIAL FLOW ABOUT AN AEROFOIL." International Journal for Numerical Methods in Fluids **5**(4): 347-356.

von Ellenrieder, K. D., K. Parker and J. Soria (2003). "Flow structures behind a heaving and pitching finite-span wing." Journal of Fluid Mechanics(490): 129-138.

von Ellenrieder, K. D., K. Parker and J. Soria (2008). "Fluid mechanics of flapping wings." Experimental Thermal and Fluid Science **32**(8): 1578-1589.

Von Kármán, T. and J. M. Burgers (1935). "General aerodynamic theory - Perfect fluids." Aerodynamic Theory **2**.

Voutsinas, S. G. and V. A. Riziotis (1996). "Vortex particle modelling of stall on rotors. Application to wind turbines." American Society of Mechanical Engineers, Fluids Engineering Division (Publication) FED **238**: 25-29.

Walker, J. A. and M. W. Westneat (1997). "Labriform propulsion in fishes: Kinematics of flapping aquatic flight in the bird wrasse gomphosus varius (labridae)." Journal of Experimental Biology **200**(11): 1549-1569.

Walker, J. A. and M. W. Westneat (2002). "Kinematics, dynamics, and energetics of rowing and flapping propulsion in fishes." Integrative and Comparative Biology **42**(5): 1032-1043.

Walker, S. M., A. L. R. Thomas and G. K. Taylor (2009). "Deformable wing kinematics in the desert locust: How and why do camber, twist and topography vary through the stroke?" Journal of the Royal Society Interface **6**(38): 735-747.

Wang, Z. J. (2000). "Vortex shedding and frequency selection in flapping flight." Journal of Fluid Mechanics **410**: 323-341.

Wang, Z. J. (2001). "Computation of insect hovering." Mathematical Methods in the Applied Sciences **24**(17-18): 1515-1521.

Wang, Z. J. (2005). Dissecting insect flight. Annual Review of Fluid Mechanics. **37:** 183-210.

Wang, Z. J., J. M. Birch and M. H. Dickinson (2004). "Unsteady forces and flows in low Reynolds number hovering flight: Two-dimensional computations vs robotic wing experiments." Journal of Experimental Biology **207**(3): 449-460.

Westneat, M. W. and J. A. Walker (1997). "Motor patterns of labriform locomotion: Kinematic and electromyographic analysis of pectoral fin swimming in the labrid fish Gomphosus varius." Journal of Experimental Biology **200**(13): 1881-1893.

Willis, D. J., J. Peraire and J. K. White (2007). "A combined pFFT-multipole tree code, unsteady panel method with vortex particle wakes." International Journal for Numerical Methods in Fluids **53**(8): 1399-1422.

Willmott, A. P. and C. P. Ellington (1997). "The mechanics of flight in the hawkmoth Manduca sexta I. Kinematics of hovering and forward flight." Journal of Experimental Biology **200**(21): 2705-2722.

Willmott, A. P. and C. P. Ellington (1997). "The mechanics of flight in the hawkmoth manduca sexta II. Aerodynamic consequences of kinematic and morphological variation." Journal of Experimental Biology **200**(21): 2723-2745.

Willmott, A. P., C. P. Ellington and A. L. R. Thomas (1997). "Flow visualization and unsteady aerodynamics in the flight of the hawkmoth, Manduca sexta." Philosophical Transactions of the Royal Society B: Biological Sciences **352**(1351): 303-316.

Wright, J. R. and J. E. Cooper (2007). "Introduction to Aircraft Aeroelasticity and Loads." Introduction to Aircraft Aeroelasticity and Loads.

Wu, T. Y. (1971). "Hydromechanics of swimming propulsion. Part 1. Swimming of a two-dimensional flexible plate at variable forward speeds in an inviscid fluid." J. of Fluid Mechanics **46**: 337–355.

Yamaguchi, N. (2001). "Analytical study on the fluid-elastic characteristics of the vibrating elastic plate flow Generators (1st Report, Estimation of the Fluid-Elastic Behavior and the Characteristics of the Flow Generators)." Nihon Kikai Gakkai Ronbunshu, B Hen/Transactions of the Japan Society of Mechanical Engineers, Part B **67**(661): 2197-2201.

Zbikowski, R., S. A. Ansari and K. Knowles (2006). "On mathematical modelling of insect flight dynamics in the context of micro air vehicles." Bioinspiration and Biomimetics **1**(2): R26-R37.

Zervos, A. and G. Coulmy (1984). UNSTEADY PERIODIC MOTION OF A FLEXIBLE THIN PROPULSOR USING THE BOUNDARY ELEMENT METHOD. Notes on Numerical Fluid Mechanics.

Zhu, Q., M. J. Wolfgang, D. K. P. Yue and M. S. Triantafyllou (2002). "Three-dimensional flow structures and vorticity control in fish-like swimming." Journal of Fluid Mechanics **468**: 1-28.